TOWARDS A PRECISION MEASUREMENT OF THE NEWTONIAN CONSTANT OF GRAVITATION AND ACCELEROMETRY WITH A LEVITATED MICROSPHERE IN A MAGNETO-GRAVITATIONAL TRAP

by

Charles Wayne Lewandowski

A dissertation submitted in partial fulfillment
of the requirements for the degree

of

Doctor of Philosophy

in

Physics

MONTANA STATE UNIVERSITY
Bozeman, Montana

April 2020

©COPYRIGHT

by

Charles Wayne Lewandowski

2020

All Rights Reserved

ACKNOWLEDGEMENTS

My brother, Chris, deserves more thanks than it is possible to give. He has constantly kept me motivated, supported me, and helped when times got stressful. As a police officer, he is tasked with keeping the streets around Pittsburgh safe. To me, he will always be a hero in more ways than just his law enforcement career. I also thank my parents, Chuck and Diane, for their support and many sacrifices to help me throughout my education.

Professor Brian D'Urso deserves much thanks for being the best advisor one can ever hope for. His brilliant ideas and insight have made the work for this dissertation possible. He has always been there to assist with any problem, not just physics.

I want to thank our collaborators Dr. Zachariah Etienne and Tyler Knowles for taking on the challenge of handling analysis of our data. The administrative staff and machine shops at the University of Pittsburgh and Montana State University deserves much thanks for their help throughout this journey.

I finally acknowledge Sir Isaac Newton and Mr. Henry Cavendish whose brilliant theoretical and experimental research inspired scientists for centuries to study classical gravity, including to help motivate the work in this dissertation.

This material is based upon work supported by the National Science Foundation under Grant No. 1707789 and 1757005, and a block gift from the II-VI Foundation.

VITA

Charles Wayne Lewandowski was born in Pittsburgh, PA in 1992 to Diane and Charles Lewandowski. He has a twin brother, Christopher Lewandowski. Charles attended Taylor Allderdice High School in Pittsburgh and graduated in 2010 with honors. In August of 2010, he started college at the University of Pittsburgh. Charles graduated with a Bachelor of Science degree in Physics with honors and Mathematics in April 2015. He started his doctorate studies at the University of Pittsburgh in August of 2015 under the advisement of Dr. Brian D'Urso. Charles transferred to Montana State University in July of 2017 to continue his dissertation work under Dr. Brian D'Urso, now at Montana State University.

TABLE OF CONTENTS

1. INTRODUCTION 1

1.1 Motivation 1
1.2 History of Measurements of G 2
1.3 Difficulties in G Measurements 6
1.4 Primary Research Contributions of this Dissertation 7
1.5 Structure of this Dissertation 8

2. REVIEW OF LEVITATED OPTOMECHANICAL SYSTEMS 11

2.1 Introduction 11
2.2 Optical Trap 12
2.3 Quadrupole Ion (Paul) Trap 14
2.4 Magneto-Optical Trap 15
2.5 Magneto-Gravitational Trap 16
2.6 Magnetic Trap 19
2.7 Conclusion 20

3. SYSTEM DESCRIPTION 22

3.1 Introduction 22
3.2 Extended Linear Quadrupole Magneto-Gravitational Trap 23
3.2.1 Permanent Magnets 25
3.2.2 Pole Pieces 26
3.2.3 Trap Construction 28
3.2.4 Trap Mount 32
3.2.5 Spherical Harmonic Approximation of Trapping Potential 38
3.2.6 Potential and Fields 40
3.3 Vacuum System 47
3.3.1 Vacuum Chamber 47
3.3.2 Pumping System 51
3.4 Optics 54
3.5 Conclusions 60

4. MEASUREMENT OF G 62

4.1 Introduction 62
4.2 Time-of-Swing Method 63
4.3 Geometries 66
4.4 Integration Times 69
4.5 Amplitudes of Motion 69

TABLE OF CONTENTS – CONTINUED

4.6 Oscillation Frequencies 70
4.7 Systematic Errors 71
4.8 Systematic Errors of Other Systems 72
4.9 Conclusions 74

5. LOADING AND TRAPPING LARGE PARTICLES 76

5.1 Introduction 76
5.1.1 Loading Horn Circuit 77
5.2 Linear Quadrupole Ion (Paul) Trap 81
5.3 Results 83
5.4 Challenges 86
5.5 Conclusions 87

6. HIGH VOLTAGE VARIABLE VOLTAGE REFERENCE 89

6.1 Introduction 89
6.2 Setup 90
6.3 Results 95
6.4 Conclusions 97

7. CAMERA CONTROL 99

7.1 Introduction 99
7.2 Setup 100
7.3 Laser Feedback 100
7.4 IIR-Filter 103
7.5 Self-Excitation Limiter 105
7.6 Challenges 109
7.7 Conclusions 109

8. TABLE STABILIZATION 111

8.1 Introduction 111
8.2 Theory 111
8.3 Setup 112
8.4 PI Controller 115
8.5 Results 117
8.6 Conclusions 121

TABLE OF CONTENTS – CONTINUED

9. FREQUENCY RESULTS 123

9.1 Introduction 123
9.2 Anharmonicity of the Magneto-Gravitational Trap 124
9.3 Low Frequency Results 128
9.4 Damping Rates 130
9.5 Conclusions 132

10. ACCELEROMETRY 133

10.1 Introduction 133
10.2 Previous Force and Acceleration Measurements 134
10.3 Accelerometer Model 136
10.3.1 Measurements and Notations 136
10.3.2 Harmonic Oscillator Response 136
10.3.2.1 Negative Frequencies 137
10.3.2.2 Newton's Law 139
10.4 Damped Harmonic Oscillator 142
10.5 Damped-Driven Harmonic Oscillator 143
10.6 Discrete Fourier Transform 146
10.7 Results 148
10.7.1 Notes 148
10.7.2 Procedure 148
10.7.3 Feedback Cooling 154
10.7.4 Offline Image Analysis 155
10.7.5 Geophone 156
10.7.6 Transient Result 157
10.7.7 DC Voltage Stabilization Results 161
10.7.8 Table Stabilization Results 161
10.7.9 Accelerometry Results 164
10.8 Noise Analysis 169
10.9 Non-Linear Feedback 177
10.10 Statistical Errors 179
10.11 Additional Data 182
10.12 Conclusions 182

11. SILICON CARBIDE IN G MEASUREMENTS 191

11.1 Introduction 191
11.2 Spherical Silicon Carbide Particle Processing 192

TABLE OF CONTENTS – CONTINUED

11.2.1 Mortar and Pestle SiC Crushing 192
11.2.2 Dry Hydrogen Etching 194
11.2.3 Wet Oxidation Etching 197
11.2.4 Jet Mill Processing 198
11.3 Results 200
11.3.1 Dry Hydrogen Etching Results 200
11.3.2 Wet Oxidation Etching Results 203
11.3.3 Jet Mill Processing Results 205
11.4 Silicon Carbide for a Measurement of G 205
11.5 Conclusions 209

12. CONCLUSION 211

12.1 Improvements 212
12.2 Future Outlook 214
12.3 Significance of this Dissertation 214

REFERENCES CITED 215

APPENDICES 229

APPENDIX A : *Trans Vacuo* Microscope Objective 230
APPENDIX B : Cryogenic System 243
APPENDIX C : Future G Measurement System 250

LIST OF TABLES

Table Page

10.1 The parameters for the geophone amplified with a OPA188 operational amplifier. The temperature is assumed to be 300 K for the geophone. The values were taken from the datasheets of the geophone and OPA188 operational amplifier. The current noise of the amplification circuit is negligible compared to other noise sources in the geophone. 172

10.2 The parameters for the particle system and optics. The temperature is cooled to 9 K or lower. The resonant frequency and Q of the particle was measured from the transient response. 174

A.1 To achieve diffraction-limited performance for a given wavelength and window thickness t, distance d_1 (see Fig. A.1) can be adjusted to the corresponding value in this table. 241

A.2 In the **Zemax** calculations, to avoid vignetted rays, the aperture stop needs to be restricted. For a given wavelength and window thickness t, the aperture stop radius a_r (see Fig. A.1) is adjusted to the corresponding value in this table. 241

LIST OF FIGURES

Figure Page

1.1 A simple illustration showing two spherical masses. Their centers are separated by a distance r. The left and right spheres have masses m_1 and m_2, respectively. The force that each exerts on the other is given by Newton's law of gravity, eq. 1.1. 2

1.2 A figure from Henry Cavendish's 1798 publication illustrating the apparatus he used [1]. The torsion pendulum and its variants have been the standard way of measuring G for centuries. 3

1.3 A plot of some precision measurements of Newton's constant of gravity, G, starting with the 1930 measurement of Heyl at NBS. The accepted value from the 2018 CODATA report is shown by the vertical line and the relative uncertainty by the blue band. It is evident that measurements have not produced consistent values of G. 6

3.1 The machining drawing of the two bottom pole pieces. The two bottom pole pieces are machined with a sharp tip and lapped once returned from the machine shop. The tapped holes are for mounting the trap. All lengths are in inches and all angles are in degrees. 27

3.2 The machining drawing of the two top pole pieces. The two top pole pieces are machined with a sharp tip and lapped once returned from the machine shop. The tips of the top pole pieces are cut shorter than the bottom two pole pieces. All lengths are in inches and all angles are in degrees. 27

LIST OF FIGURES – CONTINUED

Figure Page

3.3 (a) An assembly drawing of the magneto-gravitational trap as viewed from the axial direction. The four pole pieces form a quadrupole field in the vertical and transverse directions. The permanent magnets are labeled by M and oriented such that the poles are as labeled by N and S. (b) A close up view of (a) (black dashed box) showing the quadrupole geometry that is broken in the transverse and vertical directions. (c) The assembly drawing of the trap as viewed from the transverse direction. The top pole pieces are machined shorter than the bottom pole pieces. (d) The trap as viewed from an angle. 29

3.4 The long pole pieces originally designed for the measurement of G. The bottom pole pieces are 193 mm long in the axial direction. The top pole pieces are 187 mm long to provide the magnetic field curving effect. 31

3.5 A view at an angle to illustrate the quadrupole geometry along with the extended pole pieces in the axial direction. 31

3.6 A three dimensional rendering of the front of the trap and its mount. The four sets of adjustment screws allow for fine tuning of the vertical gap. Mounting the trap creates a nominal vertical gap of 750 μm. The mount is photographed in Fig. 3.9. 33

3.7 A three dimensional rendering of the back of the trap and its mount. The copper allows for high thermal conductivity for temperature monitoring and stabilizing of the trap to prevent magnetic field fluctuations. 33

3.8 A three dimensional rendering of the side of the trap and its mount. The use of the adjustment screws is more visible in this view. The clamping mechanism of the trap is also seen. 34

LIST OF FIGURES – CONTINUED

Figure Page

3.9 The front of the trap and mount along the transverse direction. The adjustment screws are visible. The four wires are to put an AC and DC voltage on the pole pieces. This is the same view as Fig. 3.6. 35

3.10 The back of the trap and its mount along the transverse direction. The copper heat spreader and aluminum mounts are attached though no sensor or heater is attached. This is the same view as Fig. 3.7. 36

3.11 The side view of the trap and its mount. The quadrupole geometry of the trap is visible. The vertical gap is approximately 750 μm and the transverse gap is approximately 250 μm. This is the same view as Fig. 3.8. 37

3.12 (a) The magnetic field as viewed from along the optical axis (transverse direction) of the magneto-gravitational trap. The magnetic field curves up at the edges of the trap. A subsection of the axial direction is shown. (b) The magnetic potential is shown. The particle can follow the equipotential lines, which shows the particle is not constrained axially. 43

3.13 (a) The magnetic field as viewed from the axial direction. The quadrupole moment is dominant but the broken symmetry is confirmed by the slight ellipsoidal shape. (b) The magnetic potential in the transverse-vertical plane has a minimum at the center and has a gradient in all direction, constraining the particle in these directions. 43

LIST OF FIGURES – CONTINUED

Figure Page

3.14 (a) The total potential including gravity with no electric field. The potential minimum is at the bottom pole pieces. The magnetic field gradient only is not strong enough to constrain the particle. (b) The total potential with a small qV_0 combination. The electric field is strong enough to raise the potential minimum closer to the center. There is a gradient in the potential in all directions. (c) The total potential where gravity is perfectly canceled out by the electric field. This matches perfectly to Fig. 3.12(b). (d) The total potential with a large qV_0 combination. The electric field overcompensates for gravity and the potential minimum is now at the top pole pieces. 45

3.15 A simple illustration showing qualitatively the behavior of the electric field. Near the center of the trap it is approximately constant and only has a component in the vertical direction. Near the edges of the trap, there is also an axial component that creates a restoring force. 46

3.16 (a) A 3 dimensional rendering of the vacuum chamber used in the experiment. The grabber grooves used to mount the trap are visible around the main sealing surface. The smaller ports also have grabber grooves but are unused in this experiment. (b) The front of the vacuum chamber as viewed from the transverse direction. 48

3.17 The main vacuum chamber as viewed from the front (collection objective side). The chamber sits on a 316 stainless steel pedestal and mounted on a tilt stage. The low thermal conduction pedestal prevents heat from reaching the stage, causing possible damage. The two valves and two feedthroughs are labeled. 49

LIST OF FIGURES – CONTINUED

Figure Page

3.18 The main vacuum chamber as viewed from the back (illumination optics side, see Fig. 3.21 and Fig. 3.22). The large vacuum window allows large angles of optical access for feedback cooling or excitation. 50

3.19 The turbomolecular pump used for the work in this dissertation. Two Pirani gauges and an ion gauge measures the pressure at different locations in the pumping system. Valve V4 is a needle valve used to pump the chamber slowly to prevent particle loss. 52

3.20 The roughing pump used in this experiment. Valve V5 allows the roughing pump to be opened to the vacuum chamber for faster pumping once the system is under rough vacuum from the needle valve V4. 53

3.21 The optical system used in the accelerometry measurements. A 660 nm LED is used collimated onto a 100 μm slit. The slit is then magnified and imaged on the trapped particle. The scattered light from the particle is collected by a 3× telecentric objective and imaged onto a CMOS camera. The images are analyzed in real time to determine the sign and amplitude of the feedback. The 520 nm feedback laser is coupled into a single-mode fiber and then redirected into the chamber at a large angle. The scattered light is blocked by a long pass filter before the fiber. 55

3.22 A photograph of the illumination optics. A 100 μm slit is illuminated by a 660 nm pulsed LED and magnified and imaged onto the trapped particle. 56

3.23 A top view of the collection optics. A long pass filter is attached to the front of the 3× telecentric objective. The objective collects the scattered light from the particle and images it onto a CMOS camera. 57

LIST OF FIGURES – CONTINUED

Figure Page

3.24 A side view of the collection optics. The objective lens and CMOS camera are mounted on a five axis stage for precise adjustment vertically and horizontally, tilt, and focus. 57

3.25 The 520 nm diode laser for the feedback control of the trapped particle. The laser is coupled into a single-mode fiber for cleaning the beam. The laser is housed in an enclosure for safety. 58

3.26 The optics after the single-mode fiber are shown. The light is collimated and redirected using a mirror and periscope. The light is then focused and redirected into the vacuum chamber via the large window. 59

4.1 A simple illustration of the time-of-swing method for measuring G. Two field masses are placed a distance d from the oscillator. The two field masses cause a frequency shift in the test mass. 64

4.2 (a) A plot of the spring constant k_{zG} due to a ring of mass on both sides of the trap. The black dashed lines show where the spring constant is zero. (b)A plot of the first anharmonic spring constant $k_{zG}^{(3)}$ due to a ring of mass on both sides of the trap. The black dashed lines show where this spring constant is zero. 68

5.1 A photograph of the loading horn used for loading particles. The polyimide tape around the handle prevents shorting between the various pole pieces. A piece of polyimide tape is on the tip of the horn to electrostatically hold large particles for loading. 78

5.2 A photograph of the loading circuit board mounted to an Arduino Due. The large heat sinks prevent overheating of the thermal resistors and MOSFET. 78

LIST OF FIGURES – CONTINUED

Figure Page

5.3 The schematic for the loading horn circuit. The shield is attached to an Arduino Due. A MOSFET is used to drive a piezo at varying frequencies. Three large heat sinks are used to prevent overheating of the MOSFET and two thermal resistors. 79

5.4 The circuit board layout for the compact loading circuit. The board is directly attached to an Arduino Due. Three large heat sinks are used to dissipate heat from two resistors and the MOSFET. A push-button switch is used to trigger the start of the frequency sweep. 80

5.5 The wiring diagram for the Paul trap and DC bias on the magneto-gravitational trap. A 50 s filter prevents high frequency noise from being added to the DC voltage. The dashed lines illustrate where jumpers are placed to prevent image charges in the pole pieces from going through high resistance paths. 82

5.6 A photograph of the Paul trap and DC voltage circuit. The jumpers are in place in this photo. 83

6.1 The schematic for one voltage reference board. Three boards are stacked on each other to create a 300 V voltage reference. 91

6.2 The board schematic of the voltage reference switch board. There are ten switches on each board, each controlling one of the ten voltage references. Three boards are connected in series with each other, allowing for an output up to 300 V. 92

6.3 A photograph showing the housing and switches for the boards shown in Fig. 6.2. The red circle shows a switch in the on position for a 300 V output. A high voltage input to the circuit is set at 304 V to create a current through the output resistor in a specified range from Texas Instruments. 92

LIST OF FIGURES – CONTINUED

Figure Page

6.4 A photograph of the AD5791 DAC evaluation board with the Arduino Due and shield to the right. The Grand Central board on the left is used for the feedback cooling. 93

6.5 A wiring diagram for the high voltage variable voltage reference, based on a diagram provided by Bradley Slezak. The AD5791 DAC evaluation board is floated to a variable voltage by the voltage reference board (see Figs. 6.1, 6.2, and 6.3). 94

6.6 Three days of voltage data measured on a Keithley 2000 DMM. The RMS voltage is 0.0001 V with an average voltage −34.6507 V. 96

6.7 Three days of voltage data measured on a Keithley 2000 DMM. The RMS voltage is 0.0001 V with an average voltage −33.1218 V. 96

7.1 An example image of a levitated microsphere that is analyzed for feedback in real time. The particle is a dark disk on a bright background. 101

7.2 An example of the IIR filter used in this dissertation work. The resonant frequency is $f_0 = 1\,\mathrm{Hz}$ and bandwidth $\Delta f = 0.25\,\mathrm{Hz}$. 105

7.3 The feedback velocity as a function of the velocity of the particle for different values of β and $G = 1$ and $v_0 = 100$. The larger β is, the stronger the feedback will be. With this large β, the mean of the particle velocity will converge to the target velocity quickly but will also oscillate around this value. With smaller values of β, the velocity will converge more slowly but not oscillate as much. 107

7.4 The first ten seconds of three 60 s data sets. The three sets were all prepared with the same $\beta = 1.0$ and $v_0 = 250$ μm/s. Initially, all three started at the same amplitude to within 1% of each other. 108

LIST OF FIGURES – CONTINUED

Figure Page

7.5 A close up of the first two seconds of the three data sets. The jagged features at the peaks are due to the particle finding algorithm used when analyzing this data. The three have initial amplitudes within 1% of each other, and could possibly be better if a better image analysis technique is used. 108

8.1 System diagram for the active stabilization of the optical table using two mass flow controllers. One mass flow controller adds air to the pneumatic isolators on the master-slave leg pair and one removes air depending on the tilt of the table. 113

8.2 A photograph of the Jewell Instruments A603-C tiltmeter. 114

8.3 A photograph of the Jewell Instruments LSOC-1Z inclinometer. 114

8.4 The relative tilt of the unstabilized optical table over three days (shown in red). The displacement of the particle (black) is also shown. After approximately four hours, the particle leaves the frame and never reenters. 118

8.5 The relative tilt of the actively stabilized optical table over three days (shown in red). The displacement of the particle during the same time is also shown (black). 118

8.6 A close up view of the large disturbance in the relative tilt at 33.3 hrs. The tilt exceeded the A603-C range and was corrected in approximately 1000 s. 119

9.1 Time domain data of the motion of a borosilicate microsphere. The amplitude of motion is approximately 0.8 mm. At the peak of the displacement, the motion is harmonic (sinusoidal) with a frequency of 0.23 Hz. At the other end of the displacement, the motion is not harmonic (triangular). This is due to a potential wall at that end. 125

LIST OF FIGURES – CONTINUED

Figure Page

9.2 The 0.23 Hz peak corresponding to the axial motion is seen as well as eight higher harmonics. These harmonics are due to the triangular wave motion during half of the motion. 125

9.3 A series of measurements were made with different amplitudes of motion. The frequency of each motion is plotted against their corresponding amplitudes. The point at 6 mm has the lowest frequency but not as low as expected based on results in Fig. 9.6. This is likely due to charge on the pole pieces being larger towards the turning points of the motion causing a larger anharmonicity at that amplitude. 126

9.4 The trajectory of the particle overlaid on an image of the magneto-gravitational trap. The vertical and axial motion corresponding to this trajectory is plotted in Fig. 9.5. From the trajectory and trap image, the cause of the anharmonic motion is visible. Charged contamination, indicated by the on the pole pieces is the main cause. 127

9.5 A subset of the vertical (black) and axial (red) motion in the time domain for the trajectory shown in Fig. 9.4. There is coupling between the two degrees of freedom. 127

9.6 The motion of a borosilicate particle that leaves the frame of the camera. The amplitude of motion is approximately 4 mm. The frequency of motion is the lowest measured in the magneto-gravitational trap, a frequency of 0.1 Hz. 129

9.7 The black curve shows the sinusoidal fit for the first three periods of motion. The red curve is a fit to the second set of three periods. These are out of phase from the first three. The last set of points is again out of phase. Though the frequency is extremely low, the motion is extremely anharmonic. 129

LIST OF FIGURES – CONTINUED

Figure Page

9.8 The axial motion data for a particle excited to an amplitude of approximately 300 μm (red) at an air pressure of 10^{-9} Torr. A fit of the data to an exponentially decaying sine wave is shown in black. The damping rate measured is $7 \times 10^{-4}\,\mathrm{s}^{-1}$, significantly higher than predicted from the air pressure. 131

10.1 A photograph of the Sercel, Inc. L-4C 3D geophone. The left red arrow indicates the spirit level and the right arrow indicates one of the geophone axes. 149

10.2 A connection diagram for the 7-bit divider. 152

10.3 A flow diagram showing how the accelerometry experiment was controlled and the connections between the equipment used. 153

10.4 The calibration of the geophone and its amplification circuit sensitivity. The ratio of the amplified voltage and the unamplified voltage is $S_g = 180.2$. 157

10.5 The USAF1951 calibration target imaged onto the CMOS from the collection optics of the system. The group 5 element 1 line is 15.63 μm across approximately 13.6 pixels. 158

10.6 Transient motion of the magneto-gravitationally levitated microsphere after an excitation with feedback cooling applied. The oscillation frequency is $\omega_z/(2\pi) = 1.75\,\mathrm{Hz}$ with a damping rate of $\Gamma = 6.26 \times 10^{-2}\,\mathrm{s}^{-1}$, illustrated by the black dashed lines. 158

10.7 The DC voltage across the top and bottom pole pieces during the five measurements with a 5 Hz drive on the table. 160

10.8 The DC voltage across the top and bottom pole pieces during the five measurements with no drive on the optical table. The initial anomaly is more evident than in the 5 Hz data. 160

LIST OF FIGURES – CONTINUED

Figure Page

10.9 The measured tilt during the five measurements with a 5 Hz drive acting on the table. All measured tilts are within ±0.75 μrad about its average value. The RMS tilt for all five is 0.35 μrad corresponding to an equilibrium shift of 28 nm. 163

10.10 The measured tilt during the five measurements without a drive acting on the table. All measured tilts are within ±0.9 μrad about its average value. The RMS tilt for all five is 0.42 μrad, corresponding to an equilibrium shift of 34 nm. 163

10.11 The raw data of the response of the geophone and particle with a 5 Hz drive on the optical table. The large peak at 1.75 Hz is due to the vibration of the table amplifying the motion of the particle on resonance. The peaks at 10.5 Hz and 15.2 Hz are the transverse and vertical motion of the particle, respectively. 166

10.12 The data after the harmonic oscillator responses for the geophone and particle have been divided out. This shows the accelerations that cause the measured responses. The large resonance at 1.75 Hz is no longer present. Below approximately 14 Hz, the response is vibration limited. Above 14 Hz, the response is readout noise limited. 166

10.13 A closeup of the data focusing on the 5 Hz peak after the harmonic oscillator responses for the geophone and particle have been divided out. The two spectra follow each other with the main difference being the peak at 5.3 Hz. The peak is close to half of the 10.5 Hz vertical resonance, indicating a possible subharmonic. 167

10.14 A closeup of the peak at 5 Hz. The magnitude of the peaks are within 3% of each other. The peaks appear at slightly different frequencies due to the frequency bins being different for the particle and geophone. 167

LIST OF FIGURES – CONTINUED

Figure Page

10.15 To make sure the 5 Hz peaks are from the drive, the response of the particle and geophone are measured without it. As expected, the peaks are now gone. The axial resonant frequency is visible along with the transverse and vertical peaks..... 168

10.16 The data with no drive on the optical table with the harmonic oscillator responses divided out for the geophone and particle. The axial peak is gone as well as the 5 Hz peaks. Again, the particle is vibration limited below 14 Hz and readout noise limited above 14 Hz. 168

10.17 The real part of the complex impedance of the geophone coil. The peak occurs at the resonant frequency of the oscillator and the width is given by the damping rate. The impedance is shifted up by the resistance of the coil, R_c. 171

10.18 The data after the harmonic oscillator responses for the particle and geophone have been divided out with no drive. The contributions to the noise for both the geophone (solid lines) and the particle (dashed lines) are also shown..... 176

10.19 Transient motion of the levitated microsphere after excitation with feedback cooling applied. The gain of the feedback is large (200 times larger than what was used in the data above). The large gain provided nonlinear damping indicated by non-exponential decay. 177

10.20 The raw acceleration data of the particle and geophone with a large gain with a 5 Hz drive. Because the damping was nonlinear, the harmonic oscillator responses could not be divided out. The peak at the axial oscillation frequency is no longer evident. 178

LIST OF FIGURES – CONTINUED

Figure Page

10.21 The raw acceleration data of the particle and geophone with a large gain without the drive. Because the damping was nonlinear, the harmonic oscillator responses could not be divided out. The peak at the axial oscillation frequency is no longer evident. 178

10.22 The raw acceleration data of the particle and geophone in units of $m/s^2/\sqrt{Hz}$ with a 5 Hz drive. 185

10.23 The acceleration data of the particle and geophone with their harmonic oscillator responses divided out in units of $m/s^2/\sqrt{Hz}$ with a 5 Hz drive. 185

10.24 The raw velocity data of the particle and geophone in units of $m/s/\sqrt{Hz}$ with a 5 Hz drive. 186

10.25 The velocity data of the particle and geophone with their harmonic oscillator responses divided out in units of $m/s/\sqrt{Hz}$ with a 5 Hz drive. 186

10.26 The raw displacement data of the particle and geophone in units of $m/\sqrt{Hz}$ with a 5 Hz drive. 187

10.27 The displacement data of the particle and geophone with their harmonic oscillator responses divided out in units of $m/\sqrt{Hz}$ with a 5 Hz drive. 187

10.28 The raw acceleration data of the particle and geophone in units of $m/s^2/\sqrt{Hz}$ without a drive. 188

10.29 The acceleration data of the particle and geophone with their harmonic oscillator responses divided out in units of $m/s^2/\sqrt{Hz}$ without a drive. 188

10.30 The raw velocity data of the particle and geophone in units of $m/s/\sqrt{Hz}$ without a drive. 189

10.31 The velocity data of the particle and geophone with their harmonic oscillator responses divided out in units of $m/s/\sqrt{Hz}$ without a drive. 189

LIST OF FIGURES – CONTINUED

Figure Page

10.32 The raw displacement data of the particle and geophone in units of $m/\sqrt{Hz}$ without a drive. 190

10.33 The displacement data of the particle and geophone with their harmonic oscillator responses divided out in units of $m/\sqrt{Hz}$ without a drive. 190

11.1 A photograph of the hardened tool steel mortar and pestle used for crushing silicon carbide wafers into particles. This particular mortar and pestle was experimentally determined to give the best results in coarse crushing of wafers. 193

11.2 The tube furnace used in the etching experiments and annealing of silicon carbide particles and wafers. The furnace is capable of reaching 1500 °C and experiments at atmospheric pressure or vacuum. 194

11.3 The silicon carbide crucible that was originally used for etching silicon carbide particles. In the figure, the right hand side of the crucible is etched. This led to the particles exhibiting no signs of etching, consistent with previous results. 195

11.4 (a) A SiC wafer with scratches on the c-face. The surface was scratched to measure the etching rate. (b) The SiC wafer that sat in a SiC crucible after the etching process completed. It is nearly identical to the image in (a), indicating very minimal etching. 196

11.5 The jet mill used to process particles without the need of high temperature etching. Using compressed air, the silicon carbide particles are reduced in size and rounded by collisions off of the walls of the mill and other particles. 199

11.6 A silicon carbide particle that has been crushed with the mortar and pestle shown in Fig. 11.1 before dry hydrogen etching. The particle is approximately 200 μm wide. 201

LIST OF FIGURES – CONTINUED

Figure Page

11.7 A silicon carbide particle after the dry hydrogen etching process. The etching in general reduces the size of the particles but does not round them or make them smoother. They are typically rougher with etch pits on the surfaces. 201

11.8 A bulk silicon carbide wafer before dry hydrogen etching. The surface was scratched to investigate the etching of the bulk surface. 202

11.9 The silicon carbide wafer after dry hydrogen etching. The scratches have been etched away completely. Hexagonal and circular pits were etched into the surfaces. 202

11.10 Typical silicon carbide particles crushed with the mortar and pestle before the wet oxidation etching. The particles are typically rough and have no preferred shape. 204

11.11 Particles after wet oxidation etching. They are smaller and more smooth. The particles are also more spherical, consistent with predictions. 204

11.12 Silicon carbide particles after crushing with the mortar and pestle. For this particular jet milling, the particles are extremely rough. Though this was unintentional, it helps illustrates the results from jet milling. 206

11.13 The silicon carbide particles after the jet milling procedure. It is evident that not only are the particles extremely smooth, but they are much more spherical than after the other methods. 206

11.14 A room temperature spectrum of electron irradiated 4H homoepitaxial silicon carbide wafer. The sample was irradiated with 1 MeV electrons with a fluence of $10^{-16}\,\mathrm{cm}^{-2}$. The spectrum follows the correct shape of that in the literature [2]. 207

LIST OF FIGURES – CONTINUED

Figure Page

11.15 A simple illustrating showing the splitting of the energy levels in 4H silicon carbide in the presence of an external magnetic field. With no external field, the splitting is $2D = 70\,\text{MHz}$. 208

A.1 The layout of the homemade microscope objective. Lens L_1 is plano-concave, lens L_2 is bi-convex, and L_3 is an aspherical lens. The objective is designed to correct spherical aberration that is introduced by the window of thickness t. An aperture stop of radius a_r is placed before lens L_1. 232

A.2 The spot diagram of the aspherical lens without the window using **goptical**. The spot size indicates diffraction-limited performance with the diameter of the spot that is approximately equal to the Airy disk diameter. 233

A.3 The transverse ray fan calculated by **goptical**. The plot is fifth order, indicating the dominant aberration is sixth order spherical aberration. 233

A.4 The spot diagram of the aspherical lens and a 5 mm window. The diameter, not including the outer most ring, is approximately 40 μm, almost 20 times larger than the Airy disk diameter. 234

A.5 The transverse ray fan calculated by **goptical**. The plot is third order, indicating the dominant aberration is fourth order spherical aberration. 234

A.6 The spot diagram calculated by **Zemax**. The black circle shows the Airy disk. The root-mean-square radius is 0.745 μm, well under the Airy disk radius. The outside ring contains a small fraction of the energy and does not contribute to the root-mean-square radius significantly. 236

LIST OF FIGURES – CONTINUED

Figure Page

A.7 The transverse ray fan of the objective corrected for imaging through a 5 mm thick window. The plot is seventh order corresponding to eighth order spherical aberration. 237

A.8 The result of the **Zemax** calculation for the point spread function of the objective. The theoretical Strehl ratio is 0.98. The first zeroes of the point spread function determines the numerical aperture, calculated to be 0.48. 238

A.9 The result of the **Zemax** calculation of the modulation transfer function of the objective (blue). The black curve shows the perfect diffraction limited modulation transfer function. 239

A.10 The result of the **Zemax** calculation of the enclosed energy in an image of a point source. The blue curve shows the enclosed energy of the objective and the black curve shows the perfect diffraction limited enclosed energy. 239

A.11 A 1 μm pinhole imaged through the objective and illuminated with an 830 nm diode laser. 240

A.12 A USAF1951 resolution target imaged through the objective. The target was illuminated with an 830 nm LED. Group 7 element 6 is marked with the red squares. The width of one line is 2.2 μm, the same size as the Airy disk. 240

B.1 A rendering of the copper sample mount. The mount is intended to be used in our pulse tube refrigerator and held at 4 K. Magneto-gravitational traps and silicon carbide samples have been mounted on this holder. 246

B.2 A front view of the rendering of the copper sample mount. The hole in the center allows optical access form the back. 246

LIST OF FIGURES – CONTINUED

Figure Page

B.3 A rendering of the aluminum cold shield that encloses the copper mount. The cold shield is held at 55 K to help prevent black body radiation from reaching the copper and trap or sample. 247

B.4 A front view of the rendering of the aluminum cold shield. 247

B.5 A rendering of the copper mount inside of the aluminum cold shield. Both parts are designed such that in the final assembly that the copper mount is centered in the cold shield. 248

B.6 A full assembly drawing of the cryogenic system including the Cryomech cold head. The sample or trap is mounted in the chamber at the bottom. 249

C.1 A three dimensional rendering of the new design for the trap mount for a future measurement of G as viewed from an angle. 252

C.2 A three dimensional rendering of the new design for the trap mount viewed from the transverse direction. The total width of the mount is 2 in which is significantly smaller than the mount used for the work of this dissertation. 253

C.3 A three dimensional rendering of the new vacuum chamber for the future G measurement. 254

C.4 A three dimensional rendering of the new vacuum chamber as viewed from the axial direction. 255

LIST OF ALGORITHMS

Algorithm Page

7.1 The algorithm that the digital IIR filter follows to return a filtered value of the velocity of the particle. 104

8.2 The algorithm used to determine the strength and sign of the feedback for actively stabilizing the optical table. 116

ABSTRACT

Since the theory of gravity was published by Issac Newton in the seventeenth century, scientists have studied its strength, originally for the purpose of astronomy and measuring the density of the Earth. After centuries of research and measurements, G remains the least precisely known fundamental constant. A new method for a time-of-swing measurement of G, developed a the National Bureau of Standards 1930, is proposed using a levitated microsphere in a magneto-gravitational trap. A new magneto-gravitational trap based on a previous system from our laboratory has been developed for a measurement of G. This trap has been designed to load large particles with low oscillation frequencies with large amplitudes of motion to improve sensitivity to G. Because of the weak trap, a loading method has been developed utilizing electric fields to help balance the force of gravity. A stable and variable high voltage reference has been developed to provide the necessary electric field. Camera-based feedback control has been implemented for cooling the center-of-mass motion or heating the motion in a controlled way. To limit errors due to equilibrium shifts of the particle in the trap from tilt, a simple modification was made to an optical table to actively stabilize the tilt. A measurement of G requires high sensitivity to accelerations and forces. The parameters achieved towards the measurement of G makes this system sensitive to acceleration. The first direct use of a room temperature levitated optomechanical system as an accelerometer has been achieved, with the best sensitivity to accelerations of any room temperature levitated optomechanical system. The sensitivity was measured to be $3.6 \times 10^{-8}\,\mathrm{g}/\sqrt{\mathrm{Hz}}$.

CHAPTER ONE

INTRODUCTION

For millennia, gravity has been taught, studied, and researched. Dating back to Aristotle, people of all backgrounds were interested in an object's fall towards the Earth. Studies done by Galileo Galilei had shown that similar objects of varying mass took the same amount of time to finish their journey to the Earth's surface from the same height. In the seventeenth century, while studying planets, Sir Isaac Newton theorized that two objects exert a force on each other, proportionally related to their masses, m_1 and m_2, and inversely proportional to the square of the distance r that separates their centers [3]. The constant of proportionality is often called Newton's constant of gravity, or G, despite this notation being developed in 1894 [4] by Charles Vernon Boys.

$$F = G\frac{m_1 m_2}{r^2} \tag{1.1}$$

1.1 Motivation

There is not much need to motivate the study of an entity that is such an integral part of our daily lives. After all, it is what keeps us from floating into the emptiness of space. Nonetheless, there are many reasons for conducting gravity related experiments. First, there is much interest in measuring Newton's constant of gravity. According to the Committee on Data for Science and Technology (CODATA) [5], G is one of the least precisely known fundamental constants. This has impacted experiments in all fields of physics, notably astronomy where measurements can be

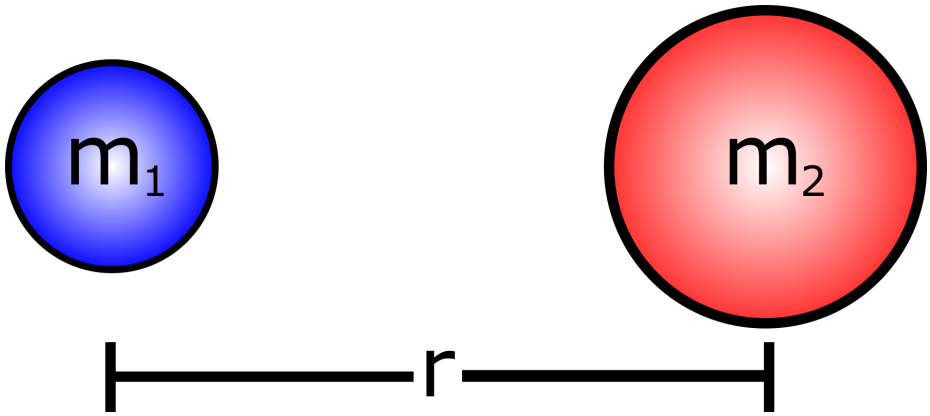


Figure 1.1: A simple illustration showing two spherical masses. Their centers are separated by a distance r. The left and right spheres have masses m_1 and m_2, respectively. The force that each exerts on the other is given by Newton's law of gravity, eq. 1.1.

quoted in terms of solar masses instead of grams due to the fractional uncertainty of G being so large [6].

This dissertation will focus only on classical, or Newtonian, gravity. However, through the equivalence principle of relativity [7,8], the gravitational force an object is the same as a pseudo-force an object feels in a non-inertial reference frame. Relativity does not treat gravity as a force, though. Systems that can measure accelerations with high sensitivities are of great interest for use in fundamental research as well as practical applications.

1.2 History of Measurements of G

Measuring the density of the Earth, a consequence of Sir Issac Newton's theory of gravity, piqued the interest of experimenters. Many scientists attempted to measure the deflection of a vertical pendulum in the presence of a large mountain, often with null results and the possibility of severe personal injury due to the extreme conditions they went through to set up their apparatus.

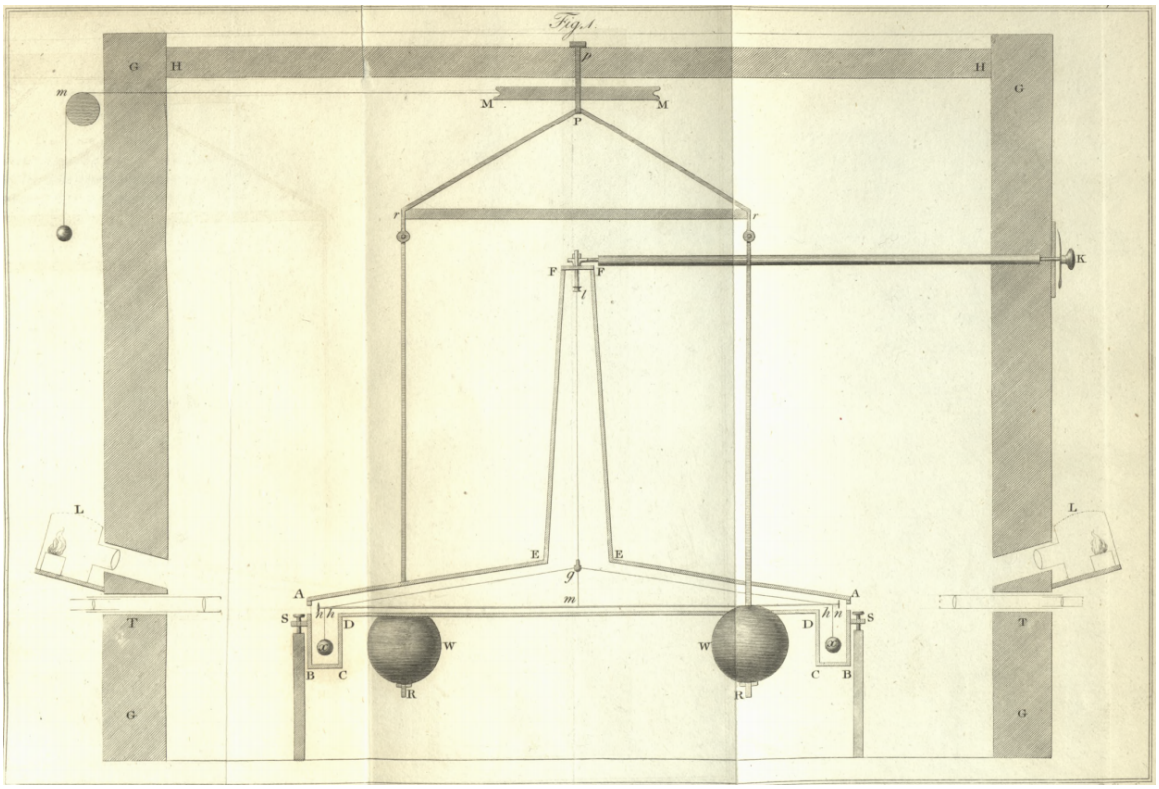


Figure 1.2: A figure from Henry Cavendish's 1798 publication illustrating the apparatus he used [1]. The torsion pendulum and its variants have been the standard way of measuring G for centuries.

In 1798, Henry Cavendish performed the first laboratory measurement of the density of the Earth at his home [1]. This measurement utilized a horizontal torsion pendulum housed in a large wooden box to prevent wind currents from causing unwanted deflections of the pendulum, as shown in Fig. 1.2. He measured the position of the small masses before and after the addition of the two large masses. The deflection of the small masses is related to G. Cavendish reported a value of $(6.74 \pm .04) \times 10^{-11}$ $\mathrm{m^3\,kg^{-1}\,s^2}$ (relative uncertainty of 6000 parts per million (ppm)). This differs from the current 2018 CODATA value by 10000 ppm [5].

For another century, measurements of Earth's density, and indirectly Newton's constant of gravity, did not improve much in terms of relative uncertainty. An

experiment to measure the density of the Earth by John Poynting in 1894 resulted in a relative uncertainty of 5500 ppm [9]. In 1898, Franz Richarz and Otto Kriger-Menzel attempted to improve the measurement by using lead blocks with masses no less than $100,000$ kg [10]. They reported a similar relative uncertainty to other experiments of the time [4, 9]. These experiments used similar deflection-based torsion pendulums.

In 1895, Boys developed a new method for measuring G that differs from that of Cavendish [11]. Instead of measuring a deflection of the pendulum, one measures a change in oscillation frequency of the pendulum before and after the addition of nearby masses. This method is called the time-of-swing (TOS) method. At the National Bureau of Standards (NBS), currently known as the National Institute of Standards and Technology (NIST), this new method was used to redetermine the constant [12, 13]. The 1930 NBS measurement yielded the result $(6.670 \pm .007) \times 10^{-11}$ $\mathrm{m^3\,kg^{-1}\,s^2}$ (relative uncertainty of 1000 ppm). The 1942 NBS measurement yielded the result $(6.673 \pm .003) \times 10^{-11}$ $\mathrm{m^3\,kg^{-1}\,s^2}$ (relative uncertainty of 450 ppm).

The NBS made another measurement in 1982 by Gabriel Luther and William Towler [14]. They used the TOS method to measure Newton's constant of gravity at $(6.6726 \pm .0005) \times 10^{-11}$ $\mathrm{m^3\,kg^{-1}\,s^2}$ (relative uncertainty of 75 ppm). In 1996, O. Karagioz and V. Izmailov presented results from ten years of measurements using the TOS method to yield $(6.6729 \pm .0005) \times 10^{-11}$ $\mathrm{m^3\,kg^{-1}\,s^2}$ (relative uncertainty of 75 ppm) [15]. It is important to note that it took them ten years of measurements to achieve their results.

Just a year after the Karagioz measurement, Charles Bagley and Gabriel Luther made a measurement of $(6.6740 \pm .0007) \times 10^{-11}$ $\mathrm{m^3\,kg^{-1}\,s^2}$ (with a relative uncertainty of 105 ppm) [16]. This is a slightly worse relative uncertainty than the measurements that came before it.

A new type of experiment was explored in 1997 by Schurr, Nolting, and Kündig

using a beam balance [17]. The beam balance, using a modified Mettler-Toledo AX1006 mass comparator, was placed in a 4.5 m deep pit for extreme vibration and thermal isolation of the experiment. The experiment yielded a measurement of $(6.6754 \pm .0014) \times 10^{-11}$ $\mathrm{m^3\,kg^{-1}\,s^2}$ (relative uncertainty of 230 ppm). The high uncertainty is quoted to being due to the state of the experiment, with 10 ppm being possible.

At the start of the new millennia, a new torsion pendulum-based experiment was developed by Jens Gundlach and Stephan Merkowitz [18–20]. A turntable that houses the field masses is set to rotate at a constant rate and a feedback angular acceleration (AAF) is applied to keep the pendulum from rotating. In doing so, the measurement is independent of any anelasticities in the fiber holding the pendulum mass. A measurement of $(6.674215 \pm .000092) \times 10^{-11}$ $\mathrm{m^3\,kg^{-1}\,s^2}$ was reported (relative uncertainty of 14 ppm).

Another torsion pendulum type experiment was designed around the same time as the Gundlach experiment. Quinn and others use a torsion strip instead of a fiber to try to eliminate errors that the material causes [21, 22]. This experiment also utilized four test masses and four source masses to reduce sensitivity to external gravitational fields. The experiment produced a measurement of $(6.67559 \pm .00027) \times 10^{-11}$ $\mathrm{m^3\,kg^{-1}\,s^2}$ (relative uncertainty of 41 ppm).

One of the last measurements, done in 2018 by Li and others used a torsion pendulum system to produce the lowest relative uncertainty measurement yet [23]. The fibers used were studied for decades in an attempt to understand system errors that may occur from material properties of the fibers. They used two independent methods: TOS and AAF methods to get two 12 ppm measurements that do not agree with each other. The TOS experiment yielded a measurement of $(6.674184 \pm .000078) \times 10^{-11}$ $\mathrm{m^3\,kg^{-1}\,s^2}$ (relative uncertainty of 12 ppm) and the AAF method

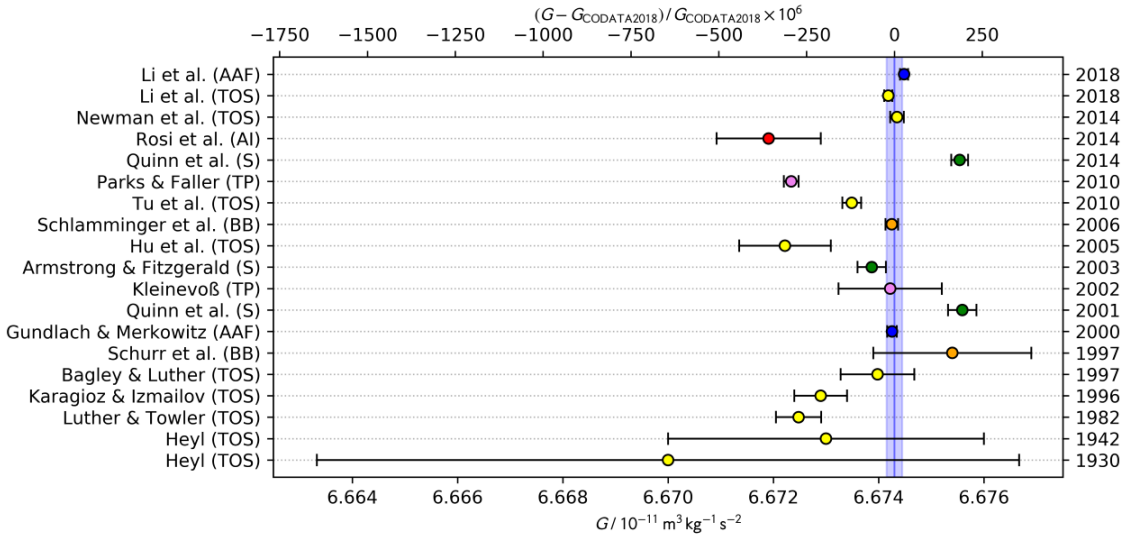


Figure 1.3: A plot of some precision measurements of Newton's constant of gravity, G, starting with the 1930 measurement of Heyl at NBS. The accepted value from the 2018 CODATA report is shown by the vertical line and the relative uncertainty by the blue band. It is evident that measurements have not produced consistent values of G.

measured G to be $(6.674484 \pm .000078) \times 10^{-11}\ \mathrm{m^3\,kg^{-1}\,s^2}$ (relative uncertainty of 12 ppm).

The above experiments are by no means fully inclusive. They were chosen to show the evolution of G measurements and give brief overview of the various types of experiments used. In some cases, experiments have taken years or decades to complete. Sometimes, experiments done within the same group do not agree to within their uncertainties.

1.3 Difficulties in G Measurements

From the previous section, we can see that experiments measuring Newton's constant of gravity have not produced results that improved substantially over the course of three hundred years. The first laboratory measurement by Henry

Cavendish had a relative uncertainty of 6000 ppm. The latest, and most precise to date, measurements by Li and others yielded 12 ppm measurements. The little improvement in precision can be attributed to several issues.

First, the force of gravity is the weakest force of nature compared to the electromagnetic, weak, and strong forces. For the case of the electromagnetic force, one can use a conductor known as a Faraday cage to shield from the force. There is no equivalent way to shield against the force of gravity. In the majority of the measurements, a torsion pendulum is typically used as well as other mechanical resonator systems. The fibers of the pendulums can have defects that are not well understood, if at all. Loss due to the mechanical clamping can also prevent high precision measurements from being made.

1.4 Primary Research Contributions of this Dissertation

In this dissertation, several contributions to fundamental and applied physics have been made. A time-of-swing measurement of the Newtonian constant of gravitation using a levitated microsphere in a magneto-gravitational trap is proposed. The system, including the newly developed magneto-gravitational trap, optics, and vacuum equipment, is described.

The magneto-gravitaional trap developed for this work was designed to be weak when compared to other levitated optomechanical systems. Due to this weakness, the magnetic field alone is not strong enough to cancel gravity and requires an electic field to accomplish this. A variable high-voltage voltage reference was designed by modifying a Texas Instruments design [24], demonstrating stability to less than 3 ppm over three days.

Feedback cooling [25] and controlled heating was implemented via real-time analysis of images acquired on a CMOS camera. Heating to approximately the same

amplitude for three measurements (a necessity for a measurement of G) to within 1%. A method for actively stabilizing the tilt of an optical table was developed and demonstrated tilt stability to a root-mean-square fluctuation of less than 0.35 μrad, three orders of magnitude better than the unstabilized table.

Because we intend on using large particles for the measurement of G in the weak magneto-gravitational trap, a new loading method was needed in order to cancel gravity and slow the particle enough that it remains trapped. The loading method combines methods used other systems in our laboratory with linear Paul trap methods [26] to successfully load particles into the trap. The target oscillation frequency of 0.1 Hz was achieved for a 60 μm borosilicate microsphere. This is the lowest oscillation frequency reported for a particle in a levitated optomechanical system.

The use of silicon carbide for a measurement of G is described along with methods used for processing silicon carbide wafers into spherical particles. The V2 silicon vacancy defect adds internal degrees of freedom that can assist for a measurement of G through magnetic field and rotation sensing. More work in the future is required to complete this silicon carbide project.

During the work of this dissertation, this system was used for high sensitivity acceleration measurement. This is the first direct measurement of accelerations using a room temperature levitated optomechanical system. Compared to other systems [27] that predict sensitivities based on thermal noise, this system reports the best sensitivity of any room temperature levitated optomechanical system. The measured sensitivity is $3.6 \times 10^{-8}\,\mathrm{g}/\sqrt{\mathrm{Hz}}$.

1.5 Structure of this Dissertation

This dissertation has been chosen to be outlined in the following way.

Chapter 2 will first describe common levitated optomechanical systems. Important parameters needed for a measurement of the Newtonian constant of gravitation will be discussed for each system.

Chapter 3 will give an in depth description of the system used for the work done in this dissertation and a brief motivation for why we propose this system based on achievable parameters. The chapter will provide information about the hardware used as well as important mathematical descriptions.

Chapter 4 will explain how the system used for the work done in this dissertation will be used for a measurement of G in detail. Systematic errors in this system will be described along with systematic errors in typical torsion pendulum measurements.

Chapter 5 explains how particles of a substantial mass are loaded and trapped into the system. Chapter 6 explains the use of a highly stable, variable, high-voltage voltage reference. Chapter 7 will describe how a CMOS camera is used in real time for detection and feedback control of the particle. Chapter 8 describes the active stabilization method developed for use in experiments described in this dissertation. These chapters all describe new methods and techniques developed for this work.

Chapter 9 will report on the first major results of the experiment. Frequencies down to the target frequency are reported. Chapter 10 reports on acceleration sensing results as a first step towards a measurement of Newton's constant of gravity. These two chapters report on major results from the experiments.

Chapter 11 describes how silicon carbide (SiC) can be used in a measurement of Newton's constant of gravity. Work done towards using this material and future goals are explained in this chapter.

Chapter 12 summarizes the work done in this dissertation as well as lays out the ground work for the future of this experiment.

The appendices describe work done that is not crucial to the main story of

the dissertation. Appendix A describes a homemade microscope objective used extensively in several other experiments. Appendix B focuses on designs of a cryogenic system that can be used for levitated optomechanical experiments. Appendix C describes a system designed for future G measurement experiments.

CHAPTER TWO

REVIEW OF LEVITATED OPTOMECHANICAL SYSTEMS

2.1 Introduction

Historically, torsion based pendulums have been the primary systems for measuring Newton's constant of gravity, G. As explored in Ch. 1, these systems have been used for hundreds of years to produce measurements with little improvement, despite an increase in sophistication, technological advancements, and carefulness. The difficulties of the measurements were explained briefly. The primary systematic errors may arise from the material properties of the fibers of the pendulums.

In order to eliminate this systematic error altogether, a system that consists of an oscillator with no coupling to its environment can be used. Levitated optomechanical systems in vacuum provide extraordinary isolation from the environment. Several methods can be used to levitate an oscillator, including optical traps, quadrupole ion (Paul) traps, magneto-optical traps, magnetic traps, and magneto-gravitational traps.

In this chapter, a review of these levitated optomechanical systems will be presented. The trapping mechanisms are described for the most common systems: optical traps, Paul traps, magneto-optical traps, and magnetic-based traps. The most relevant parameters for a measurement of Newton's constant of gravitation are reported with emphasis on optical traps and magnetic-based traps since optical trapping has dominated the levitated optomechanical community since its development [28] and since magnetic-based trapping shows the most promise for the measurement (as will be explained at the end of this chapter). References to publications on these subjects are given along with observations from our laboratory that have not been

published. Magneto-optical traps are discussed briefly.

The first parameter discussed is the size and material of particles successfully trapped. A large mass is ideal to limit the effects of thermal noise on the measurement. Thermal noise also becomes less significant when the center-of-mass motion of the particle is much larger than the thermal amplitude. Maximum center-of-mass motion amplitude for each levitated optomechanical system is discussed. The oscillation frequencies are also discussed. Low oscillation frequencies are required to observe a larger frequency change in a time-of-swing measurement as will be discussed in chapter 4. Natural damping must be minimal for the G measurement so collisions between the particle and background gas should be minimized. For this review, the vacuum pressures achieved are reported.

2.2 Optical Trap

Optical trapping has lead research in levitated optomechanics since its development in the 1970s [28]. Single beam optical traps, typically a tightly focused 1064 nm neodymium-doped YAG (Nd:YAG) laser, oriented vertically opposite the direction of gravity relies on the scattering force to balance the force of gravity and the gradient force to push the particle back towards the center of the beam. Dual beam optical traps utilize counterpropagating beams to cancel the scattering force from each other while doubling the strength of the gradient force in the vertical direction to cancel the force of gravity [29].

Dielectric materials are levitated by large gradients in electric fields that can be produced by focused lasers. Typically, high numerical aperture (NA) objective lenses are required to achieve the necessary intensity. Dielectric materials tend to be pushed towards the maximum electric field point, occurring at the highest intensity part of the laser beam. Common dielectric materials that can be levitated in optical traps are

silica (SiO_2) [29–47], silicon (Si) [48], diamond [49, 50], and vaterite (μ-$CaCO_3$) [33]. Diamonds containing nitrogen vacancy (NV) centers are particularly useful because the defects can be manipulated to provide a coupling between the defect's quantum spin and the classical center-of-mass motion of the diamond [51–53]. The birefringence quality of the vaterite allows for trapped spherical particles to be rotated.

A wide range of particle sizes have been successfully levitated in optical traps. Some of the smallest particles include a 26 nm diameter silica sphere [43]. More typical sizes are in the range of 100 nm to a few micrometers in diameter [29–34,36–42,44–50], with the majority between 100 nm to 150 nm in diameter. At the upper end of the range are silica particles with diameters that are tens of micrometers [35, 54].

The center-of-mass motion of levitated particles in an optical trap can be described by simple harmonic motion. The oscillation frequency f of a particle of mass m is

$$f = \frac{\omega}{2\pi} = \frac{1}{2\pi}\sqrt{\frac{k}{m}}, \tag{2.1}$$

where ω is the angular frequency of the oscillation and k is the spring constant of the optical trap. Typical frequencies for sub-micrometer sized particles are in the range $f \approx 100 - 200$ kHz [33, 38, 40, 41, 44–49]. Frequencies as high as $f \approx 300$ kHz [43] and as low as $f \approx 20$ Hz [35, 36] have been reported.

It also important to note the maximum center-of-mass amplitude for optical traps. For particles of radius r trapped in a beam with wavelength λ in the Rayleigh scattering limit, $r \ll \lambda$, the maximum amplitude is approximately the beam waist. Larger maximum amplitudes can be achieved in the opposite regime, $r \gg \lambda$. Using the Optical Tweezers in Geometrical Optics (OTGO) software [55] (calculation perform by Randy Babbitt) that has been modified to calculate maximum center-of-mass motion amplitudes for a variety of trap geometries [56], it was found that

in the direction along the trapping beam's optical axis the maximum amplitude is approximately twice the particle radius divided by the NA of the trapping beam [57]. Perpendicular to the optical axis, the maximum amplitude is approximately twice the particle radius. Typical amplitudes range from approximately 400 nm to 20 μm.

Early experiments in optical trapping have been done in air and liquid. To reduce the damping from background gases, going to vacuum is necessary to achieve most goals of levitated optomechanics. Because of the the high intensity lasers needed to provide the trapping potential, levitated particles in vacuum typically need active center-of-mass cooling to avoid losing the particle due to the radiometric forces intensified by differential particle heating [35, 58]. Diamond has been successfully trapped down to several Torr [49] but evidence shows that the particles graphitize and burn in vacuum [59]. Silica spheres have been trapped down to 10^{-8} Torr [46,48].

2.3 Quadrupole Ion (Paul) Trap

Due to Earnshaw's theorem, which states that no combination of forces that are proportional to $1/r^2$ can create a stable trap [60], AC electric fields must be used to levitate charged particles. In 1953, Wolfgang Paul showed that an AC quadrupole field can stably levitate a charged particle [61]. There are several uses for these quadrupole ion (Paul) traps including mass spectrometry [62], quantum computing [63], and atomic frequency standards [64].

The motion of a charged particle in a Paul trap is more complicated than that of an optical trap. The particle oscillates at the same frequency as the AC electric field frequency (micromotion). A particle with charge, q, and mass, m, in an oscillating electric field, $E(t) = E_0 \sin(\omega t)$, will have the equation of motion

$$x(t) = x_0 + v_0 t - \frac{qE_0}{m\omega^2} \sin(\omega t). \tag{2.2}$$

The micromotion is 180° out of phase from the electric field. The secular motion is the motion of the particle due to the restoring force of the quadrupole potential and depends on the geometry of the system.

The quadrupole ion trap typically consists of a ring electrode with the AC voltage on and two hyperbolic electrodes on either side of the ring with DC voltages on them [61]. The ring electrode is usually hyperbolic in shape as well. Because of increased simplicity in manufacturing, the electrodes are often cylindrical instead of hyperbolic [65–68]. Instead of a ring electrode, four linear rod-type electrodes can be used to form a two-dimensional trap [26, 69]. Confinement in the third dimension is from two electrodes on the ends.

Charged particles can be trapped in the quadrupole ion trap provided the parameters of the system create a stable solution to the Mathieu equation [70]. Sizes of particles range from hundreds of nanometers [71, 72] to hundreds of micrometers [71, 73]. Typical materials include diamond and polystyrene [71], silica [72], aerosols [74, 75], and cells [76].

2.4 Magneto-Optical Trap

Magneto-optical traps combine optical trapping with a weak magnetic field where the motion of the particle(s) is cooled by three orthogonal trapping lasers aligned with each Cartesian axis [77, 78]. Trapping of relatively large mesoscopic particles [79] as well as single atoms [80] have been demonstrated. These traps are especially useful when the particle(s) to be levitated are not charged, as a Paul trap will not work. The added quadrupole magnetic field causes a Zeeman shift in the atom's energy levels that increase with the distance away from the center of the trap. The energy transition frequency becomes closer to the laser frequency making the atom more likely to absorb a photon and be pushed back towards the center of the

trap. The lasers must be polarized in the correct way so the particle is not repelled from the center as it drifts towards the outside of the trap.

2.5 Magneto-Gravitational Trap

Earnshaw's theorem prohibits classical static fields from creating a stable trap. As described above, charged particles can be trapped in an AC electric field Paul trap or a dielectric particle in an optical trap. Classically, a magnetic based trap is not possible. Diamagnetism is a purely quantum mechanical magnetic effect that is induced by a change in the orbital motion of electrons due to an external magnetic field. It has been shown that diamagnetism allows for passive and static trapping with magnetic fields [81]. Diamagnetic materials have a magnetic susceptibility $\chi < 0$ and are repelled by magnetic fields [82].

The total potential energy on a diamagnetic volume, V, with magnetic susceptibility, χ, and mass, m, in an external magnetic field subject to Earth's gravity, g, is

$$U = -\frac{\chi B^2 V}{2\mu_0} + mgy, \tag{2.3}$$

where $B = |\vec{B}|$ is the magnitude of the magnetic field, μ_0 is the vacuum permeability, and y is the vertical displacement away from equilibrium of the volume [81]. For diamagnetic materials, a stable trap is formed at a magnetic field minimum in the absence of gravity. To counteract the force of gravity, either a large magnetic field or large magnetic field gradient is required.

Two such magneto-gravitational traps have been realized. The linear quadrupole-based magneto-gravitational (LQMG) trap [83–85] uses four pole pieces to concentrate the magnetic field from two permanent magnets sandwiched between the pole pieces (see Fig. 3.3). The second system is an axisymmetric magneto-gravitation (AMG)

trap [86] uses two cylindrically symmetric pole pieces to concentrate the magnetic field from a single permanent magnet. In both, Earth's gravity is used to constrain the particle in at least one direction. The two systems will be compared and contrasted in the following paragraphs.

Two samarium-cobalt (SmCo) permanent magnetics are sandwiched by four pole pieces, made of Hiperco-50A (iron-cobalt alloy), in the LQMG trap form a quadrupole magnetic field in the xy (transverse-vertical) plane. In the z (axial) direction, the top two pole pieces are machined shorter than the bottom pole pieces. This curves the magnetic field upwards at both ends of the trap and gravity pulls the particle back towards the center of the trap in the axial direction, constraining the particle in that direction.

The pole pieces are designed to concentrate the magnetic flux to a smaller region, increasing the magnetic field gradient. The gaps in the pole pieces are approximately 75 μm in the transverse direction and approximately 200 μm in the vertical direction. The bottom pole pieces are approximately 2.54 mm long in the axial direction and the top pole pieces are approximately 380 μm long in the axial direction. The LQMG trap shown in Fig. 3.3 gives a qualitative picture of the trap description above. The trap in Fig. 3.3 is a modification of the above LQMG trap and is the trap used for the work in this dissertation.

Diamagnetic materials that have been successfully loaded in the linear quadrupole magneto-gravitational are diamond, silica, borosilicate glass and silicon carbide (SiC) [83–85]. Soda lime glass, dibutyl sebacate (DBS), silicone oils, water, isopropyl alcohol, polystyrene, vaterite, and graphite have been trapped in our laboratory, though not reported in any publications [57]. This trap has successfully levitated silica spheres from approximately 1 μm to approximately 8 μm in diameter [84, 85]. Diamond crystals approximately 3.5 μm in diameter have also been trapped [83].

Because the magnitude of the magnetic susceptibilities are much lower than that of dielectric susceptibilities, the spring constant of the traps are lower, resulting in lower frequencies than typical optical trapping systems. The LQMG trap demonstrated frequencies $f_z \approx 7$ Hz, $f_y \approx 100$ Hz, and $f_x \approx 60$ Hz in the axial, vertical, and transverse directions, respectively.

The maximum amplitude of motion of the LQMG trap is limited by the dimensions of the four pole pieces [83–85]. The maximum amplitude in the transverse direction is approximately half of the distance from the center of one pole piece tip to the other, which is approximately 125 µm. Vertically, it is approximately half of the 200 µm vertical gap. In the axial direction, the maximum amplitude is approximately half of the width of the 380 µm long top pole pieces.

Achieving vacuum is important for magneto-gravitational traps, as with any levitated optomechanical system, to reduce damping from background gases. Because of the passive nature of the trap, feedback cooling [25] is not needed for the particle to remain trapped. High intensity lasers are also not needed which prevents loss of particles due to heating in vacuum. Pressures down to 10^{-10} Torr have been reported for experiments using the LQMG trap [84].

In contrast to the LQMG trap, the AMG trap [86] consists of two cylindrically symmetric pole pieces made from O1 tool steel centered axially above a neodymium-iron-boron (NdFeB) permanent magnet. The pole pieces concentrate the magnetic flux to a smaller region, increasing the magnetic field gradient. The gap between the top and bottom pole pieces are separated by 350 µm. The top pole piece is hollowed out to allow loading of particles from the top.

The AMG trap exhibited trapping of galium nitride (GaN) spheres and nanowires, graphite powder, and silica [86]. The AMG trap demonstrated trapping of GaN nanowires 20 µm in length, 6 µm diameter silica spheres, 10 µm diameter

GaN spheres, and graphite from 50 μm to 300 μm [86]. The AMG trap system demonstrated trapping of silica spheres with diameters comparable to the LQMG trap.

The AMG trap demonstrated a vertical frequency of $f_y \approx 30$ Hz and radially $f_r \approx 25$ Hz. This is comparable to the oscillation frequencies achieved in the LQMG trap. The maximum amplitude of motion for the AMG trap is limited by the boundaries of the pole pieces. In the vertical direction, the maximum amplitude is approximately 200 μm, and in the radial direction, approximately 350 μm [86]. The amplitudes are also comparable for the two systems.

Pressures down to 0.001 Torr have been reported for experiments using the AMG trap [86]. This is eight orders of magnitude higher than the pressure obtained in the LQMG trap system. For this trap to achieve ultra-high vacuum and comparable pressures to the LQMG trap system, a different permanent magnet will need to be used, as the NdFeB's Curie temperature does not allow it to be baked.

2.6 Magnetic Trap

Magnetic based traps that do not require gravity to create confinement in one or more directions exist, also relying on diamagnetism to stably levitate particles. One such system is based on two permanent magnets and no pole pieces [87]. Diamond was reported trapped with diameters between 1.5 μm and 2.5 μm. The frequencies of the trapped particle are $f_h \approx 200$ Hz in the horizontal directions and $f_v \approx 400$ Hz in the vertical direction. The center-of-mass motion of the particle is limited by the magnets in the vertical direction, giving a maximum amplitude of motion of 15 μm. In the horizontal directions, a good approximation for the maximum center-of-motion amplitude is the vertical gap size of 30 μm. Pressures down to 0.1 Torr were achieved.

Electromagnet systems [81, 88, 89] can be used to generate very large magnetic

fields. Superconductors, being perfect diamagnets ($\chi = -1$), can be levitated over magnets or used to levitate magnets at cryogenic temperatures [90–92].

2.7 Conclusion

Five levitated optomechanical systems have been described above. The mass of the particle, its oscillation frequency, center-of-mass motion amplitude, and damping rate are crucial parameters for these systems for a precision measurement of G. As mentioned above and will be explained in chapter 4, large particle mass, low oscillation frequency, large amplitudes of motion, and low natural damping are ideal for the measurement.

For optical trapping systems, typical particle diameters are approximately 100 nm for silica spheres. Typical diameters for silica spheres in a magnetic-based trap are approximately 1 μm. This factor of ten results in a difference in mass of one thousand. Magnetic-based traps have demonstrated typical oscillation frequencies on the order of 10 Hz. Optical traps have typical frequencies of 100 kHz, approximately 10^4 times higher. Since optical traps typically rely on high NA objectives to focus the light down to provide the strength to levitate the particle, the amplitude of motion for the particle is limited to approximately the beam diameter (10 μm). The magnetic-based traps described above can be designed to allow for large amplitudes of several hundred micrometers. Magnetic-based trap systems have also demonstrated vacuum pressure two order of magnitude better than that of any optical trapping system.

It can be concluded that a magnetic-based trap will be more suited for a measurement of G than an optical trap. Magnetic-based traps that do not rely on gravity for trapping do not allow for large amplitudes of motion or low oscillation frequencies [87]. For the work in this dissertation, a modified LQMG trap (see chapter 3) has been designed and has demonstrated stable trapping of borosilicate

particles with diameters up to 63 μm, oscillation frequencies as low as 0.1 Hz, and center-of-mass motion amplitudes of 6 mm. A vacuum pressure of 10^{-9} Torr (ten times better than optical trap systems) was achieved, though the damping is not limited by collisions of the particle with background gas.

The following chapter describes in detail the magneto-gravitational trap that was used for the work of this dissertation. Though it is intended for measuring Newton's constant of gravity, this trap has been used in high sensitivity acceleration measurements (due to these parameters achieved).

CHAPTER THREE

SYSTEM DESCRIPTION

3.1 Introduction

In the previous chapter, several levitated optomechanical systems were described. The important parameters for a measurement of G was discussed. Based on the parameters each system offers, the linear quadrupole magneto-gravitational trap shows the most promise for such a measurement. In the work for this dissertation, a linear quadrupole magneto-gravitational trap that has been modified from the linear quadrupole magneto-gravitational trap described in chapter 2 was designed and used. This chapter describes the system used for this work.

The trap was designed to allow for trapping of microspheres with large masses (up to $2.5 \times 10^{-10}\,\mathrm{kg}$, as reported in chapter 10). The trap was also designed to allow for large amplitudes of motion up to 10 mm, orders of magnitude larger than previous magneto-gravitational traps [84, 86, 87] and optical traps [30, 93]. Oscillation frequencies were also in mind when the trap was designed by creating a weak trap. The design and theoretical description, based on previous calculations [94], of the trap is presented. This trap is intended on being used for a measurement of G. In chapter 10, results from a high sensitivity acceleration measurement are reported with a particle in this trap.

In addition to the trap design and assembly, the mount that holds the magneto-gravitational trap is described. This mount, designed special for this experiment, allows for easy and controllable adjustment for the vertical gap of the trap. The vacuum system that houses the trap and is used to achieve high and ultra-high vacuum (see chapter 9 and 10 for a discussion on vacuum pressure) is described. The optical

system used to illuminate the particle and image it onto a CMOS camera. Feedback control [25] is implemented and the optics for feedback control is explained.

3.2 Extended Linear Quadrupole Magneto-Gravitational Trap

The magneto-gravitational trap used in the work for this dissertation is a modified version of the linear quadrupole-based magneto-gravitational trap [83–85]. Writing Eq. 2.3 again here for convenience,

$$U(x,y,z) = -\frac{\chi B(x,y,z)^2 V}{2\mu_0} + mgy, \tag{3.1}$$

where U is the potential energy due to an external magnetic field and gravity, acting on the levitated particle. Here, χ is the volume magnetic susceptibility, $B = |\vec{B}|$ is the magnitude of the magnetic field, V is the volume of the particle, μ_0 is the vacuum permeability, m is the mass of the particle, g is the acceleration due to gravity, and y is the vertical displacement of the particle. For the particle to be levitated, the total force on the particle must vanish. The force on the particle at its equilibrium is

$$\vec{F}(x_{eq},y_{eq},z_{eq}) = -\vec{\nabla}U(x_{eq},y_{eq},z_{eq}) = \frac{\chi V}{\mu_0}B(x_{eq},y_{eq},z_{eq})\vec{\nabla}B(x_{eq},y_{,eq}\,z_{eq}) - mg\hat{y} = \vec{0} \tag{3.2}$$

Therefore, to balance gravity,

$$B(x,y,z)\vec{\nabla}B(x,y,z)\cdot\hat{y} = \frac{\mu_0 mg}{\chi V}. \tag{3.3}$$

Away from equilibrium, the force needs to be restoring, pushing the particle back to its equilibrium from all directions.

For the magneto-gravitational trap to be stable, the potential energy needs to

increase in all directions away from its equilibrium position. In vertical direction, this is equivalent to

$$\frac{\partial^2 U(x,y,z)}{\partial y^2} = -\frac{\chi V}{2\mu_0}\frac{\partial^2 B(x,y,z)^2}{\partial y^2} > 0. \tag{3.4}$$

For diamagnetic materials, $\chi < 0$, we get

$$\frac{\partial^2 B(x,y,z)^2}{\partial y^2} > 0. \tag{3.5}$$

Consider a Taylor expansion of the magnetic field about the equilibrium position $(x, y, z) = (0, y_0, 0)$

$$B(x,y,z) = B_0 + B_1(y-y_0) + B_2(y-y_0)^2 + \ldots. \tag{3.6}$$

The square of the expansion is then

$$B(0,y,0)^2 = B_0^2 + B_0B_1(y-y_0) + B_1^2(y-y_0)^2 + B_0B_2(y-y_0)^2 + \mathcal{O}(y^3) \tag{3.7}$$

Using Eq. 3.6,

$$\frac{\partial^2 B(0,y,0)^2}{\partial y^2} = 2B_1^2 + 2B_0B_2 + \mathcal{O}(y). \tag{3.8}$$

The magnetic field is stable if $B_1^2 + B_0B_2 \neq 0$. Nonzero linear terms in the magnetic field expansion in Eq. 3.6 provide harmonic motion for the levitated particle. Higher order terms lead to anharmonicities in the trapping potential but become negligible near or at the vertical equilibrium position. If the position of the particle deviates too far from this equilibrium position, the anharmoncity can lead to errors in the precision measurement of G. However, all three translational degrees of freedom can be used to map out the magnetic field to give a more accurate model including the higher order terms.

From Eq. 3.3, to balance gravity, a large gradient in B^2 is required. In order to achieve this, pole pieces can be utilized to concentrate the magnetic flux from permanent magnets to a smaller region, increasing the gradient.

3.2.1 Permanent Magnets

The choice of permanent magnets is extremely important to the success of these experiments. Two of the most common magnets are rare earth magnets: samariumcobalt (SmCo) and neodymium-iron-boron (NdFeB). They are both in the Lanthanide series of the periodic table, so many properties are similar to each other despite many key differences. The SmCo, containing approximately 60% cobalt, an element found in stainless steel, is more corrosion resistant than NdFeB. Some elements in the NdFeB magnets are not corrosion resistant and can oxidize, preventing efficient pumping to high or ultra-high vacuum. The NdFeB are coated typically with nickel (Ni) to prevent this.

Magnetic remanence, the magnetization of ferromagnetic materials after an external magnetic field is removed, determines the strength of the magnet. The NdFeB has one of the largest room temperature magnetic remanence of any permanent magnet. The volume independent maximum energy product, $BH_{\max}$, is another common measure of magnetic strength. For SmCo, $BH_{\max}$ is between 150 to 240 kJ/m^3 [95] and between 200 to 440 kJ/m^3 for NdFeB [96]. Here, B is the magnetic flux density and H is the magnetic field. $H_{\max}$ is the magnetic field that maximized the product of B and H. In other words, on a BH field, $H_{\max}$ is the magnetic field that maximized the area of a rectangle constrained to be within the curve.

Despite the larger maximum energy product, NdFeB magnets have disadvantages when compared to SmCo. One of the most important properties to us is the

Curie temperature of the magnets. The Curie temperature is the temperature at which the magnet becomes completely demagnetized. Because many vacuum experiments require ultra-high vacuum ($\sim 10^{-10}$ Torr), baking of the system is needed. The magnets have to survive this process. The Curie temperature for NdFeB is approximately 350°C and approximately 800°C for SmCo. Demagnetization, however, starts to happen well below the Curie temperature and since baking can reach temperatures of 200°C, NdFeB will not work.

Both magnet types were used during the work of this dissertation, though the final results were achieved with SmCo magnets. The NdFeB magnets were replaced by the SmCo magnets to prevent demagnetization of the magnets when baking the system.

3.2.2 Pole Pieces

The design of the pole pieces is equally as important as the magnet selection. The pole pieces must concentrate the magnetic flux to a small region to maximize the flux gradient. In this dissertation, the directions of the system are chosen to be x (transverse) (along the optical axis of the trap), y (vertical) (anti-parallel to Earth's gravity), and z (axial) (along the weak direction of the trap, as will be explained). Machining drawings of the pole pieces are shown in Figs. 3.1 and 3.2.

To constrain the particle in two dimensions, four pole pieces are used to create a quadrupole field in the transverse and vertical directions, as shown in Fig. 3.3(a) and Fig. 3.3(b). A permanent magnet is placed between the two top pole pieces and another is placed between the bottom two. The magnets are oriented so their magnetization axis is anti-parallel to each other's. In this orientation, a quadrupole field is formed. The symmetry is broken by the vertical gap differing from the transverse gap. This shifts the vertical oscillation frequency from the transverse

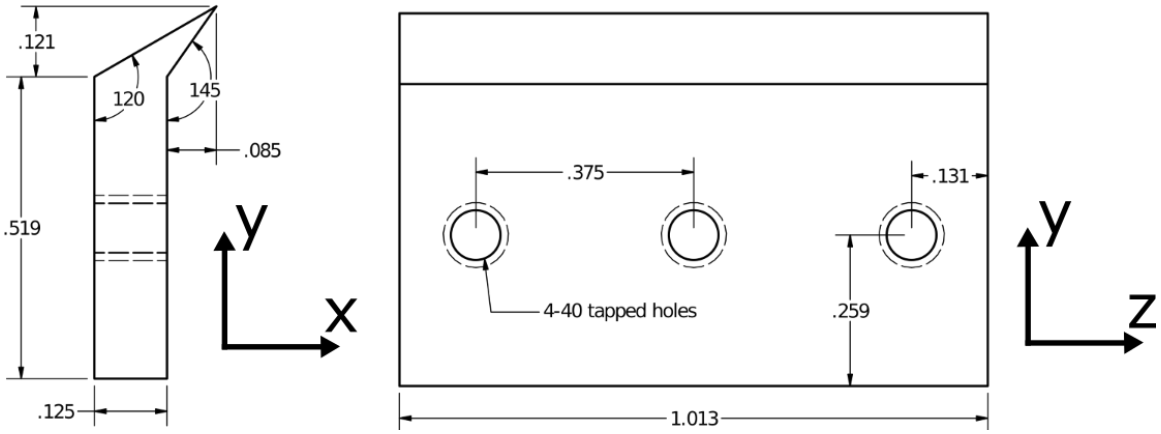


Figure 3.1: The machining drawing of the two bottom pole pieces. The two bottom pole pieces are machined with a sharp tip and lapped once returned from the machine shop. The tapped holes are for mounting the trap. All lengths are in inches and all angles are in degrees.

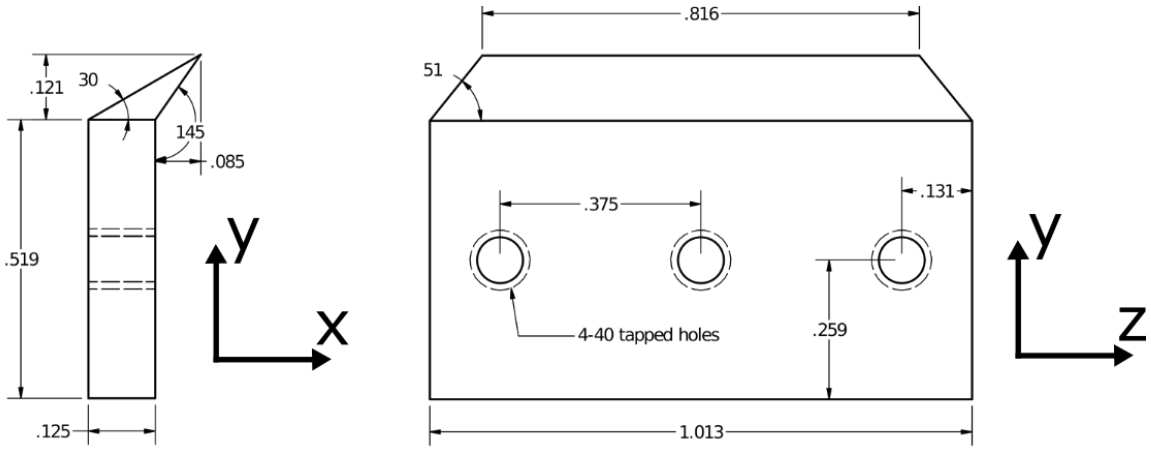


Figure 3.2: The machining drawing of the two top pole pieces. The two top pole pieces are machined with a sharp tip and lapped once returned from the machine shop. The tips of the top pole pieces are cut shorter than the bottom two pole pieces. All lengths are in inches and all angles are in degrees.

frequency to prevent unwanted coupling of those degrees of freedom.

When viewing the trap from the axial direction, the vertical symmetry is broken. To help provide the restoring force, the magnetic field is curved in order to provide a field gradient in the axial direction. To achieve this, the tips of the top pole pieces can be cut shorter than the bottom pole pieces. Another option is to curve the pole pieces themselves, whose radii of curvature determine the oscillation frequency. The center of curvature for both sets of pole pieces would lie on top of each other

The material for the pole pieces needs to have a large saturation magnetization. That is to say, the material becomes saturated at a larger magnetic field. We want to maximize the magnetic flux in the trapping region by using the pole pieces. The larger the saturation magnetization, the larger the field and the gradient is in the region of interest. An iron-cobalt alloy, Hiperco 50A (Ed Fagan, Inc.), is chosen as the pole piece material due to it having the highest saturation magnetization of all soft-magnetic alloys [97]. The saturation magnetization is 2.4 T as compared to, for example iron (Fe) at 2.1 T [98].

3.2.3 Trap Construction

With the pole piece material and permanent magnets chosen, and with the general idea for constraining the particle in three dimensions, the trap itself needs to be built. The four poles are machined out of Hiperco 50A. Typically, this is done on a milling machine. The pole pieces can also be machined using wire electrical discharge machining (EDM) or ground.

The pole pieces are machined to be 1.0125 inches long in the axial direction. Three, 4-40 tapped holes are machined into the pole pieces to allow the trap to be mounted more rigidly. Both the top and bottom pole pieces are machined with a sharp tip. Machining to a sharp tip allows us to lap the tips flat for a more precise finish.

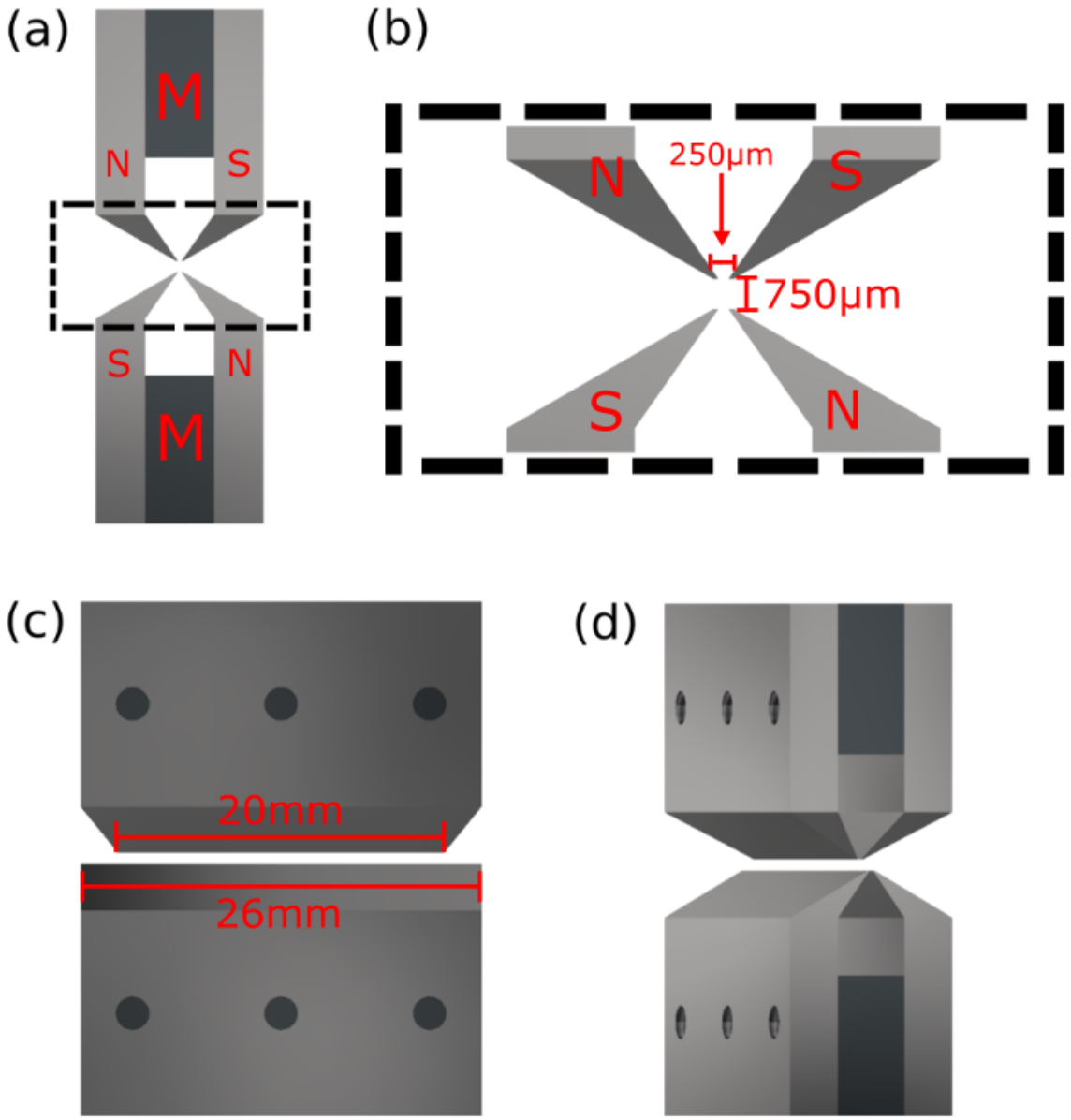


Figure 3.3: (a) An assembly drawing of the magneto-gravitational trap as viewed from the axial direction. The four pole pieces form a quadrupole field in the vertical and transverse directions. The permanent magnets are labeled by M and oriented such that the poles are as labeled by N and S. (b) A close up view of (a) (black dashed box) showing the quadrupole geometry that is broken in the transverse and vertical directions. (c) The assembly drawing of the trap as viewed from the transverse direction. The top pole pieces are machined shorter than the bottom pole pieces. (d) The trap as viewed from an angle.

The distance from the inside face of the pole pieces to the tips is 0.085 inches. The magnets are 1/8 inches thick in their magnetization direction (transverse direction of the trap). The oversizing of the pole pieces allow the pole pieces to be shimmed for a precise transverse gap as well as being able to lap the tips multiple times in the case of damage to the tips.

The four pole pieces are lapped on fine grit sand paper carefully until the flat portion of the tip is 0.005 inches and uniform across the entire pole piece. Lapping is more precise than conventional machining due to the sharpness of the tips and brittle nature of Hiperco 50A. By having a larger surface area at the tips, more magnetic flux can be concentrated into the trapping region. One SmCo permanent magnet is sandwiched between the top two pole pieces and one is sandwiched between the bottom two pole pieces. To prevent the tips of the two sets of pole pieces from hitting each other and obtain the desired gap size in the transverse direction, nonmagnetic 316 stainless steel shims in addition to insulating, high-temperature tolerant polyether ether ketone (PEEK) shims are used to separate the two pole pieces. The target transverse gap size is 250 μm from tip to tip at the closest points. The insulating shims electrically isolate the pole pieces from each other.

The top pole piece tips are cut shorter than the bottom to create the magnetic field curving effect in the axial direction (see Fig. 3.2 and Fig. 3.3). The top pieces are cut to a total length 5 mm shorter than that of the bottom. The outside angle of the pole pieces are cut to 30° allowing for the numerical aperture (NA) of the collection objective to reach 0.5, though a much lower NA objective is used for the work in this dissertation. The magnets need to be orientated correctly to form the quadrupole moment. This results in an attracting force between the top and bottom sets of pole pieces. If the pole pieces repel each other, the orientation needs to be changed.

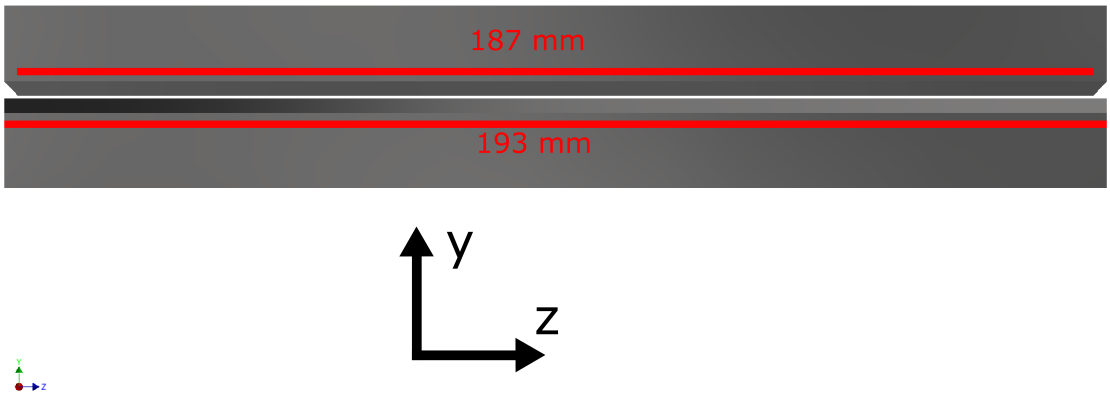


Figure 3.4: The long pole pieces originally designed for the measurement of G. The bottom pole pieces are 193 mm long in the axial direction. The top pole pieces are 187 mm long to provide the magnetic field curving effect.

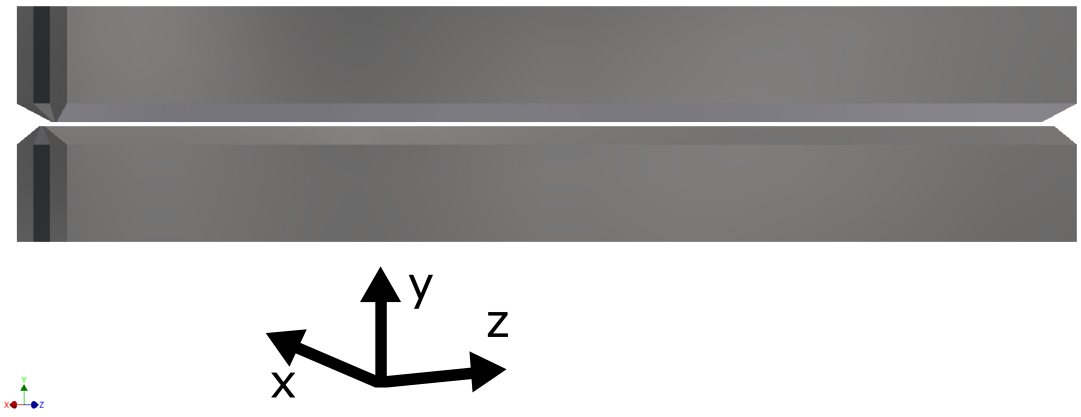


Figure 3.5: A view at an angle to illustrate the quadrupole geometry along with the extended pole pieces in the axial direction.

3.2.4 Trap Mount

In the original design of the experiment, the pole pieces were intended to be 7.598 in (193 mm) in the axial direction along with 13 to 15 SmCo permanent magnets sandwiched between them across the length, as shown in Fig 3.4 and Fig. 3.5. Because of the strength of the magnetic field produced, a custom mount was needed to adjust the vertical gap to prevent the pole pieces from slamming together, possibly damaging the pole pieces or injuring the user. These pole pieces were abandoned for two main reasons. The first is due to the difficulty in assembly. Since an AC and DC voltage is applied to the pole pieces (see chapter 5), the pole pieces must be electrically isolated from each other. In practice, it was extremely difficult to keep electrically conducting material from shorting the pole pieces across the transverse gaps. Since a smaller trap was ultimately designed and used, a mount was needed to hold the trap. A similar mount was designed and machined because of its convenience to assemble the trap. Three dimensional renderings of the mount assembly with the magneto-gravitational trap attached are shown in Figs. 3.6, 3.7, and 3.8. Photographs of the mount with the trap are shown in Fig. 3.9, 3.10, and 3.11.

Because the vacuum chamber and trap need to be able to be baked, thermal expansion and contraction needs to be considered. Grade 5 titanium is used to match the coefficient of thermal expansion (CTE) to that of Hiperco 50A. Grade 5 titanium has a CTE of 9.2 μm/m/°C and Hiperco 50A has a CTE of 10.4 μm/m/°C. With mismatched CTEs, the trap can stick and slip on the mount, causing particle loss.

The mount consists of three main pieces. The back piece acts as the anchor for the trap, where back means the side closest to the optics used to illuminate the particle onto a CMOS camera (optics shown in Fig. 3.21 and Fig. 3.22). A cutout is made in the back piece that is 1 inch vertically and 4.5 inches wide to allow large angles of optical access for feedback cooling or excitation. The front bottom piece

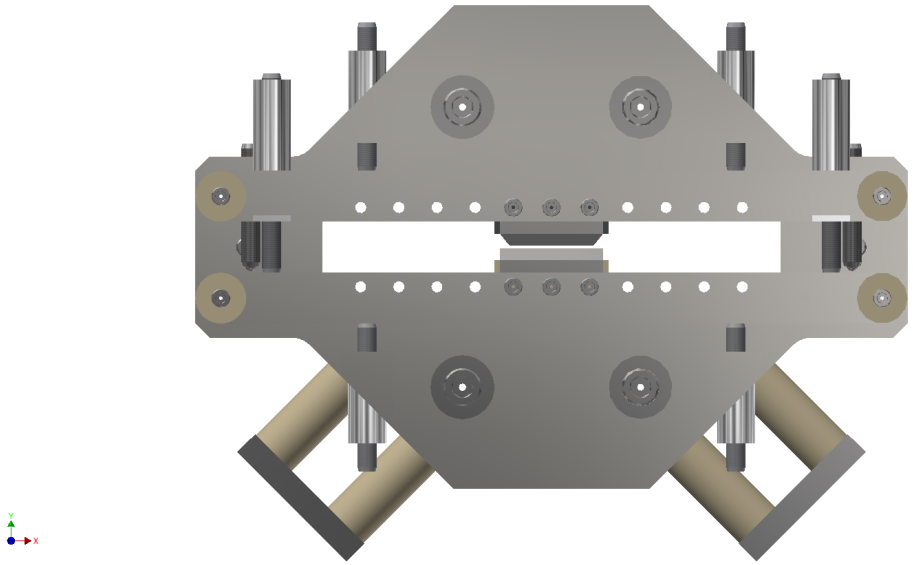


Figure 3.6: A three dimensional rendering of the front of the trap and its mount. The four sets of adjustment screws allow for fine tuning of the vertical gap. Mounting the trap creates a nominal vertical gap of 750 µm. The mount is photographed in Fig. 3.9.

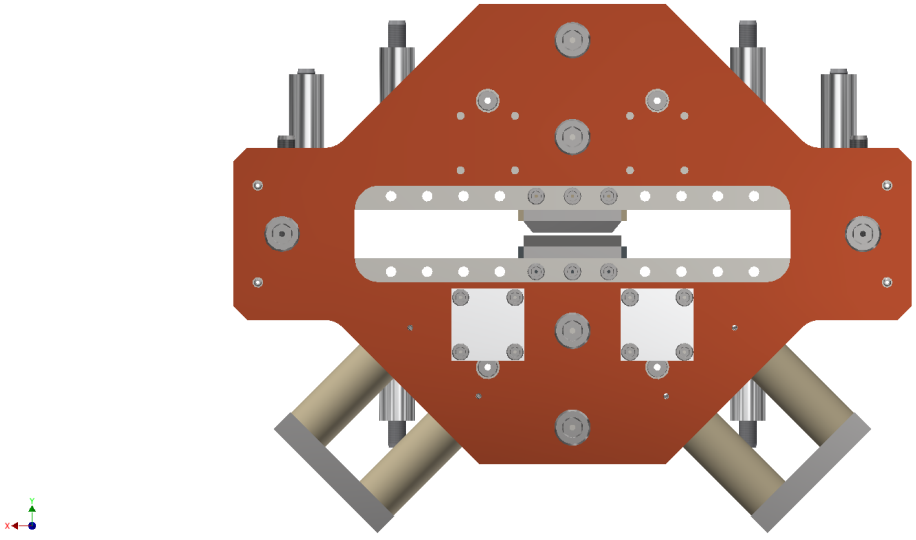


Figure 3.7: A three dimensional rendering of the back of the trap and its mount. The copper allows for high thermal conductivity for temperature monitoring and stabilizing of the trap to prevent magnetic field fluctuations.

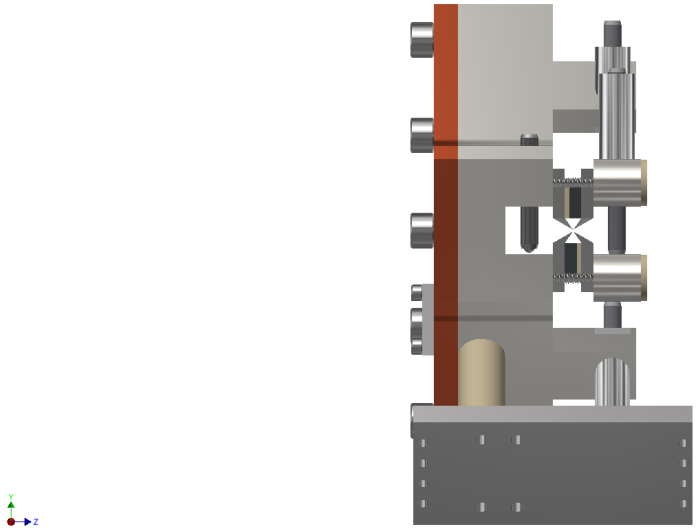


Figure 3.8: A three dimensional rendering of the side of the trap and its mount. The use of the adjustment screws is more visible in this view. The clamping mechanism of the trap is also seen.

is rigidly attached to the back piece. The trap is attached to this piece via three 4-40 vented screws. The vented screws prevent virtual leaks. The front top piece is free to slide up and down along the back piece via two slits instead of clearance holes. PEEK film is placed between the front top piece and the back piece to prevent electrical contact. The screws that hold this to the back are insulated via PEEK sleeve bearings.

There are four sets of 3/16-100 adjustment screws (Thorlabs, Inc.) that are used to control the vertical gap. One set of screws sets the vertical gap of the two back pole pieces. Adjustment screws in the top clamp sets the vertical gap of the two front pole pieces. The bottom-most adjustment screws prevents the bottom clamp from drifting downward, causing misalignment of the pole pieces. The top most adjustment screws lock everything in place. It is extremely important to insulate the adjustment screws from what they press on as all the pieces are in contact with different pole pieces.

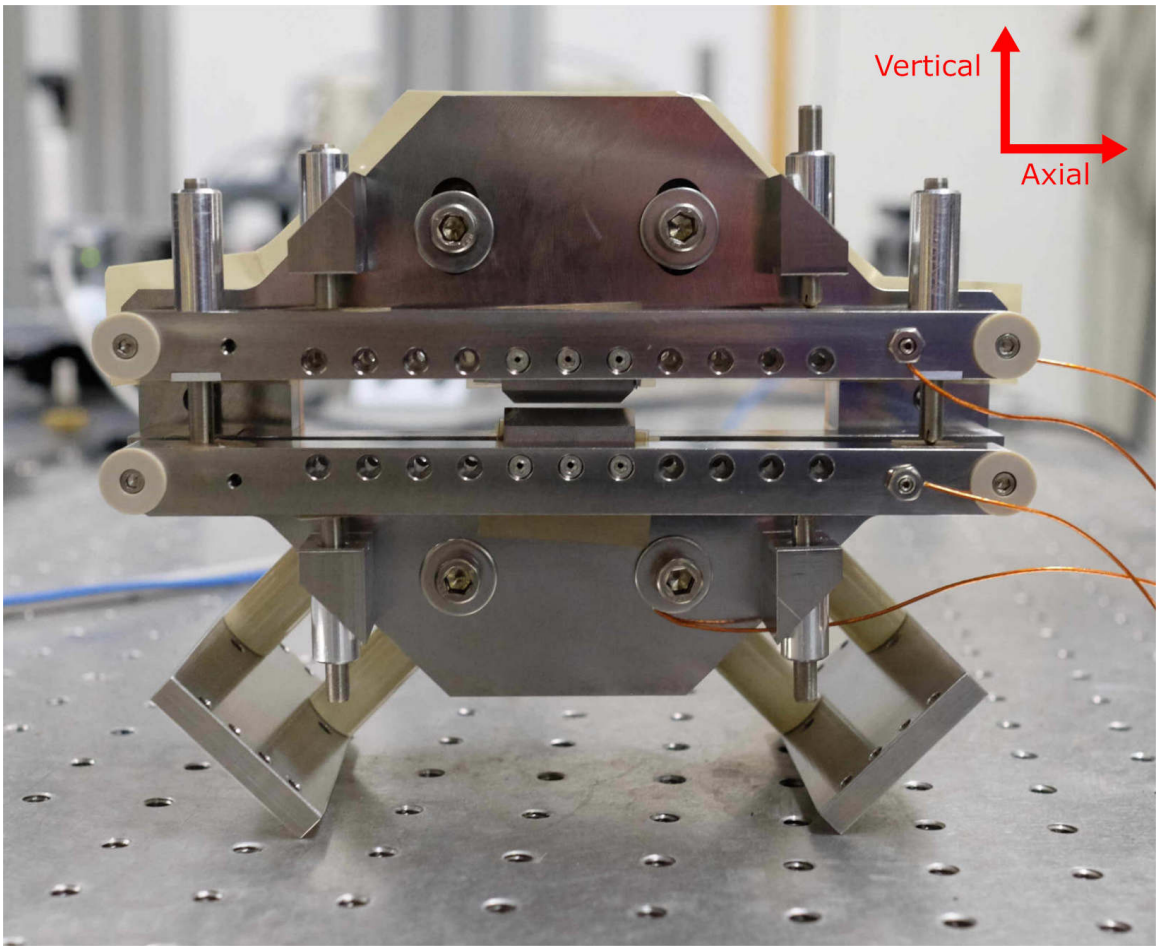


Figure 3.9: The front of the trap and mount along the transverse direction. The adjustment screws are visible. The four wires are to put an AC and DC voltage on the pole pieces. This is the same view as Fig. 3.6.

The adjustment screws were made custom to not include ball bearings in their tips to prevent virtual leaks caused by slow diffusion of air from the volume behind the ball bearings. Because they do not include ball bearings, the epoxy that glues the ball bearings to the screws are not present. The use of epoxy would make the screws incompatible with ultra-high vacuum.

The front two pole pieces are attached to the two clamps via three 4-40 screws each. The clamps are attached to the mount via long 4-40 screws. The choice of these

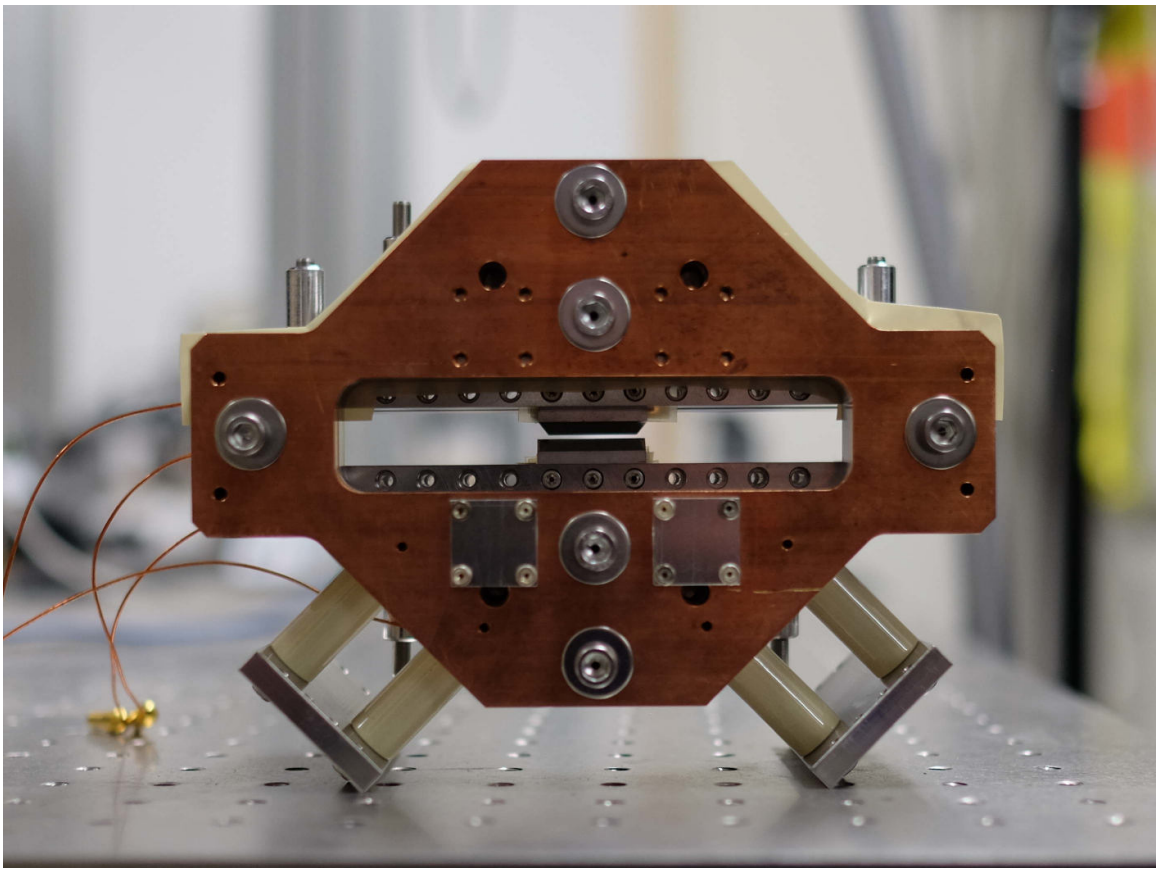


Figure 3.10: The back of the trap and its mount along the transverse direction. The copper heat spreader and aluminum mounts are attached though no sensor or heater is attached. This is the same view as Fig. 3.7.

screws allow the clamps to be adjusted vertically to fine tune the vertical gap of the front two pole pieces. The screws are insulated by PEEK sleeve bearings.

On the back of the anchor piece, a piece of copper is attached. Copper has a much larger thermal conductivity than titanium. Heaters can be mounted to the copper piece allowing a more efficient heating of the mount for use in temperature stabilization of the trap. Four ceramic standoffs are attached to the anchor piece that allows the mount to be mounted in the vacuum chamber. Four groove grabbers (Kimball Physics MCF1000-GrvGrb-C01) are then used to hold the mount in the chamber.

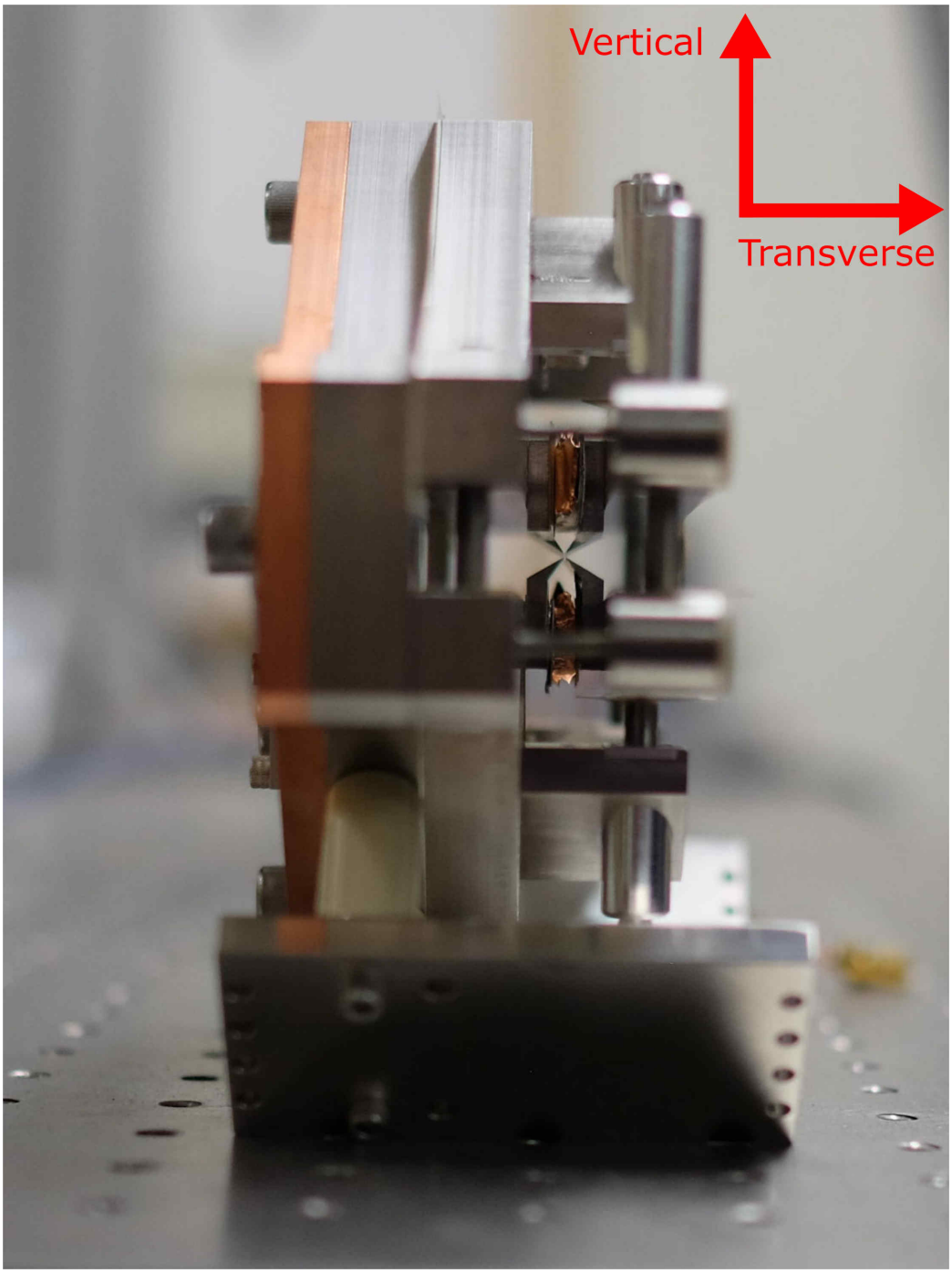


Figure 3.11: The side view of the trap and its mount. The quadrupole geometry of the trap is visible. The vertical gap is approximately 750 μm and the transverse gap is approximately 250 μm. This is the same view as Fig. 3.8.

3.2.5 Spherical Harmonic Approximation of Trapping Potential

To determine if the trap geometry described above will constrain the particle, we can look at a small region near the equilibrium position of the trap. The magnetic field and magnetic scalar potential must obey Maxwell's equations. The magnetic field is divergence free,

$$\vec{\nabla} \cdot \vec{B}(x, y, z) = 0. \tag{3.9}$$

The magnetic scalar potential is defined such that

$$\vec{B}(x, y, z) = -\vec{\nabla}\Phi_B(x, y, z). \tag{3.10}$$

Therefore, the magnetic scalar potential obeys Laplace's equation,

$$\vec{\nabla}^2\Phi_B = 0. \tag{3.11}$$

In spherical coordinates, the general solution of Laplace's equation is well known [82]

$$\begin{aligned}\Phi_B(r, \theta, \phi) &= \sum_{l=0}^{\infty} \sum_{m=-l}^{l} \left[A_l r^l + B_l r^{-(l+1)}\right] P_l^m(cos\phi) e^{-im\phi} \\ &= \sum_{l=0}^{\infty} \sum_{m=-l}^{l} \left[A_l r^l + B_l r^{-(l+1)}\right] Y_l^m(\theta, \phi)\end{aligned} \tag{3.12}$$

where P are the associated Legendre polynomials and Y are the spherical harmonics. The spherical harmonics are normalized such that

$$\int_0^{\pi} \int_0^{2\pi} Y_l^m Y_{l'}^{m'} d\Omega = \delta_{ll'}\delta_{mm'}. \tag{3.13}$$

In a small region around the equlibrium position of the particle, we know the magnetic scalar potential and the magnetic field must be finite. The second term blows up when r goes to zero, so all B_l must be zero for all values of l.

Because we have three independent parameters of the system (i.e., the oscillation frequencies in the three dimensions), we can only use three terms in Eq. 3.12 to model the field and potential by determining the necessary A_l coefficients. Symmetry arguments can be made to determine which terms will suffice [94]. It is a good approximation to describe the harmonic component of the trap in all three directions by this expansion.

The dominant term in the series is the quadrupole moment, Y_2^{-2}. In the transverse-vertical plane, the quadrupole moment creates the constraining potential. Since the potential is purely real, we use the real spherical harmonics, defined as

$$R\left[Y_l^m\right] = \begin{cases} \frac{i}{\sqrt{2}}(Y_l^m - (-1)^m Y_l^{-m}), & m < 0 \\ Y_l^0, & m = 0 \\ \frac{i}{\sqrt{2}}(Y_l^{-|m|} + (-1)^m Y_l^{-|m|}), & m > 0. \end{cases} \tag{3.14}$$

Writing in rectangular coordinates, $R[Y_2^{-2}]$ is

$$R[Y_2^{-2}] = \frac{1}{2}\sqrt{\frac{15}{\pi}}\frac{xy}{r^2} \tag{3.15}$$

where $r^2 = x^2 + y^2 + z^2$. We can see that this spherical harmonic is symmetric in the axial direction and anti-symmetric in the transverse and vertical directions. The correction to the quadrupole spherical harmonic needs to have the same symmetry but add to the transverse and vertical directions differently, shifting those oscillation frequencies apart from each other. The first spherical harmonic that satisfies this is

the Y_4^{-4}. In rectangular coordinates, the real spherical harmonic is

$$R[Y_4^{-4}] = \frac{3}{4}\sqrt{\frac{35}{\pi}}\frac{xy(x^2-y^2)}{r^4} \tag{3.16}$$

The last spherical harmonic needs to create the restoring force in the axial direction. Since the field needs to curve upward at the edge of the trap, the potential must be symmetric in the axial direction but anti-symmetric vertically. The Y_3^1 spherical harmonic satisfies this and the real spherical harmonic is

$$R[Y_3^1] = \frac{1}{4}\sqrt{\frac{21}{2\pi}}\frac{x(4z^2-x^2-y^2)}{r^3}. \tag{3.17}$$

3.2.6 Potential and Fields

This model of the magnetic field and the electric field is appropriate to understand the general physics of the trap far from its edges. At the edges, however, the spherical harmonic approximation breaks down and a more in depth model is needed. Numerical calculations that include magnetic saturation, gravity, and voltages on the pole pieces are needed. This was not done in the work for this dissertation.

The total potential, determined by the spherical harmonics above, is

$$\Phi_B = A_2 r^2 R[Y_2^{-2}] + A_3 r^3 R[Y_3^1] + A_4 r^4 R[Y_4^{-1}]. \tag{3.18}$$

In order to make the coefficients A_n have the same units for ease of comparison, we can explicitly take out the necessary factors. Because the magnetic potential energy contains B^2 and not Φ_B, we can define alternative coefficients such that the units of the a_n coefficients are Tesla (T). Currently as written, the units of the A_n are $\mathrm{T/m^n}$.

The a_n coefficients can be defined as

$$A_n = \frac{\sqrt{4\pi} a_n r_0^{1-n}}{n} = \left(\frac{\sqrt{4\pi} a_n r_0}{n}\right)\left(\frac{1}{r_0}\right)^n \tag{3.19}$$

where r_0 can be a characteristic length in the system (i.e., vertical gap distance of trap). The division by n is designed to cancel out when taking the r component of the gradient. A factor of $\sqrt{4\pi}$ is factored because our normalization of the spherical harmonics. The normalization is a factor of $\sqrt{4\pi}$ too small to keep the power of the spherical harmonics unity. The interpretation of the coefficients a_n is that a_n is the strength of the n^{th} term of the magnetic field expansion at the characteristic length r_0. With the right-most factorization, Eq. 3.18 becomes

$$\begin{aligned}\Phi_B = &\left(\frac{\sqrt{4\pi} a_2 r_0}{2}\right)\left(\frac{r}{r_0}\right)^2 R[Y_2^{-2}] + \left(\frac{\sqrt{4\pi} a_3 r_0}{3}\right)\left(\frac{r}{r_0}\right)^3 R[Y_3^1] \\ &+ \left(\frac{\sqrt{4\pi} a_4 r_0}{4}\right)\left(\frac{r}{r_0}\right)^4 R[Y_4^{-1}]\end{aligned} \tag{3.20}$$

The magnetic field components in rectangular coordinates calculated by Eq. 3.10 and evaluated using Mathematica 11.3,

$$\begin{aligned}B_x(x,y,z) = &-\left(\frac{\sqrt{15}}{2}\right)\left(\frac{y}{r_0}\right) a_2 + \left(\frac{1}{2}\right)\sqrt{\frac{7}{6}}\left(\frac{4z^2 - x^2 - y^2}{r_0^2}\right) a_3 \\ &+ \sqrt{\frac{7}{6}}\left(\frac{x^2}{r_0^2}\right) a_3 - \left(\frac{3\sqrt{35}}{4}\right)\left(\frac{x^2 y}{r_0^3}\right) a_4 \\ &- \left(\frac{3\sqrt{35}}{8}\right)\left(\frac{y(x^2 - y^2)}{r_0^3}\right) a_4,\end{aligned} \tag{3.21}$$

$$B_y(x,y,z) = -\left(\frac{\sqrt{15}}{2}\right)\left(\frac{x}{r_0}\right)a_2 + \sqrt{\frac{7}{6}}\left(\frac{xy}{r_0^2}\right)a_3 + \left(\frac{3\sqrt{35}}{4}\right)\left(\frac{xy^2}{r_0^3}\right)a_4 - \left(\frac{3\sqrt{35}}{8}\right)\left(\frac{x(x^2-y^2)}{r_0^3}\right)a_4, \tag{3.22}$$

$$B_z(x,y,z) = -2\sqrt{\frac{14}{3}}\left(\frac{xz}{r_0^2}\right)a_3. \tag{3.23}$$

The coefficients a_2, a_3, and a_4 are determined by the three oscillation frequencies. The oscillation frequencies for the data presented in chapter 10 are $\omega_x/2\pi = 10.5\,\text{Hz}$, $\omega_y/2\pi = 15.2\,\text{Hz}$, and $\omega_z/2\pi = 1.75\,\text{Hz}$. In my calculations, the vertical gap size $y_0 = 750\ \mu\text{m}$ is used as characteristic length r_0. Using Mathematica 11.3, the coefficients were found to be $a_2 = -0.2028346$ T, $a_3 = 0.0005219$ T, and $a_4 = 0.0007447$ T.The potential energy of the system can then be calculated by Eq. 3.1. The magnetic field and magnetic potential are shown in Fig. 3.12.

The magneto-gravitational trap used in this dissertation differs from the linear quadrupole magneto-gravitational traps used before in our laboratory [84, 94]. The gaps in the vertical and transverse directions are larger, as well as the length of the pole pieces in the axial direction being longer. Because of the larger gaps, the gradient of B^2 is no longer large enough to balance gravity. In order to help cancel gravity, because the particles are typically charged from the loading process, an electric field is applied in the trapping region. The bottom two pole pieces are grounded while a DC voltage is applied to the top two pole pieces. In the center of the trap, far from the edges of the trap in the axial direction (a reasonable assumption considering the length of the pole pieces), the electric field is assumed to be uniform, $\vec{E} = E_0\hat{y}$. The

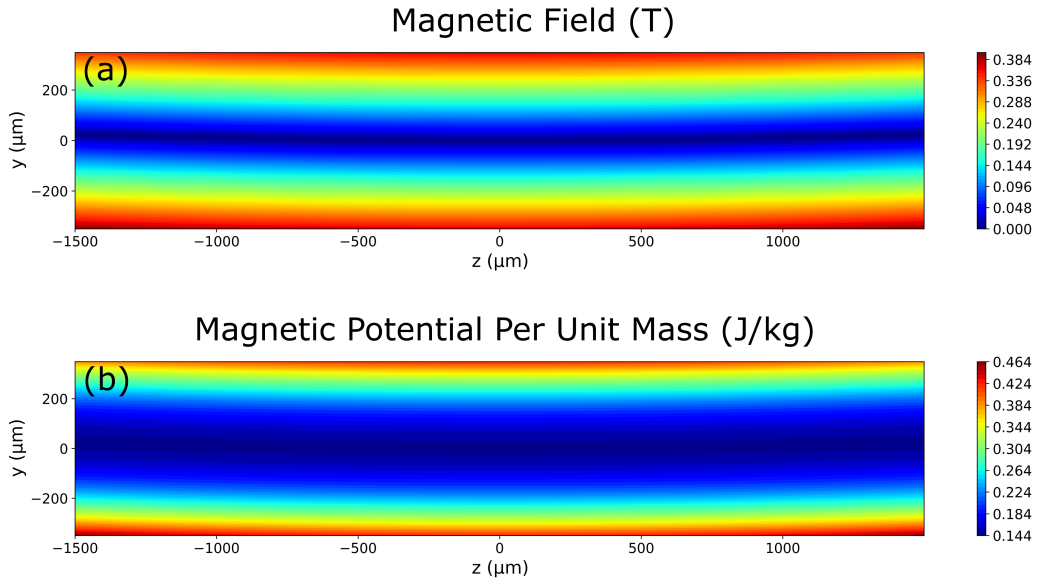


Figure 3.12: (a) The magnetic field as viewed from along the optical axis (transverse direction) of the magneto-gravitational trap. The magnetic field curves up at the edges of the trap. A subsection of the axial direction is shown. (b) The magnetic potential is shown. The particle can follow the equipotential lines, which shows the particle is not constrained axially.

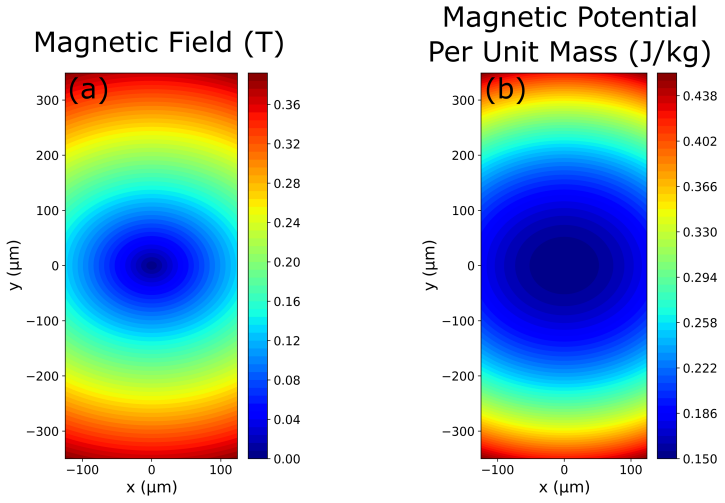


Figure 3.13: (a) The magnetic field as viewed from the axial direction. The quadrupole moment is dominant but the broken symmetry is confirmed by the slight ellipsoidal shape. (b) The magnetic potential in the transverse-vertical plane has a minimum at the center and has a gradient in all direction, constraining the particle in these directions.

electric potential due to an electric field is

$$\Phi_E = -\int_c \vec{E} \cdot d\vec{l}. \tag{3.24}$$

Integrating vertically from the bottom to top pole pieces, $\Phi_E = -E_0 y$, where y is the height of the particle in the vertical position. To ensure that the boundary conditions are met, $E_0 = -V_0/y_0$ where V_0 is the DC voltage on the top pole pieces and y_0 is the vertical gap size. The electric potential energy is given by $U_E = q\Phi_E$ where q is the charge on the particle.

The total potential energy in the magneto-gravitational trap with the DC bias is then

$$U(x, y, z) = -\frac{\chi B(x, y, z)^2 V}{2\mu_0} + mgy + q\frac{V_0}{y_0}y. \tag{3.25}$$

This equation can be written per unit mass $u = U/m$,

$$u(x, y, z) = -\frac{\chi B(x, y, z)^2}{2\rho\mu_0} + gy + \left(\frac{q}{m}\right)\frac{V_0}{y_0}y. \tag{3.26}$$

The important parameters are now the density of the material, magnetic susceptibility, and the charge-to-mass ratio.

In the absence of gravity and electric fields, calculations show that the particle is not constrained in the axial direction (see Fig. 3.12(b)). The particle can follow an equipotential line, all of which would lead to the particle leaving the trap. In the transverse-vertical plane (see Fig. 3.13(b)), the particle is constrained.

The magnetic potential along with the gravitational potential without an electric field is shown in Fig. 3.14(a). The potential minimum is at the bottom pole pieces showing that the particle will fall out of the trap vertically. In Fig. 3.14(b), an electric field is applied. The gradient in all directions constrain the particle axially

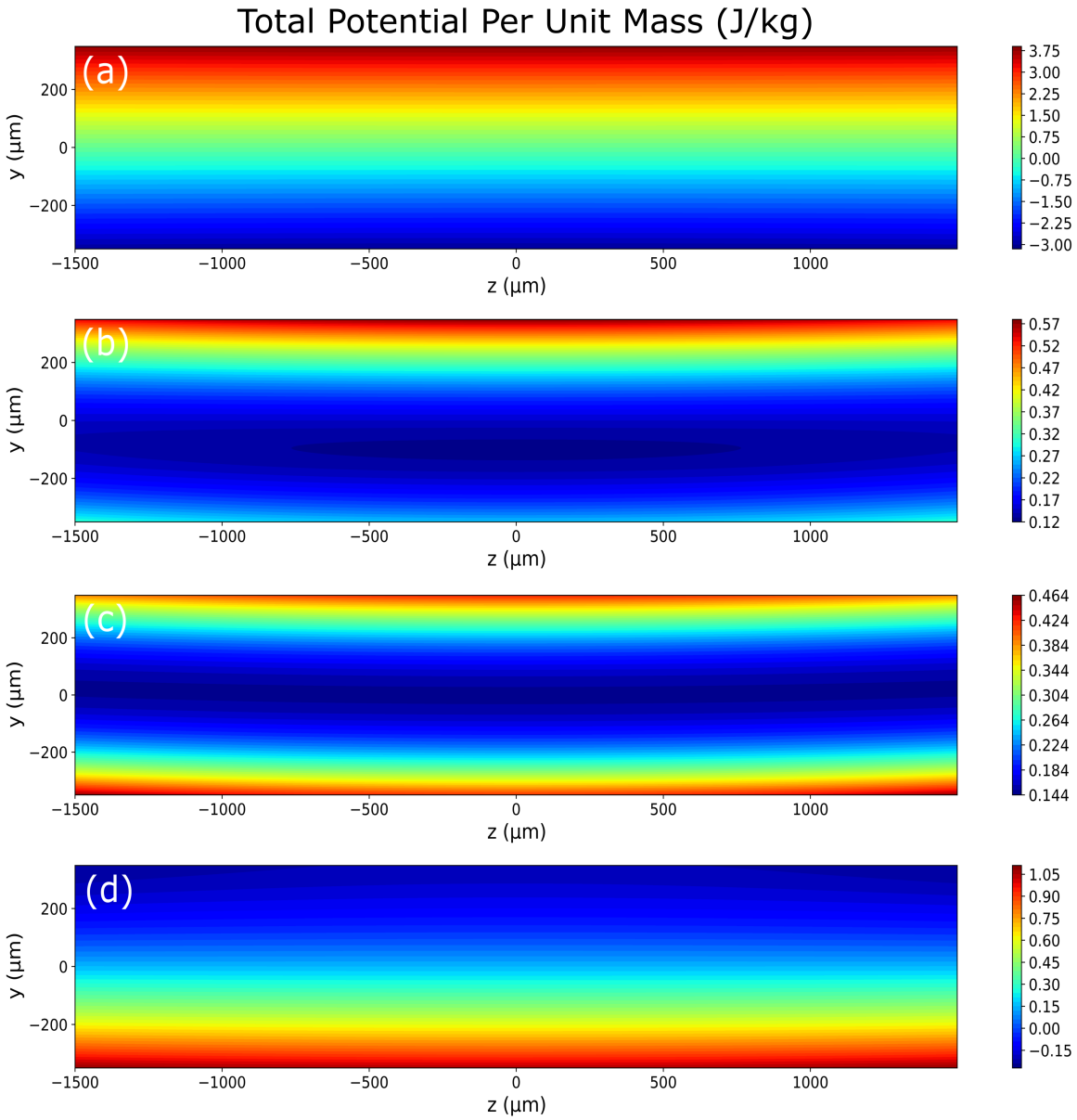


Figure 3.14: (a) The total potential including gravity with no electric field. The potential minimum is at the bottom pole pieces. The magnetic field gradient only is not strong enough to constrain the particle. (b) The total potential with a small qV_0 combination. The electric field is strong enough to raise the potential minimum closer to the center. There is a gradient in the potential in all directions. (c) The total potential where gravity is perfectly canceled out by the electric field. This matches perfectly to Fig. 3.12(b). (d) The total potential with a large qV_0 combination. The electric field overcompensates for gravity and the potential minimum is now at the top pole pieces.

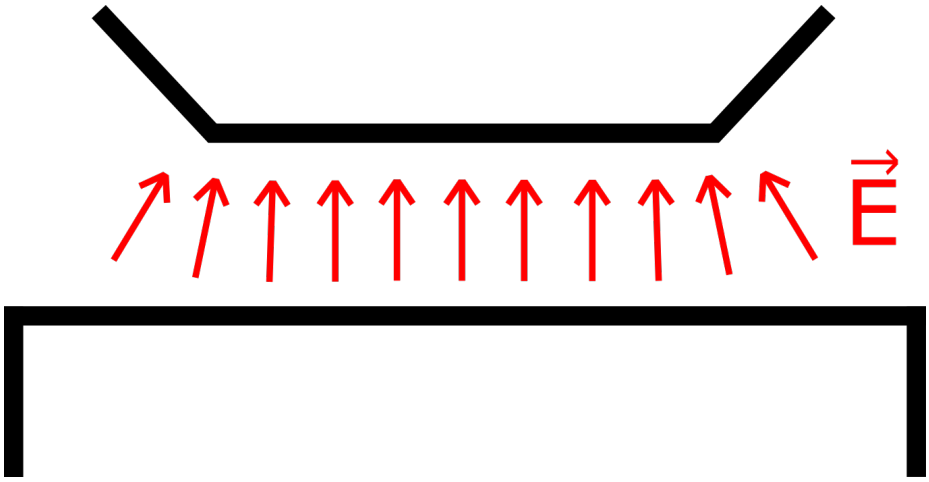


Figure 3.15: A simple illustration showing qualitatively the behavior of the electric field. Near the center of the trap it is approximately constant and only has a component in the vertical direction. Near the edges of the trap, there is also an axial component that creates a restoring force.

and vertically.

For a given charge q on the levitated particle, an electric field of a particular magnitude will cancel gravity completely. In such a case, as shown in Fig. 3.14(c), the total potential of the system matches that of the purely magnetic potential (Fig. 3.12(b)) as expected. Electric fields have been applied to where the particle sits vertically centered in the trap. The particle, in theory, would not be constrained axially but that has not been observed. The electric field near the edges of the trap has an axial component that creates the restoring force.

If the electric field is too strong, however, the total potential will be minimized at the top pole pieces, as shown in Fig 3.14(d). This will result in the particle, against gravity, being forced out of the trap vertically. All four of these cases have been observed for microspheres in the magneto-gravitational trap.

If the trap dimensions in the transverse and vertical directions are scaled up by the same factor, then the magnetic field remains constant. However, the magnetic

potential energy depends on the gradient of the magnetic field amplitude. The gradient scales inversely to the trap dimensions. As the trap is scaled up, the magnetic potential provides a weaker trap. If the trap is scaled down, the potential provides a stronger trap.

3.3 Vacuum System

3.3.1 Vacuum Chamber

The main vacuum chamber that contains the magneto-gravitational trap is a 10 inch spherical octagon (Kimball Physics MCF1000-SphOct-H2C8) (three dimensional rendering shown in Fig. 3.16(a) and 3.16(b)). The main sealing surfaces are 10 inch conflat flanges. There are eight 2.5 inch flanges around the outside of the chamber that are situated every 45°. These secondary ports allow for many different attachments, including valves, feedthroughs, and vacuum nipples. The large diameter chamber was chosen to allow for magneto-gravitational traps that are up to 8 inches long in the axial direction.

The back surface of the chamber is sealed with a 10 inch fused silica vacuum window (Kurt J. Lesker VPZL-1000Q), as shown in Fig. 3.18. The large diameter window allows for optical access of a magneto-gravitational trap that are up to 7.78 inches in the axial direction. Anti-reflection (AR) coating for this window was not available. The fused silica window allows for greater than 90% transmission for wavelengths between 300 nm and 1200 nm. It is recommended that an annealed copper gasket is used to prevent damage to the window. Due to their softness, it was practically too difficult to keep the gaskets flat enough to make a proper seal. A non-annealed gasket was used.

The front surface of the chamber is sealed with a 10 inch to 4.5 inch zero length reducer (Kurt J. Lesker RF1000X450). This flange is sealed to the chamber with a

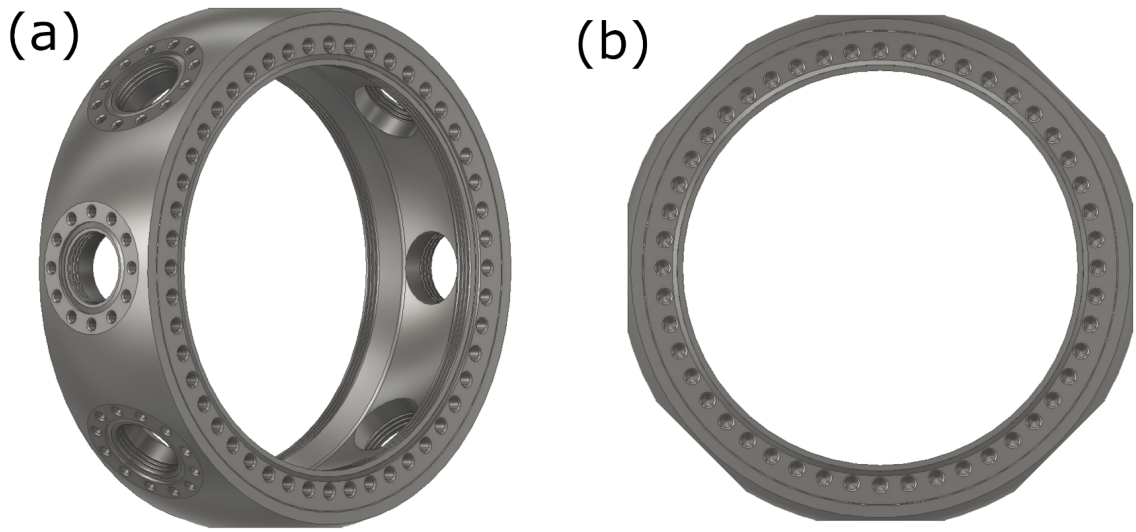


Figure 3.16: (a) A 3 dimensional rendering of the vacuum chamber used in the experiment. The grabber grooves used to mount the trap are visible around the main sealing surface. The smaller ports also have grabber grooves but are unused in this experiment. (b) The front of the vacuum chamber as viewed from the transverse direction.

non-annealed copper gasket. A homemade re-entrant flange [99] is attached to the 4.5 inch side of the reducer. The re-entrant flange allows for the collection objective to sit closer to the center of the chamber. A 50 mm diameter, 5 mm thick visible AR coated window is used in this flange (Edmund Optics #84-458). The window allows greater than 90% transmission for wavelengths between 300 nm and 1000 nm.

Two vacuum nipples are attached and sealed opposite of each other at the zero and 180° positions. One vacuum nipple serves as the loading port for the chamber. Though the vacuum nipple is not necessary, it is convenient as it limits the wear and tear on the chamber at that port since the seal is frequently remade when new particles are loaded. Because this seal is constantly being remade every time a particle is loaded, the likelihood of a bolt seizing in the chamber or damaging the threads in the chamber is greater. Using a vacuum nipple shifts the potential damage to a

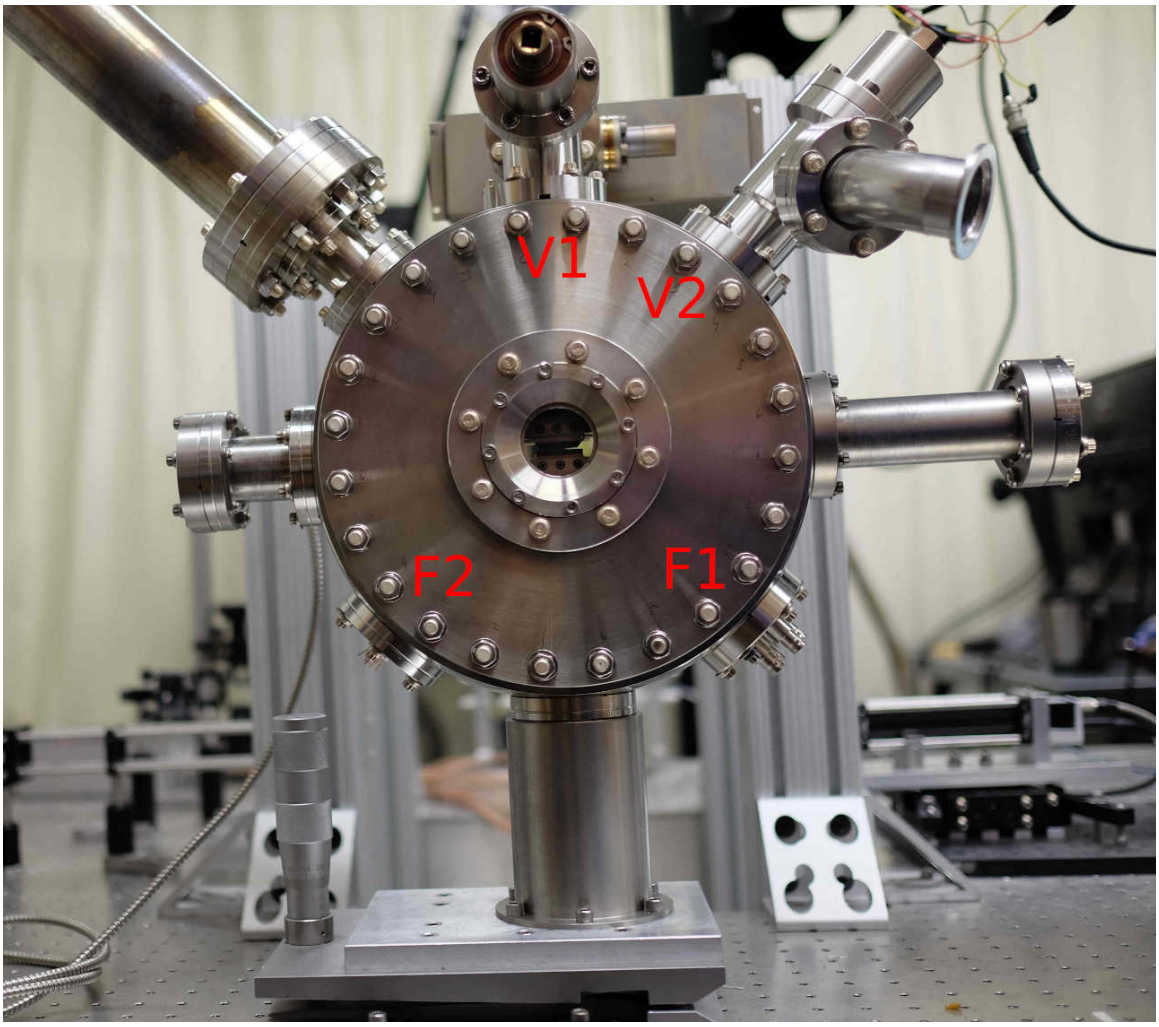


Figure 3.17: The main vacuum chamber as viewed from the front (collection objective side). The chamber sits on a 316 stainless steel pedestal and mounted on a tilt stage. The low thermal conduction pedestal prevents heat from reaching the stage, causing possible damage. The two valves and two feedthroughs are labeled.

cheaper, more easily replaced part. The vacuum nipple is sealed to the chamber with a copper gasket. A blank flange is sealed to the other end of the vacuum nipple with a fluoroelastomer gasket. This gasket is reusable and easier to seal with, however, it is not ultra high vacuum compatible as it cannot withstand baking temperatures. The nipple, though, moves this seal further from the main chamber which can keep the gasket temperature below its melting point. The second vacuum nipple is needed

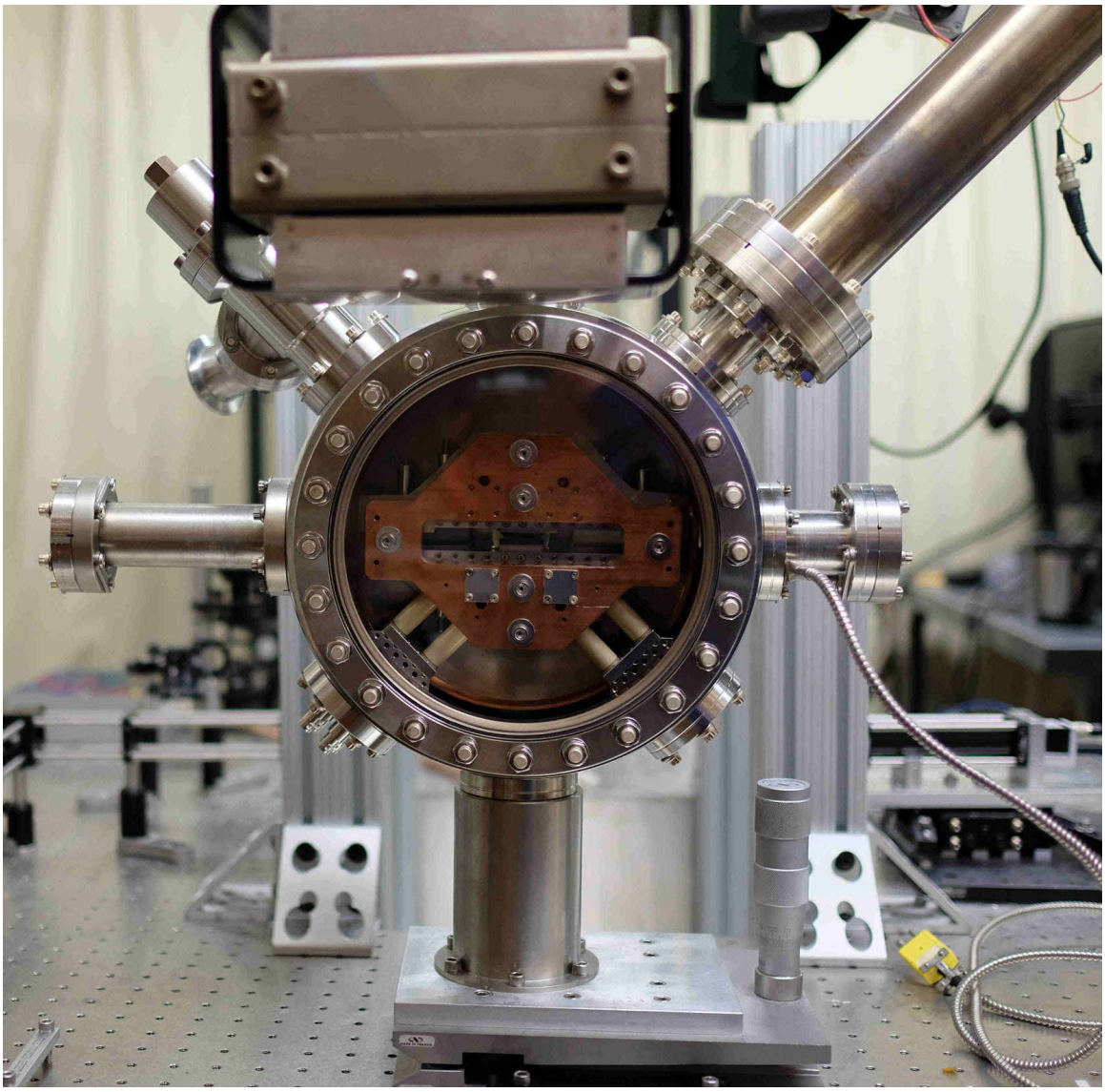


Figure 3.18: The main vacuum chamber as viewed from the back (illumination optics side, see Fig. 3.21 and Fig. 3.22). The large vacuum window allows large angles of optical access for feedback cooling or excitation.

to lift the chamber out of the optical table evenly. Lifting mounts with lifting straps are attached to both vacuum nipples and lifted using a hoist. A window is attached to the second vacuum nipple to allow optical access along the axial direction.

Two right angle, all metal valves (VAT Series 541) are attached and indicated by

V1 and V2 in Fig. 3.17. Valve V1, located on the 90° port, allows the chamber to be opened to an ion pump. Valve V2 allows the chamber to be opened to the pumping system cart. These valves were chosen to be all metal to allow baking of the vacuum chamber. They are easy close to allow for lower torque actuation of the valve while the chamber is under vacuum with a lower risk of losing trap particles.

Lastly, there are two electrical feedthroughs that are attached and sealed to the chamber, indicated by F1 and F2 in Fig. 3.17. Feedthrough F1 is a four pin feedthrough with BNC connectors on the air side. This feedthrough is used to supply the AC and DC voltage to the pole pieces of the magneto-gravitational trap. Feedthrough F2 is a bare wire feedthrough for connections to temperature stabilization equipment. This equipment is not used for the work in this dissertation.

3.3.2 Pumping System

The main vacuum chamber is connected to the pumping system cart by a long, quick flange (QF, ISO standard quick release flange) bellows. A conflat to quick flange adapter is attached to valve V2. The bellows is orientated in a "U" shape, experimentally determined to give the lowest vibration transfer to the main chamber. As the chamber is pumped on, the bellows contract in such a way that does not pull on the chamber. The other end of the bellows is attached to valve V3 (see Fig. 3.19).

The pumping system cart consists of two mechanical pumps. The first pump is a dry mechanical roughing pump (Edwards XDS35) with a peak pumping speed of 9.72 l/s. The second pump is a turbomolecular (turbo) pump (Leybold 1000C) with a peak pumping speed of 1000 l/s. To maintain proper function, the backing pressure for the turbo pump must be 10^{-2} Torr or lower.

Two valves exist on the pumping system cart between the roughing pump and the turbo pump. Valve V4 is a diaphragm valve used to easily throttle the pumping

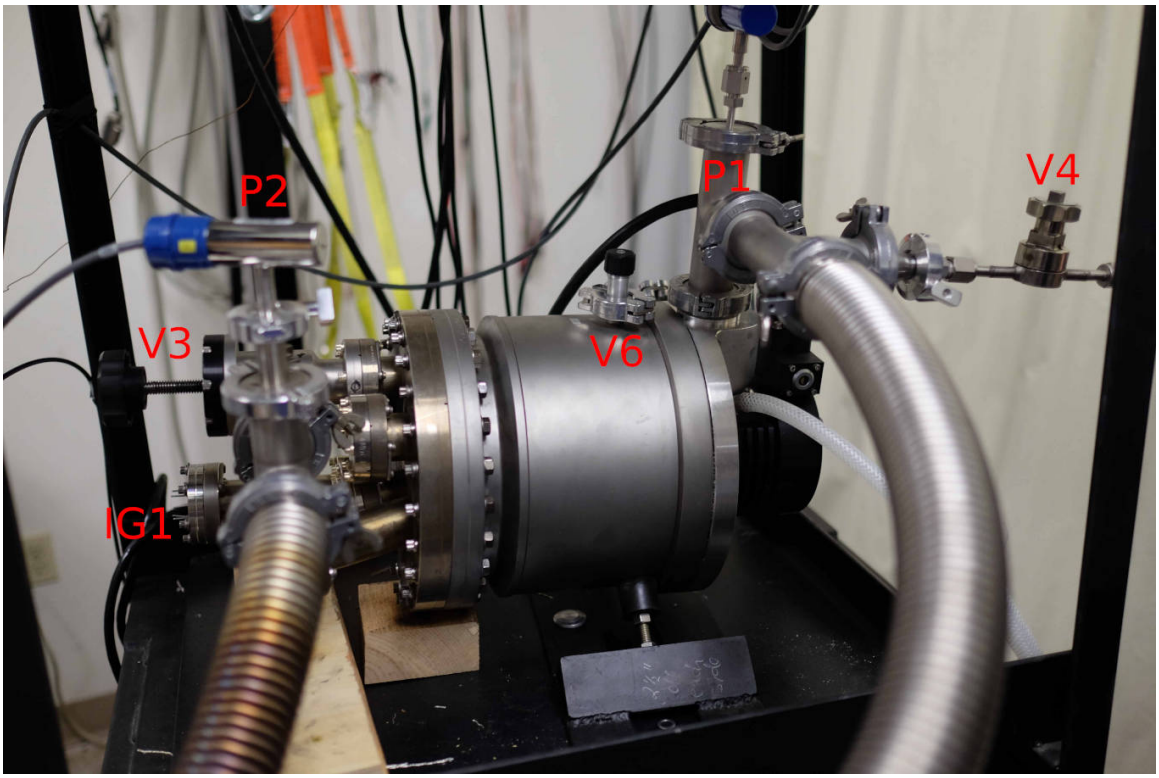


Figure 3.19: The turbomolecular pump used for the work in this dissertation. Two Pirani gauges and an ion gauge measures the pressure at different locations in the pumping system. Valve V4 is a needle valve used to pump the chamber slowly to prevent particle loss.

speed from the roughing pump. If there is a large change of pressure in the chamber, the particle can be pushed out of the magneto-gravitational trap. Valve V5 is a right angle valve that allows full speed pumping once the needle valve is opened completely. This ensures that the backing pressure can stay low enough once the turbo pump is on.

On the pumping system cart are two Pirani gauges and a nude ion gauge. Pirani gauge P1 monitors the pressure on the back side of the turbo pump to ensure the backing pressure is low enough to safely run the turbo pump. Pirani gauge P2 monitors the pressure on the front end of the turbo pump. The ion gauge monitors the pressure on the front end of the turbo pump as well. Since a bellows is used to



Figure 3.20: The roughing pump used in this experiment. Valve V5 allows the roughing pump to be opened to the vacuum chamber for faster pumping once the system is under rough vacuum from the needle valve V4.

connect the pumping system to the main vacuum chamber, pumping speed is lower than the theoretical maximum speed based on the pumps used. The pressure in the vacuum chamber can be significantly higher than is read by the ion gauge on the pumping system cart. To vent the system in a controlled way, valve V6 can be opened.

Mounted directly on the chamber are two non-mechanical pumps. The first, located after valve V1 is an ion pump (Duniway Stockroom VA-020-DD-M). This pump has no mechanical vibrations and is capable of pumping the chamber down to ultra-high vacuum pressures. The pump also reports the pressure inside of the pump based on the current through the pump. This allows a more accurate pressure

reading of the chamber itself since the gauge is directly attached to the main vacuum chamber. The second pump is a titanium sublimation pump (TSP). A large current sublimates titanium on the inner surface of the housing of the pump which is reactive to the background gas in the chamber. This pump was tested but not used for results presented in this dissertation.

3.4 Optics

The optics for this system are relatively simple when compared to other optomechanical experiments [99]. Once successfully levitated, the particle needs to be imaged onto the CMOS camera. To illuminate the levitated particle from the back of the chamber, a 660 nm LED was chosen. The wavelength was chosen based on the maximum spectral response of the CMOS camera, which is around 600 nm. At 660 nm, the relative spectral response is greater than 90%. The light from the LED is collected by an aspheric lens and collimated. The light is then projected onto a 100 µm slit (Thorlabs S100RD). The light that passes through the slit is collimated by a 75 mm achromatic lens and imaged onto the particle with a 150 mm achromatic lens. The focal lengths of these two lenses were chosen so that the slit is magnified to be slightly larger than the region of interest on the CMOS camera. The LED is pulsed to provide stroboscopic illumination to minimize blurring, similar to flash photography.

The collection optics are equally simple. The objective used is a Mitutoyo telecentric 3× objective lens (Edmund Optics #56-985). Telecentric lenses do not change magnification with defocus, keeping the levitated particle the same size on the CMOS camera, even if it is moving in the transverse direction. The objective has a 77 mm working distance allowing the objective to be placed outside of the main vacuum chamber. The objective is attached to a Edmund Optics lens tube that keeps

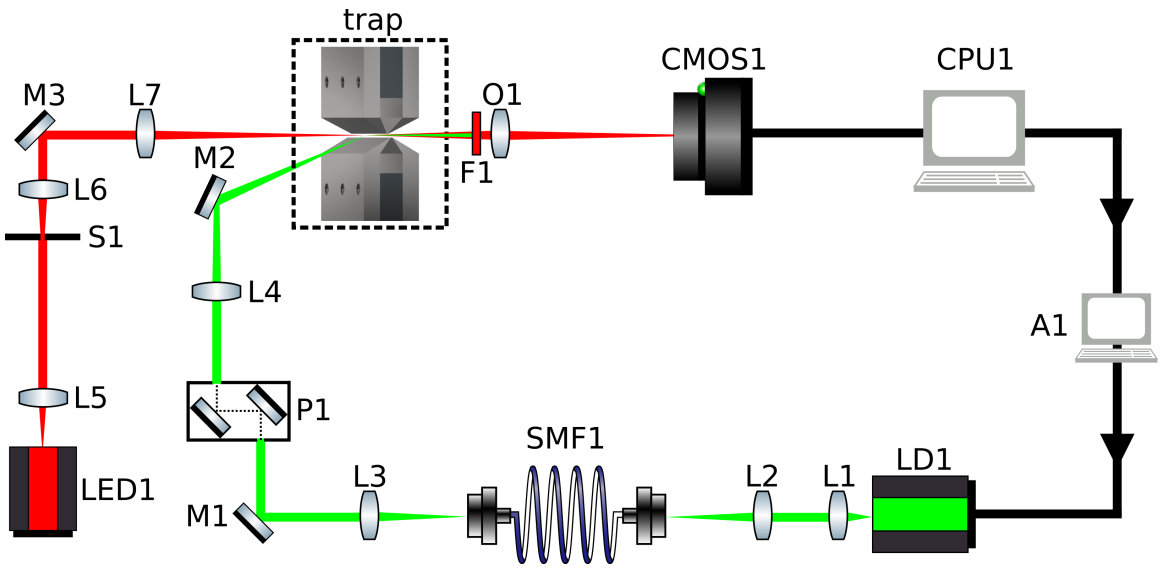


Figure 3.21: The optical system used in the accelerometry measurements. A 660 nm LED is used collimated onto a 100 µm slit. The slit is then magnified and imaged on the trapped particle. The scattered light from the particle is collected by a 3× telecentric objective and imaged onto a CMOS camera. The images are analyzed in real time to determine the sign and amplitude of the feedback. The 520 nm feedback laser is coupled into a single-mode fiber and then redirected into the chamber at a large angle. The scattered light is blocked by a long pass filter before the fiber.

it a fixed distance to the CMOS camera. The CMOS camera is attached to the opposite end of the lens tube.

The feedback optical system is again as simple as the rest of the optical system. A 520 nm diode laser is used to apply radiation pressure to the particle to either cool or heat its center-of-mass motion [25]. The laser is coupled into a single-mode fiber by an aspheric lens. At the output of the fiber, the light is collimated by a 19 mm achromatic lens. The light is then raised above the optical axis of the illumination and collection systems by a periscope. The light is focused by a 500 mm focal length lens and reflected by a mirror. The light enters the 10 inch window on the back of the main vacuum chamber at a large angle to maximize the radiation pressure on the particle in the axial direction. The scattered 520 nm light is blocked by a 600 nm long

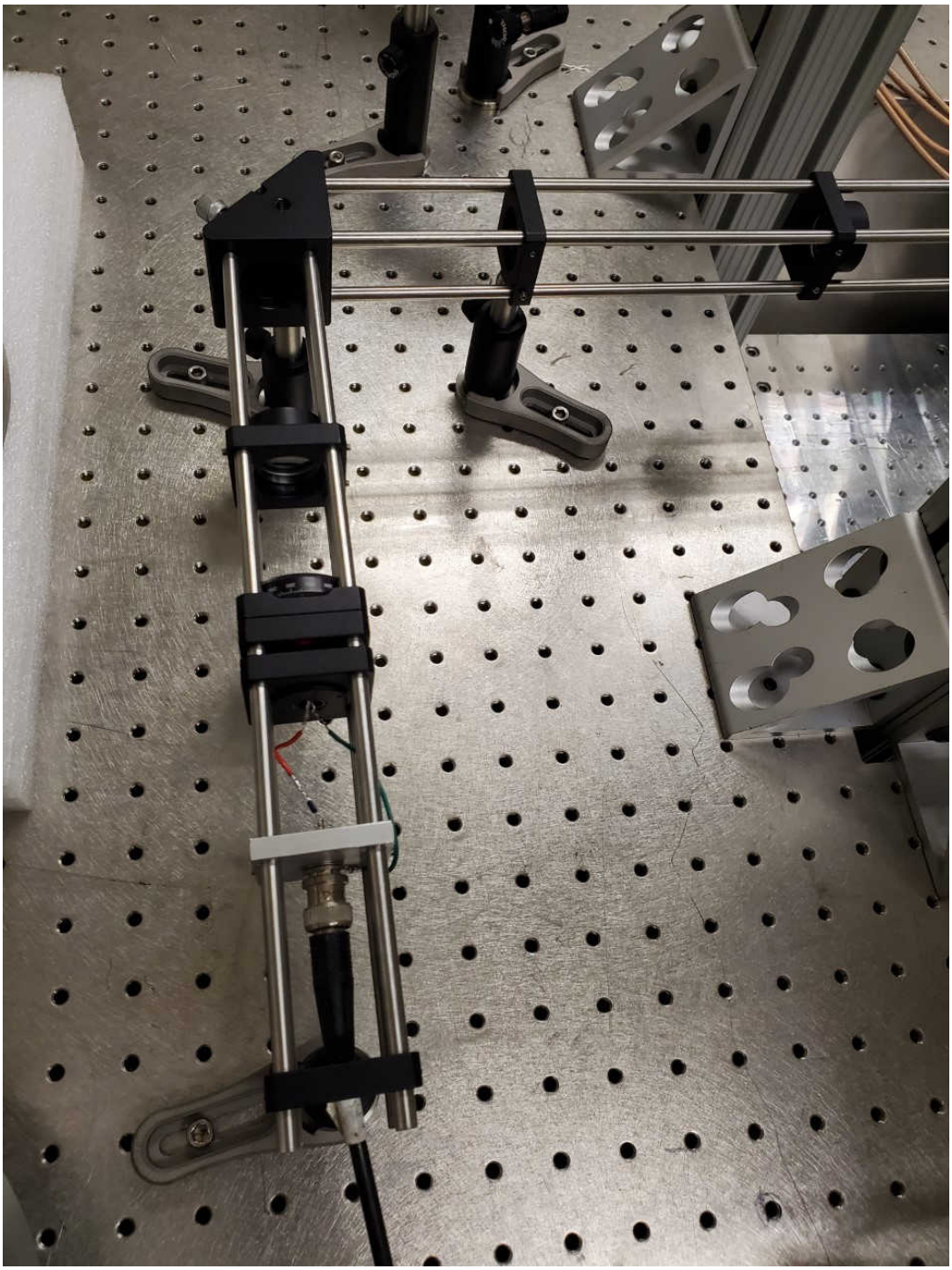


Figure 3.22: A photograph of the illumination optics. A 100 μm slit is illuminated by a 660 nm pulsed LED and magnified and imaged onto the trapped particle.

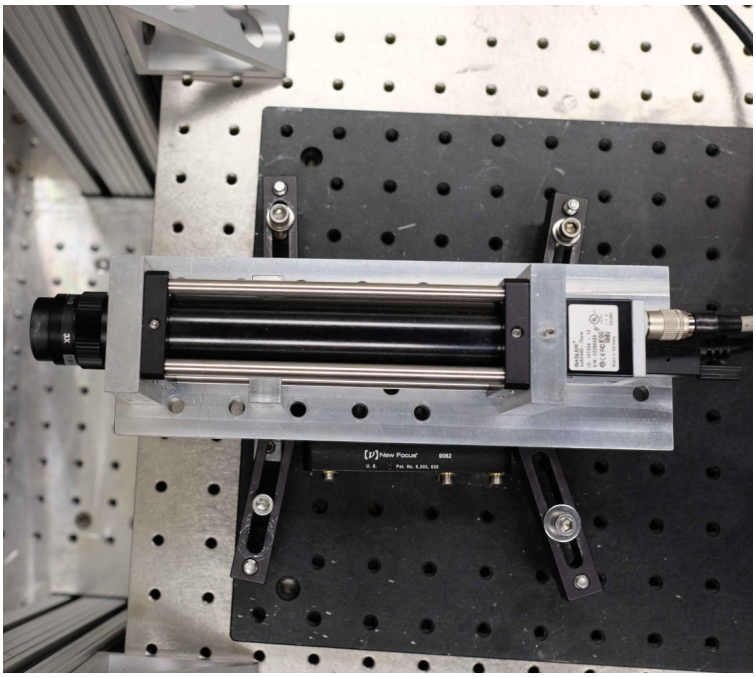


Figure 3.23: A top view of the collection optics. A long pass filter is attached to the front of the 3× telecentric objective. The objective collects the scattered light from the particle and images it onto a CMOS camera.

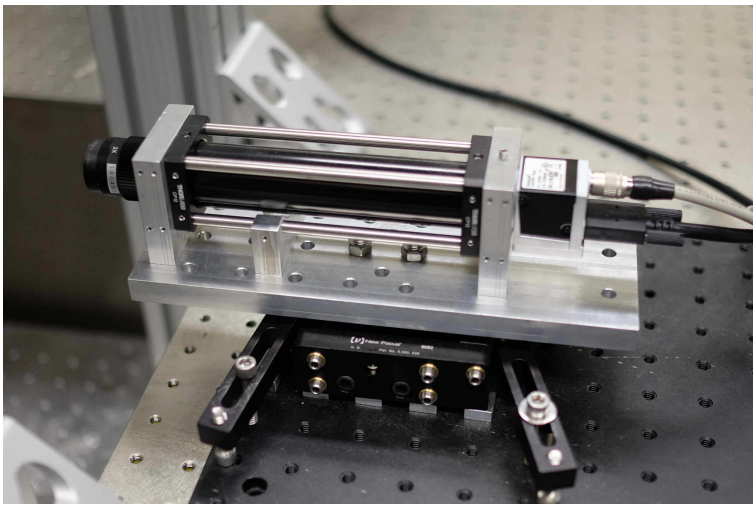


Figure 3.24: A side view of the collection optics. The objective lens and CMOS camera are mounted on a five axis stage for precise adjustment vertically and horizontally, tilt, and focus.

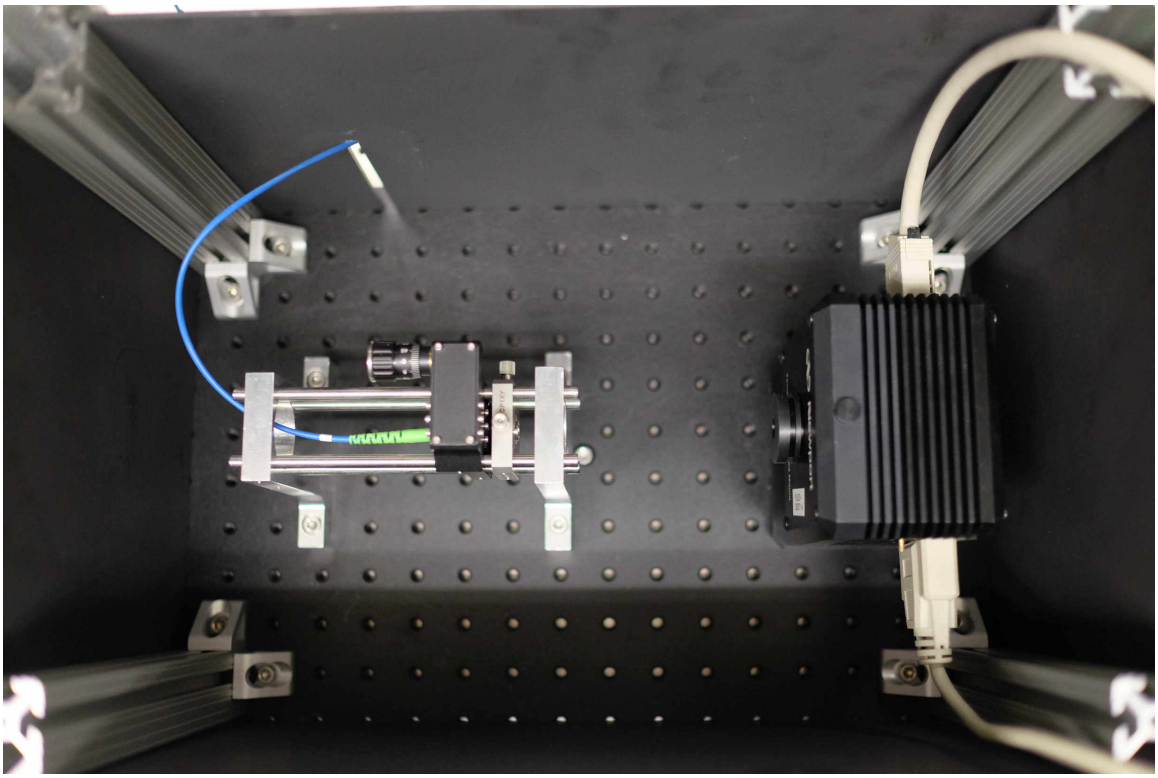


Figure 3.25: The 520 nm diode laser for the feedback control of the trapped particle. The laser is coupled into a single-mode fiber for cleaning the beam. The laser is housed in an enclosure for safety.

pass filter mounted on the front of the objective lens.

In accordance to Fig. 3.21, the full list of optics is:

- M1 - Thorlabs BB1-E02
- M2 - Thorlabs PF10-03-P0
- M3 - Thorlabs BB1-E02
- P1 - Thorlabs BB1-E02 × 2
- L1 - Thorlabs 352671-A
- L2 - Thorlabs C560TME-A

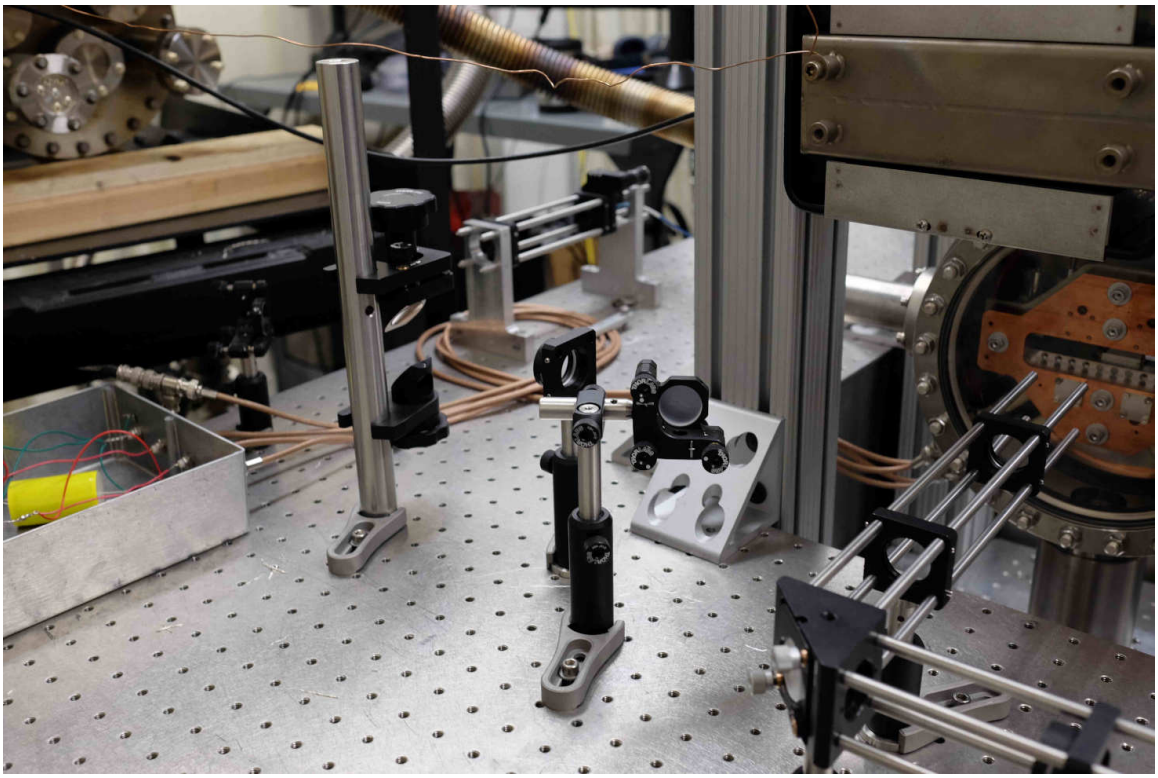


Figure 3.26: The optics after the single-mode fiber are shown. The light is collimated and redirected using a mirror and periscope. The light is then focused and redirected into the vacuum chamber via the large window.

- L3 - Thorlabs AC127-019-A-ML
- L4 - Thorlabs AC254-500-A-ML
- L5 - Thorlabs C240TME-B
- L6 - Thorlabs AC254-075-A-ML
- L7 - Thorlabs AC254-150-A-ML
- S1 - Thorlabs S100RD
- F1 - Thorlabs FELH0600
- O1 - Edmund Optics #56-985

- LED1 - Marktech Optoelectronics MTE5066WS-UR
- LD1 - Thorlabs PL520
- SMF1 - Thorlabs P5-488PM-FC-2
- CMOS1 - Basler Ace acA2440-75um
- A1 - Arduino Due and shield
- CPU1 - Computer.

3.5 Conclusions

This chapter described the system used for the work for this dissertation. The linear quadrupole magneto-gravitational trap consists of four Hiperco-50A pole pieces to concentrate the magnetic field from two samarium-cobalt permanent magnets. Because of the large gaps between the pole pieces, a DC voltage across the top and bottom pole pieces is required to help balance gravity. The DC voltage source is discussed in chapter 6. The custom-designed mount used to hold the trap is described as well.

In addition to the trap and its mount, the vacuum system is also explained in this chapter. The system consists of a roughing pump, turbomolecular pump, ion pump, and titanium sublimation pump (TSP). The system is capable of being baked and achieving ultra-high vacuum pressures. The TSP is not used for the work in this dissertation. The optics have also been described. The optics consist of three different paths: illumination optics for illuminating the particle for imaging, collection optics for collecting scattered light off of the particle and image the particle onto a CMOS camera, and the feedback optics to control the motion of the particle using radiation pressure from a diode laser.

With the system description laid out, the next chapter focuses on how a time-of-swing measurement of G [12] will be carried out in this system. The systematic errors of the magneto-gravitationally levitated microsphere are compared with the systematic errors of a torsion pendulum system [23].

CHAPTER FOUR

MEASUREMENT OF G

4.1 Introduction

In the previous chapter, the magneto-gravitational trap system, vacuum system, and optics for the work of this dissertation were described in detail. In chapter 1, a brief history of previous measurements of the Newtonian constant of gravitation was given. Torsion pendulum-based systems dominating the majority of the experiments [1, 23]. The primary source of systematic error is inelastic properties of the torsion fibers [23].

To eliminate this source of error all together, a levitated optomechanical system can be used instead of a torsion pendulum because of its extreme isolation from its environment. Chapter 2 gives an overview of five such systems. Typical values of important parameters for a measurement of G are reported.

In this chapter, the theoretical groundwork for a time-of-swing measurement, originally developed by the National Bureau of Standards in the 1930s [12], is presented for a levitated microsphere in a magneto-gravitational trap. Details of how this system will be used for this measurement will be laid out, including the insensitivity of the levitated particle's properties such as mass. Due to the simple nature of the geometry of the system, the sensitivity to some system parameters can be minimized.

As will be presented, once the microsphere is levitated, the oscillation frequency will be measured with no field masses. The frequency will then be measured with two field masses near the particle. The addition of the masses will cause a shift in frequency that is related to G. The frequency shift for different field mass geometries

are discussed.

Sources of systematic errors, such as precision in field mass geometry and location, are presented. Several estimates are made for some of the errors. For comparison, sources of systematic errors are reported for system used in the most precise measurement of G, a torsion pendulum experiment [23].

4.2 Time-of-Swing Method

A precision measurement of Newton's constant of gravity G can be made via the time-of-swing method. Consider a spherical oscillator (test mass) of mass, m, that is subject to a harmonic potential. The resonant angular frequencies in the transverse, vertical, and axial directions are ω_x, ω_y, and ω_z, respectively. Consider two spherical masses (field masses) with mass of, M, and radii of, r, placed a distance d from the equilibrium position along the axial axis as shown in Fig. 4.1.

The force on the test mass due to the two field masses along the axial direction is

$$F_{zG} = \frac{GmM(d-z)}{(x^2+y^2+(d-z)^2)^{3/2}} - \frac{GmM(d+z)}{(x^2+y^2+(d-z)^2)^{3/2}}. \tag{4.1}$$

We can consider small displacements from equilibrium $x_{eq} \to x_{eq}+\Delta x$, $y_{eq} \to y_{eq}+\Delta y$, and $z_{eq} \to z_{eq}+\Delta z$ in the transverse, vertical, and axial directions, respectively. By taking the equilibrium position to the original of the coordinate system, the spring constant due to the field masses is then

$$k_{zG} = -\frac{dF_{zG}}{dz} = -\frac{4GMm}{d^3}\left[1 - 3\left(\frac{\Delta x}{d}\right)^2 - 3\left(\frac{\Delta y}{d}\right)^2 + 6\left(\frac{\Delta z}{d}\right)^2 + \cdots\right]. \tag{4.2}$$

From Eq. 4.2, the spring constant due to the field masses are independent of any misalignments to first order due to the symmetry of the system. Now consider the

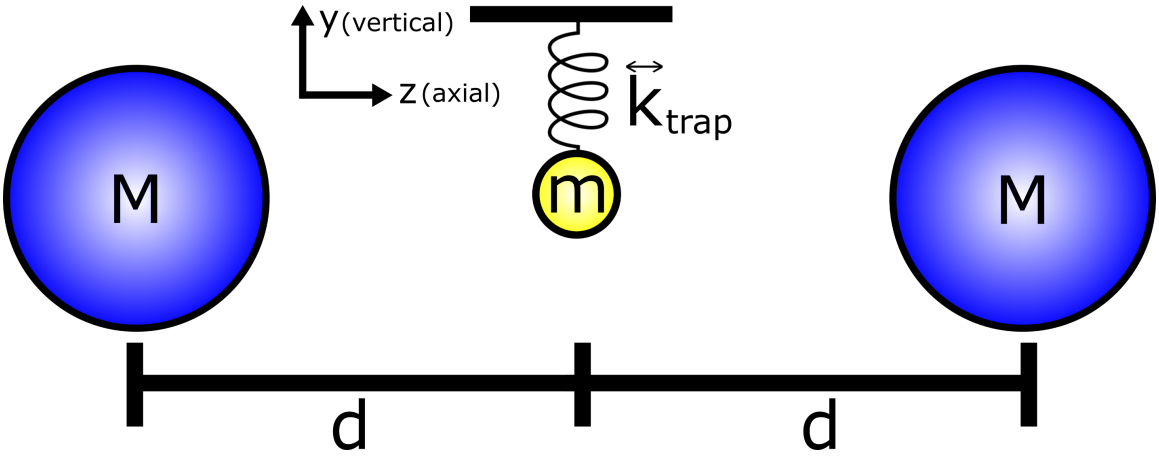


Figure 4.1: A simple illustration of the time-of-swing method for measuring G. Two field masses are placed a distance d from the oscillator. The two field masses cause a frequency shift in the test mass.

original harmonic potential of the trap, described by the spring constant in the axial direction, k_{z0}. The total spring constant of the system is then $k = k_{z0} + k_{zG}$. If we neglect higher order terms of Δx, Δy and Δz, the total spring constant is simply

$$k'_z = k_{z0} - \frac{4GmM}{d^3}. \tag{4.3}$$

The spring constant of the magneto-gravitational trap is not directly measured. We can measure the frequency of the oscillator, and therefore it is beneficial to write the total spring constant in terms of frequency, $\omega'_z = \sqrt{k'_z/m}$. Then making the proper substitutions,

$$\omega'_z = \sqrt{\frac{k_{z0} + k_{zG}}{m}}. \tag{4.4}$$

We can substitute for k_{zG} to get

$$\omega'_z = \sqrt{\frac{k_{z0}}{m} - \frac{4GM}{d^3}} = \sqrt{\omega_z^2 - \frac{4GM}{d^3}}. \tag{4.5}$$

Since $4GM/d^3$ is an extremely small correction to the frequency, to gain insight we can expand Eq. 4.5,

$$\omega_z' \approx \omega_z - \frac{2GM}{\omega_z d^3}. \tag{4.6}$$

Solving for G exactly from Eq. 4.5,

$$G = \frac{d^3}{4M}\left(\omega_z^2 - (\omega_z')^2\right). \tag{4.7}$$

In order to make a precision measurement of Newton's constant, the frequency of the oscillator needs to be known before and after the addition of the two field masses. The mass of the field masses also need to be known as well as the distance from the field masses to the equilibrium position of the particle. The precision required for M and d for the measurement is discussed later in this chapter. In practice, it will be a phase accumulation, $\Delta\omega_z T$ that is measured, where T is the integration time and $\Delta\omega_z = \omega_z' - \omega_z$.

From Eq. 4.6, $\Delta\omega_z \approx -2GM/\omega_z d^3$. In order to increase the measured phase accumulation, $\Delta\omega_z$ must be as large as possible, or T must be as large as practically possible. To increase $\Delta\omega_z$, we can increase the mass of the field masses, decrease the distance from their centers to the magneto-gravitational trap equilibrium, or decrease the oscillation frequency. However, this is not practical as massive field masses would be extremely expensive, hard to manipulate and mount, and difficult to machine precisely. We will also be limited on how close the masses can get due to the physical size of vacuum equipment, optics, and electronics that are needed to operate the experiment successfully.

The change in oscillation frequency also depends inversely on the original oscillation frequency. The linear magneto-gravitational trap as described in chapter 2 has the lowest oscillation frequency of 7 Hz in the axial direction. The linear magneto-

gravitational described in chapter 3, that is used for the work of this dissertation, has achieved frequencies consistently below 1 Hz and as low as 0.1 Hz, as will be described in chapter 9.

4.3 Geometries

For the case of two spherical masses, we can place the centers of them at $d = 2r$ where r is the radius of the field masses. Then Eq. 4.2 without the misalignment terms becomes

$$k_{zG} = -\frac{2\pi}{3} G\rho m \tag{4.8}$$

where ρ is the density of the field mass material. We can make the substitution $\beta = -2\pi/3$ to get $k_{zG} = \beta G\rho m$.

By considering the effect of two arbitrary shaped field masses with uniform density, the force on a test mass m is

$$\vec{F}_G = G\rho m \iiint_{V_1} \frac{\vec{r}_1}{|\vec{r}_1|^3} dV_1 + G\rho m \iiint_{V_2} \frac{\vec{r}_2}{|\vec{r}_2|^3} dV_2 \tag{4.9}$$

where $\vec{r}_1$ is the vector from the origin to a point in field mass 1 and $\vec{r}_2$ is the vector from the origin to a point in field mass 2. By considering field masses with symmetry about the axial axis, then only the z component of the force is nonzero. If we write

$$\vec{\alpha}(x, y, z) = \iiint_{V_1} \frac{\vec{r}_1}{|\vec{r}_1|^3} dV_1 + \iiint_{V_2} \frac{\vec{r}_2}{|\vec{r}_2|^3} dV_2, \tag{4.10}$$

then we can write the force as

$$F_{zG} = G\rho m \vec{\alpha}(x, y, z) \cdot \hat{z}. \tag{4.11}$$

The spring constant is then

$$k_{zG} = -\frac{dF_{zG}}{dz} = -G\rho m\frac{d(\alpha\cdot\hat{z})}{dz} = \beta G\rho m. \tag{4.12}$$

The dependence of alpha on the coordinates has been explicitly removed for simplicity. We can now see that the parameter $\beta = -d(\alpha\cdot\hat{z})/dz$ depends only on the geometry of the field masses. For example, $\beta = -2\pi/3$ for a spherical field mass.

Because of the symmetry of the field masses along the axial direction about the transverse-vertical plane, the force on the test mass in the axial direction depends only on odd powers of z,

$$F_z(z) = -k_{zG}z - k_{zG}^{(3)}z^3 + \ldots \tag{4.13}$$

where k_{zG} is the spring constant due to the field masses and $k_{zG}^{(n)}$ for $n = 3, 5, \ldots$ are the anharmonic spring constants. In the measurement, we want to maximize k_{zG} while minimizing the anharmonicities. We can consider the gravitational effect of a ring of radius R located a distance Z from the center of the trap acting on a test mass located a distance z from the origin. The force from an infinitesimal ring [100] is given by

$$dF_z(z) = G\rho\frac{2\pi R(Z-z)}{\left[R^2+(Z-z)^2\right]^{3/2}}dRdZ. \tag{4.14}$$

To find the spring constant k_{zG}, we can take the derivative of Eq. 4.14 with respect to z evaluated at $z = 0$ since we care about the effect at the origin. We find that

$$dk_{zG} = 2\pi RG\rho\frac{R^2-2Z^2}{\left[R^2+Z^2\right]^{5/2}}dRdZ. \tag{4.15}$$

A factor of 6 is obtained when taking the third derivative of Eq. 4.14. To find $k_{zG}^{(3)}$,

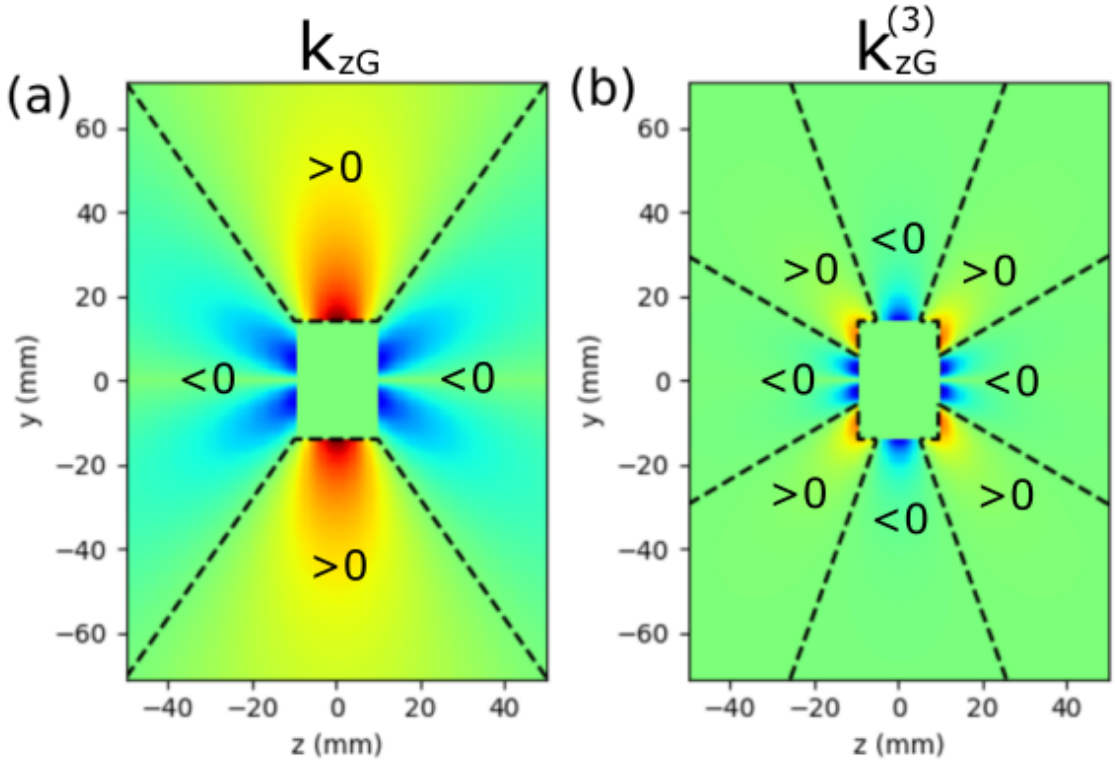


Figure 4.2: (a) A plot of the spring constant k_{zG} due to a ring of mass on both sides of the trap. The black dashed lines show where the spring constant is zero. (b)A plot of the first anharmonic spring constant $k_{zG}^{(3)}$ due to a ring of mass on both sides of the trap. The black dashed lines show where this spring constant is zero.

we take the third derivative of Eq. 4.14 and divide by 6 to get

$$dk_{zG}^{(3)} = \pi RG\rho \frac{24R^2Z^2 - 3R^4 - 8Z^4}{[R^2 + Z^2]^{9/2}} dRdZ. \tag{4.16}$$

We can see in Fig. 4.2(a) that different field mass geometries can have a positive (red) or negative (blue) spring constants. The dashed lines show where the spring constant is zero, given by the curves $R = \pm\sqrt{2}Z$. The rectangle at the center is where we prohibited any mass from being added due to physically limitations of the vacuum chamber. We can put frustum shaped field masses on either side of the trap in the axial direction that fill between the dashed lines to maximize k_{zG}. In Fig. 4.2(b), the

first anharmonic spring constant, $k_{zG}^{(3)}$, is shown. To minimize this, the frustum can be machined with a concave inner face.

4.4 Integration Times

In order to maximize the accumulated phase shift, we can integrate for a longer period of time. Three measurements will need to be carried out to successfully get a measurement of Newton's constant. The first will be with the two field masses in the far position. The second measurement is with the field masses in place to cause a frequency shift of the particle. The third will again be with the two field masses in the far position to ensure that the same results as the first measurement are repeated. If the two far position measurements yield different results, indicating something in the experiment is not consistent with itself. This set of measurements will be thrown out.

There is a trade off between integration time for a measurement and the number of measurements performed. Three, 24 hour measurements, two without the field masses and one with, will allow for one hundred measurements to be performed in the course of a year which improves the precision of the measurement by a factor of 10. The choice of these three measurements is arbitrary but is the minimum to obtain a linear time dependent measurement of drift.

4.5 Amplitudes of Motion

In order to minimize the effect of thermal noise on the levitated particle, a large amplitude compared to the thermal noise is required. By the equipartition theorem,

$$\frac{1}{2}m\omega_z^2 A_{\text{therm}}^2 = \frac{1}{2}k_B T \tag{4.17}$$

for a harmonic oscillator at thermal equilibrium with its environment at temperature T. Therefore, the amplitude of thermal motion is

$$A_{\text{therm}} = \frac{1}{\omega_z}\sqrt{\frac{k_B T}{m}}. \tag{4.18}$$

In the magneto-gravitational trap used in this dissertation work, an amplitude of 7.5 mm can be achieved and still be far from the edge of the trap, preventing extremely anharmonic motion. With a 63 µm borosilicate particle with oscillation frequency $\omega_z/2\pi = 0.1$ Hz and that amplitude at room temperature, $A_{\text{therm}}/A \sim 10^{-4}$. This can be improved by going to cryogenic temperatures (i.e., 4 K). Because of the large amplitudes of motion and the ability to levitate large particles, this system has an advantage over other optomechanical systems.

4.6 Oscillation Frequencies

From Eq. 4.6, the change in frequency induced by the addition of field masses is inversely proportional to the original frequency of the oscillator. To increase the frequency shift, and the accumulated phase shift, a lower frequency is required. A good starting point is an oscillation frequency of $\omega_z/2\pi = 0.1$ Hz. With the large dimension in the axial direction of the magneto-gravitational trap in addition to the electric field capable of canceling gravity, these low frequencies can be achieved. Performing the measurement in micro-gravity, such as in low Earth orbit, even lower frequencies can be achieved.

For two spherical masses of tungsten with radius 0.25 m placed $d = 2R$ from the center of the trap, there will be a change in angular frequency of approximately $\Delta\omega_z \approx 3 \times 10^{-7}\,\text{s}^{-1}$. For a 10 ppm measurement, the frequency needs to be stable to within $|\Delta\omega_z|/\omega_z \times 10^{-5} \approx 10^{-11}$.

4.7 Systematic Errors

There are several sources of systematic errors in this system. The field mass geometry is extremely important no matter what system is being used. To first order in k_{zG}, the system is independent on the location of the field masses. Without tuning $k_{zG}^{(3)}$ to be small, a 10 ppm measurement will require the inner faces of frustum shaped field masses to be within $\sim 1\,\mu$m relative to each other, calculated from Eq. 4.14 by considering a small displacement $z \to z + \delta z$. From Fig. 4.2, we can see that the inner faces contribute the most to the spring constant and the other faces are less sensitive. With certain materials, such as copper, the field masses can be machined on a single point diamond turning machine that has sub-100 nm precision. The ease of machining, especially in-house, will allow several field masses to be machined for measurements with different sets of masses. Since the field masses will have cylindrical symmetry, the field masses can be rotated about the axial axis to average non-uniform shapes over many measurements. The field masses could contain voids which can be hard to detect, but a transparent material such as lead tungstate can be used to locate them, if any.

A second source of systematic errors is in the test mass geometry. To first order in displacements from equilibrium, Eq. 4.7, tells us that the measurement of G is independent of the mass, size, and position of the test mass. We have to, however, be able to determine the position of the test mass relative to the field masses. The most convenient way is measuring the location of the particle with respect to the collection optics and the field masses with respect to the collection optics. The shape of the test mass matters because a non-spherical particle, such as an ellipsoidal particle, cannot be treated as a point mass anymore. An ellipsoidal particle will align itself with the weak direction of the trap (along the axial direction). As a simple model, such a

particle can be thought of as two spherical particles separated by a distance δz, each with mass $m/2$. From Eq. 4.2, the error from this will be $\sim (\delta z/d)^2$. Assuming a spherical, copper field mass of radius 0.1 m placed a distance $d = 2R$ from the center of the trap, this will give an error of ~ 0.1 ppm, well below the target uncertainty.

Another source of error is the anharmonicity created by the field masses. The spring constant k_{zG} could be dependent on the oscillation amplitude. The field masses can be machined such that for a small window of amplitudes around the actual amplitude, the oscillation frequency is amplitude independent. Depending on how small $k_{zG}^{(3)}$ is, the size of this window can vary.

It is important to note that there are three main sources of anharmonicity in this system: the trapping potential, the field masses, and local anharmonicity due to charge on the pole pieces or another source of fine structure to the total potential. A discussion of this fine structure anharmonicity and how it affects results is in chapter 9.

4.8 Systematic Errors of Other Systems

Above, the three main sources of systematic errors were described with the order of magnitude of the systematic errors estimated. In the typical torsion pendulum measurement, there are some similar and some unique systematic errors. The estimates and description of the errors in this section are from the most precise measurement of G [23].

The first is the density homogeneity of the field masses and test mass, in this case a pendulum. The density distribution of the pendulum was determined by optical interferometry [101] which contributes less than .5 ppm error to the measurement. The density distribution of the field masses was calculated three different ways to give an uncertainty of 0.1 ppm for both of their systems.

A magnetic damper is used to prevent the pendulum from swinging but adds

its own errors. These errors depend on the moments of inertia of the pendulum and fiber as well as the spring constants. This requires a correction of 455.40 ppm to the measurement of G with an uncertainty of 1.95 ppm. For the angular acceleration feedback (AAF) method, the field masses are positioned in air. As the field mass stage is rotated, the field masses displace the air, introducing a 1.51 ppm uncertainty.

In order to reduce negative effects due to electrostatic charge on the pendulum, the glass pendulum is coated in gold-copper layers. This coating introduces a higher gravitational torque on the pendulum due to their increased moment of inertia. This results in a 0.34 ppm uncertainty in the AAF method and 2 ppm uncertainty in their time-of-swing (TOS) method. The conductive coating only reduces the effect of electrostatic charge but does not eliminate it completely. These effects introduce an uncertainty of 0.17 ppm.

Due to thermoelasticity, the spring constant of the fibers are temperature dependent. For the AAF method, the fiber does not twist, resulting in negligible uncertainty. The TOS method, with a temperature variation of less then 1°C, has an uncertainty of 0.91 ppm. Interaction between local magnetic fields and residual magnetic moments of the test masses create an additional torque on the pendulum. This introduced errors up to 2.08 ppm.

Possibly the largest problem with torsion pendulum based experiments is the anelasticity of the fibers used [102]. Defects in the fiber can cause uncertainties in the measurements that are extremely hard to measure. The AAF method seeks to reduce this by applying an angular force to prevent the pendulum from rotating. However, these defects still cause problems. Levitated optomechanical systems have the advantage due to there being no mechanical clamping to the oscillator of any kind.

4.9 Conclusions

In this chapter, the mathematical background for the time-of-swing method was presented. This method relies on measuring a change in oscillation frequency of the levitated particle before and after the introduction of field masses. With cylindrical symmetry, it has been shown that the ideal shape for field masses are truncated cones. Three frequency measurements will be taken: once with no field masses, once with the field, and again without the field masses. Accumulating data for one day for each frequency measurement will allow for approximately 100 measurements per year.

The linear quadrupole magneto-gravitational trap used in this system shows great promise for this measurement. The design allows for large amplitudes, which decrease the effect of thermal noise, up to 10 mm. As will be shown in chapter 9, the target oscillation frequency of 0.1 Hz has been reached in this system.

Systematic errors for the system have been discussed in this chapter. There are several sources: geometry of field masses, location of the field masses, the anharmonicity introduced by the field masses, and anharmonicity of the trapping potential itself. This was compared and contrasted to that of the most precise measurement of G [23]. Estimates for both systems are provided.

Since the mass of the levitated particle is also a critical parameter (the larger the mass, the better), a method is needed successfully levitate one of these particles. As shown in chapter 3, the vertical and transverse gaps used in the trap utilized for this work does not provide a magnetic field gradient large enough to cancel gravity. In order to do so, a method was developed to load the particles into a Paul trap [61] and transition into a magnetic-based trap with a DC voltage across the top and bottom pole pieces. Particles up to 63 μm have been trapped in the system used for the work in this dissertation.

The following chapter describes how the particles are loaded with results for various sized particles and various particle materials. Including the next chapter, the following four chapters describe technological techniques developed and used for this dissertation. These techniques are to assist in limiting errors in a measurement of G and high sensitivity acceleration measurements.

CHAPTER FIVE

LOADING AND TRAPPING LARGE PARTICLES

5.1 Introduction

As was shown in chapter 3, the vertical and transverse gaps in the pole pieces of the magneto-gravitational trap used in this dissertation are too large to provide a magnetic field gradient to cancel gravity and levitate the particle. As mentioned in the conclusion of the previous chapter and chapter 3, a DC voltage can be used to help balance the force of gravity.

The method to load particles into the trap has been used in our laboratory [83,84] and is based off of a previous design [50]. The circuit used to drive an ultra-sonic horn that sprays particles off of it tips has been modified in this dissertation to be more compact and more robust to damage.

When the particles are sprayed off of the horn, they come off with some amount of energy, and are typically charged. The restoring force from the magnetic field must be strong enough, along with air resistance, to slow the particle down before it escapes the trap. This magneto-gravitational trap was designed to have a target oscillation frequency of 0.1 Hz or lower in the axial direction. Because the trap is so weak, another mechanism is required to load the particles. In this dissertation, a modification was made to the magneto-gravitaional trap. A quadrupole ion (Paul) trap [61] was used on the pole pieces to provide the restoring force to trap the particle. Because the Paul trap is significantly stronger than the magneto-gravitational trap, it is also used to initially cancel gravity. The Paul trap is turned off while adjusting the DC voltage to keep the particle centered vertically. The combination of the Paul trap and magneto-gravitational trap, along with the DC bias, provided the necessary

components to trap the particles.

In this chapter, the method for loading and the loading circuit used in this dissertation is described. The configuration of the pole pieces and circuit for the Paul trap is presented along with circuitry for the DC voltage as well. The methods described in this chapter allow for trapping of 63 μ borosilicate microspheres with great success, with the results presented. Challenges that arise with this loading method are also discussed.

5.1.1 Loading Horn Circuit

In order to load particles into the magneto-gravitational trap, we use an ultrasonic horn driven by a piezo. Originally, the horn was designed to nebulize a liquid on the tip of the horn to a fine spray [94, 103], where the droplets of the mist can contain nanometer and micrometer sized particles. The ultrasonic horn can also be used to spray dry particles. Typically, this method relies on van der Waals forces to hold the particle to the tip of the horn. However, this is not viable for large particles [104–106] because the van der Waals forces are not strong enough.

We can use the fact that insulators can be charged by friction to load particles. We stick a piece of insulating polyimide tape on the tip of the horn. The tape is rubbed on a piece of synthetic cloth to charge the tape. Particles then, through Coulomb attraction, can now be lifted by the horn.

A new circuit was designed based on the circuit of Hsu [94]. An Arduino Due is used to sweep a frequency range (150 kHz to 200 kHz) containing the resonance of the horn. When the resonance is hit, the horn nebulizes the liquid or sprays off particles. The original design consisted of four very large power resistors and heat sinks, two push buttons to control the length of each burst at each frequency, a ±15 V power supply, and two boards in addition to the Arduino. The circuit needed

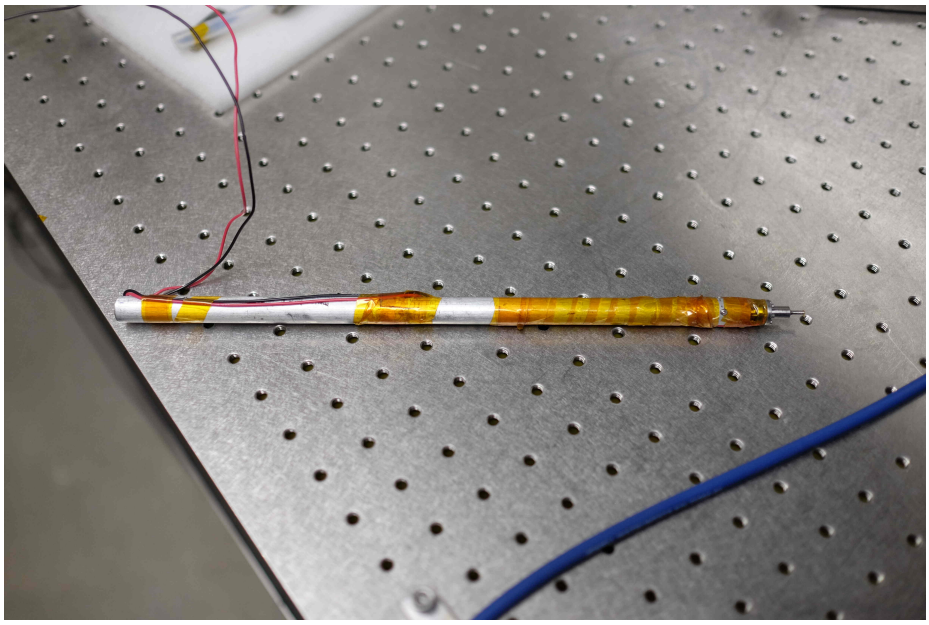


Figure 5.1: A photograph of the loading horn used for loading particles. The polyimide tape around the handle prevents shorting between the various pole pieces. A piece of polyimide tape is on the tip of the horn to electrostatically hold large particles for loading.

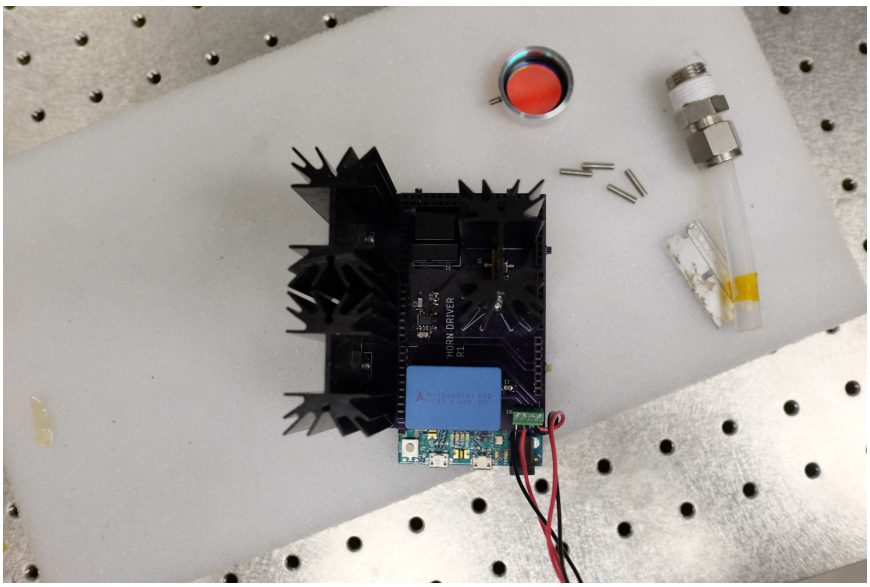


Figure 5.2: A photograph of the loading circuit board mounted to an Arduino Due. The large heat sinks prevent overheating of the thermal resistors and MOSFET.

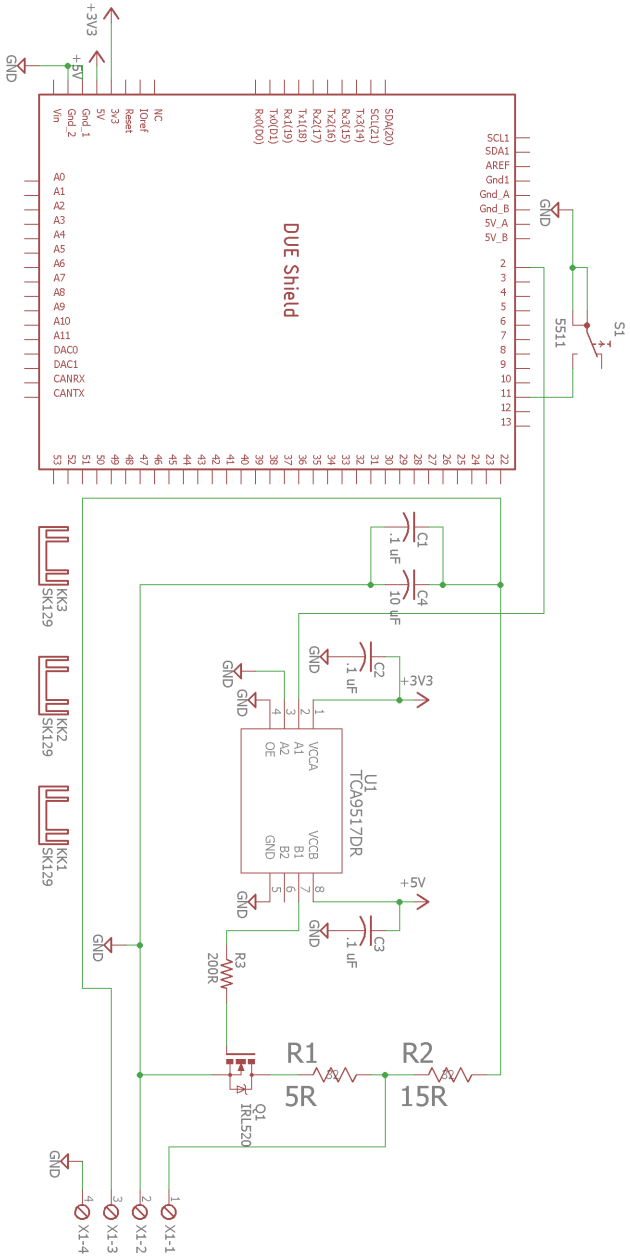


Figure 5.3: The schematic for the loading horn circuit. The shield is attached to an Arduino Due. A MOSFET is used to drive a piezo at varying frequencies. Three large heat sinks are used to prevent overheating of the MOSFET and two thermal resistors.

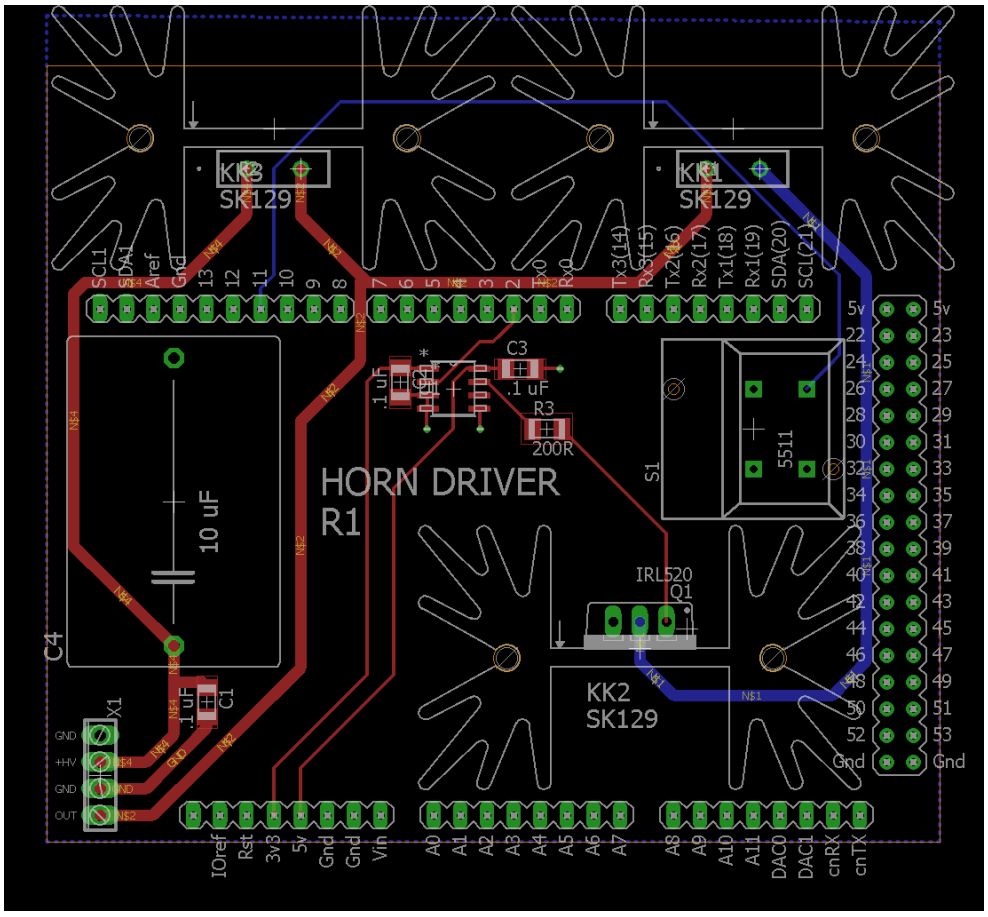


Figure 5.4: The circuit board layout for the compact loading circuit. The board is directly attached to an Arduino Due. Three large heat sinks are used to dissipate heat from two resistors and the MOSFET. A push-button switch is used to trigger the start of the frequency sweep.

careful placement as to not short anything. The new circuit, designed for compactness and robustness, eliminates two of the power resistors, the ±15 V power supply, and combines everything onto a single Arduino Due shield, with very little risk of shorts.

Previously, for small particles ($\sim 1\,\mu$m), typically ~ 30 V needed to be applied to the circuit. For the large particles used in the work of this dissertation ($\sim 60\,\mu$m), only 5 V are required to overcome the electrostatic and van der Waals forces. The loading horn and a photograph of the circuit are shown in Fig. 5.1 and Fig. 5.2. The

schematic and board design are shown in Fig. 5.3 and Fig. 5.4.

5.2 Linear Quadrupole Ion (Paul) Trap

Since the magneto-gravitational trap is so weak because of its dimensions and is sensitive on the exact DC voltage across the bottom and top pole pieces, loading particles is extremely difficult. Even with the low voltages used to drive the ultrasonic horn, and if the DC voltage is correct for the charge on a particular particle, the particles are sprayed into the trapping region with too much energy to remain trapped axially. Since the particles are charged, we can employ a quadrupole ion (Paul) trap to assist in loading.

As described in chapter 2, the Paul trap can consist four linear rods to provide two dimensional confinement. The four pole pieces can be used in this geometry. Instead of two electrodes on both ends of the trap, the top pole pieces being cut shorter will create the confinement in the axial direction.

An AC voltage is applied to one bottom pole piece and the opposite top pole piece, as shown in Fig. 5.5 and photographed in Fig. 5.6. The source of the AC voltage is a Tektronix AFG1022 function generator that has been amplified by a 50 to 1 step up transformer. A 1 MΩ current limiting resistor keeps the current at a safe level. The largest voltage that can be output from the function generator and transformer is 500 V, so the resistor keeps the current under 0.5 mA. The 10 μF capacitor acts a short to AC voltage. In the diagram, the bottom left and top right pole pieces have an AC voltage.

The DC voltage is applied from the high voltage reference described in chapter 6. The two 10 μF capacitors block DC voltage. There is a 50 s filter that filters out high frequency noise in the DC voltage. The top left pole piece has only DC voltage, the top right has both AC and DC voltages, the bottom left pole piece has only AC

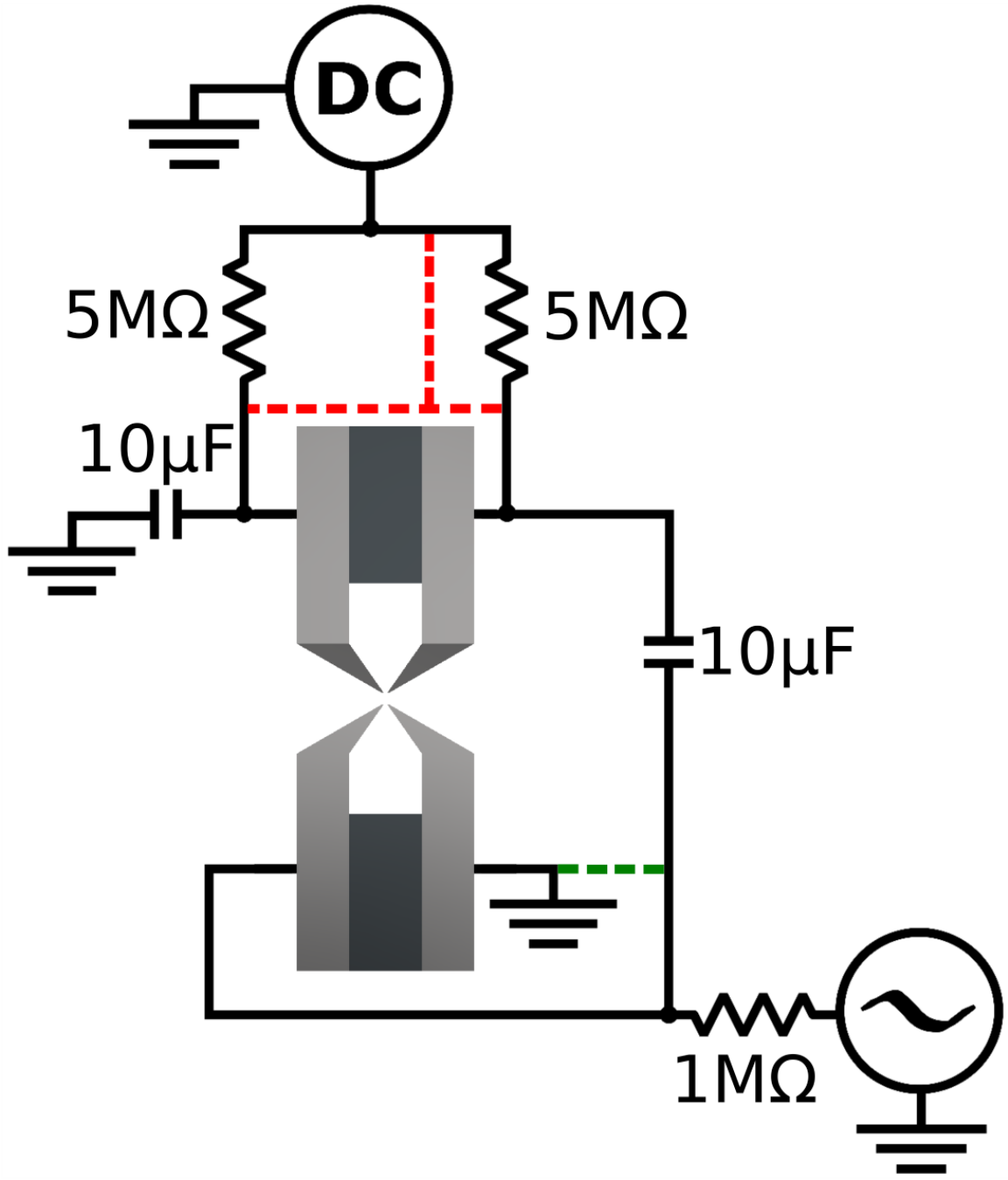


Figure 5.5: The wiring diagram for the Paul trap and DC bias on the magneto-gravitational trap. A 50 s filter prevents high frequency noise from being added to the DC voltage. The dashed lines illustrate where jumpers are placed to prevent image charges in the pole pieces from going through high resistance paths.

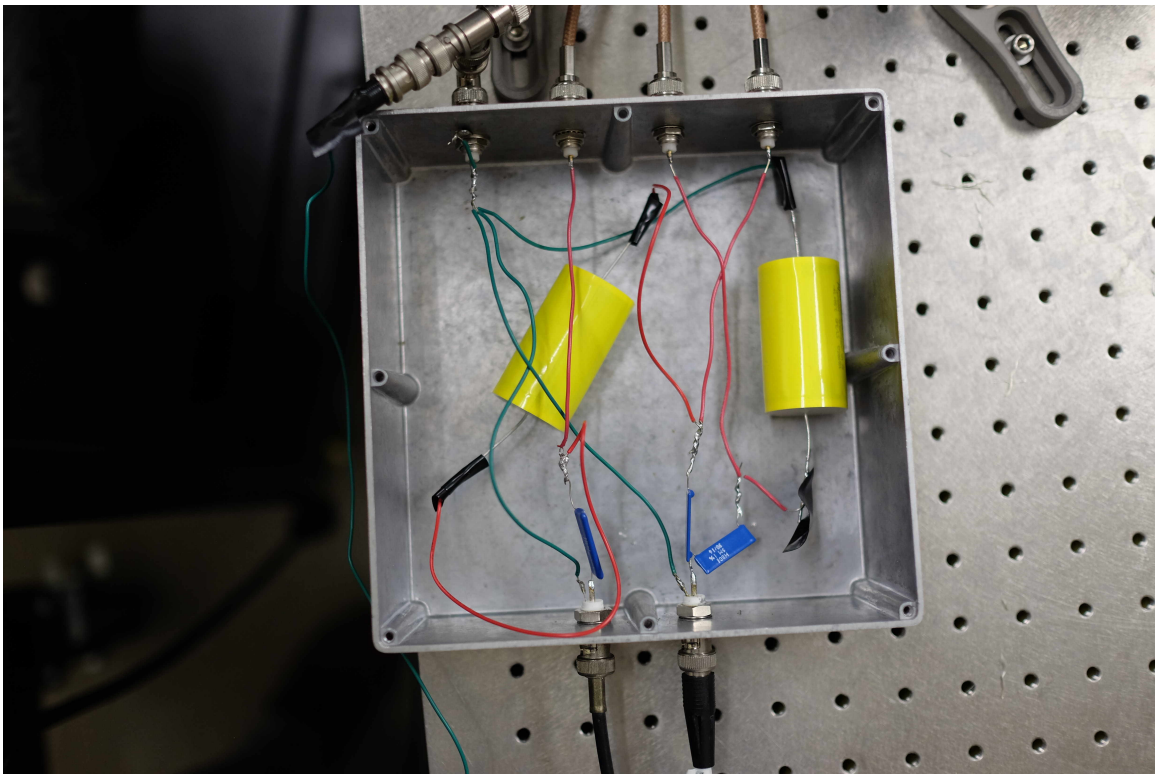


Figure 5.6: A photograph of the Paul trap and DC voltage circuit. The jumpers are in place in this photo.

voltage, and the bottom right pole piece is always grounded.

5.3 Results

By solving the Mathieu equation, it can be shown that for a ring electrode Paul trap in vacuum, the charge-to-mass ratio must satisfy [61, 107]

$$0.4\frac{r_0^2\omega^2}{V_0} < \frac{q}{m} < 1.2\frac{r_0^2\omega^2}{V_0} \tag{5.1}$$

where r_0 is the inner radius of the ring, ω is the angular frequency of the AC voltage and V_0 is the amplitude of the AC voltage. It has been shown that the stability range is extended when trapping in air [108]. In the linear quadrupole ion trap geometry,

the characteristic length is on the order of the gap sizes of the pole pieces. Since this is fixed, the stability condition can only be changed by varying the voltage or frequency of the AC voltage.

The amplitude of the AC voltage and its frequency have been experimentally determined for different particle sizes. To reduce the parameter space from two dimensions to one, a frequency that consistently traps particles with diameters in a useful range is kept constant. A frequency of 300 Hz was experimentally determined to give results that work. More experimentation can determine what the frequency is the best in terms of consistent loading. At this frequency, the 50 to 1 step up transformer is no longer as efficient as it is at 60 Hz. At 300 Hz, the gain of the transformer is approximately 45 to 1.

In the trap geometry described in chapter 3, particles from 7.75 μm in diameter to 63 μm in diameter have been successfully trapped in the magneto-gravitational-Paul hybrid trap. The 7.75 μm silica microspheres (Cospheric SiO2MS-2.0 7.75um-1g) have been trapped with amplitudes of the AC voltage from 45 V to 225 V. These particles have only been trapped with no DC voltage across the top and bottom pole pieces. While changing the DC voltage to attempt to keep the particle trapped without the Paul trap, the charge of the silica microspheres is typically positive.

Soda lime glass particles with diameters in the range 23 μm to 27 μm (Cospheric S-SLGMS-2.5 23-26um-1g) have been trapped with the amplitude of the AC voltage from 225 V to 450 V and with DC voltages from 0 V to approximately 25 V. The soda lime glass particles are negatively charged typically. Borosilicate microspheres with diameters in the range 53 μm to 63 μm (Co-spheric BSGMS-2.2 53-63um-10g) have been successfully trapped using an AC voltage with a 450 V amplitude with DC voltages from approximately −10 V to −40 V. Typically, the borosilicate spheres are positively charged. The reason for the sign of the charge on the soda lime glass being

different than the borosilicate and silica is unknown to us at this time.

The above DC voltage ranges are only approximate due to the lack of accurate monitoring during most loading attempts and data collection. The voltage was read off of an analog meter on the power supply (HP 6218A) that was used. A new DC voltage source was developed from a modification of a Texas Instruments design [24] to provide a more stable source and is described in chapter 6.

Once the particles have been confined in the hybrid trap, the Paul trap needs to be turned off in order to pump down the chamber. Without feedback cooling, the Paul trap becomes unstable in vacuum. To turn the Paul trap off, the amplitude of the AC voltage is slowly decreased while adjusting the DC voltage to keep the particle centered vertically in the trap. Once the AC voltage is completely off, jumpers are attached to the circuit as shown in Fig. 5.5. The charged particle will produce image charges in the conducting pole pieces and as the particle oscillates, the image charges can go through high resistance paths in the circuit. The addition of jumpers eliminates these.

The $7.75\,\mu\text{m}$ microspheres have never been trapped with only the magneto-gravitational trap and DC voltage in this large trap. During the attempts to levitate these particles, it was observed that a very low DC voltage ($\sim 1\,\text{V} - 2\,\text{V}$) was required to eject the particle from the trap vertically upward. The HP 6218A power supply does not have the precision required to cancel gravity and has also been observed to drift up to $1\,\text{V}$ over the course of a day.

Another observation is that it is significantly easier to turn the Paul trap off when the DC voltage amplitude is relatively large. By easier, it is meant that when the magnitude of the charge on the microsphere is relatively small, the range that the DC voltage can have to keep the particle trapped is larger. The soda lime glass particles have not remained trapped when a DC voltage of less than approximately

15 V is applied. Borosilicate microspheres have not remained trapped with a DC voltage amplitude of less than 20 V.

5.4 Challenges

While the magneto-gravitational-Paul trap hybrid is extremely successful at loading particles, it has a very important disadvantage. For stable trapping of 60 μm particles, nonzero charge is required, as evident in Fig. 3.14. However, for a particular particle with a given charge-to-mass ratio to be trapped, the DC voltage must be in the correct range. This range is typically very small, making loading difficult. For particles with less charge, the range is usually larger. However, particles that are not very close to the charge required for a given voltage on the pole pieces will not be trapped either.

Charged particles that are sprayed into the trapping region by the ultrasonic horn but not trapped may stick to the pole pieces. Since the trapped particle is also charged, this leads to an unwanted Coulomb interaction with the trapped particle and the contaminant particles, causing anharmonicities in the potential. A cleaner loading method is required to prevent this. At the time of writing this dissertation, an effort to achieve this is being made.

A second challenge is that the pole pieces are susceptible to shorts between them. If any two pole pieces become electrically shorted, the electric field will no longer have a quadrupole geometry and particles will not be trapped. Because the SmCo permanent magnets are very brittle, small pieces tend to break off and short the pole pieces across the transverse gap, requiring the trap to be removed from the chamber and cleaned. Also, if not careful, the loading horn or its handle can come into contact with two pole pieces, causing a short. This has been attempted to be fixed by covering the horn with insulating tape (see Fig. 5.1) but some metal is still

exposed.

The analysis in chapter 3 assumes that the particle is a point charge. As a point charge, with the same DC voltage on the pole pieces, the same particle will always have the same equilibrium position. It has been observed that some particles will return to one of two equilibrium positions vertically despite the same DC voltage being applied. As the Paul trap voltage is slowly turned down but not completely off, the particle settles into one position. When the Paul trap is turned back on and then slowly turned down again, the particle will settle into a different position. This is currently believed to be caused by the point charge assumption breaking down because the particle has non-negligible, higher moments (e.g., electric dipole moment).

5.5 Conclusions

In this chapter, the method that which particles are loaded into the magneto-gravitational trap for the work in this dissertation was discussed. To load the particles, a DC voltage is placed across the vertical gap of the trap to help balance the force of gravity. The transverse and vertical gaps are too large to provide a magnetic field gradient big enough to cancel gravity.

Also, because of the gap sizes and the length of the trap in the axial direction, the trap is very weak in that direction (results in a low axial oscillation, reported in chapter 9). Because of how weak the trap is, the particle may have too much kinetic energy during loading that the restoring force of magneto-gravitational trap along with air resistance may not be strong enough to slow the particle down enough to remain trapped. Therefore, in addition to the DC voltage, a Paul trap [61] was implemented on the magneto-gravitational trap. Since the pole pieces are oriented in a quadrupole geometry, this is a fitting system to add on top of the magnetic field.

The Paul trap method has demonstrated successful loading of particles ranging from 7.75 μm diameter silica microspheres to 63 μ diameter borosilicate microspheres. Paul trap AC voltages from 45 V to 450 V with a frequency of 300 Hz have been used to trap particles in this range. Silica particles and borosilicate particles are typically positively charged while soda lime glass has been observed to be typically be negative. For the positive particles, DC voltages of 0 V to −40 V have been used during loading. 7.75 μm diameter particles have never been trapped with the Paul trap turned off. Soda lime glass particles with a diameter of 25 μm have been trapped with DC voltages 0 V to 25 V. Challenges that have been observed from this method have also been discussed.

Since a DC voltage is used to center the particle vertically in the magneto-gravitational trap to cancel gravity, the stability of the DC source should be as good as possible. The vertical height in the trap should be stable as to not change the frequency of the particle over time. This stability requires a detailed model to understand how well it should be stabilized and is not done in this dissertation. Typically, voltage references have high stability but are limited to low voltages (10 V). Based on a previous design [24], a high voltage variable voltage reference has been developed for use as the DC voltage source. This source and use of the source is described in the next chapter along with results over three days of monitoring the voltage.

CHAPTER SIX

HIGH VOLTAGE VARIABLE VOLTAGE REFERENCE

6.1 Introduction

As described in chapters 3 and 5, a DC voltage is required to balance gravity in the magneto-gravitational trap used in this dissertation (geometry described in chapter 3). Though a more in depth model is required to understand the full potential of the trap, the DC voltage provides the restoring force in the axial direction.

Because of the important nature of the DC voltage, stability of the voltage is crucial. A detailed model of the potential is required to investigate the effects that a change in the vertical equilibrium position of the trapped particle will have on a measurement of Newton's constant of gravity. Initially, the DC voltage source used was only stable to within 10% (estimated). A new model of the trapping potential is not required to know that this is not good enough. Voltage references, though stable to within a couple parts per million (ppm), they are typically limited to low voltages ($\sim 10\,\mathrm{V}$).

A Texas Instruments (TI) design [24] stacks an arbitrary number of 10 V voltage references in series to provide a high-voltage voltage reference. Because of the inconvenience of adding or removing voltage references from a printed circuit board (compact, convenient, and more robust than through hole breadboard circuits), the TI circuit has been modified for the work in this dissertation to allow for adjustment of the voltage in 10 V increments. A 1 ppm 20-bit Analog Devices AD5791 DAC board is used for fine adjustment of the voltage.

In this chapter, the design of the variable voltage reference is presented along with its connection diagram with the DAC board and necessary power supplies. As

explained in chapter 4, each measurement of G will consist of three separate phase accumulation measurements: two with the field masses in the far position and one with them in the near position. These measurements will be one day each (3 days for the total measurement). In this chapter, the data from three days of monitoring the DC voltage is presented.

6.2 Setup

Single voltage references, though extremely stable, have only a limited range of voltage outputs. Voltages in the range of 30 V to 40 V are frequently used in levitating the particle, which is beyond the output range of most voltage references. Voltages up to 300 V could possibly be used in the experiment. The Acopian power supplies typically used in our laboratory can be floated up to 300 V.

To achieve a voltage reference that can reach 300 V is not trivial but has been done by stacking Texas Instruments REF5010 (10 V output) in series [24]. Texas Instruments demonstrated a fixed 100 kV voltage reference by using 10000 single references with a precision of 3 ppm.

In the magneto-gravitational trap, a fixed voltage reference will not work since the DC voltage typical needs to be adjusted to keep the particle centered in the trap. Following the same approach as Texas Instruments, a variable voltage reference was developed. Using 30 Texas Instruments REF5010 voltage references, they are stacked together in series, each connected to a switch, as shown in Fig. 6.1, 6.2, and 6.3.

The 100 kΩ resistors before each switch were chosen to keep the current drawn from the voltage references within their specifications. By swapping the R12 and R1 resistors, the polarity of the voltage reference can be changed. The 1 kΩ resistor was chosen to keep the current drawn from the entire voltage reference circuit within the range 3 mA and 7 mA. This current was determined by Texas Instruments to

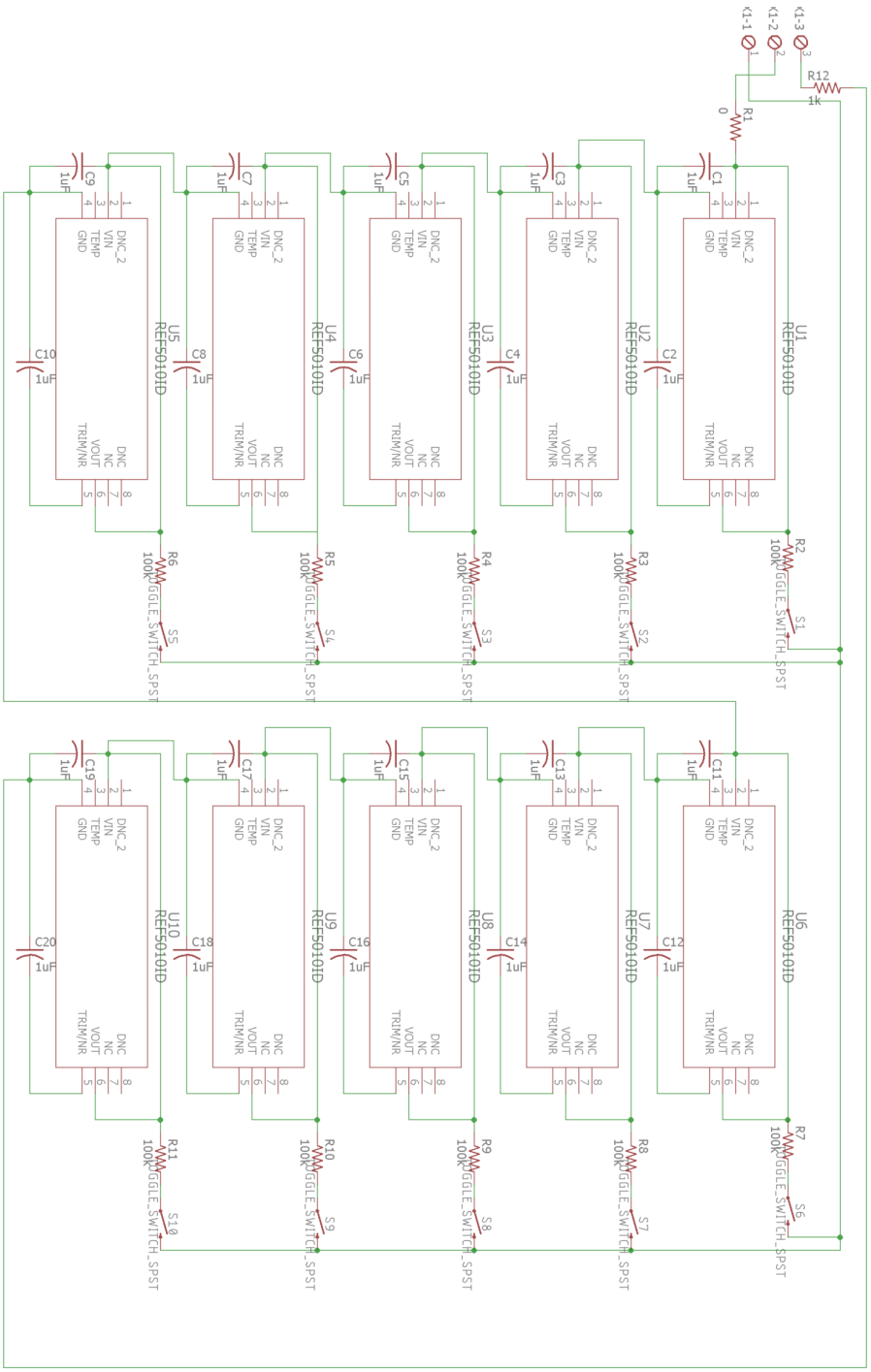


Figure 6.1: The schematic for one voltage reference board. Three boards are stacked on each other to create a 300 V voltage reference.

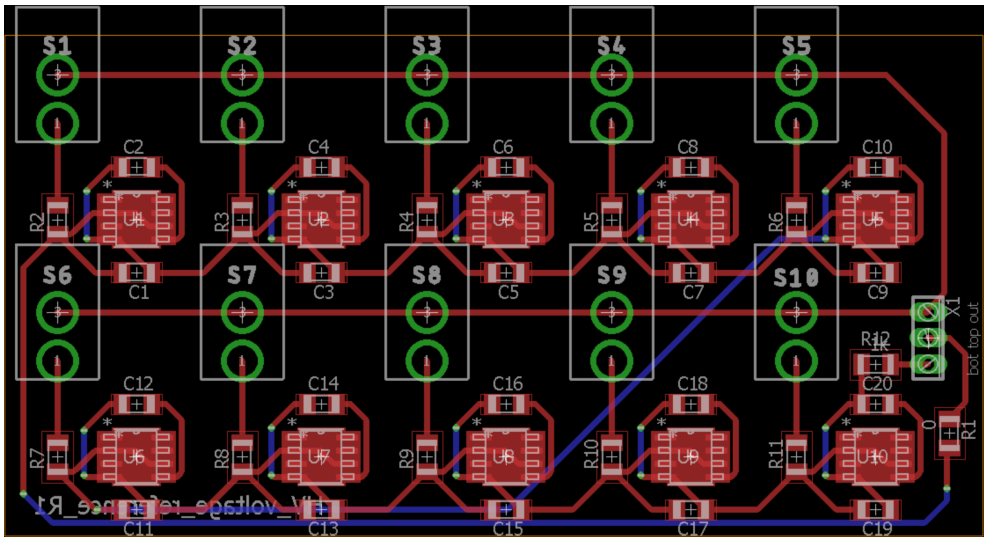


Figure 6.2: The board schematic of the voltage reference switch board. There are ten switches on each board, each controlling one of the ten voltage references. Three boards are connected in series with each other, allowing for an output up to 300 V.

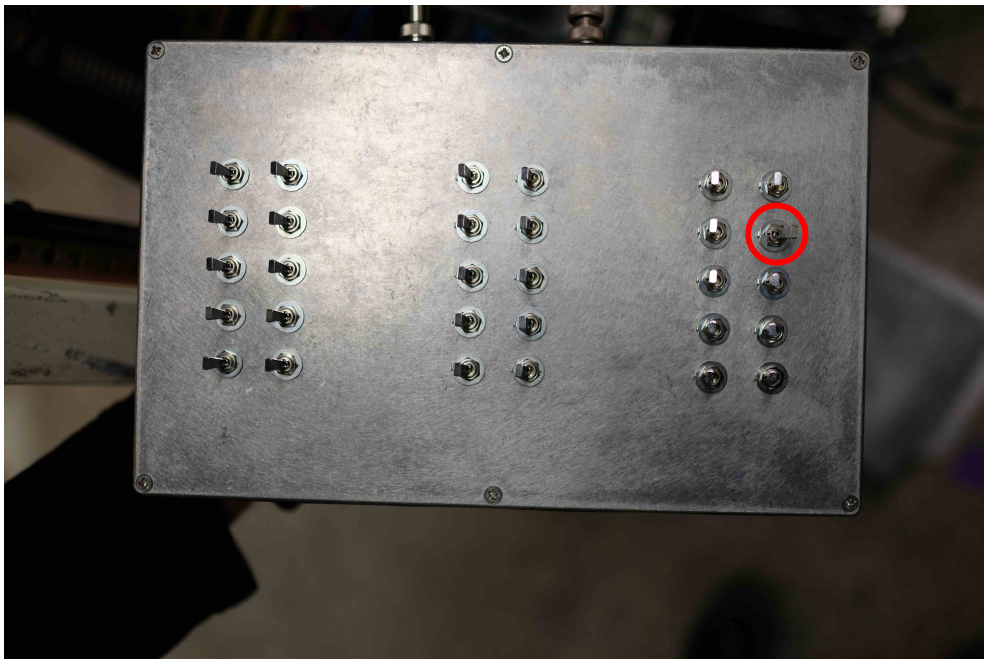


Figure 6.3: A photograph showing the housing and switches for the boards shown in Fig. 6.2. The red circle shows a switch in the on position for a 300 V output. A high voltage input to the circuit is set at 304 V to create a current through the output resistor in a specified range from Texas Instruments.

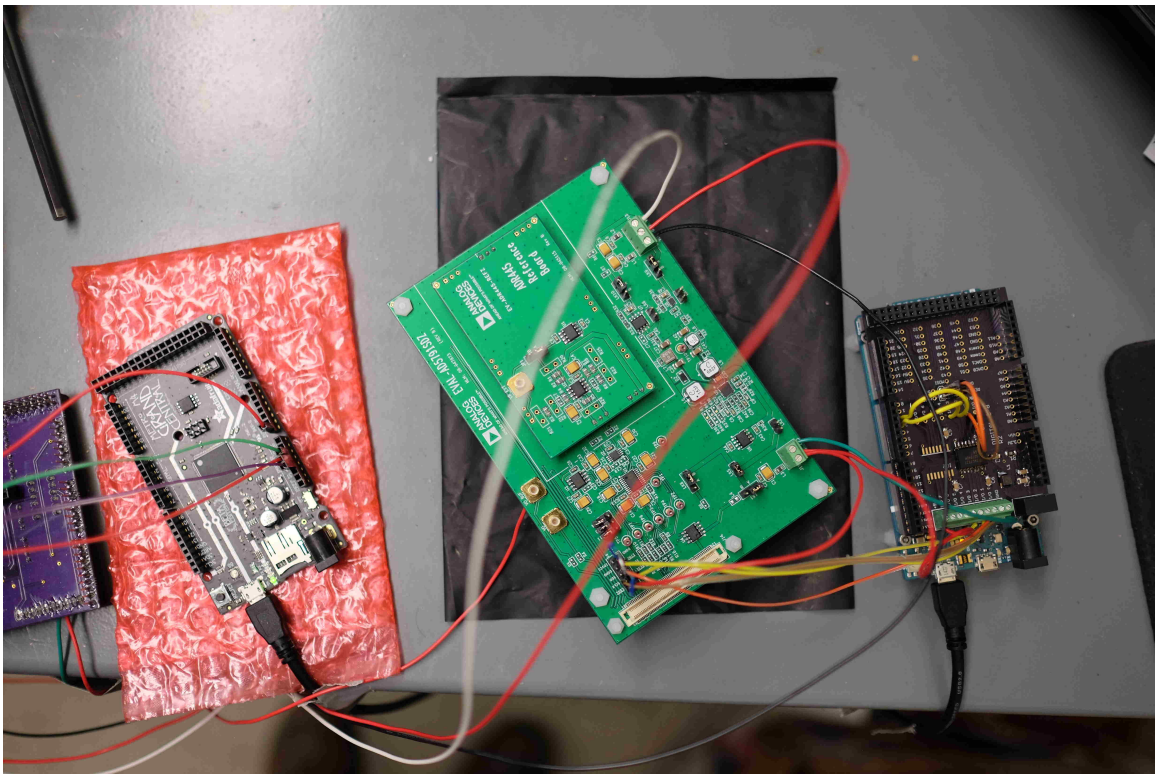


Figure 6.4: A photograph of the AD5791 DAC evaluation board with the Arduino Due and shield to the right. The Grand Central board on the left is used for the feedback cooling.

provide the most stable voltage. The input voltage needs to supply the 300 V for the 30 references, plus the voltage to supply the necessary current through resistor R12. Each board consists of ten voltage references, so to get 300 V, three boards need to be connected in series.

The Stanford Research Systems PS325 power supply was used to provide the voltage to the reference circuit due to its high voltage capabilities as well as being able to output positive and negative polarities. A voltage of 304 V was used, theoretically having 4 mA through resistor R12. The current reported by the power supply is 3.9 mA, still within the acceptable range.

The switches control the coarse voltage output to the trap. By only having one

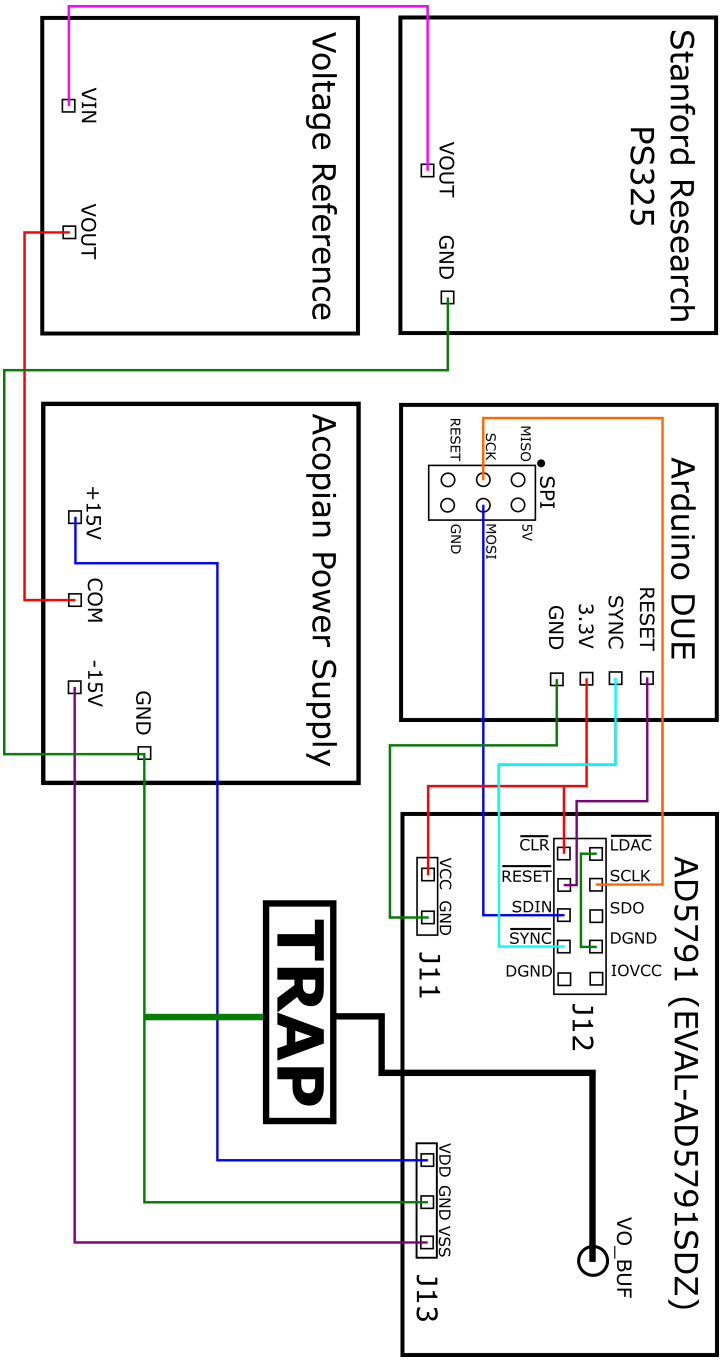


Figure 6.5: A wiring diagram for the high voltage variable voltage reference, based on a diagram provided by Bradley Slezak. The AD5791 DAC evaluation board is floated to a variable voltage by the voltage reference board (see Figs. 6.1, 6.2, and 6.3).

switch on at a time, the voltage can be changed in steps of 10 V. Having two switches activated will change the voltage in steps of 5 V. The fine voltage is controlled by an Analog Devices AD5791 (EVAL-AD5791SDZ) 1 ppm digital-to-analog converter (DAC).

The DAC evaluation board is floated to the voltage outputted by the voltage reference circuit. The wiring diagram is shown in Fig. 6.5. The output of the DAC relative to the voltage reference output is controlled in software. The DAC board is powered off of a floating Acopian TD15-100 power supply (±15 V, 100 mA).

6.3 Results

In order to test the stability of the variable voltage reference, data was taken for 259,200 s (3 days), during the same time as the table stabilization measurement described in chapter 8. Two such data sets were taken. The voltage was measured directly out of the DAC board in parallel with the trap.

The first data set, shown in Fig. 6.6, has an average voltage of −34.6507 V. The root-mean-square (RMS) voltage fluctuation is 0.0001 V. The total spread from minimum to maximum is 0.0010 V over three days. The plot only shows every hundredth point. The second data set, shown in Fig. 6.7, has an average voltage of −33.1218 V.

The voltage was set to be the same between the two data sets, however there is more than 1 V difference between them. After observing abnormal fluctuations in the first data set every time the BNC coax cable was moved or bumped gently, the cable was switched out. The RMS voltage fluctuation of data 2 is 0.0001 V, equal to the precision of the Keithley 2000 digital multimeter (DMM) (0.0001 V for the 100 V range). The total voltage spread from minimum to maximum is 0.0007 V over three days including all outliers. Without these points, the spread of voltages is

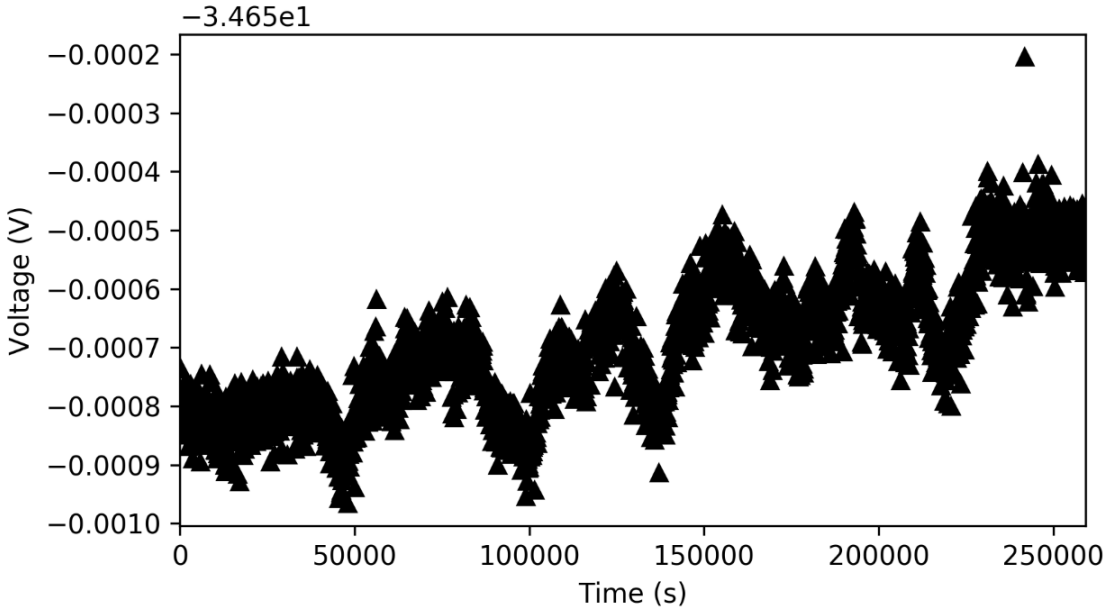


Figure 6.6: Three days of voltage data measured on a Keithley 2000 DMM. The RMS voltage is 0.0001 V with an average voltage −34.6507 V.

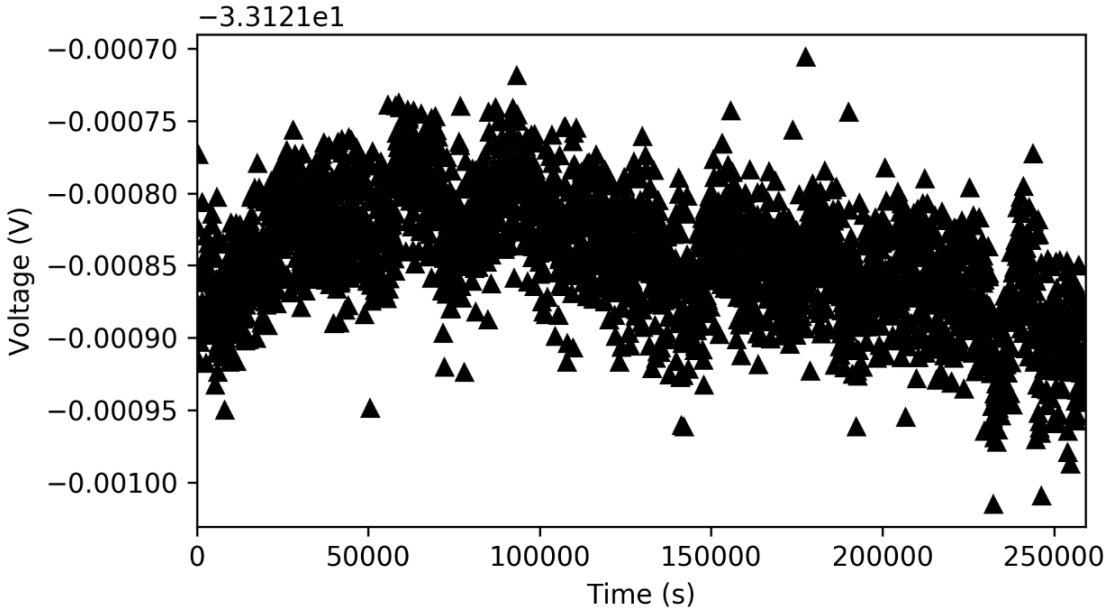


Figure 6.7: Three days of voltage data measured on a Keithley 2000 DMM. The RMS voltage is 0.0001 V with an average voltage −33.1218 V.

approximately 0.0002 V. Over shorter time periods, the voltage is much more stable, well under the precision of the DMM, as reported in chapter 10.

The system is extremely sensitive to the coax cable, its position, and any small perturbation. Despite being sensitive to the monitoring hardware, an issue anytime a coax cable is used, the RMS voltage fluctuation is still at the precision specification of the multimeter. The reported RMS voltage fluctuation for the second data is within the DMM specification as well with an even smaller total range of voltages. The calculated RMS fluctuation for data 2 is significantly under the DMM precision.

Though important, it is unknown at this time if the achieved precision is good enough for the measurement of Newton's constant of gravitation. A more advanced model of the trap is required to investigate this matter. This affect will also depend on the trap geometry and the trap may be designed to relax the condition on the stability required for the DC voltage. One improvement to the stability of the voltage is to thermally isolate and temperature regulate the circuit.

6.4 Conclusions

This chapter has presented a high-voltage, variable voltage reference, a modification of a Texas Instruments design. This voltage reference consists of thirty 10 V voltage references in series to source from 0 V to 300 V in magnitude. Since borosilicate particles are used for the work of this dissertation, the voltage reference was configured to source negative voltages. A 1 ppm 20-bit DAC board was used for fine adjustment of the voltage.

Since the measurement of G will consist of three days of data acquisition, measurements of voltage over three days were made, saving data once a second. This was repeated with slightly different voltages. Over three days, the voltage was stable to within 3 ppm. The required stability is not currently known as a more in depth

model is required as well depending on the trap geometry.

Once a particle is loaded in the magneto-gravitational trap and centered vertically with the DC voltage, the particle is illuminated with a 660 nm LED and imaged onto a CMOS camera. For a measurement of G, large amplitudes obtained by controlled feedback heating lower the effects of thermal noise (see chapter 4) and for accelerometry the particle needs to be feedback cooled to reduce the damping time of transients (see chapter 10). In the following chapter, a description of the methods used for the feedback controlling of the particle are presented, using the images from the camera that are already being saved.

CHAPTER SEVEN

CAMERA CONTROL

7.1 Introduction

Once the particle is loading into the magneto-gravitational trap using the methods in chapter 5 and technology in chapter 6, the particle is imaged onto a CMOS camera by a a modulated 660 nm LED (see chapter 3 for a diagram of the optics). To obtain the large amplitudes of motion for a measurement of Newton's constant of gravity, the particle needs to be excited (heated) in a controlled way to a particular amplitude. For high sensitivity acceleration measurements, the particle's center-of-mass motion needs to be cooled [61] so the damping time of transients is not too long to be able to perform the measurement in a reasonable amount of time.

The images of the particle, that are already acquired for displacement calculations after all of the images are taken, can be used to calculate the velocity of the particle in real time. Feedback control of the particle can be accomplished by applying a force proportional to particle's velocity [109, 110] using radiation pressure from a 520 nm diode laser. Applying feedback 180 ° out of phase with the particle's velocity will damp its motion [25]. A self-excitation limiter [111] can be used to excite the particle to a target amplitude. Feedback cooling and controlled heating has been implemented in this system. Results from controlled heating of a particle is demonstrated with three consecutive measurements achieving amplitudes within 1% percent of each other. Cooling results are presented in chapter 10.

7.2 Setup

As described in chapter 3, the levitated particle is illuminated by a 660 nm LED and imaged onto a Basler Ace acA2440-75um CMOS camera. The LED illuminates a 100 μm slit which is then imaged onto the particle to scramble any spacial information that the LED might have. The scattered 660 nm light passes through a long pass filter and is collected by the Mitutoyo 3× telecentric objective (Edmund Optics #56-985) and imaged onto the CMOS camera. We can use the information in the scattered light to provide feedback to the particle in real time. The long pass filter is to block the feedback control laser.

7.3 Laser Feedback

Using the information gained in the scattered light, we can apply feedback to the particle. The feedback can either cool or excite the center-of-mass motion of the particle, depending on the phase of the feedback [25, 99]. When photons hit the CMOS detector, the light is converted to electrons that can be read out to determine the brightness of each pixel. The images are read on a computer and saved to disk immediately. Images can be saved to RAM and then to disk after data collection if the data does not exceed the amount of free RAM. For a measurement of G, data is collected over the course of 24 hours at a frame rate that is as high as possible. Saving the data to RAM is not feasible.

Once the images are read by the computer and before the image is saved to disk, they are analyzed in real time to determine the position of the particle. When the particle is illuminated from the back of the chamber, the particle appears as a dark disk with a bright background, as shown in Fig. 7.1. Since the borosilicate particle has over 90% trasmission at 660 nm, the spherical particle acts as a lens and forms

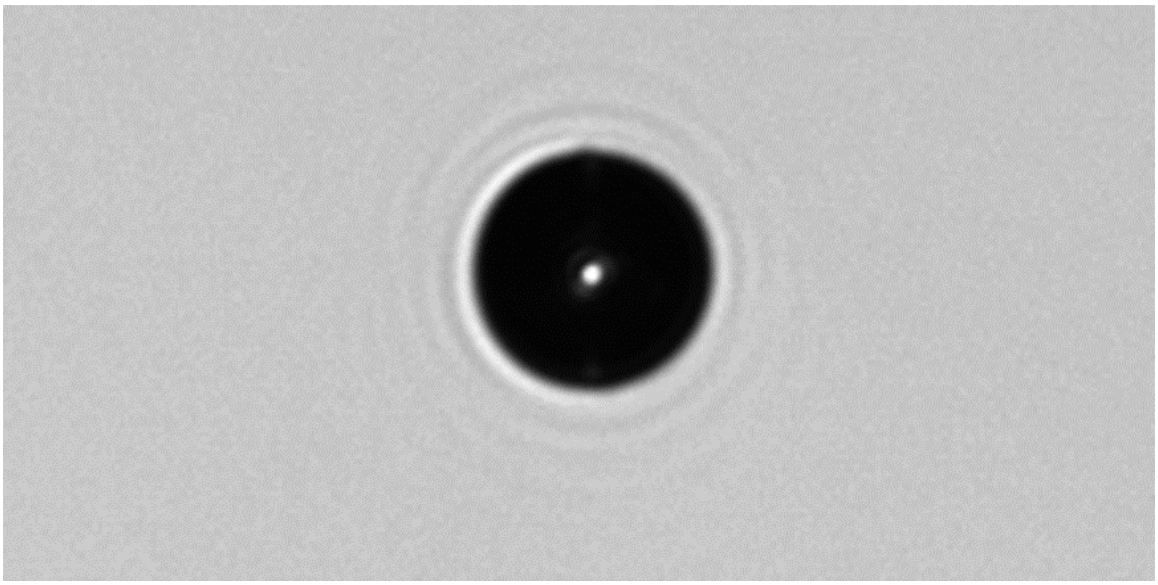


Figure 7.1: An example image of a levitated microsphere that is analyzed for feedback in real time. The particle is a dark disk on a bright background.

a focused spot in the center of the particle. For maximum speed, each pixel in the image is examined in a C-based library or program. If the pixel brightness is above a given value, a variable the experimenter can change, then that pixel is set to zero. If the pixel brightness is below the given value, that pixel is set to 4095, the maximum brightness. Once the entire image is remade using this technique, we can more easily calculate the center-of-mass of the particle. The center-of-mass is calculated by

$$(z_{com}, y_{com}) = \left(\frac{\sum_{n=0}^{N} b_n z_n}{\sum_{n=0}^{N} b_n}, \frac{\sum_{n=0}^{N} b_n y_n}{\sum_{n=0}^{N} b_n} \right) \tag{7.1}$$

where N is the total number of pixels in the image, b_n is the brightness of the n^{th} pixel, z_n is the axial position of the n^{th} pixel, and y_n is the vertical position of the n^{th} pixel.

When the center-of-mass is found, the original, unaltered image is saved to disk

and the center-of-mass coordinates is saved to a variable in RAM. The second image is then analyzed in the same way. Once at least two images have been analyzed, using the latest image and the image before it, the velocity of the particle is calculated. The velocity information is then used to provide feedback to the particle. In the work of this dissertation, the damping or drive to the particle is chosen to be proportional to the velocity [109, 110]

$$F_{\text{fb}} = -c\dot{z}e^{i\phi} \tag{7.2}$$

where ϕ is the phase of the feedback. For cooling, the phase is $\phi = 0$ rad and for heating, the phase is $\phi = \pi$ rad.

In order to provide the feedback, the gain of the feedback needs to be nonzero. The velocity information is used to modulate the feedback control laser. The laser enters the chamber at a large angle relative to the optical axis of the trap (see Fig. 3.26). Without the modulation, radiation pressure shifts the equilibrium position of the particle. For cooling the center-of-mass motion, as the particle moves towards the control laser, radiation pressure needs to be applied that is larger than the equilibrium radiation pressure. As the particle moves away from the control laser, a lesser radiation pressure is required as to not apply a positive acceleration the particle. The opposite is the case for heating the particle, where we want to apply a positive acceleration to the particle.

When the sign and strength of the feedback has been calculated, that signal is filtered according to the method in the following section. The feedback signal is then sent to an Adafruit Grand Central microcontroller board. A custom analog-IO shield [94] is used to output an analog signal that is sent to the laser diode controller. The modulation input on the controller is used.

7.4 IIR-Filter

As mentioned above, the feedback can either cool or heat the center-of-mass motion of the levitated particle. When the velocity is calculated by the above method, high frequency noise can be added to the system through the feedback. To eliminate this noise, a filter can be added in software (digital filter).

A second order resonant infinite impulse response (IIR) filter is used. The filter is a high quality factor bandpass filter [112]. The filter can be created by specifying the resonant frequency and quality factor required for a particular use. The quality factor is determined by the resonant frequency f_0 and the bandwidth Δf, $Q = f_0/\Delta f$. Typical values used in the work for this dissertation range from $f_0 = 0.5\,\mathrm{Hz}$ to $f_0 = 2\,\mathrm{Hz}$. This filter was not used during the low frequency measurements (see chapter 9). The bandwidths used were in the range from $\Delta f = 0.25\,\mathrm{Hz}$ to $\Delta f = 0.5\,\mathrm{Hz}$. A plot of an example filter for $f = 1\,\mathrm{Hz}$ and $\Delta f = 0.25\,\mathrm{Hz}$ is shown in Fig. 7.2.

The digital filter takes the current velocity and the gain the user wants as the arguments and returns the filtered velocity. The algorithm that the filter uses is described in algorithm 7.1.

The output signal from the filter is given by the relation

$$y_n = \frac{1}{a_0}\left(\sum_{i=0}^{P} b_i x_{n-i} - \sum_{j=1}^{Q} a_j x_{n-j}\right) \tag{7.3}$$

where x is the input signal and y is the output signal. In this relation, P is the order of the feedforward filter, Q is the feedback filter order, and b_i and a_j are the the feedforward and feedback coefficients, respectively. The coefficients are returned by the filter function, `scipy.signal.iirpeak(`ω_0`, Q)` [112]. In the filter used, $P = 2$ and $Q = 2$.

1: **INPUT:** Gain, Value

2: **OUTPUT:** Filtered Valued

3: // Initialize variables

4: $b, a = \text{iirpeak}(f0, Q)$

5: $a1 = -a$

6: index $= 0$

7: ins $= \text{array}(\text{len}(b))$

8: outs $= \text{array}(\text{len}(a1))$

9: // Continue until no more velocities to be filtered

10: **while next velocity = True**

11: $i = \text{index}$

12: **output** $= b[0] \times$ **value** $+ b[1] \times \text{ins}[i-1] + b[2] \times \text{ins}[i-2] +$
$a1[1] \times \text{outs}[i-1] + a1[2] \times \text{outs}[i-2]$

13: $\text{ins}[i] =$ **value**

14: $\text{outs}[i] =$ **output**

15: $\text{index} = \text{index} + 1$

16: // Return filtered value

17: **return gain** $\times$ **output**

Algorithm 7.1: The algorithm that the digital IIR filter follows to return a filtered value of the velocity of the particle.

The algorithm is ran until the data collection is finished. This bandpass filter does not introduce any phase shifts so the output filtered value has the same phase as the input velocity and therefore can be used directly to apply the feedback damping to the particle. Cooling results are discussed in chapter 10.

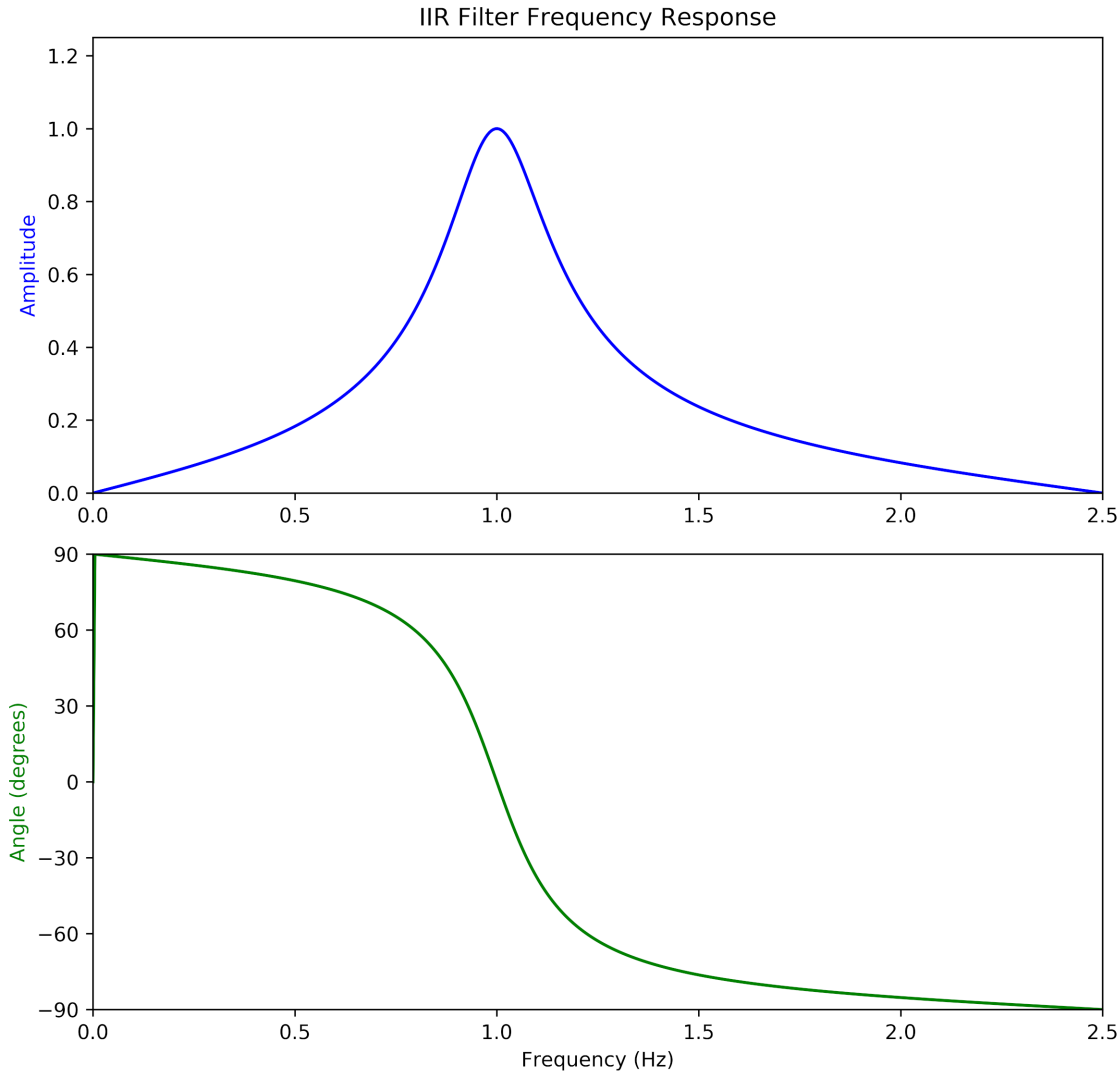


Figure 7.2: An example of the IIR filter used in this dissertation work. The resonant frequency is $f_0 = 1\,\mathrm{Hz}$ and bandwidth $\Delta f = 0.25\,\mathrm{Hz}$.

7.5 Self-Excitation Limiter

For precise measurements of the Newtonian constant of gravity, we have discussed why large amplitudes of motion are required. In the set of three measurements, the particle needs to be prepared with amplitudes of motion close to each other. Anharmonicities in the trapping potential as well as anharmonicities due

to fine structure in the trapping potential make this requirement even more important, since the measurement of G depends on the initial frequency of the oscillator. An estimate of how close these amplitudes need to be depends on these anharmoncities. A more in-depth model needs to be developed to understand the full trapping potential. Currently, as will be discussed in chapter 9, local charge on the pole pieces due to charged particles failing to load is a largest source of anharmonicity observed. This is almost impossible to understand as it depends on the particle's location in the trap and also changes with particle.

Instead of cooling the motion, heating the center-of-mass motion is required. A primitive approach is to apply a positive feedback to the particle and then stop all feedback when the particle is at the desired amplitude. This is difficult, however, since the total field of view of the camera is approximately 2.4 mm and the target full range of motion is 15 mm. We can apply positive feedback when the amplitude is smaller than the target, and negative feedback when the amplitude is too large. Equivalently, we can prepare the particle to a target velocity instead of position. To do so, we want the sign of the feedback to change as the velocity crosses the target value, and obviously zero at the target value. The use of such limiters have been shown to control chaotic systems [111].

We can consider the equation

$$\mathrm{FB}(v) = Gv\left(1 - \left|\frac{v}{v_0}\right|^{\beta}\right) \tag{7.4}$$

where G is the user set gain, v_0 is the target velocity, and β is a user set parameter that controls how quickly the velocity converges. When the velocity is less than the target velocity, FB is is positive, resulting in heating of the center-of-mass motion. When the target velocity is greater than the target velocity, FB is negative, resulting

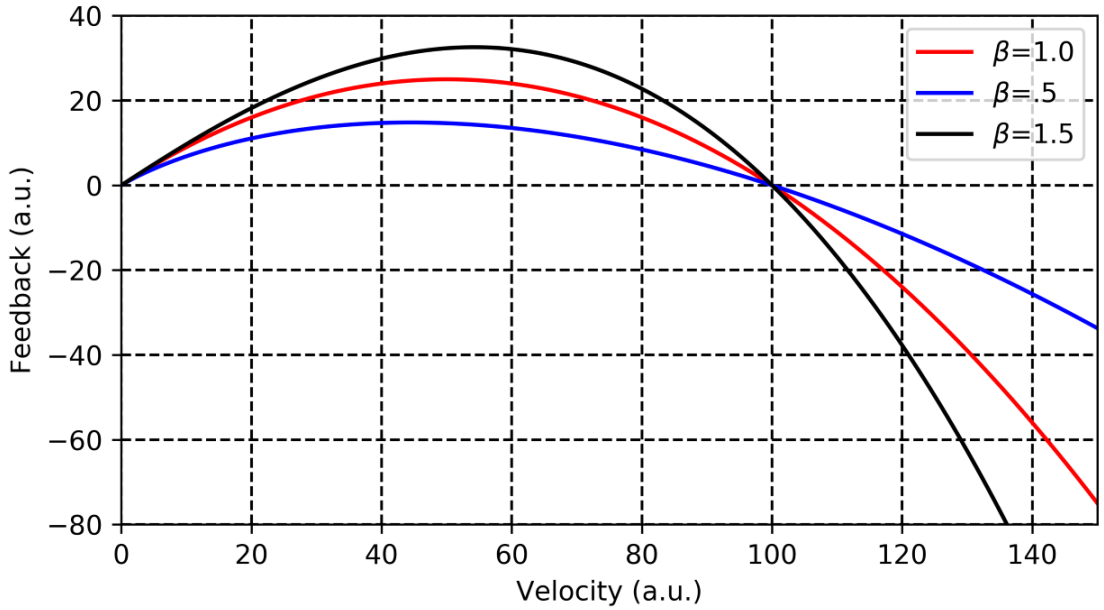


Figure 7.3: The feedback velocity as a function of the velocity of the particle for different values of β and $G = 1$ and $v_0 = 100$. The larger β is, the stronger the feedback will be. With this large β, the mean of the particle velocity will converge to the target velocity quickly but will also oscillate around this value. With smaller values of β, the velocity will converge more slowly but not oscillate as much.

in cooling.

In Fig. 7.3, we can see how different values of β changes the feedback strength. As β increases, the slope of the feedback increases, resulting in the velocity oscillating around the target velocity before converging. When β is smaller, the velocity converges more slowly, but without oscillating as much. For small enough values, the velocity will not oscillate about the target velocity.

In Fig. 7.4, three separate data sets were acquired with a target velocity of $v_0 =$ 250 μm/s and $\beta = 1.0$. With an oscillation frequency of $\omega_z/2\pi = 0.57$ Hz, assuming the particle is a perfect harmonic oscillator, this would equate to an amplitude of 439 μm. The actual amplitude is approximately 400 μm, due to anharmonicities of the trap. In Fig. 7.5, a close up of the first peak amplitude of each data set is shown.

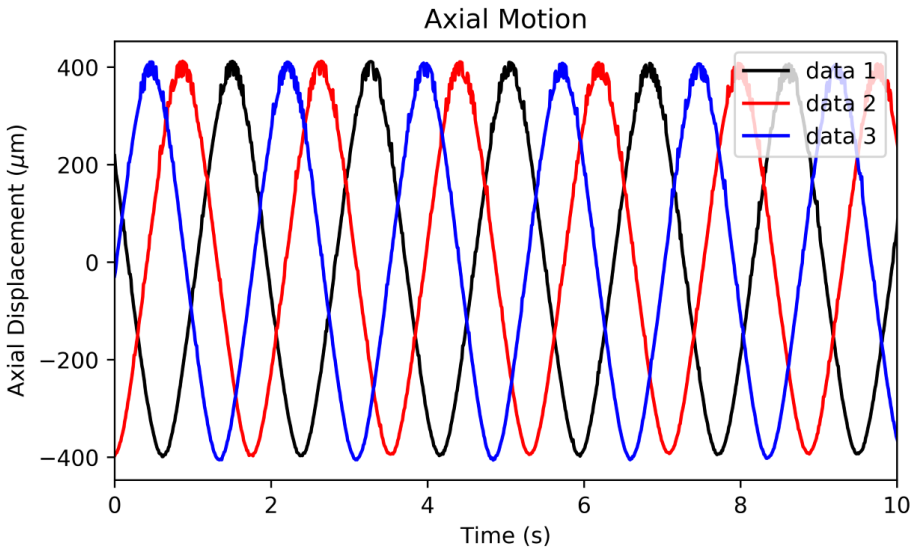


Figure 7.4: The first ten seconds of three 60 s data sets. The three sets were all prepared with the same $\beta = 1.0$ and $v_0 = 250$ μm/s. Initially, all three started at the same amplitude to within 1% of each other.

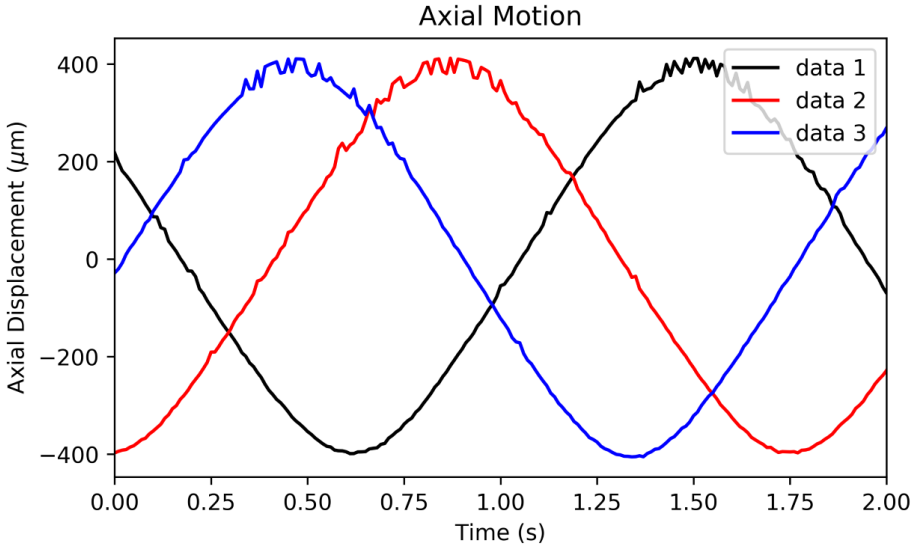


Figure 7.5: A close up of the first two seconds of the three data sets. The jagged features at the peaks are due to the particle finding algorithm used when analyzing this data. The three have initial amplitudes within 1% of each other, and could possibly be better if a better image analysis technique is used.

All three data sets are within 1% of each other. With current anharmonicities of the trap, 1% will not be good enough. Improvement of the anharmoncities will relax the need for better consistency in the amplitudes.

The jagged features at the positive amplitude is due to the image analysis technique breaking down. This is most likely due to the particle moving in the transverse direction or the camera being tilted relative to the optical axis of the trap. When the particle is at its peak amplitude, the particle is out of focus and the image analysis cannot locate the particle as precisely. With a better image analysis technique, the displacement will be more accurately determined.

7.6 Challenges

Though the camera control results look promising, there are several challenges in these methods. The threshold method is crude and throws away a lot of information in locating the position of the particle. Throwing away position information about the particle creates noise in the feedback. A more sophisticated method will be required. The velocity oscillation around the target velocity can also be a problem because with sufficient energy, the particle can leave the trap.

7.7 Conclusions

In this chapter, an implementation of feedback control using a CMOS camera has been developed. Cooling of the center-of-mass motion was achieved by applying feedback that is proportional to and 180 ° out of phase of the velocity of the particle. The results of the center-of-mass cooling is presented in chapter 10.

Controlled feedback heating has also been reported in this chapter. Using a self-excitation limiter, the amplitude of three consecutive data sets are within 1% of each

other, with a mean amplitude of approximately 400 μm. The analysis of the amplitude is currently limited by the image analysis technique used. A more detailed model of the anharmoncities of the trapping potential and the anharmonicities introduced by the field masses (see chapter 4) is needed to determine how close the amplitudes need to be for the three measurements.

With the technology developed in this chapter and the previous two, one more advancement was made for the work of this dissertation. The DC voltage source (chapter 6) prevents the vertical equilibrium position from changing substantially over the course of a G measurement. The axial equilibrium position is also important. If the particle is close to the edge axially of the magneto-gravitational trap, the harmonic approximation breaks down and the potential becomes anharmonic. If the trap tilts, the equilibrium position shifts. The next chapter describes a modification to a vibration isolation optical table to stabilize the drift in the tilt of the table.

CHAPTER EIGHT

TABLE STABILIZATION

8.1 Introduction

The magneto-gravitational trap used for the work in this dissertation (see chapter 3) was designed for low oscillation frequencies in the axial direction (see results in chapter 9). Because of the weakness of the trap, if the trap tilts about the transverse axis, the axial equilibrium position of the particle will shift proportional to the change in the tilt. This effect is more significant with lower oscillation frequencies.

In this chapter, a method of stabilizing the relative tilt of a vibration isolation optical table, such as the one used for the work of this dissertation, is presented. The tilt is monitored in real time by a high precision tiltmeter and that information is used to add or remove air from the isolators of the table via a modification to the isolation system. This method of active stabilization improves the relative tilt of the table by three orders of magnitude.

8.2 Theory

Trapped particles in levitated optomechanical systems are often subject to a harmonic potential. The motion can be described as a simple harmonic oscillator. For motion in the magneto-gravitational trap used in the work for this dissertation, the angular frequency of oscillation in the axial direction can be written as

$$\omega_z = \sqrt{\frac{k_z}{m}} \tag{8.1}$$

where k_z is the spring constant in the axial direction and m is the mass of the oscillator.

When the optical table tilts, the equilibrium position of the particle shifts. For a tilt of $\Delta\theta$ and using Eq. 8.1, the shift is calculated to be

$$\Delta z = \frac{g}{\omega_z^2}\Delta\theta \tag{8.2}$$

where g is the acceleration due to gravity. When the oscillation frequency is low, such as required for precision measurement of Newton's constant of gravity (see chapter 2 and 4, the equilibrium shift can be large enough to disrupt the measurement.

8.3 Setup

The optical table used for the work in this dissertation is a custom TMC vibration isolation table. The table is very good at eliminating vibrations above its resonant frequency of approximately 1 Hz. Because of changing environmental conditions, such as pressure and temperature changes and typical laboratory activities, slow and long term drifts in the tilt of the table are possible. The optical table is not equipped to solve this problem.

Pneumatic isolators are designed to minimize vibrations that can be transmitted from the floor to the table. The optical table used for the work in this dissertation is 8 feet by 4 feet in the transverse and axial direction, respectively. The table is supported by four TMC Gimbal Piston Isolators.

The table originally consisted of a regulator-valve system on master leg, labeled R and M in Fig. 8.1, respectively. Since only three regulator-valve systems are necessary, one slave leg (labeled S in Fig. 8.1) is tied to one master leg. Since we care about stabilization in the axial direction (weak trapping direction), the master-slave leg pair

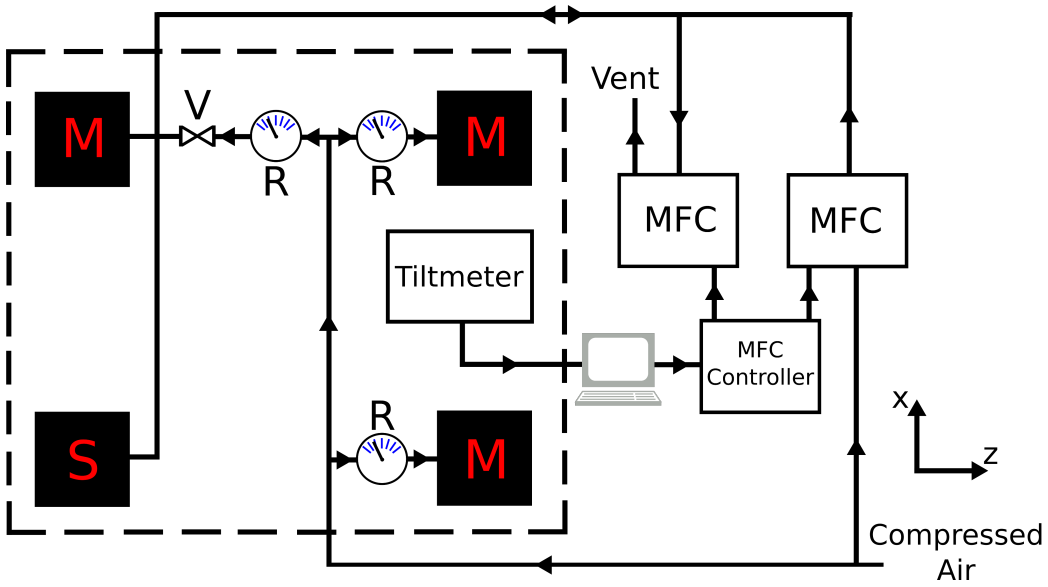


Figure 8.1: System diagram for the active stabilization of the optical table using two mass flow controllers. One mass flow controller adds air to the pneumatic isolators on the master-slave leg pair and one removes air depending on the tilt of the table.

is parallel to the transverse direction. These regulator-valve systems add or remove compressed air from the isolated to approximately level the table.

To stabilize the tilt of the table, a simple yet effective modification was made to the isolator regulation. An air line is inserted in the master-slave leg pair between the regular-valve system and the isolator. This air line is split off into two and connected to two mass flow controllers (MFCs) (MKS 1179C01312CR1BV). One MFC allows gas flow towards the legs and the other allows gas flow out of the legs.

These two MFCs are controlled by a 4-channel flow controller power supply and readout (MFC controller) (MKS type 247). Between the master-slave leg pair and regulator-valve system is an inline valve. This valve prevents the regulator-valve system from competing with the flow from the MFCs when the active stabilization is in use by isolating the master-slave leg pair from the regulators.

A two-axis tiltmeter (Jewell Instruments A603-C) is placed on the optical table

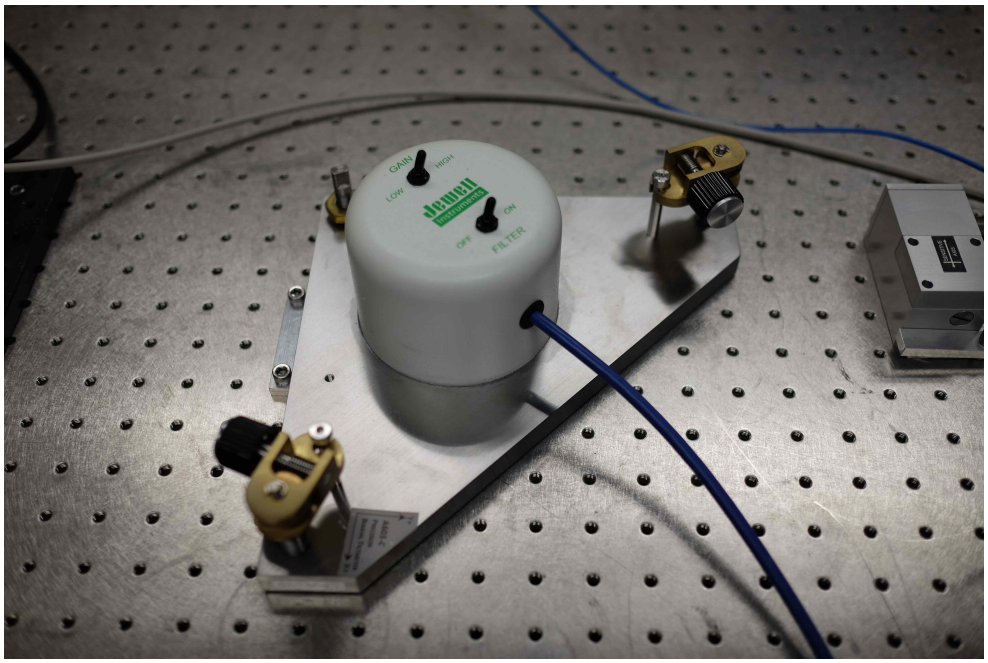


Figure 8.2: A photograph of the Jewell Instruments A603-C tiltmeter.

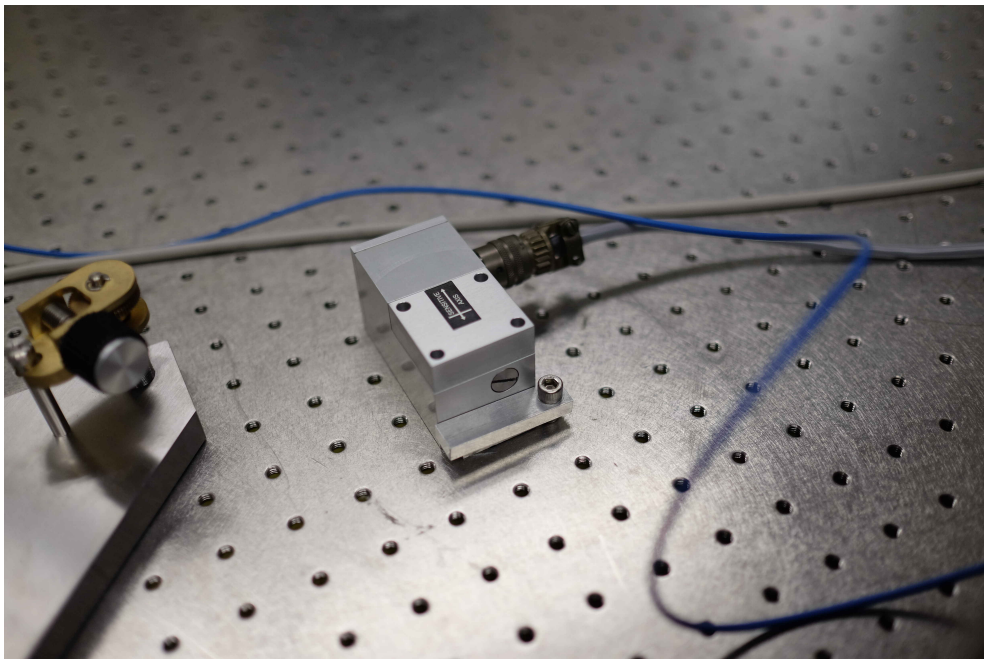


Figure 8.3: A photograph of the Jewell Instruments LSOC-1Z inclinometer.

(shown in Fig. 8.2) and centered in the axial direction. This tiltmeter is used to monitor the tilt of the optical table with a precision of less than 2.5 nrad along its two axes, oriented in the transverse and axial directions. This tiltmeter has two gain settings: high gain has an angular range of ±40 µrad and low gain has an angular range of ±400 µrad. An optional 7 s output filter can also be used for lower noise. The outputs are monitored on Keithley 2000 digital multimeters (DMM).

For initial alignment, the tiltmeter is adjusted using the worm-gear feet until the output voltage is near zero. A zero output corresponds to zero absolute tilt. Since we only care about the relative tilt $\Delta\theta$, it is not crucial to completely zero the tiltmeter.

When the A603-C tiltmeter does not provide enough angular range for large tilts, a second tiltmeter is also used. A Jewell Instruments LSOC-1Z fluid damped single-axis inclinometer (see Fig. 8.3) is placed on the optical tabled centered in the axial direction. This tiltmeter has an angular range of ±0.017 rad and a resolution of 1 µrad. The output is also monitored on a Keithley 2000 DMM.

8.4 PI Controller

Once the measured tilt data is read on the computer via GPIB, the in-flow and out-flow rates need to be calculated. These values are determined by a digital proportional-integral (PI) controller. For every new tilt measurement, the difference between the target tilt and measured tilt, Δ_i, is calculated. This value is then multiplied by the proportional constant P and integral constant I. The algorithm to determine the feedback flow F_i corresponding the i^{th} tilt measurement is

$$F_i = P\Delta_i + I\sum_{n=0}^{i}\Delta_n. \tag{8.3}$$

Detailed pseudocode of the calculation is given in algorithm 8.2.

```
1: // Initialize variables
2: set target
3: set P
4: set I
5: set cap
6: intTotal = 0
7: while measuring tilt = True
8:     err = target − tilt
9:     prop = P × err
10:    int = I × err
11:    intTotal = intTotal + int
12:    if intTotal > cap
13:        intTotal = cap
14:    feedback = prop + intTotal
15:    return feedback
```

Algorithm 8.2: The algorithm used to determine the strength and sign of the feedback for actively stabilizing the optical table.

To prevent excessive integral windup of the algorithm, the integral term is limited to $\pm 216\,\mu\text{rad}$. This choice was arbitrarily chosen but experimentally determined to provide the desired result. Another problem that can occur is when F_i changes sign. To avoid the abrupt crossover when one MFC is switched on while the other is switched off, both outputs are kept at a nonzero flow rate when $F_i = 0$.

8.5 Results

Throughout this dissertation, without active stabilization is referred to as unstabilized. The relative tilt of the optical table was monitored with and without active stabilization for 3 days (the total proposed time of the G measurement). A tilt measurement was taken once every second. The stabilized data was taken first followed by the unstabilized data. For the unstabilized, the feedback MFC controller was turned and the inline valve between the isolator on the master-slave leg pair and the regulator-valve system was opened allowing the table to be fully controlled by the original regulators.

For the unstabilized data, the tilt was first stabilized to approximately ± 1.35 μrad. The active stabilization was then turned off and the tilt monitoring started. The tilt immediately started to drift as shown in Fig. 8.4. The tilt eventually settled after approximately 8 hrs and started drifting back in the opposite direction. Throughout the three days, the root-mean-square (RMS) variation in the tilt was approximately 270 μrad. The total drift, from minimum to maximum tilt values, was approximately 1500 μrad. Because of the large drift, the LSOC-1Z tiltmeter was required. This illustrates how long the isolators take to settle, that the drift over three days is significant, and that a stabilization technique is required.

To measure the tilt of the actively stabilized table, the inline valve between the regulator-valve system and the master-slave leg pair isolator was closed. The table was stabilized to approximately 1.35 μrad before the data acquisition was started. Again, three days of data was recorded as shown in Fig. 8.5.

The tilt is well stabilized except for four disturbances at approximately 33.3 hrs, 52.5 hrs, 59 hrs, and 61.7 hrs. The causes of the disturbances are unknown. The RMS tilt variation for this data is 2.8 μrad. Including the four large disturbances, the RMS

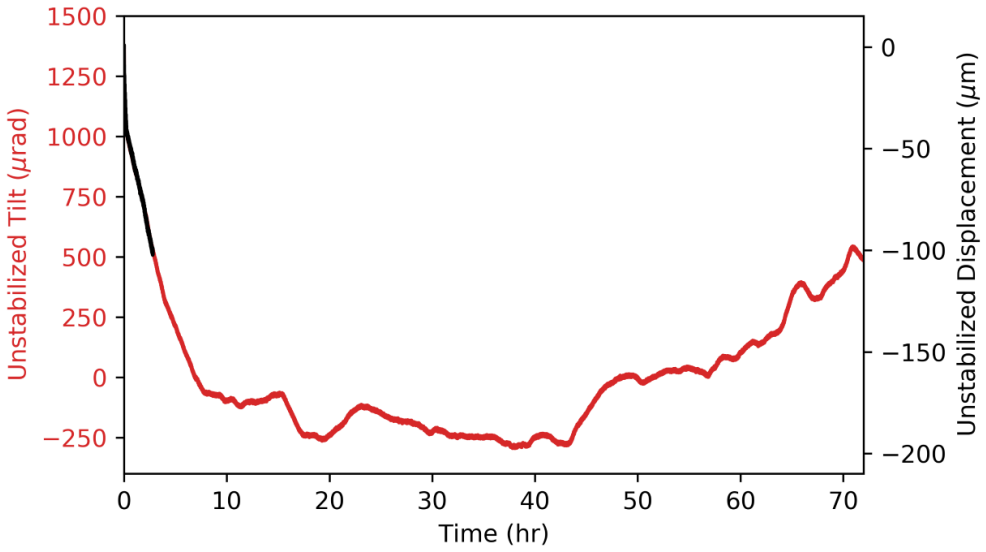


Figure 8.4: The relative tilt of the unstabilized optical table over three days (shown in red). The displacement of the particle (black) is also shown. After approximately four hours, the particle leaves the frame and never reenters.

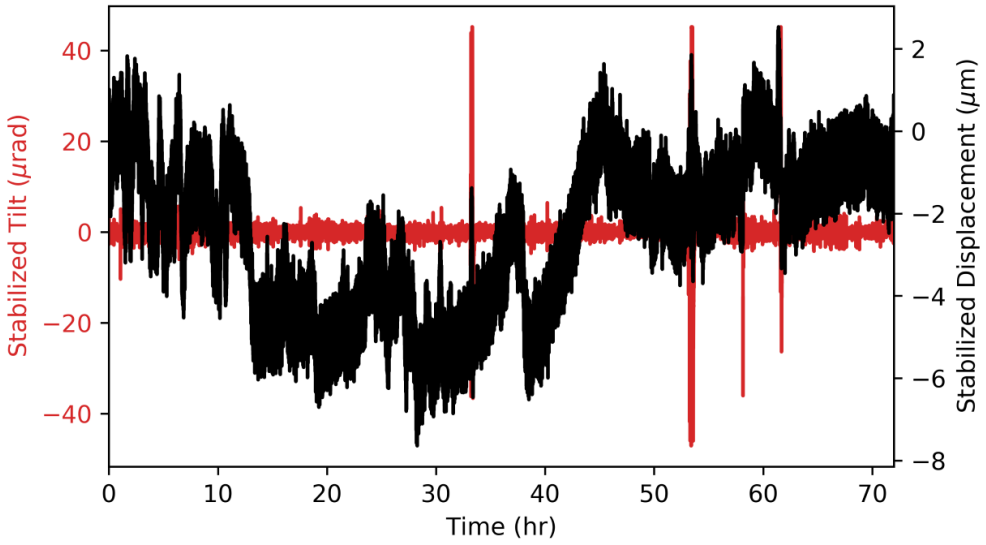


Figure 8.5: The relative tilt of the actively stabilized optical table over three days (shown in red). The displacement of the particle during the same time is also shown (black).

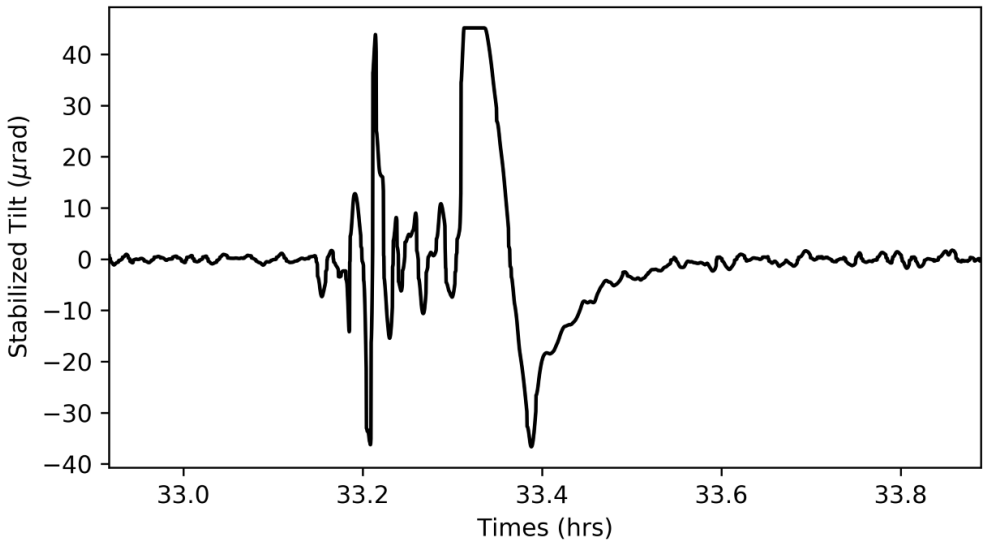


Figure 8.6: A close up view of the large disturbance in the relative tilt at 33.3 hrs. The tilt exceeded the A603-C range and was corrected in approximately 1000 s.

tilt is two orders of magnitude better than that of the unstabilized table.

We can investigate the disturbance at 33.3 hrs as shown in Fig. 8.6. The optical table is well stabilized to within $\pm 1.2\,\mu$rad until 33.1 hrs. After the table starts to tilt, the stabilization overshoots before correcting this tilt. From start to finish, the stabilization only took approximately 1000 s. Not only does the active stabilization has long term drift benefits in stabilizing the optical table tilt, but it can also correct large transients in the tilt in short amounts of time.

The unstabilized table can have significant effects on levitated optomechanics experiments. Particles in the magneto-gravitational trap used in this demonstration have demonstrated frequencies down to approximately $\omega_z/2\pi \approx 0.1\,$Hz, as will be shown in chapter 9. Since the equilbrium shift depends on ω_z^{-2} (see Eq. 8.2), the drift can disrupt measurements of G. To investigate this effect, a 60 μm diameter borosilicate microsphere was trapped and the chamber was left at atmospheric pressure to provide damping.

The particle was imaged onto the CMOS camera while acquiring both stabilized data and unstabilized data. The particle images are recorded once every second, which is synchronized with the tilt data. The images are analyzed once all of the data was acquired using the eigenframe method described in [113] and chapter 10 for obtaining sub-pixel displacement of the particle. The images were approximately 250 μm horizontally and 125 μm vertically.

The displacement of the particle during the unstabilized measurement is shown as the black curve in Fig. 8.4. To determine the oscillation frequency of this particle, the scale is adjusted appropriately for the particle displacement to match the relative tilt data. By Eq. 8.2, the oscillation frequency is found to be $\omega_z/2\pi = 0.17\,\mathrm{Hz}$. During the first four hours, the particle drifts approximately 125 μm until it drifted out of the frame. Throughout the measurements, the tilt of the table never returned to the angle required for the particle to return to the frame. The particle likely drifted much further than this during the three days, possibly up to approximately 400 μm.

During the active stabilization measurement, the particle displacement is shown by the black curve in Fig. 8.5. The total range of displacement is $\Delta z \approx 10\,\mu\mathrm{m}$. The particle always remained near the center of the frame. During the four large disturbances, the particle is also seen jumping accordingly. Despite this, the particle displacement shows very little correlation with the relative tilt. This shows that the particle motion is not limited by the tilt of the optical table in this measurement. The origin of this motion is currently unknown though it may be due to the charge of the particle changing over time likely due to the air in the chamber.

Several comments can be made about these results. The RMS tilt variation of the actively stabilized table is 2.8 μrad including the four large disturbances. In a quieter environment, as a measurement of G is most likely to take place, the RMS tilt variation not including these transients would be 0.35 μrad, three orders of magnitude

lower than the unstabilized data. The thermal noise with the oscillation $\omega_z/2\pi = 0.17\,\mathrm{Hz}$ and the particle properties will be $A_{\mathrm{therm}} \approx 4\,\mu\mathrm{m}$ (calculated from Eq. 4.18). The measured $\Delta z \approx 10\,\mu\mathrm{m}$ is a little more than twice the thermal noise amplitude. This shows that thermal noise is not likely the reason for the particle displacement.

8.6 Conclusions

This chapter has demonstrated active stabilization of the relative tilt of the vibration isolation optical table used in the work for this dissertation. The tilt of the table was measured with a Jewell Instruments A603-C tiltmeter. The tilt is read on a digital multimeter and processed on a computer in real time. Depending on the direction of the tilt, two mass flow controllers either add or remove air from the isolators through a simple modification to the table.

As explained in chapter 4, a measurement of the Newtonian constant of gravitation will consist of three 1-day phase accumulation measurements. To test the stabilization, three days of tilt measurements were made, one measurement per second. Several large anomalies are seen in the data. The cause of these are unknown. The root-mean-square fluctuation in the relative tilt including the large disturbances is $2.8\,\mu\mathrm{rad}$. In a more quiet environment, where a measurement of G is likely to take place, these large tilts can be prevented. Without them, the root-mean-square fluctuation in the tilt is $0.35\,\mu\mathrm{rad}$. The displacement of a $60\,\mu\mathrm{m}$ borosilicate particle was also monitored with the tilt. Analysis of both the tilt and the displacement show that with the stabilized table, the noise in displacement is not limited by tilt.

Without the active stabilization, relative tilt data was acquired for three days. The root-mean-square fluctuation in the tilt is approximately $270\,\mu\mathrm{rad}$, approximately three orders of magnitude larger than that of the stabilized table. Again, particle displacement data was saved with the tilt data. There was clear correlation between

the tilt of the table and the displacement of the particle until the particle leaves the field of view of the camera.

The following chapters report results obtained during the work for this dissertation that have used some or all of the techniques used in this chapter and the previous three. The following chapter reports frequency results, including an experimental study of local anharmonicities due to charge.

CHAPTER NINE

FREQUENCY RESULTS

9.1 Introduction

As described in chapter 2 and 4, the axial oscillation frequency of the oscillator is extremely important for a time-of-swing measurement of Newton's constant of gravity. The change in frequency in the axial direction measured through an accumulated phase shift is inversely proportional to the axial oscillation frequency when the field masses are in the far position. To maximize the phase accumulation, the oscillation frequency should be as low as possible. The target axial frequency for the work for this dissertation is 0.1 Hz.

This chapter presents results of axial frequency measurements during the work for this dissertation. Using methods developed in the previous chapters, in particular the controlled feedback heating in chapter 7, studies of the local anharmonicity due to charged particles or patch charges on the pole pieces were performed. Currently, these anharmonic effects are much larger than the anharmonicity of the trapping potential. Before a measurement of G can be made, this needs addressed and has not been in the work for this dissertation.

These issues arise from the loading method described in chapter 5. Because the particles are required to be charged, the ones that failed to trap interact via the Coulomb force with the particle that is trapped. Despite this, our target axial frequency of 0.1 Hz was achieved. For this oscillation frequency, a 10 ppm measurement will require a relative axial frequency stability of 10^{-11} (see chapter 4).

In addition to oscillation frequency analysis, a study of the damping rate in this system is discussed. The damping rate is observed to be orders of magnitude

larger than predicted by collisions of the particle with background gas. The source of damping will need to be addressed to help relax the anharmonicity conditions.

9.2 Anharmonicity of the Magneto-Gravitational Trap

In chapter 4, consequences of anharmonicities in the trapping potential were described. Once a particle is loaded in the magneto-gravitational trap, several tests can be done to access the harmonic nature of the trap. Shown in Fig. 9.1 is the motion of a borosilicate particle with a diameter of approximately 60 μm. The particle was excited to an amplitude of approximately 0.8 mm. Positive values indicate motion to the right side of the CMOS camera and negative values indicate motion to the left side of the camera.

On the peak of the motion in the axial direction, the displacement versus time is sinusoidal, indicating harmonic motion. At the other end, however, the motion would be best described by a triangle wave, indicating anharmonic motion. This triangular motion is due to charged particles on the pole pieces that failed to be trapped. Since the levitated particle is also charged, with typically the same kind of charge, the levitated one is repelled by them. This repulsion creates a hard potential barrier for the trapped particle, leading to the triangular motion.

To further investigate this particle's motion, we can look at its Fourier spectrum. Instantly, we can see that the motion is anharmonic, following the pattern of the Fourier transform of a triangle wave, as expected. At least eight higher order harmonics are seen. The frequency of the first harmonic is 0.23 Hz. Frequencies of trapped particles in a magneto-gravitational trap are typically $\sim$ 10 Hz in the axial direction. Since the spring constant scales proportionally to ω^2, an approximate frequency of 0.25 Hz is the result of a 1600 times weaker trap.

With a different particle, a series of axial oscillation frequency measurements

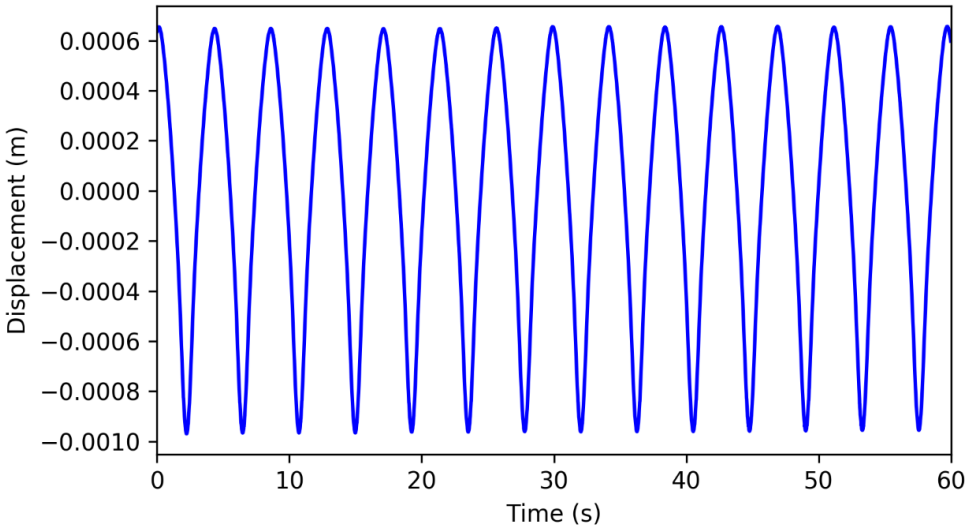


Figure 9.1: Time domain data of the motion of a borosilicate microsphere. The amplitude of motion is approximately 0.8 mm. At the peak of the displacement, the motion is harmonic (sinusoidal) with a frequency of 0.23 Hz. At the other end of the displacement, the motion is not harmonic (triangular). This is due to a potential wall at that end.

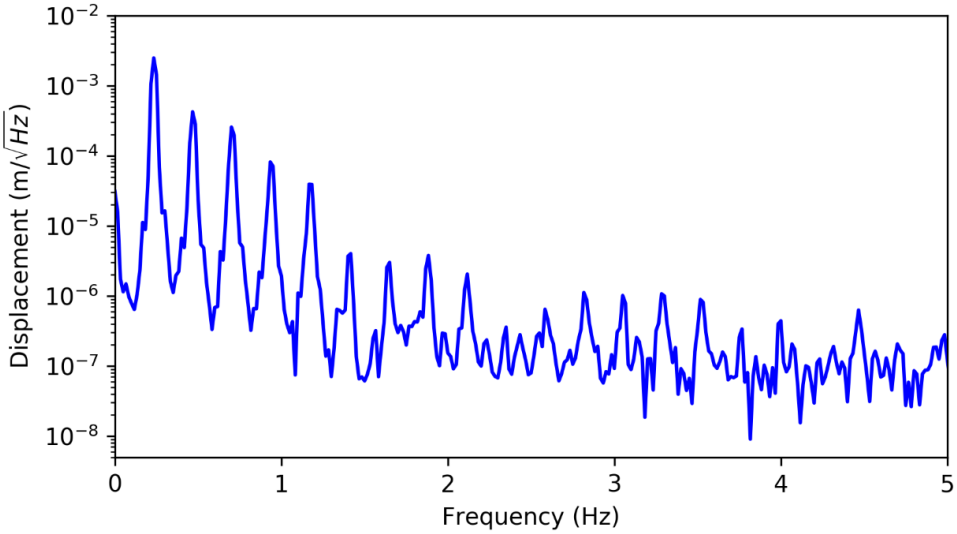


Figure 9.2: The 0.23 Hz peak corresponding to the axial motion is seen as well as eight higher harmonics. These harmonics are due to the triangular wave motion during half of the motion.

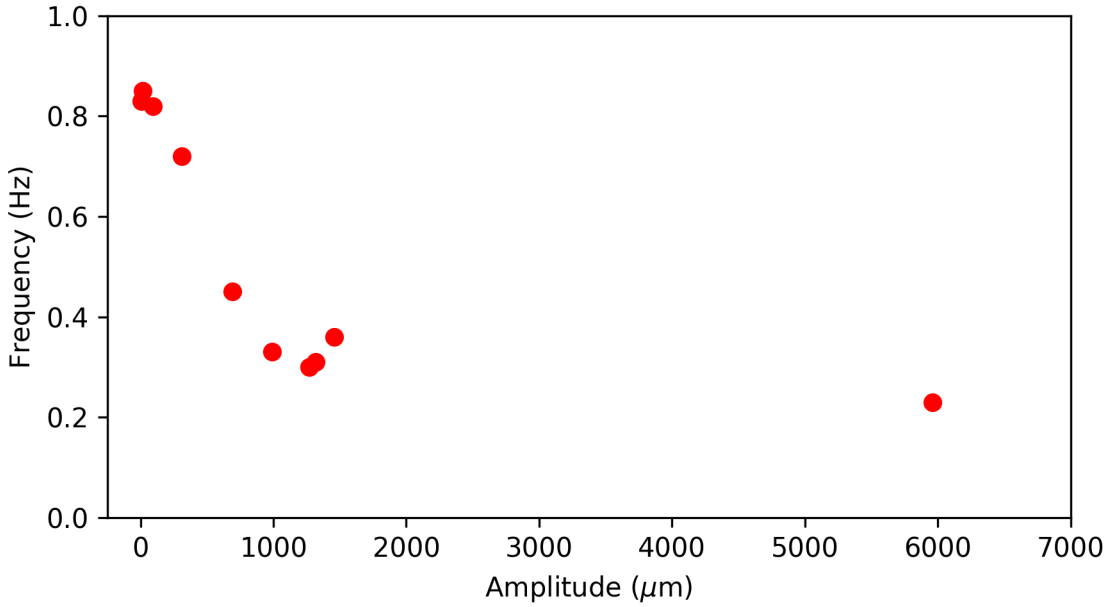


Figure 9.3: A series of measurements were made with different amplitudes of motion. The frequency of each motion is plotted against their corresponding amplitudes. The point at 6 mm has the lowest frequency but not as low as expected based on results in Fig. 9.6. This is likely due to charge on the pole pieces being larger towards the turning points of the motion causing a larger anharmonicity at that amplitude.

were made for different amplitudes. It is important to note that a different particle means that the charged particles on the pole pieces that are not trapped can be different than in previous measurements. The amplitude of each of the ten measurements was controlled by the self-limited camera control. The axial frequency of the motion versus its amplitude is plotted in Fig. 9.3. The outlier at an amplitude of 6 mm is believed to be caused by a hard potential barrier at one or both ends of the motion, however, the particle left the field of view of the camera so it was not able to be analyzed completely. It is expected, however, that when the motion of the particle approaches the edge of the trap, the frequency will increase due to the anharmonicity of the potential at the edges.

In Fig. 9.4, the trajectory of the particle is overlaid on an image of the trap

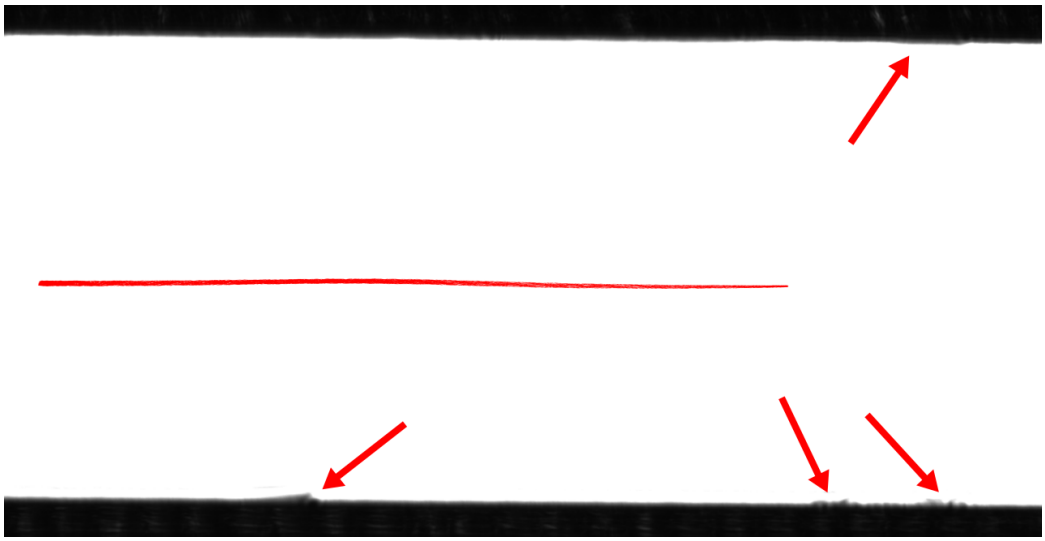


Figure 9.4: The trajectory of the particle overlaid on an image of the magneto-gravitational trap. The vertical and axial motion corresponding to this trajectory is plotted in Fig. 9.5. From the trajectory and trap image, the cause of the anharmonic motion is visible. Charged contamination, indicated by the on the pole pieces is the main cause.

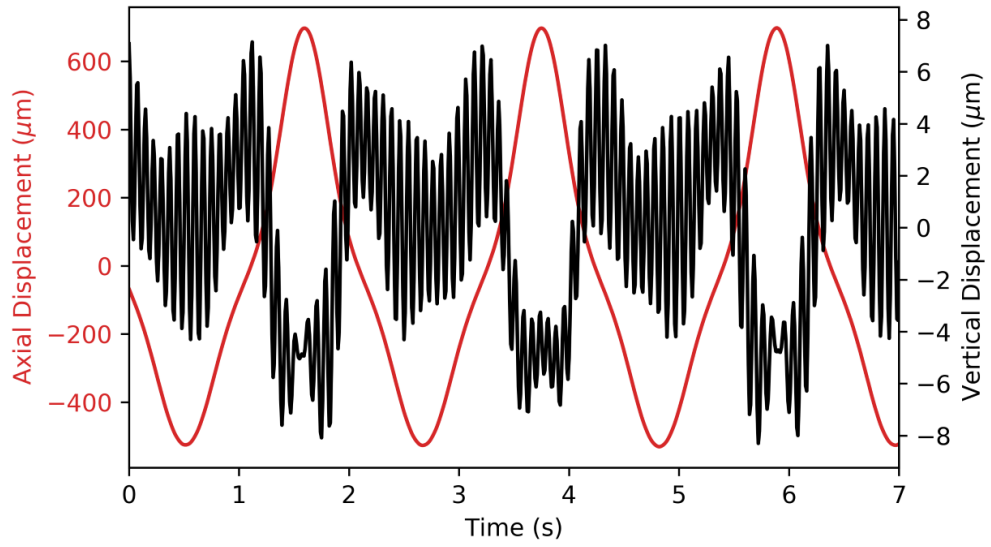


Figure 9.5: A subset of the vertical (black) and axial (red) motion in the time domain for the trajectory shown in Fig. 9.4. There is coupling between the two degrees of freedom.

where the particle was located, before it was knocked out of the trapping region. At the right hand side of the motion, there is clear evidence of particles on the pole pieces themselves. Just left of center, there is evidence of another source of contamination, possibly a fragment of the brittle magnet. It is obvious from the trajectory that the left of center contamination caused a vertical displacement in the motion.

The axial and vertical displacements of the particle are shown in Fig. 9.5. The vertical displacement oscillates at the natural vertical frequency but also shows a dependence on the axial motion. In addition to anharmonicities in a single degree of freedom, coupling between two or more degrees of freedom can create extra issues.

9.3 Low Frequency Results

Though anharmonic motion is evident in many measurements, this has not stopped progress to the 0.1 Hz goal. In Fig. 9.6, a small subset of the data is shown. The amplitude of the motion in the axial direction is approximately 4 mm where the particle leaves the field of view of the camera on both sides. In Fig. 9.7, three different fits are applied. The first three periods are fit to the black sinusoidal curve, the second three are fit to the red curve, and the last is fit to the blue curve.

Between the different fits, there is a change in phase corresponding to anharmonicity of the trapping potential. Ignoring this phase change, the fit returns an axial oscillation frequency value that averages 0.1 Hz. This shows that it is possible to reach our goal frequency with amplitudes as low as 4 mm. We expect the frequency to be even lower with larger amplitudes, provided that anharmonicities of the trap are not too large.

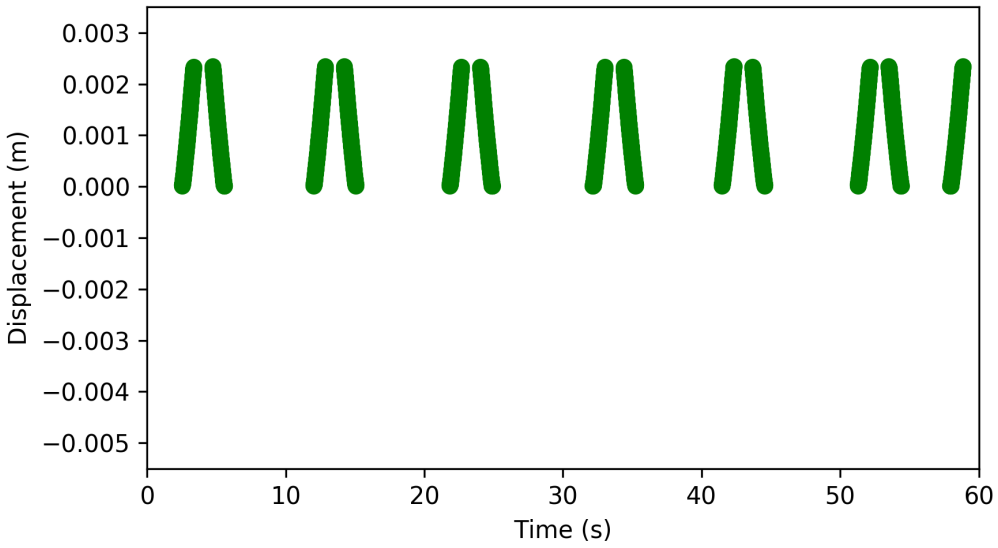


Figure 9.6: The motion of a borosilicate particle that leaves the frame of the camera. The amplitude of motion is approximately 4 mm. The frequency of motion is the lowest measured in the magneto-gravitational trap, a frequency of 0.1 Hz.

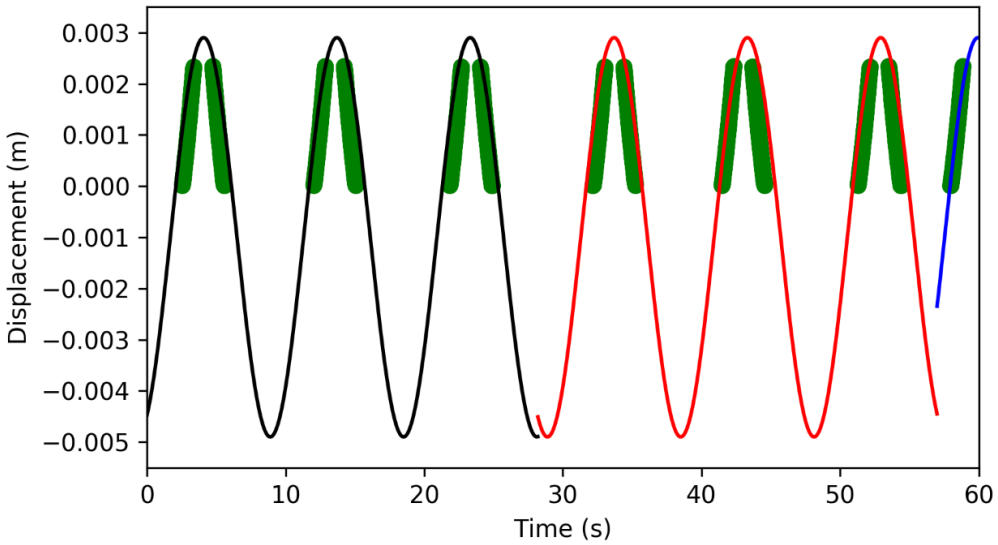


Figure 9.7: The black curve shows the sinusoidal fit for the first three periods of motion. The red curve is a fit to the second set of three periods. These are out of phase from the first three. The last set of points is again out of phase. Though the frequency is extremely low, the motion is extremely anharmonic.

9.4 Damping Rates

Another challenge that was experienced and will need addressed before a precision measurement of the Newtonian constant of gravitation is made is that the natural damping rate of the levitated particle is not limited by collisions with background gas. This is currently a problem as damping is seven orders of magnitude larger than predicted by collisions with air molecules. The source of the damping is unknown at this time. Problems from anharmonicities in the trapping potential are exasperated when damping is large. As discussed in chapter 4, long decay times are necessary to decrease systematic errors, especially with anharmonicities in the trapping potential.

The damping rate due to collisions with air molecules can be calculated by the equation [99, 114],

$$\Gamma = \frac{P}{\rho r}\sqrt{\frac{8m_g}{\pi k_B T}} \tag{9.1}$$

where P is the chamber pressure, ρ is the density of the levitated sphere, r is the radius of the sphere, m_g is the mass of an air molecule (weighted average of 78.5% N_2 and 22.5% O_2), k_B is Boltzmann's constant, and T is the temperature of the background gas.

Data was acquired for 60 s for a 60 µm borosilicate particle after an excitation to an amplitude of approximately 300 µm in vacuum with an air pressure on the order of 10^{-9} Torr. Using this pressure, $\rho = 2230\,\mathrm{kg/m^3}$ for borosilicate, $r = 30\,\mu\mathrm{m}$, $T = 300\,\mathrm{K}$, $m_g = 4.8 \times 10^{-26}\,\mathrm{kg}$, the damping rate is predicted to be $\Gamma = 8 \times 10^{-11}\,\mathrm{s^{-1}}$.

The data, shown in Fig. 9.8, has a measured damping rate of approximately $7 \times 10^{-4}\,\mathrm{s^{-1}}$. This rate has been consistently measured throughout all high vacuum experiments in this dissertation, from 10^{-6} Torr to 10^{-9} Torr. This damping rate is seven orders of magnitude larger than predicted by Eq. 9.1 and is independent of

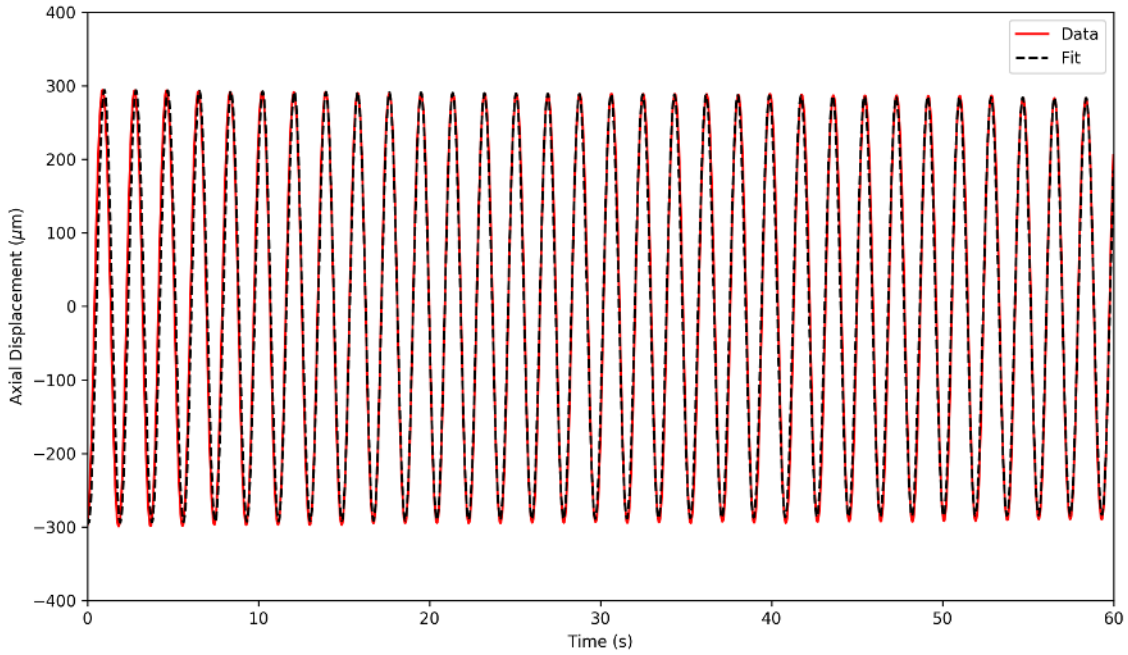


Figure 9.8: The axial motion data for a particle excited to an amplitude of approximately 300 μm (red) at an air pressure of 10^{-9} Torr. A fit of the data to an exponentially decaying sine wave is shown in black. The damping rate measured is $7 \times 10^{-4}\,\mathrm{s}^{-1}$, significantly higher than predicted from the air pressure.

pressure below 10^{-6} Torr.

The source of this excess damping has not been tracked down in the work of this dissertation. The particle material, borosilicate, is impure and can contain materials such as iron. Eddy currents can be induced in the particle and cause loss. The interaction between the charged particle and charge on the pole pieces can also contribute. Charged particles on the pole pieces or patch charges on the pole pieces can move, transferring energy from the levitated particle. Another possible source of damping is energy transferring between different degrees of freedom, such as the center-of-mass motion coupling to rotation of the particle.

9.5 Conclusions

In this chapter, several important results have been reported. First, the main source of anharmoncity, due to Coulomb interactions, in the magneto-gravitation trap is discussed. The first observation made is when the particle's kinetic energy is not large enough to pass one of these potential barriers. In such cases, the particle bounces off of the barrier as if it is a hard wall instead of a harmonic potential. This can happen at one or both ends of the motion. A plot of oscillation frequency as a function of amplitude was presented. Strong amplitude dependence is clearly seen but behaves as expected. Large amplitudes will average the local anharmonicities due to the charged pole pieces.

For an amplitude of approximately 4 mm (almost half of the trap length), an oscillation frequency of 0.1 Hz has been measured. Though the motion is anharmonic, this is not just the target frequency for the measurement of G, it is also the lowest oscillation frequency measured in any levitated optomechanical system. The damping of the system is also discussed. For unknown reasons at this time, the damping is seven orders of magnitude larger than predicted by collisions between the particle and background gas.

A combination of the anharmoncities due to the charge on the pole pieces as well as the excess damping will cause errors too large for a 10 ppm measurement of G. The anharmonicity becomes less important when the particle's amplitude does not change significantly over the course of the measurement, where significantly is defined for a given anharmonicity. However, the damping in this system is large enough that the anharmonicity is a problem. Over the course of an hour, the motion almost damps completely to thermal equilibrium with its environment. As observed and reported in this chapter, this can lead to an order of magnitude difference in the frequency.

CHAPTER TEN

ACCELEROMETRY

10.1 Introduction

A precision measurement of the Newtonian constant of gravitation requires high-sensitivity acceleration and force sensing. We have seen that particles with diameters in the range of 53 μm to 63 μm have been successfully trapped consistently, with masses large enough for the initial measurements.

Oscillation frequencies down to 0.1 Hz have also been demonstrated, reaching the target frequency of the proposed experiment for measuring G. The damping rates of the levitated particle, however, have not been ideal with damping up to nearly seven orders of magnitude higher than what is predicted by collisions with background gas. Anharmonic motion has also been observed. With the short decay times, the anharmonicities become significant and a real problem for the precision measurement. Despite these issues, a high-sensitivity acceleration measurement can be performed.

In this chapter, a theoretical background for acceleration sensing using a levitated particle is laid out. The procedure that is followed to obtain the results in this chapter is explained in detail, including the synchronization the necessary equipment.

For this chapter, a 60 μm diameter borosilicate microsphere is loaded using the methods of chapter 5 and 6. Once the particle is loaded, the optical table is stabilized using the active stabilization described in chapter 8. The results of the stable DC voltage applied to the pole pieces as well as the table stabilization results are presented.

The self-calibration nature of the particle system is described. To test the

calibrations, the particle response to a 5 Hz drive (arbitrarily chosen) is compared to that of a commercial geophone. To eliminate any free parameters in the system, the transient response of the particle is measured with feedback cooling (see chapter 7). The oscillation frequency and damping rate is measured.

Unlike previous experiments [27, 92], accelerations measured by the levitated particle are directly compared to accelerations measured by the commercial geophone. During the measurements, the camera-based feedback cooling is implemented to reduce the damping time of transients.

A comprehensive noise analysis is performed for both the geophone and the particle system. An upper bound of the acceleration sensitivity is determined. An image analysis technique has been developed by Tyler D. Knowles at West Virginia University and is briefly described in this chapter. Our collaborators have also performed all of the image analysis for this experiment.

10.2 Previous Force and Acceleration Measurements

Typical accelerometers are based on clamped resonator systems [115–117]. With cryogenic temperatures, force sensitivities as low as $S_F^{1/2} \sim 10^{-21}\,\mathrm{N}/\sqrt{\mathrm{Hz}}$ are predicted [118]. Using a Si_3N_4 membrane [119], quality factors of 10^8 can be achieved at room temperature with oscillation frequencies of $\sim 150\,\mathrm{kHz}$, and thermal noise limited force sensitivities of $S_F^{1/2} \sim 10^{-17}\,\mathrm{N}/\sqrt{\mathrm{Hz}}$ are possible. Mechanical devices have the advantage of typically being extremely compact [120, 121]. Systems with very large test masses, such as LISA Pathfinder, can have acceleration sensitivities of $S_a^{1/2} \sim 10^{-16}\,g/\sqrt{\mathrm{Hz}}$ [122] ($g = 9.8\,\mathrm{m/s^2}$). Cold atom interferometry systems have also been proposed for measuring small changes in gravity [123–125] with acceleration sensitivities as low as $S_a^{1/2} \sim 10^{-9}\,g/\sqrt{\mathrm{Hz}}$ [126, 127].

Levitated systems avoid dissipation associated with the mechanical contact of

the resonator with its environment. Force sensitivities of $S_F^{1/2} \sim 10^{-16}\,\mathrm{N}/\sqrt{\mathrm{Hz}}$ and $S_F^{1/2} \sim 10^{-18}\,\mathrm{N}/\sqrt{\mathrm{Hz}}$ have been measured with particles in optical traps [31, 32]. Acceleration sensitivities of $S_a^{1/2} \sim 10^{-10}\,g/\sqrt{\mathrm{Hz}}$ [92] have been reported using a permanent magnet levitated above a superconductor at cryogenic temperatures.

Cooling the center-of-mass motion is important to acceleration measurements to allow the transients to die down in a practical amount of time without loss of sensitivity [128].

Magneto-gravitational traps have been developed [83, 86] and have exhibited stable trapping to a pressure of $\sim 10^{-10}\,\mathrm{Torr}$ with a feedback cooled center-of-mass motion from room temperature to $140\,\mu\mathrm{K}$ [85]. Recent cooling experiments in an optical trap have demonstrated a center-of-mass motion temperature of $50\,\mu\mathrm{K}$ for large particles ($\approx 10\,\mu\mathrm{m}$) [27]. Cooling to the quantum ground state of a sub-micrometer particle has also been shown, reaching a temperature of $12\,\mu\mathrm{K}$ from room temperature [129].

Though there are several issues that have not been solved in the work of this dissertation, high sensitivity accelerometry has been demonstrated. To the best of our knowledge, it is the first result of directly measuring accelerations with a levitated particle at room temperature. This is also the first system to make a measurement utilizing feedback cooling to allow the transients to die down in a practical amount of time without loss of sensitivity. Accelerations measured with a commercial geophone are compared the accelerations measured with the particle. The geophone model of the particle is developed as well as a comprehensive noise analysis of the geophone and particle.

10.3 Accelerometer Model

In order to understand the measured acceleration sensitivities, a model for the harmonic response of the particle as an accelerometer needs to be developed.

10.3.1 Measurements and Notations

The displacement of the particle in the axial direction relative to an inertial (laboratory) frame is z. Because the CMOS camera used in this experiment is rigidly held to the optical table, the displacement of the particle measured by the camera is not in an inertial reference frame. The displacement of the camera relative to the laboratory is z_0 and the displacement of the particle as recorded by the camera is then $z' = z - z_0$. It is assumed that the trap moves with the camera such that z' is also the motion of the particle relative to the trap.

Throughout this chapter, a capital letter is used to denote the result of a Fourier transform into the frequency domain.

10.3.2 Harmonic Oscillator Response

The displacement of the optical table in the laboratory frame, for example due to vibrations, can be written as an integral over all angular frequencies

$$z_0(t) = \int_{-\infty}^{\infty} d\omega' A_0(\omega') \sin(\omega' t + \phi(\omega')). \tag{10.1}$$

where A_0 is the amplitude of oscillation and is a real number corresponding to real valued accelerations.

10.3.2.1 Negative Frequencies Since z_0 represents a physical drive, $z_0 \colon \mathbb{R} \to \mathbb{R}$. Then if z_0 can be represented by an inverse Fourier transform of Z_0,

$$\begin{aligned} z_0(t) = z_0^*(t) &= \frac{1}{2\pi}\int_{-\infty}^{\infty} d\omega Z_0(\omega) e^{i\omega t} \\ &= \frac{1}{2\pi}\int_{-\infty}^{\infty} d\omega Z_0^*(\omega) e^{-i\omega t} \\ &= \frac{1}{2\pi}\int_{-\infty}^{\infty} d\omega Z_0^*(-\omega) e^{i\omega t}. \end{aligned} \tag{10.2}$$

Therefore, it follows that $Z_0(\omega) = Z_0^*(-\omega)$. We can then write z_0 as

$$\begin{aligned} z_0(t) &= \frac{1}{2\pi}\int_{-\infty}^{\infty} d\omega Z_0(\omega) e^{i\omega t} \\ &= \frac{1}{2\pi}\int_{-\infty}^{0} d\omega Z_0(\omega) e^{i\omega t} + \frac{1}{2\pi}\int_{0}^{\infty} d\omega Z_0(\omega) e^{i\omega t} \\ &= \frac{1}{2\pi}\int_{0}^{\infty} d\omega Z_0(-\omega) e^{-i\omega t} + \frac{1}{2\pi}\int_{0}^{\infty} d\omega Z_0(\omega) e^{i\omega t} \\ &= \frac{1}{2\pi}\int_{0}^{\infty} d\omega Z_0^*(\omega) e^{-i\omega t} + \frac{1}{2\pi}\int_{0}^{\infty} d\omega Z_0(\omega) e^{i\omega t} \\ &= \frac{1}{2\pi}\int_{0}^{\infty} d\omega (Z_0^*(\omega) e^{-i\omega t} + Z_0(\omega) e^{i\omega t}) \end{aligned} \tag{10.3}$$

It suffices to only consider the positive frequency spectrum.

Without loss of information, let us define an analytic signal z_{a0} such that the real position of the camera $z_0 = \mathrm{Re}\{z_{a0}\}$,

$$z_{a0} = z_0 + i\mathcal{H}\{z_0\}, \tag{10.4}$$

where $\mathcal{H}$ denotes the Hilbert transform. The Hilbert transformation of a function f is defined as the convolution of f with $1/(\pi t)$. Taking the Fourier transform of a

Hilbert transform,

$$\begin{aligned}\mathcal{F}\{\mathcal{H}\{f(t)\}\} &= \mathcal{F}\Big\{f(t) * \frac{1}{\pi t}\Big\} = \mathcal{F}\{f(t)\}\mathcal{F}\Big\{\frac{1}{\pi t}\Big\} \\ &= F(\omega)\mathcal{F}\Big\{\frac{1}{\pi t}\Big\}.\end{aligned} \tag{10.5}$$

It can be shown that the Fourier transform of $1/(\pi t)$ is $-i\,\mathrm{sgn}(\omega)$ where sgn is the sign function,

$$\mathrm{sgn}(\omega) = \begin{cases} -1, & \omega < 0 \\ 0, & \omega = 0 \\ 1, & \omega > 0. \end{cases} \tag{10.6}$$

It follows that

$$(\mathcal{F} \cdot \mathcal{H})f(t) = -i\,\mathrm{sgn}(\omega)F(\omega). \tag{10.7}$$

We can then split the analytic signal into two parts z_{a0+} and z_{a0-} corresponding to positive and negative frequencies, respectively. If we first take the Fourier transform of Eq. 10.4 for any analytic signal corresponding to any physical signal, then

$$\begin{aligned}Z_{z0}(\omega) &= Z_0(\omega) + \mathrm{sgn}(\omega)Z_0(\omega) = (1 + \mathrm{sgn}(\omega))Z_0(\omega) \\ &= \begin{cases} 0, & \omega < 0 \\ Z_0(\omega), & \omega = 0 \\ 2Z_0(\omega), & \omega > 0. \end{cases}\end{aligned} \tag{10.8}$$

By taking the Fourier transform of a real valued signal, we can integrate over positive frequency where the amplitude of the signal is doubled.

10.3.2.2 Newton's Law In the inertial reference frame that is the laboratory, we can write the equation of motion for the particle as

$$m\frac{d^2z(t)}{dt^2} = -c\frac{d}{dt}(z(t) - z_0(t)) - k(z(t) - z_0(t)) \tag{10.9}$$

where m is the mass of the particle, c is the damping coefficient, and k is the spring constant of the trap. Rearranging this and using dot notation and dropping the explicit time dependence, the equation of motion becomes

$$\ddot{z} + \Gamma\dot{z} + \omega_0^2 z = \Gamma\dot{z_0} + \omega_0^2 z_0 \tag{10.10}$$

where $\Gamma = c/m$ and $\omega_0 = \sqrt{k/m}$. z_0 is described by Eq. 10.1. For power spectral density (PSD) analysis in a linear system, we can consider $\phi = 0$ case since it only changes the response of the particle by a phase shift.

Substituting Eq. 10.1 into Eq. 10.10 and taking the time derivative, we get

$$\ddot{z} + \Gamma\dot{z} + \omega_0^2 z = \Gamma\int_{-\infty}^{\infty} d\omega' A_0(\omega')\omega'\cos(\omega' t) + \omega_0^2\int_{-\infty}^{\infty} d\omega' A_0(\omega')\sin(\omega' t). \tag{10.11}$$

In order to solve this differential equation for z, we can take the Fourier transform of both sides to convert it into an algebraic equation. A useful identity of Fourier transforms is

$$\mathcal{F}\left\{\frac{df}{dt}\right\} = i\omega f \tag{10.12}$$

The left hand side of Eq. 10.11 is

$$\mathcal{F}\{\text{l.h.s.}\} = (-\omega^2 + i\Gamma\omega + \omega_0^2)Z(\omega). \tag{10.13}$$

The Fourier transform of the right hand side of Eq. 10.11 is

$$\begin{aligned}\mathcal{F}\{\text{r.h.s.}\} = \Gamma \int_{-\infty}^{\infty} dt e^{-i\omega t} \int_{-\infty}^{\infty} d\omega' A_0(\omega')\omega' \cos(\omega' t) \\ + \omega_0^2 \int_{-\infty}^{\infty} dt e^{-i\omega t} \int_{-\infty}^{\infty} d\omega' A_0(\omega') \sin(\omega' t).\end{aligned} \tag{10.14}$$

After rearranging the integrals,

$$\begin{aligned}\mathcal{F}\{\text{r.h.s.}\} = \Gamma \int_{-\infty}^{\infty} d\omega' A_0(\omega')\omega' \int_{-\infty}^{\infty} dt \cos(\omega' t) e^{-i\omega t} \\ + \omega_0^2 \int_{-\infty}^{\infty} d\omega' A_0(\omega') \int_{-\infty}^{\infty} dt \sin(\omega' t) e^{-i\omega t}.\end{aligned} \tag{10.15}$$

We now have to compute the Fourier transforms of cos and sin, which can be done trivially to get

$$\begin{aligned}\mathcal{F}\{\text{r.h.s.}\} = \frac{\Gamma}{2} \int_{-\infty}^{\infty} d\omega' A_0(\omega')\omega' [\delta(\omega' - \omega) + \delta(\omega' + \omega)] \\ + \frac{\omega_0^2}{2i} \int_{-\infty}^{\infty} d\omega' A_0(\omega') [\delta(\omega' - \omega) - \delta(\omega' + \omega)].\end{aligned} \tag{10.16}$$

where δ is the Dirac delta function. As shown above, we can look at just the positive frequencies using the results above by $A_0 \to 2A_0$ since A_0 is real. Then the Fourier transform of the right hand side is

$$\begin{aligned}\mathcal{F}\{\text{r.h.s.}\} = \Gamma \int_{-\infty}^{\infty} d\omega' A_0(\omega')\omega' [\delta(\omega' - \omega) + \delta(\omega' + \omega)] \\ + \frac{\omega_0^2}{i} \int_{0}^{\infty} d\omega' A_0(\omega') [\delta(\omega' - \omega) - \delta(\omega' + \omega)].\end{aligned} \tag{10.17}$$

Since we are not integrating over negative frequencies, the second term in each integral is zero. Evaluating what is left,

$$\mathcal{F}\{\text{r.h.s.}\} = \Gamma\omega A_0(\omega) - i\omega_0^2 A_0(\omega) = (\Gamma\omega - i\omega_0^2) A_0(\omega). \tag{10.18}$$

Putting everything together, we get that the Fourier transform of Eq. 10.11 is

$$(-\omega^2 + i\Gamma\omega + \omega_0^2)Z(\omega) = (\Gamma\omega - i\omega_0^2)A_0(\omega). \tag{10.19}$$

The particle's response relative to the laboratory as a function of the amplitude of the drive at a given frequency is then

$$Z(\omega) = \left(\frac{\Gamma\omega - i\omega_0^2}{\omega_0^2 - \omega^2 + i\Gamma\omega}\right)A_0(\omega). \tag{10.20}$$

In order to find the particle's response relative to the camera, z', which is the data that is directly measured, we need to subtract z_0 from z. Then taking the Fourier transform,

$$\mathcal{F}\{z'\} = \mathcal{F}\{z - z_0\} = \mathcal{F}\{z\} - \mathcal{F}\{z_0\}. \tag{10.21}$$

We only have the Fourier transform of z_0 left to calculate.

$$\mathcal{F}\{z_0\} = \int_{-\infty}^{\infty} dt e^{-i\omega t} \int_{-\infty}^{\infty} d\omega' A_0(\omega') \sin(\omega' t) \tag{10.22}$$

Similarly to above, we find that

$$\mathcal{F}\{z_0\} = -iA_0(\omega). \tag{10.23}$$

Therefore,

$$Z'(\omega) = \left(\frac{\Gamma\omega - i\omega_0^2}{\omega_0^2 - \omega^2 + i\Gamma\omega} + i\right)A_0(\omega). \tag{10.24}$$

This can be simplified to

$$Z'(\omega) = \left(\frac{-i\omega^2}{\omega_0^2 - \omega^2 + i\Gamma\omega}\right)A_0(\omega). \tag{10.25}$$

We can find the amplitude of Z' to be

$$|Z'(\omega)| = \left\{ \left(\frac{-i\omega^2}{\omega_0^2 - \omega^2 + i\Gamma\omega} \right) \left(\frac{i\omega^2}{\omega_0^2 - \omega^2 - i\Gamma\omega} \right) \right\}^{1/2} |A_0(\omega)|, \tag{10.26}$$

or more conveniently,

$$\frac{|Z'(\omega)|}{|A_0(\omega)|} = |H(\omega)| = \frac{\omega^2}{((\omega_0^2 - \omega^2)^2 + \Gamma^2\omega^2)^{1/2}}. \tag{10.27}$$

This is the harmonic oscillator response of the particle acting as a geophone per unit amplitude of the external drive acting on the system.

10.4 Damped Harmonic Oscillator

In order for there to be no free parameters in the system, the decay, or damping, rate and the resonant frequency need to be measured. To determine these parameters, a simple model of a damped, undriven harmonic oscillator needs to be developed.

Consider a damping force proportional to the velocity $F_d = -c\dot{z}$. The equation of motion for the driven damped harmonic oscillator in the axial direction subject to an external time-dependent force F is

$$\ddot{z} + \Gamma\dot{z} + \omega_0^2 z = \frac{F(t)}{m} \tag{10.28}$$

where $\Gamma = c/m$ is the decay rate, $\omega_0 = \sqrt{k/m}$ is the resonant angular frequency, and m is the mass of the oscillator. We will consider the underdamped regime, $\Gamma^2 < 4\omega^2$.

To measure the necessary parameters, will also consider the decay of the oscillator after a small transient and no external driving force. The equation of motion is simply

$$\ddot{z} + \Gamma\dot{z} + \omega_0^2 z = 0. \tag{10.29}$$

The solution is well known to be

$$z(t) = z_0 \sin(\omega' t + \phi) e^{-\frac{\Gamma}{2}t} \tag{10.30}$$

where $\omega' = \sqrt{\omega_0^2 - \Gamma^2/4}$. To find the resonant angular frequency and damping rate, we will fit the time domain data of the undriven transient response to Eq. 10.30.

10.5 Damped-Driven Harmonic Oscillator

Consider the underdamped harmonic oscillator subject to random force f, such as thermal motion. The equation of motion is

$$\ddot{z} + \Gamma \dot{z} + \omega_0^2 z = \frac{f(t)}{m}. \tag{10.31}$$

For thermal fluctuations, two properties must hold:

$$\begin{cases} \langle f(t) \rangle = 0 \\ \langle f(t) f(t+\tau) \rangle = A\delta(\tau) \end{cases} \tag{10.32}$$

The average value of the random force f is zero and the auto-correlation function of f is a delta function with strength A. Using the identity of Fourier transforms, Eq. 10.12, the Fourier transform of Eq. 10.31 is

$$(-\omega^2 + i\Gamma\omega + \omega_0^2) Z(\omega) = \frac{F(\omega)}{m} \tag{10.33}$$

where Z and F are the Fourier transforms of z and f, respectively. Solving for Z,

$$Z(\omega) = \frac{F(\omega)}{m} \frac{1}{\omega_0^2 - \omega^2 + i\Gamma\omega}. \tag{10.34}$$

We can consider the ensemble average of the Fourier domain random force F squared over an integration time of $t_{\rm int}$,

$$\begin{aligned}\left\langle |F(\omega)|^2 \right\rangle &= \left\langle \int_{-t_{\rm int}/2}^{t_{\rm int}/2} F(\omega) e^{i\omega t} dt \int_{-t_{\rm int}/2}^{t_{\rm int}/2} F^*(\omega) e^{-i\omega t} dt' \right\rangle \\ &= \left\langle \int_{-t_{\rm int}/2}^{t_{\rm int}/2} \int_{-t_{\rm int}/2}^{t_{\rm int}/2} F(\omega) F^*(\omega) e^{i\omega(t-t')} dt dt' \right\rangle \\ &= \int_{-t_{\rm int}/2}^{t_{\rm int}/2} \int_{-t_{\rm int}/2}^{t_{\rm int}/2} \left\langle F(\omega) F^*(\omega) \right\rangle e^{i\omega(t-t')} dt dt'\end{aligned} \tag{10.35}$$

Using Eq. 10.32,

$$\begin{aligned}\left\langle |F(\omega)|^2 \right\rangle &= \int_{-t_{\rm int}/2}^{t_{\rm int}/2} \int_{-t_{\rm int}/2}^{t_{\rm int}/2} A\delta(t-t') e^{i\omega(t-t')} dt dt' \\ &= A \int_{-t_{\rm int}/2}^{t_{\rm int}/2} dt \\ &= A t_{\rm int}.\end{aligned} \tag{10.36}$$

The single sided displacement power spectral density (PSD) is given by

$$S(\omega) = \frac{2|Z(\omega)|^2}{t_{\rm int}}. \tag{10.37}$$

Taking the ensemble average of the displacement PSD,

$$\begin{aligned}\left\langle S(\omega) \right\rangle &= \frac{2\left\langle |F(\omega)|^2 \right\rangle}{t_{\rm int} m^2} \left[\frac{1}{(\omega_0^2 - \omega^2)^2 + \Gamma^2 \omega^2} \right] \\ &= \frac{2A}{m^2} \left[\frac{1}{(\omega_0^2 - \omega^2)^2 + \Gamma^2 \omega^2} \right].\end{aligned} \tag{10.38}$$

When the harmonic oscillator is in thermal equilibrium with its environment at

temperature T, the equipartition theorem says there is energy $\frac{1}{2}k_BT$ for every degree of freedom, where k_B is Boltzmann's constant. After a long enough time,

$$\frac{1}{2}m\omega_0^2\left\langle z(t)^2\right\rangle = \frac{1}{2}k_BT. \tag{10.39}$$

The time average is

$$\left\langle z(t)^2\right\rangle = \lim_{t_{\text{int}}\to\infty}\int_{-t_{\text{int}}/2}^{t_{\text{int}}/2}|z(t)|^2dt. \tag{10.40}$$

By Parseval's theorem [130],

$$\int_{-\infty}^{\infty}|z(t)|^2dt = \frac{1}{2\pi}\int_{-\infty}^{\infty}|Z(\omega)|^2d\omega. \tag{10.41}$$

The integral over positive frequencies of the ensemble average of the displacement PSD is

$$\begin{aligned}\int_0^\infty\langle S(\omega)\rangle\,d\omega &= \int_0^\infty\frac{2A}{m^2}\left[\frac{1}{(\omega_0^2-\omega^2)^2+\Gamma^2\omega^2}\right]d\omega\\ &= \lim_{t_{\text{int}}\to\infty}\frac{2}{t_{\text{int}}}\int_0^\infty|Z(\omega)|^2d\omega\\ &= \lim_{t_{\text{int}}\to\infty}\frac{1}{t_{\text{int}}}\int_{-\infty}^\infty|Z(\omega)|^2d\omega\\ &= \lim_{t_{\text{int}}\to\infty}\frac{2\pi}{t_{\text{int}}}\int_{-\infty}^\infty|z(t)|^2dt\\ &= 2\pi\left\langle z(t)^2\right\rangle.\end{aligned} \tag{10.42}$$

From Eq. 10.39,

$$\left\langle z(t)^2\right\rangle = \frac{k_BT}{m\omega_0^2}. \tag{10.43}$$

Therefore,

$$\int_{-\infty}^\infty\frac{A}{m^2}\left[\frac{1}{(\omega_0^2-\omega^2)^2+\Gamma^2\omega^2}\right]d\omega = \frac{2\pi k_BT}{m\omega_0^2}. \tag{10.44}$$

To simplify this,

$$A\int_{-\infty}^{\infty}\left[\frac{1}{(\omega_0^2-\omega^2)^2+\Gamma^2\omega^2}\right]d\omega=\frac{2\pi mk_BT}{\omega_0^2}. \tag{10.45}$$

Evaluating the integral,

$$\frac{A\pi}{\Gamma\omega_0^2}=\frac{2\pi mk_BT}{\omega_0^2}. \tag{10.46}$$

Solving for A yields

$$A=2mk_B\Gamma T. \tag{10.47}$$

We can substitute this into the ensemble average displacement PSD to get

$$\langle S(\omega)\rangle=\frac{4k_B\Gamma T}{m}\left[\frac{1}{(\omega_0^2-\omega^2)^2+\Gamma^2\omega^2}\right]. \tag{10.48}$$

10.6 Discrete Fourier Transform

Since the real data is finite and sampled at discrete times, to obtain frequency information, the discrete Fourier transform (DFT) needs to be used. Consider the DFT Parseval's theorem,

$$\sum_{n=0}^{N-1}|z[n]|^2=\frac{1}{N}\sum_{k=0}^{N-1}|Z[k]|^2 \tag{10.49}$$

where z is the time domain data, Z is the frequency domain data determined from the DFT of z, and N is the total number of sampled points. The variance in z, if the mean of z is zero, is defined to be

$$\left\langle z^2\right\rangle=\frac{1}{N}\sum_{n=0}^{N-1}|z[n]|^2. \tag{10.50}$$

Combining Eq. 10.49 with Eq. 10.50, we find that

$$\left\langle z^2 \right\rangle = \frac{1}{N^2} \sum_{k=0}^{N-1} |Z[k]|^2. \tag{10.51}$$

The frequency spacing is $\Delta f = (1/N)\Delta t$ for a time spacing of Δt. We can rewrite Eq. 10.51 as

$$\begin{aligned} \left\langle z^2 \right\rangle &= \frac{1}{N^2 \Delta f} \sum_{k=0}^{N-1} |Z[k]|^2 \Delta f \\ &= \frac{\Delta t}{N} \sum_{k=0}^{N-1} |Z[k]|^2 \Delta f \\ &= \sum_{k=0}^{N-1} \frac{\Delta t |Z[k]|^2}{N} \Delta f \\ &= \sum_{k=0}^{N-1} S[k] \Delta f \end{aligned} \tag{10.52}$$

where S is the double-sided PSD, according the continuous analog, Eq. 10.42. To compute the single-sided PSD, $S \to 2S$, so

$$S[k] = \frac{2\Delta t}{N} |Z[k]|^2. \tag{10.53}$$

In the Python library numpy, the discrete Fourier transformed is defined to be

$$Z[k] = \sum_{n=0}^{N-1} z[n] e^{-2\pi i \frac{nk}{N}}. \tag{10.54}$$

In order to normalize properly to obtain the correct units for a PSD, the result of the FFT algorithm magnitude squared needs to be multiplied by $2\Delta t/N$.

10.7 Results

10.7.1 Notes

It is important to make note of the notation used in this dissertation, especially in this chapter. The angular frequency is related to the frequency of the oscillator by $\omega = 2\pi f$. We can define an equivalent damping rate γ as $\Gamma = 2\pi\gamma$. With proper substitutions, Eq. 10.27 becomes

$$\frac{|\bar{Z}'(f)|}{|\bar{A}_0(f)|} = \frac{f^2}{((f_0^2 - f^2)^2 + \gamma^2 f^2)^{1/2}}. \tag{10.55}$$

where the bars indicate the change of variables. The solution to the equation of motion given by Eq. 10.29 and Eq. 10.30 is

$$\bar{z}(t) = \bar{z}_0 \sin(2\pi f t + \phi) e^{-\gamma\pi t}. \tag{10.56}$$

10.7.2 Procedure

Before a particle is loaded, the active table stabilization is started. Any time that the optical table is disturbed, for example, leaning on it or moving equipment, it is allowed to settle down. It is important that the table is stabilized when a particle is loaded, because as we have seen in chapter 8, the equilibrium position can shift dramatically with tilt. The tilt data is measured on Keithley 2000 digital multimeters and read on a computer via GPIB and saved. In the PI controller algorithm (algorithm 8.2), P was set to 0.05 and I was set to 0.00025.

The geophone procured and used in the work for this dissertation is a Sercel, Inc. L-4C 3D (shown in Fig. 10.1). The geophone is placed on the optical table before a particle is loaded. The geophone is leveled to the table using the three feet. The geophone is level when the bubble on the bull's eye spirit level is centered, indicated

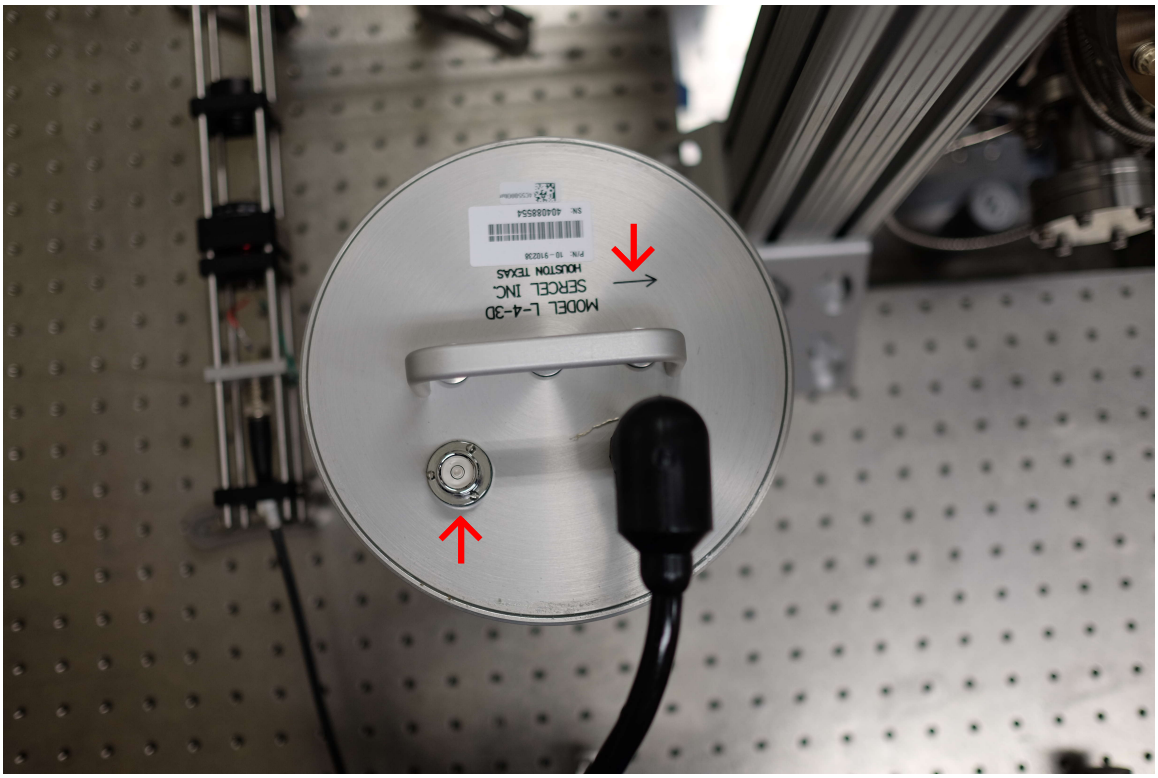


Figure 10.1: A photograph of the Sercel, Inc. L-4C 3D geophone. The left red arrow indicates the spirit level and the right arrow indicates one of the geophone axes.

by the red arrow in Fig. 10.1. The geophone outputs are connected to Stanford Research Systems (SRS) SR640 low-pass filters, each set to no gain with the cutoff frequency at 1 kHz. The output of the low-pass filters go into a custom Arduino Due shield (analog-to-digital converter board [94]). The vibration data can then be read on a computer and saved. The second red arrow indicates one axis of oscillation of one geophone mass.

A surface transducer (speaker) is attached to the table, oriented to shake along the axial direction of the trap. A 0.1875 kg ductile iron mass attached to the surface transducer for added mass. This speaker is used to test the calibration of the particle and geophone. A Stanford Research Systems DS345 Synthesized Function Generator drives the speaker after being amplified by an Electronic Measurements

BOSS amplifier. The current limit is set to 1 A on the amplifier to prevent the speaker from being destroyed. When the speaker is being operated, the DS345 output voltage is set to 0.5 V.

The illumination during the loading process is from a 660 nm LED that is run continuously. The tilt stage that the chamber sits on is tilted so that the axial equilibrium position of the particle is shifted to the edge of the trap closest the loading port. Because of the limited field of view of the collection objective, this insures the easiest location of the particle once loaded (without scanning across the entire trap).

The data presented here was acquired with a 60 μm borosilicate microsphere (Co-spheric BSGMS-2.2 53-63um-10g). During the loading process, the Paul trap's AC voltage was set to 450 V with a frequency of 300 Hz. The particle is loaded into the trapping region using the ultrasonic horn, driven with a voltage of 5 V. To center the particle in the trap, a DC voltage of −37.2313 V was used. Once the particle was centered properly, the AC voltage was slowly turned down, being careful to keep the particle centered vertically by adjusting the DC voltage. When the Paul trap is completely off, the tilt stage is tilted to shift the equilibrium position particle to the center of the trap in the axial direction.

Once the particle is centered axially in the trap, the vacuum chamber was closed by adding a blank flange on the loading port. Once the chamber is properly sealed, the valve to the pump cart (V2 in Fig. 3.17) was opened completely. Valve V3 (Fig. 3.19) is kept opened during all steps of the experiment. Valves V4 and V5 (Fig. 3.19 and 3.20) are initally closed. With this setup, the roughing pump was turned on. As the roughing pump quickly spins, the particle gets excited in the axial direction but quickly damps.

With the roughing pump on, the needle valve (V4) is carefully opened. On the

valve knob, a 3/8 inch wrench is used to provide more torque while being gentle. While opening the valve, the Pirani gauge (P1) is carefully monitored. The valve is opened until the air pressure read drops by approximately 1 Torr to 3 Torr per second. If the pressure drops by less than this, the valve is opened more to speed up the pumping again. This process is repeated until the V4 valve is completely opened.

Once valve V4 is opened, the pressure is allowed to drop to below 0.1 Torr on both Pirani gauges (P1 and P2). At this point, valve V5 is carefully opened completely, but slowly. Valve V5 allows the roughing pump to keep the backing pressure of the turbomolecular (turbo) pump below its maximum specification. The system is left pumping with just the roughing pump for several minutes. The turbo pump is then turned on. The turbo pump is monitored on its controller. The turbo spun up completely in only a couple minutes and the load indication goes to a minimum a few moments later (on the order of a minute), indicating no significant leak. Once the turbo pump is on and pumping at full speed, the table is not touched until the tilt is stabilized once again.

Once the table is stabilized, the illumination system is swapped from the continuous 660 nm LED to the pulsed 660 nm system. The repetition rate, controlled from a Stanford Research Systems DG645 Digital Delay Generator, for the camera and LED is set to 100 Hz. Imaging the LED illuminated slit onto the particle creates illumination that appears as a wide illuminated strip on the CMOS camera. The pulse time for the LED is chosen to be 1 ms, the value that maximizes the brightness on the CMOS without saturating it. The exposure time of the camera is chosen to be 2 ms, longer than the LED pulse but short enough that stray and background light is minimized. It is important that the utmost care is taken while switching LED configurations to prevent the particle from drifting or being knocked out of the trap. When the pulsed LED is in place, the 520 nm control laser is aligned to hit the

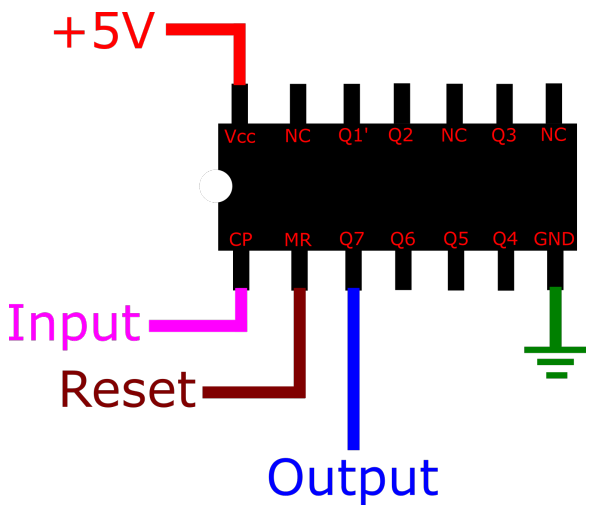


Figure 10.2: A connection diagram for the 7-bit divider.

particle. The dark disk becomes illuminated when the laser is properly aligned. After it is aligned, the long-pass filter is attached to the objective to block the 520 nm laser.

The DG645 controls the camera frame rate, LED pulse width, exposure time of the camera, the triggering of the Keithley 2000s, and a start trigger to the Arduino Due that reads the geophone. The Keithley 2000s are triggered externally, after going through a 7-bit divider (Texas Instruments CD74HC4024E) (connection diagram shown in Fig. 10.2). With a repetition rate of 100 Hz, this triggers the digital multimeters 46 times a minute. The DG645 also sends pulses to the Arduino Due that controls the geophone output. The data that is read from the Arduino Due starts before the camera's first image. The first pulse that the Arduino Due reads indicates the time when the first image is acquired. The data before that is thrown away. Typically, one half of the DG645 pulse peak is used as the threshold for determining the first data point. A flow diagram showing the connections between the equipment used is shown in Fig. 10.3.

When the pressure on the ion gauge (IG1 in Fig. 3.19) reads in the low 10^{-7} Torr range, the V1 valve (Fig. 3.17) is carefully opened. As this is opened, it is likely

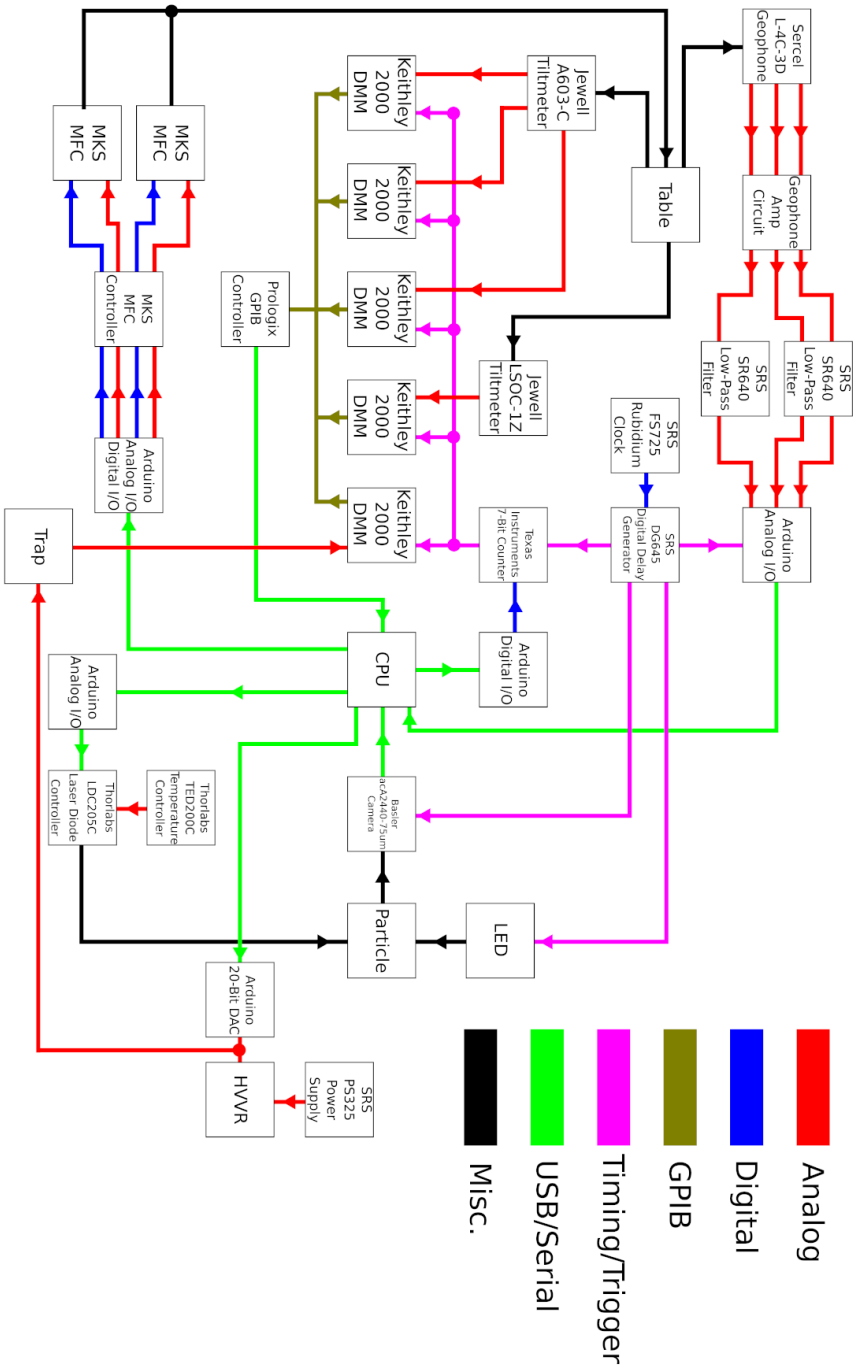


Figure 10.3: A flow diagram showing how the accelerometry experiment was controlled and the connections between the equipment used.

that the chamber is torqued in a way that will shift the equilibrium position of the particle. In theory, the particle would return to its original location, but as described in chapter 9, charged contamination on the pole pieces can prevent the particle from moving. If the particle moves, either the optics need to be readjusted to get back onto the particle, or the particle needs to be moved back. The particle for this experiment sat in a location axially between two charged particles that failed to get trapped and are on the pole pieces. The valve V2 is then closed and the turbo and roughing pump are turned off.

When valve V1 is opened and V2 is closed, the chamber is now solely being pumped by the ion pump. At this point, the pressure in the chamber, read off of the ion pump controller, stayed in the low to mid 10^{-7} Torr (1.0×10^{-7} Torr to 5.0×10^{-7} Torr).

10.7.3 Feedback Cooling

With feedback cooling implemented, ΓT can at best be constant, where Γ is the damping rate and T is the temperature associated with the center-of-mass motion. In order to prevent transients from being damped naturally, possibly taking a significant amount of time, feedback cooling can be implemented without compromising sensitivity significantly [128]. We can then place an upper bound on temperature,

$$\Gamma_N T_N \leq \Gamma_{fb} T_{fb} \tag{10.57}$$

where N demotes the natural damping and ambient temperature and fb denotes the feedback cooled damping and temperature. To determined the cooled temperature by assuming a negligible loss in sensitivity,

$$T_{fb} = \frac{\Gamma_N}{\Gamma_{fb}} T_N. \tag{10.58}$$

The cooling results are discussed in the noise analysis section.

10.7.4 Offline Image Analysis

The image analysis in this section was developed and performed by Tyler D. Knowles and Dr. Zachariah Etienne at West Virginia University.

A resolution of 1 pixel, which is easy to accomplish on the CMOS camera, would result in a resolution of approximately 1 μm (see below for calibration). Alternatively, the images can be analyzed using sophisticated image analysis techniques to achieve sub-pixel resolution. The measured displacement in each frame is measured against one reference frame, initially arbitrarily chosen in our case to be the first frame. All of the pixel data in each frame is used to provide sub-pixel resolution. Though the image analysis for feedback needs to be done in real time, post-processing of the images for precise displacement measurements can be much more computationally intensive.

As an initial attempt to determine the displacement of the particle, the data in the first frame was cross-correlated against the first frame of the data using the `register_translation()` available in the `scikit-image` Python package [131, 132]. This choice of reference frame seemingly worked well, but closer analysis showed discontinuities in the data [113]. This problem is attributed to noise in the reference frame.

Since the choice of reference frame was arbitrary, it is suspected that any other choice of frame will result in similar discontinuities. A new approach was developed to largely eliminate this noise, which we name the "eigenframe" approach. This method is attributed to Tyler D. Knowles of West Virginia University, Department of Mathematics. In this naming scheme, the original reference is labeled the zeroth eigenframe. The method proceeds as followed: compute the axial and vertical translation of each frame against the zeroth eigenframe in the spatial domain. Each

frame is lined up to their inferred displacements with respect to the zeroth eigenframe and create a globally average frame, called the first eigenframe.

To prevent loss of information due to the discrete pixels in the spatial domain, the translations and averaging are performed in the Fourier domain (k-space). This averaging smooths out the noise leading to a reduction in the discontinuities in the translations. The translation values can be refined by correlating each frame against a translation of the first eigenframe to the inferred particle location. These translations can then be used to make a second and refined eigenframe. The data is then cross-correlated to the n^{th} eigenframe. This method can be used for as many iterations as required. For the data presented here, the fifth eigenframe was used. The difference between the fifth eigenframe and fourth eigenframe was found to be less than 1 nm for all times, less than the noise of the system. The results are discussed in Lewandowski, et al [113].

10.7.5 Geophone

As listed on the specification sheet for the geophone that was purchased, the resonant frequency is $\omega_0/2\pi = 0.97\,\text{Hz}$. The damping is specified as a fraction (0.271) of the critical damping rate. According to Eq. 10.29, critical damping occurs when $\Gamma_c^2 = 4\omega_0^2$. Since the frequency (and damping rate) is positive, this is equivalent to $\Gamma_c = 2\omega_0$. The damping is then $\Gamma = 0.271\Gamma_c = 0.542\omega_0$. The resistance of the geophone coil is also given in the data sheet as $R_c = 5546\,\Omega$. The mass of the oscillator is given as 0.957 kg.

To finish the calibration, the gain of the amplification circuit needs to be determined. The circuit is modeled after that in [133]. In order to so, a Tektronix AFG1022 function generator was set to output a sine wave arbitrarily at 60 Hz with an amplitude a peak-to-peak voltage of 0.01 V. In hindsight, a more appropriate

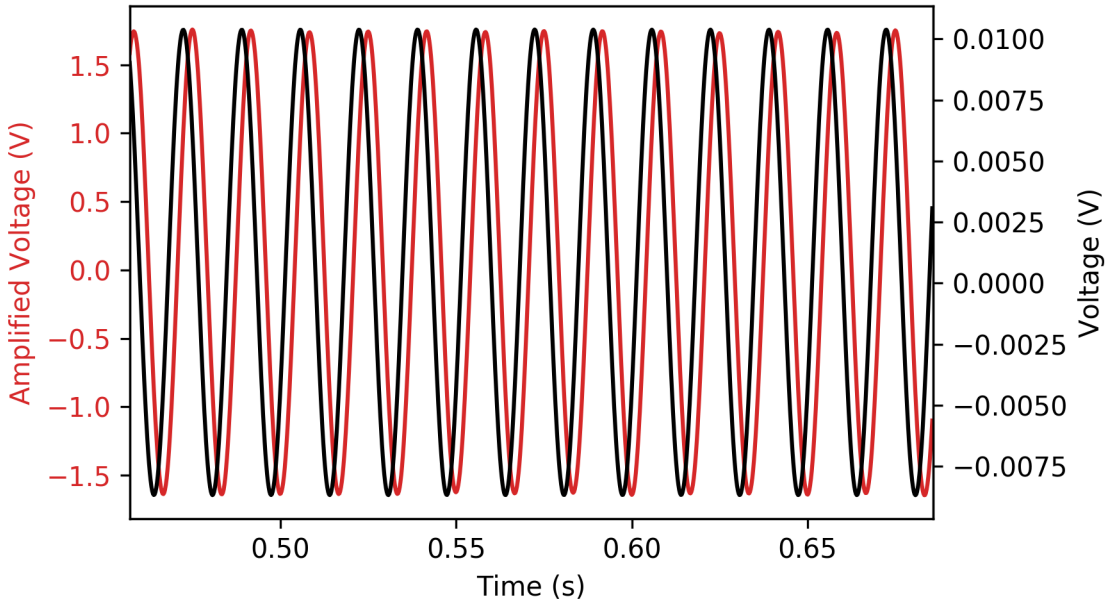


Figure 10.4: The calibration of the geophone and its amplification circuit sensitivity. The ratio of the amplified voltage and the unamplified voltage is $S_g = 180.2$.

frequency would have been 5 Hz. The output was connected to the amplification circuit, and is shown in Fig. 10.4 as the red curve. The amplification circuit was also bypassed with the same frequency but a peak-to-peak voltage of 1 V was used to increase the signal-to-noise ratio. The output recorded was then divided by 100 to match the amplified data (since the amplified data used a peak-to-peak voltage that was 100 times smaller). The reduced output is shown in Fig. 10.4 as the black curve. The gain is then determined to be $G_g = 180.2$.

10.7.6 Transient Result

The levitated microsphere in the magneto-gravitational trap has the unique feature of being self-calibrating. The only calibration required is to convert the pixels of the CMOS camera to units of position (e.g. μm). This calibration was done by imaging a USAF1951 calibration target (Edmund Optics #58-198) through



Figure 10.5: The USAF1951 calibration target imaged onto the CMOS from the collection optics of the system. The group 5 element 1 line is 15.63 µm across approximately 13.6 pixels.

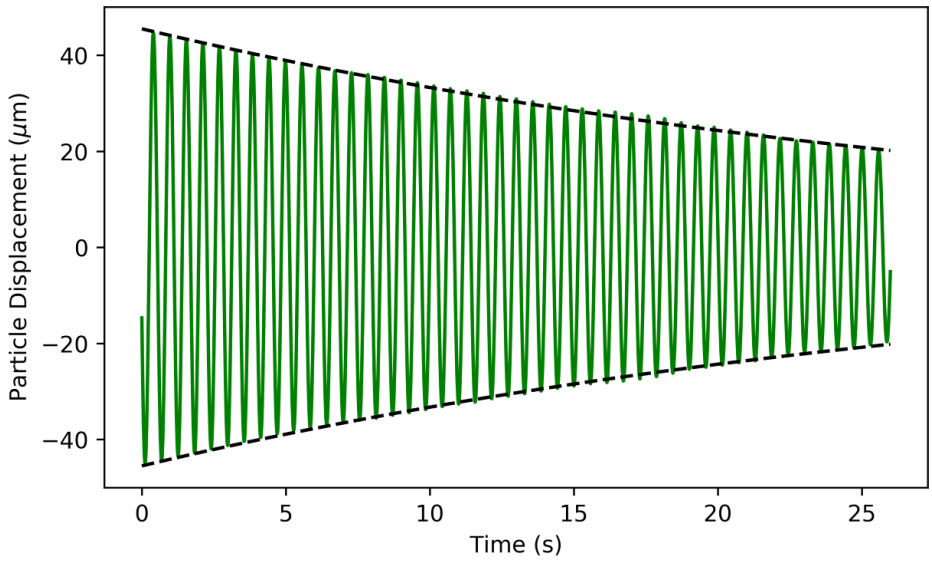


Figure 10.6: Transient motion of the magneto-gravitationally levitated microsphere after an excitation with feedback cooling applied. The oscillation frequency is $\omega_z/(2\pi) = 1.75\,\mathrm{Hz}$ with a damping rate of $\Gamma = 6.26 \times 10^{-2}\,\mathrm{s}^{-1}$, illustrated by the black dashed lines.

the optics of the system. The group 5 element 1 was used for the calibration. This line is 15.63 μm spanning 13.6 pixels, measured using the software GIMP. This conversion is then found to be 1.15 μm/pixel. The digital delay generator (Stanford Research Systems DG645) is tied to a rubidium frequency standard (Stanford Research Systems FS725), providing the frequency calibration.

Once the system is calibrated, all free parameters of the system can be eliminated. For the harmonic oscillator response, the resonant frequency and the damping rate of the particle needs to be measured. In theory, a fit can be made to determine these two parameters but they are easy enough to measure. With the cooling laser to provide radiation pressure to cool the motion of the particle (with a gain of 0.5), the particle was excited via a small tap on the side of the optical table. The measurement was repeated five times, only saving the data when the tap on the table did not tilt the table by more than 1.35 μrad. Out of the five data sets, the last one was chosen to extracting the necessary parameters.

The fifth data set was used because over time the cooling optics may drift. Since the fifth and last measurement was the closest to the accelerometry data in time, this data was chosen. A subset of the transient response data is shown in Fig. 10.6. Only a subset was chosen so that vibrational noise is negligible (it is not negligible at small amplitudes) as well as long enough after the transient for the table to equilibrate from the tap.

The green curve in Fig. 10.6 shows approximately 26 s of the axial motion after the transient on the table. Fitting to an exponential decaying sine wave, the resonant frequency was found to be $\omega_0/2\pi = 1.75\,\mathrm{Hz}$ with a decay rate of associated with the feedback is $\Gamma_{fb}/2\pi = 9.96 \times 10^{-3}\,\mathrm{Hz}$. These two parameters are used for all harmonic oscillator response calculations for the particle.

This frequency is much higher than the typical frequency measured or observed

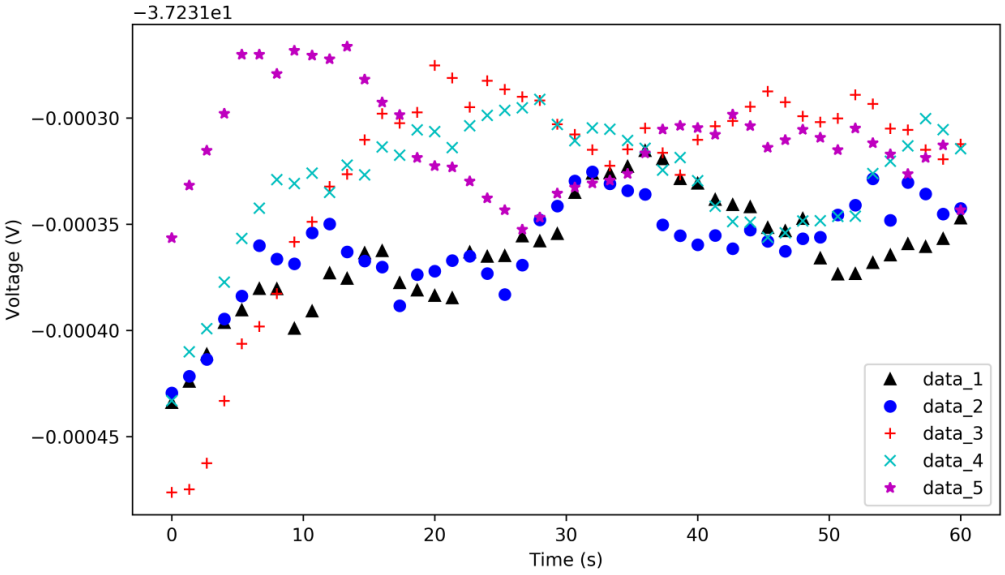


Figure 10.7: The DC voltage across the top and bottom pole pieces during the five measurements with a 5 Hz drive on the table.

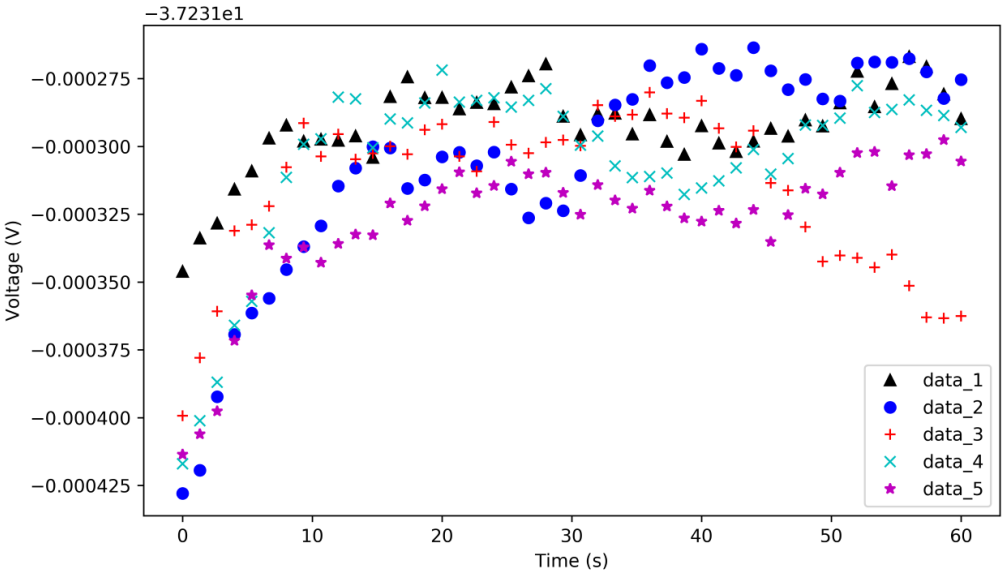


Figure 10.8: The DC voltage across the top and bottom pole pieces during the five measurements with no drive on the optical table. The initial anomaly is more evident than in the 5 Hz data.

in this magneto-gravitational trap. When the chamber was susceptible to a large torque during the ion pump opening process, the particle moved significantly in the trap. It came to rest between two repulsive charges unseen by the camera. This location prevented the particle from experiencing large drifts during the rest of the opening process. However, the oscillation frequency is higher than normal. Low frequencies were traded for ease of experimental manipulation of the chamber.

10.7.7 DC Voltage Stabilization Results

The DC voltage across the top and bottom pole pieces was monitored throughout the five measurements with the 5 Hz drive and the five measurements with no drive on the optical table. The voltage was measured on a Keithley 2000 digital multimeter and read on a computer via GPIB. The results for the 5 Hz drive voltage are shown in Fig. 10.7 and the other are shown in Fig. 10.8. The average value during all ten measurements to the precision of the digital multimeter is -37.2313 V. The measured RMS fluctuations for all of the measurements are on the order of 10^{-5} V, well under the digital multimeter precision. This results in the voltage being stable to within 3 ppm for all ten measurements.

It is important to note that all ten data sets have the same characteristic increase at the beginning of the acquisition. In all cases, it lasts approximately 15 s. After this time, the voltage settles to an approximately constant value. This is believed to be caused by the Keithley 2000 multimeter requiring this time to stabilize. Despite this, however, the voltage was stable to within the precision of the multimeter.

10.7.8 Table Stabilization Results

To insure that equilibrium drifts due to tilts of the optical table are not significant, the relative tilt of the optical was monitored during all of the measurements presented here, using the methods described in chapter 8 and above. The outputs

of the Jewell Instruments A603-C tiltmeter were read on Keithley 2000 digital multimeters and read on a computer via GPIB. The results for the tilt during the 5 Hz drive measurements are shown in Fig. 10.9 and the results for the tilt during the measurements with no drive are shown in Fig. 10.10.

Data 1 of the 5 Hz drive measurement has a total tilt range, from minimum to maximum, of 0.84 μrad. Data 2 has a total tilt range of 1.15 μrad. The total tilt range of data 3 is 0.78 μrad. Data 4 has the worst total tilt range, 1.25 μrad, and data 5 has the best at 0.69 μrad. By considering the absolute maximum value of the tilt from all five data sets as well as the minimum, the total difference is 1.4 μrad, within ±0.75 μrad. The average relative tilt of all five data sets is 0.02 μrad with an RMS fluctuation of 0.35 μrad.

The five data sets corresponding to the measurements with no drive are slightly worse, but still not significant. The total tilt range of data 1 is 0.74 μrad. Data 2 has a total tilt range of 1.27 μrad and data 3 is 1.54 μrad. Data 4 is the best of the data sets with 0.53 μrad total tilt range. Data 5 has the same as data 3 with 1.54 μrad. The maximum of the five data sets minus the minimum of the five data sets is 1.76 μrad. The average value of all five data sets is −0.01 μrad with an RMS fluctuation of 0.42 μrad.

With the oscillation frequency measured by the transient response of the particle, 1.75 Hz, we can calculate the equilibrium shift for a given tilt by Eq. 8.2, rewritten here for convenience,

$$\Delta z = \frac{g}{\omega_z^2}\Delta\theta. \tag{10.59}$$

For the 5 Hz measurements, using the total absolute tilt difference of 1.4 μrad, we find an equilibrium shift of 110 nm. Using the RMS value, 0.35 μrad, we find a shift of 28 nm, significantly less than the diameter of the particle. For the measurements

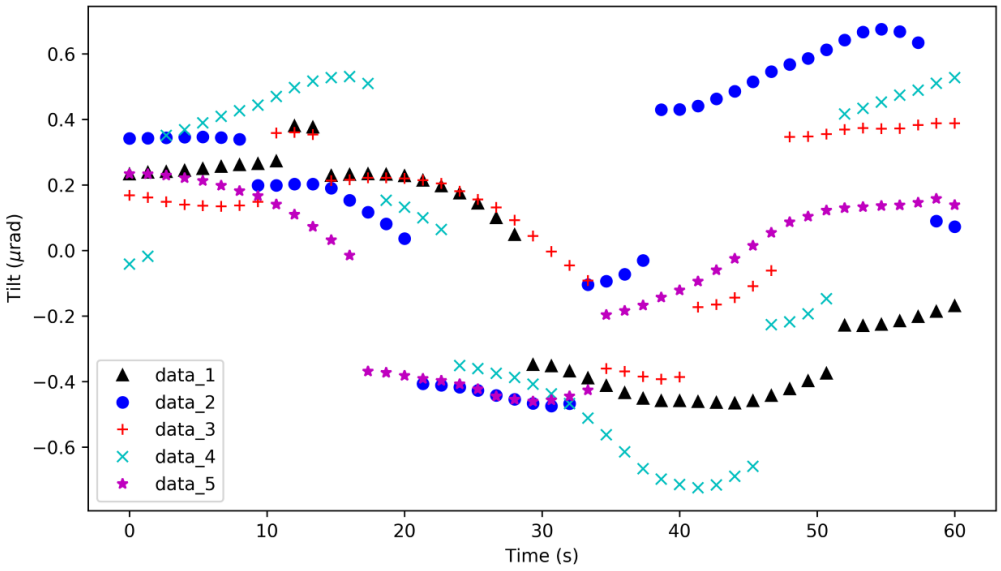


Figure 10.9: The measured tilt during the five measurements with a 5 Hz drive acting on the table. All measured tilts are within ±0.75 μrad about its average value. The RMS tilt for all five is 0.35 μrad corresponding to an equilibrium shift of 28 nm.

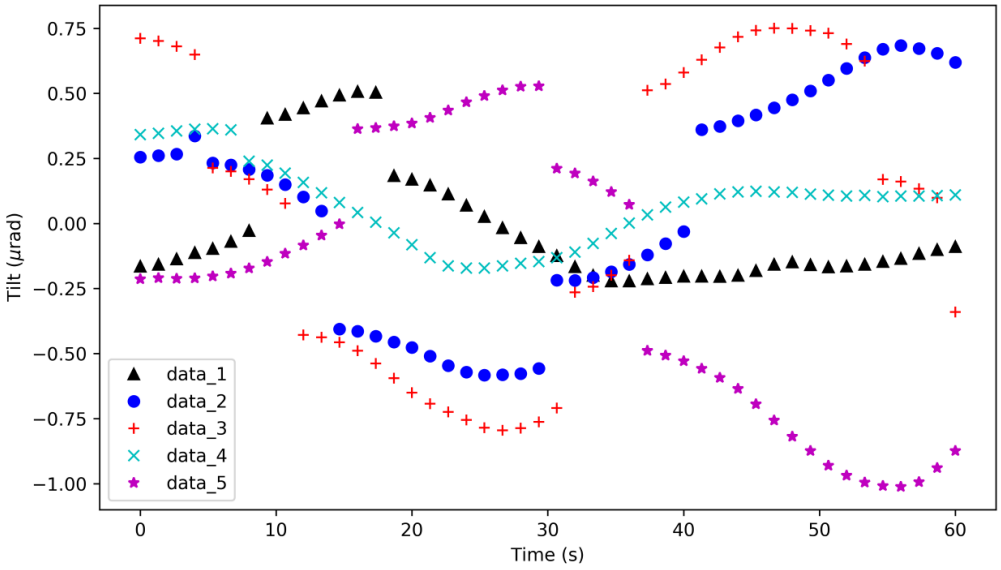


Figure 10.10: The measured tilt during the five measurements without a drive acting on the table. All measured tilts are within ±0.9 μrad about its average value. The RMS tilt for all five is 0.42 μrad, corresponding to an equilibrium shift of 34 nm.

without a drive, using the total absolute tilt difference of 1.76 µrad, the equilibrium shift is 140 nm. Using the RMS value, 0.42 µrad, the shift is 34 nm. In all cases, the shift is much smaller than diameter of the particle and any other length scale in the system (e.g.transverse or vertical gap).

10.7.9 Accelerometry Results

The response of the particle to accelerations is tested by applying a 5 Hz to the table in the axial direction, provided by the surface transducer as described above. With this external drive applied, five 60 s measurements were made. The CMOS camera recorded images at a rate of 100 fps, controlled precisely by the DG645, for a total of 6000 frames for each measurement. These images are analyzed by the method described in a previous section. The geophone measurements during the measurements of the particle displacement with the 5 Hz were also recorded.

The particle displacement and geophone data are Fourier transformed according to Eq. 10.53 to find the power spectrum. The five data sets for each the particle and geophone are averaged in power

$$S_{\text{avg}}[k] = \frac{1}{m}\sum_{j=1}^{m}\frac{2\Delta t}{N}|Z_j[k]|^2. \tag{10.60}$$

where m is the number of data sets. The displacement amplitude spectrum of the average for both, given by $|\sqrt{S_{\text{avg}}}|$, are shown in Fig. 10.11.

The raw particle data is its displacement, determined by the image analysis above. In contrast, the geophone directly measures velocity. In order to plot the acceleration of each system, as shown in Fig. 10.11, the data needs to be converted. To do so, the second derivative of the particle data needs to be calculated as well as the first derivative of the geophone data. However, in the Fourier domain, this is

trivial. For the n^{th} derivative, we simply need to multiply the data by ω_z^n. To put the acceleration in terms of standard gravity, $\mathrm{g} = 9.8\,\mathrm{m/s^2}$, we divide by g.

The large, broad peak at 1.75 Hz is the resonant frequency in the axial direction. The broadening is due to the feedback cooling providing artificial damping. Two prominent peaks are visible at frequency 10.5 Hz and 15.2 Hz which are the transverse and vertical resonant frequencies, respectively. The vertical frequency was determined by taking the Fourier transform of vertical position data. Those peaks are sharp because those degrees of freedom were not cooled during the experiment.

Because we want to use the particle as an accelerometer, we want to use the measured data to determine what vibrations and accelerations that caused it. The raw data is divided by the harmonic oscillator response of the particle as an accelerometer, Eq. 10.55. The results are shown in Fig. 10.12. The large peak at the axial resonance is no longer visible.

The 5 Hz drive is used to test the calibration of both systems. The peaks at 5 Hz is shown in the close up views in Fig. 10.13 and Fig. 10.14. The peaks are within 3% of each other, showing the calibrations are in close agreement with each other. We can infer that the calibrations are correct to 3%. This close agreement is significant since the mass of the particle, $2 \times 10^{-10}\,\mathrm{kg}$, is four billion times smaller than the geophone mass. The peaks occur at slightly different frequencies due to the total sampling time being slightly different for the particle and geophone data, resulting in different sized frequency bins. Data was taken with the drive oscillating from 0.25 Hz to 10 Hz in steps of 0.25 Hz. Though 5 Hz was arbitrarily chosen, it is far enough away from all of the particle resonances in the three directions to prevent them from affecting the calibration test.

There are three observations we can make about the data. Across most of the spectrum from DC to approximately 14 Hz, the particle data follows the geophone

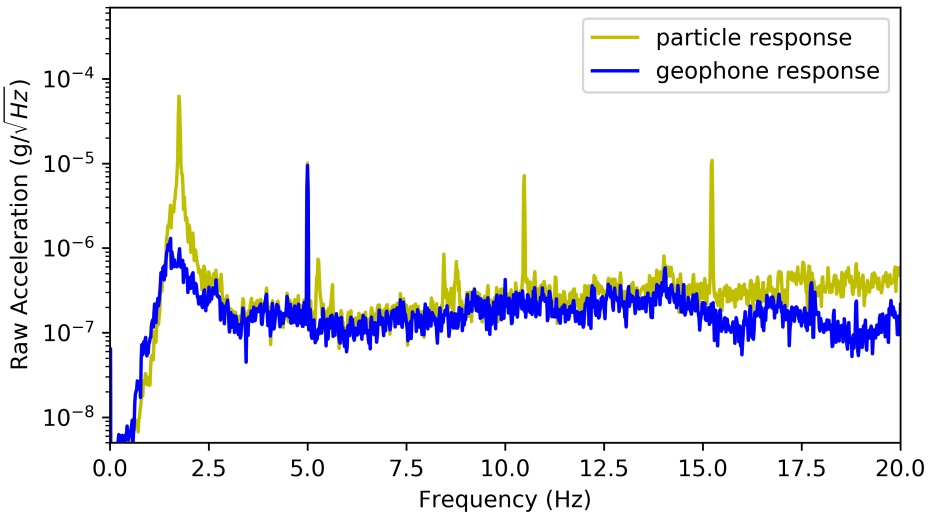


Figure 10.11: The raw data of the response of the geophone and particle with a 5 Hz drive on the optical table. The large peak at 1.75 Hz is due to the vibration of the table amplifying the motion of the particle on resonance. The peaks at 10.5 Hz and 15.2 Hz are the transverse and vertical motion of the particle, respectively.

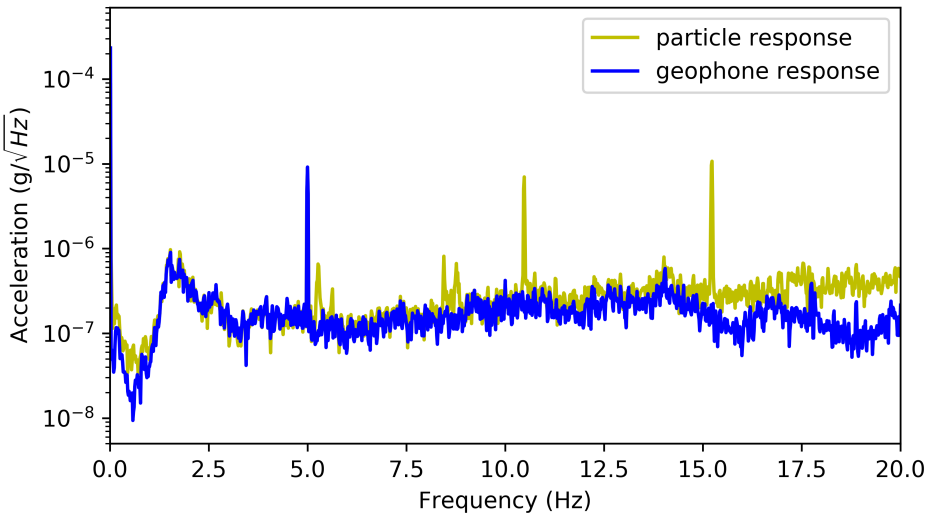


Figure 10.12: The data after the harmonic oscillator responses for the geophone and particle have been divided out. This shows the accelerations that cause the measured responses. The large resonance at 1.75 Hz is no longer present. Below approximately 14 Hz, the response is vibration limited. Above 14 Hz, the response is readout noise limited.

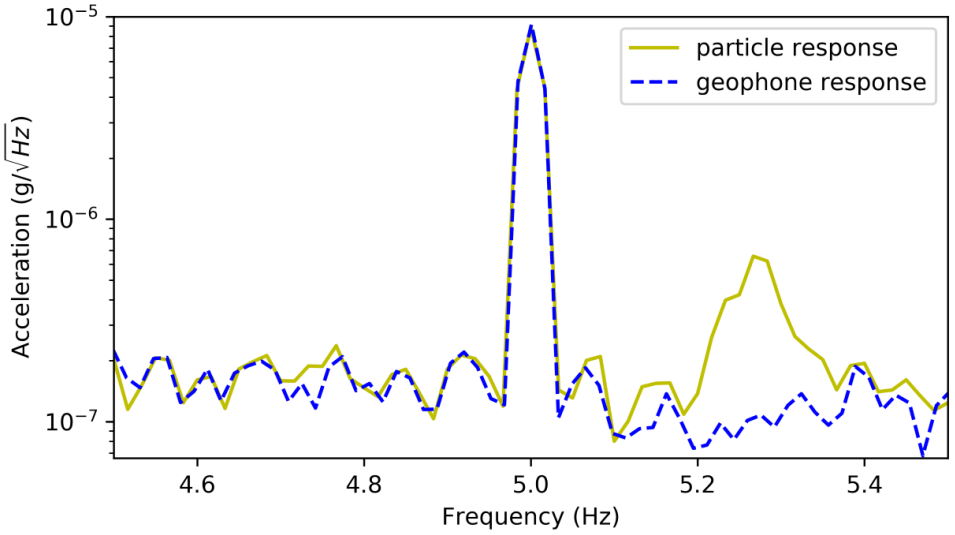


Figure 10.13: A closeup of the data focusing on the 5 Hz peak after the harmonic oscillator responses for the geophone and particle have been divided out. The two spectra follow each other with the main difference being the peak at 5.3 Hz. The peak is close to half of the 10.5 Hz vertical resonance, indicating a possible subharmonic.

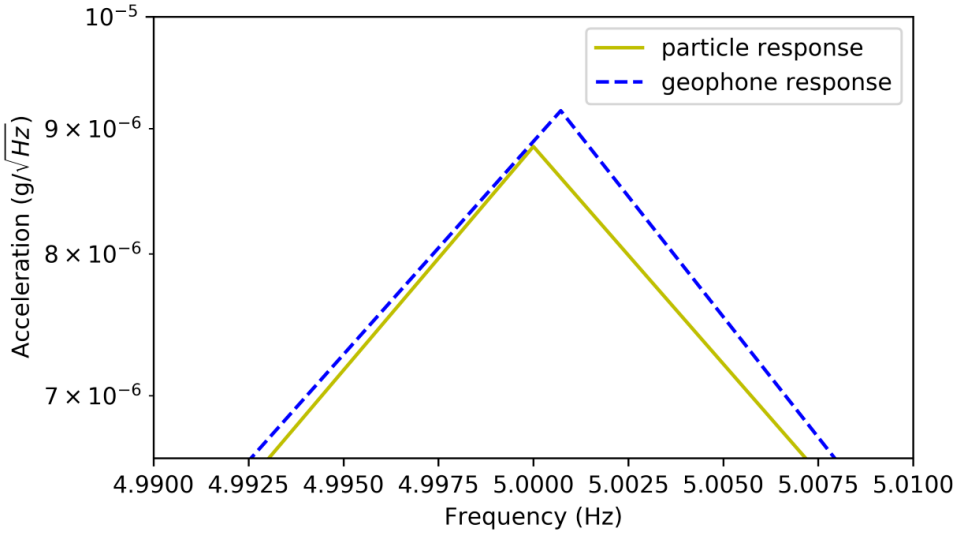


Figure 10.14: A closeup of the peak at 5 Hz. The magnitude of the peaks are within 3% of each other. The peaks appear at slightly different frequencies due to the frequency bins being different for the particle and geophone.

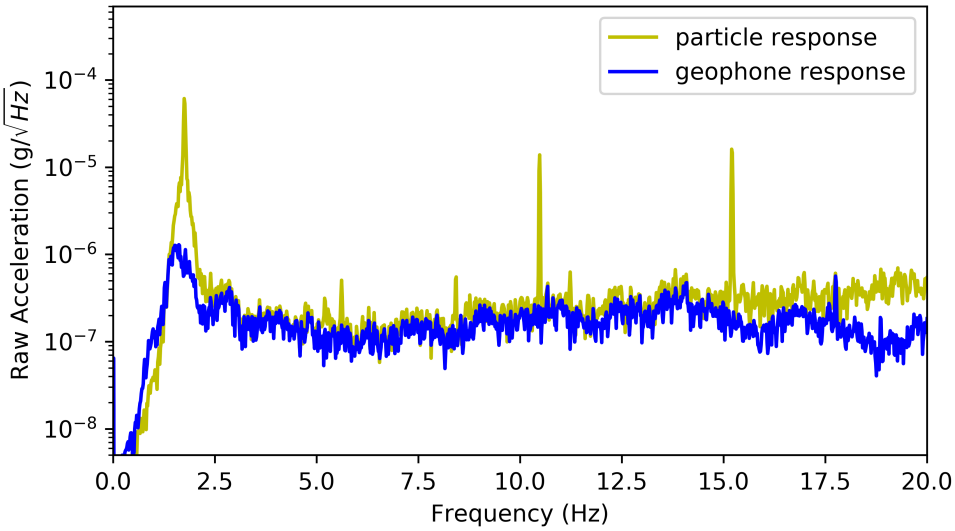


Figure 10.15: To make sure the 5 Hz peaks are from the drive, the response of the particle and geophone are measured without it. As expected, the peaks are now gone. The axial resonant frequency is visible along with the transverse and vertical peaks.

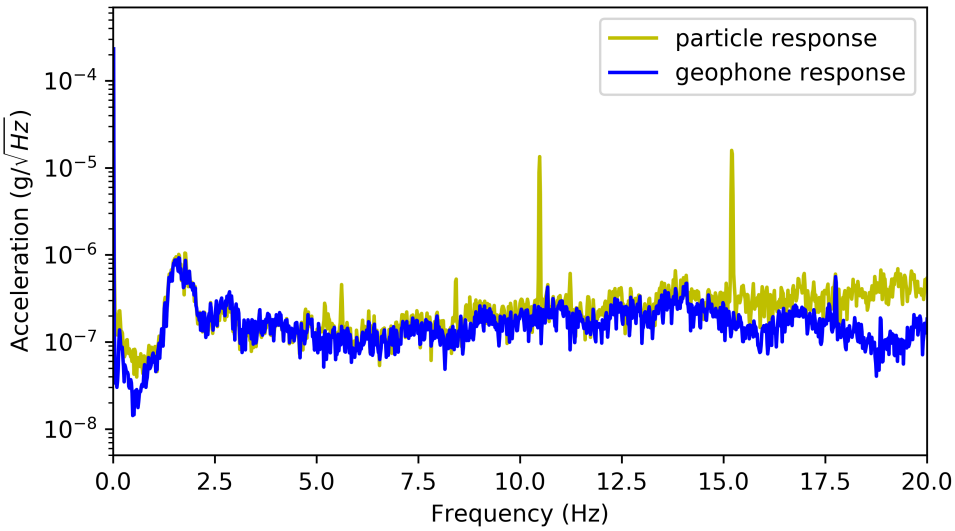


Figure 10.16: The data with no drive on the optical table with the harmonic oscillator responses divided out for the geophone and particle. The axial peak is gone as well as the 5 Hz peaks. Again, the particle is vibration limited below 14 Hz and readout noise limited above 14 Hz.

data. This implies that the data is vibration limited. Above 14 Hz, the particle acceleration spectrum starts to diverge from the geophone data due to a white noise source (white in displacement), as will be described later. Near 0.5 Hz, the particle data also differs from the geophone data. This is also explained in a later section.

10.8 Noise Analysis

To understand the performance of the geophone and particle systems, the sources of noise need to be analyzed. The noise of the geophone and its amplification circuit can be broken down into four parts [133]. The geophone is an underdamped harmonic oscillator of mass, m, damping rate, Γ, and resonant angular frequency, ω_0, in thermal equilibrium with its environment at temperature, T.

To calculate the thermal noise of the accelerometer, we can start with the displacement amplitude spectral density (ASD), which is the square root of the PSD of the harmonic oscillator subject to a random driving force,

$$\begin{aligned} \langle S_a(\omega)\rangle &= \sqrt{\langle S(\omega)\rangle} \\ &= \sqrt{\frac{4k_B\Gamma T}{m}}\left[\frac{1}{(\omega_0^2-\omega^2)^2+\Gamma^2\omega^2}\right]^{1/2}. \end{aligned} \tag{10.61}$$

We need to divide out the harmonic oscillator response, Eq. 10.27, to compare to the ASD of the data. The ASD of the thermal noise of a harmonic oscillator is then

$$\langle S_a(\omega)\rangle = \mathrm{n}_{\mathrm{therm}}(\omega) = \sqrt{\frac{4k_B\Gamma T}{m}}\frac{1}{\omega^2}. \tag{10.62}$$

The second noise source of the geophone is Johnson noise of the geophone coil and feedback resistors in the amplification circuit. The geophone coil dominates the Johnson noise, so other sources can be neglected. The Johnson noise of a resistor at

temperature T is

$$\mathrm{n}_{\mathrm{Johnson}}(\omega) = \frac{\sqrt{4k_B T R(\omega)}}{G(\omega)} \tag{10.63}$$

where R is the real part of the complex, frequency dependent impedance of the coil. The coil itself has a resistance R_c. The oscillating mass generates a voltage proportional to the velocity of the mass,

$$V = S_g \dot{x} \tag{10.64}$$

where S_g is the sensitivity of the geophone. The equation of motion of the geophone mass is

$$\ddot{x} + \Gamma \dot{x} + \omega_0^2 x = I S_g, \tag{10.65}$$

where I is the current through the coil. By taking the Fourier transform,

$$(-\omega^2 + i\Gamma\omega + \omega_0^2)x = I S_g. \tag{10.66}$$

The Fourier transform of Eq. 10.64 is $V(\omega) = i\omega x$. Solving for x and substituting,

$$(-\omega^2 + i\Gamma\omega + \omega_0^2)\frac{iV}{\omega} = I S_g. \tag{10.67}$$

Solving for V yields

$$V = I\frac{i\omega S_g}{\omega_0^2 - \omega^2 + i\Gamma\omega} = I Z_g \tag{10.68}$$

where Z_g is the complex impedance due to the motion of the geophone mass. The total impedance of the geophone coil is

$$Z = R_c + Z_g = R_c + \frac{i\omega S_g}{\omega_0^2 - \omega^2 + i\Gamma\omega}. \tag{10.69}$$

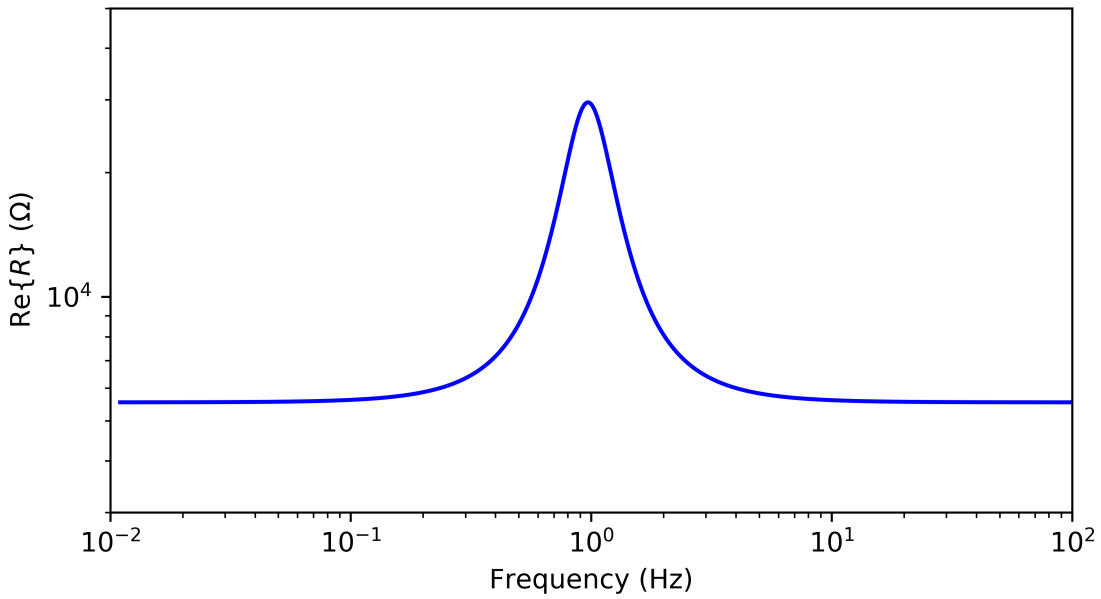


Figure 10.17: The real part of the complex impedance of the geophone coil. The peak occurs at the resonant frequency of the oscillator and the width is given by the damping rate. The impedance is shifted up by the resistance of the coil, R_c.

The real part of Eq. 10.69 is plotted in Fig. 10.17 for the values of R_c, ω_0, and Γ given table 10.1.

The voltage and current noise of the geophone and amplification circuit are dominated by the amplification circuit because of the large gain of the first-stage OPA188 operational amplifier. The voltage and current noise are simply the input-referred voltage and current noise specified by the data sheet [134]. The voltage noise is in general frequency dependent, as shown in the data sheet. Over the frequency range that is relevant to us, to good approximation, the voltage noise is constant. The current noise is several orders of magnitude smaller than any other noise source in the system, so it is neglected in our noise calculations. To compare to the data,

Parameter	Description	Geophone Value
T	Temperature	300 K
$\omega_0/2\pi$	Resonant frequency of oscillator	.97 Hz
m	Mass of oscillator	.957 kg
Q	Quality factor of oscillator	1.845
R_c	Resistance of geophone coil	5546 Ω
S_g	Sensitivity of geophone oscillator	281.7 Vs/m
G_g	Gain of amplifcation circuit	180.2
N_V	Input-referred voltage noise	8.8 nV/$\sqrt{\text{Hz}}$
N_A	Input-referred current noise	Negligible

Table 10.1: The parameters for the geophone amplified with a OPA188 operational amplifier. The temperature is assumed to be 300 K for the geophone. The values were taken from the datasheets of the geophone and OPA188 operational amplifier. The current noise of the amplification circuit is negligible compared to other noise sources in the geophone.

the geophone harmonic oscillator response,

$$G(\omega) = \frac{\omega^3 S_g}{\sqrt{(\omega_0^2 - \omega^2)^2 + \Gamma^2\omega^2}}, \tag{10.70}$$

is divided out of the noise. To recap, the four noise sources for the geophone are:

$$\mathrm{n}_{\mathrm{therm}}(\omega) = \sqrt{\frac{4k_B T\omega_0}{mQ}}\frac{1}{\omega^2}, \tag{10.71}$$

$$\mathrm{n}_{\mathrm{Johnson}}(\omega) = \frac{\sqrt{4k_B T R(\omega)}}{G(\omega)}, \tag{10.72}$$

$$\mathrm{n}_{\mathrm{voltage}}(\omega) = \frac{N_V(\omega)}{G(\omega)}, \tag{10.73}$$

$$\mathrm{n}_{\mathrm{current}}(\omega) = \frac{N_A(\omega)R(\omega)}{G(\omega)}, \tag{10.74}$$

where N_v and N_A are the input-referred voltage and input-referred current, respectively. All of the necessary parameters are given in table 10.1. The four noises add in quadrature to give the total noise of the geophone system as

$$\mathrm{n}^2_{\mathrm{total},g} = \mathrm{n}^2_{\mathrm{therm}} + \mathrm{n}^2_{\mathrm{Johnson}} + \mathrm{n}^2_{\mathrm{voltage}} + \mathrm{n}^2_{\mathrm{current}}. \tag{10.75}$$

The noise of the particle system consists of only two terms. The first is the thermal noise due to the particle being an underdamped harmonic oscillator with resonant angular frequency, ω_0, and damping rate, Γ, in thermal equilibrium with its environment at temperature, T. The thermal noise is then given by Eq. 10.62. Assuming the temperature associated with feedback damping to be room temperature, 300 K, the thermal noise calculated to be $2.1 \times 10^{-7}\,\mathrm{g}/\sqrt{\mathrm{Hz}}$. Inspecting the particle data around 0.5 Hz, the average value around the minimum is approximately $3.6 \times 10^{-8}\,\mathrm{g}/\sqrt{\mathrm{Hz}}$.

Physically, the measured data cannot be below the calculated noise. The temperature of the particle must be lower than room temperature. We can estimate the cooled temperature T_{fb}, rewritten as T for convenience, from the data as approximately 9 K by placing the upper bound on the thermal noise to be $3.6 \times 10^{-8}\,\mathrm{g}/\sqrt{\mathrm{Hz}}$. The temperature may be much lower but due to difficulties in measuring the natural damping rate, this cannot be calculated. Because of the location of the particle relative to repulsive charges around it, excitations of the

Parameter	Description	Particle Value
T	Temperature	$9\,\mathrm{K}$
$\omega_0/2\pi$	Resonant frequency of oscillator	$1.75\,\mathrm{Hz}$
m	Mass of oscillator	$2.5 \times 10^{-10}\,\mathrm{kg}$
Q	Quality factor of oscillator	175
S_c	Sensitivity	$1.15\,\mu\mathrm{m/pixel}$
I_0	Energy density of scattered light	$2.76 \times 10^{-4}\,\mathrm{J/m^2}$
Δz	Readout noise	$160\,\mathrm{pm}/\sqrt{\mathrm{Hz}}$

Table 10.2: The parameters for the particle system and optics. The temperature is cooled to 9 K or lower. The resonant frequency and Q of the particle was measured from the transient response.

particle were difficult to obtain without permanent relocation of the particle to another area of the trap.

The second noise source is from the analysis of the images and readout noise from the CMOS camera. This noise is expected to be dominated by shot noise of the illumination light and camera noise. To place a lower bound on the shot noise, consider the particle as a point particle. The precision that we can resolve the position of a diffraction-limited spot for N number of photons is [135]

$$\left\langle (\Delta z)^2 \right\rangle = \frac{\sigma_{\mathrm{PSD}}^2}{N} \tag{10.76}$$

where σ_{PSD} is the standard deviation of the point spread function (PSF) of the collection optics.

The standard deviation of the PSF is given by $\sigma_{\mathrm{PSD}} = 0.225\lambda/\mathrm{NA}$ where λ is the wavelength of the illumination light and NA is the numerical aperture of the

collection objective. For this system, the wavelength is 660 nm and the numerical aperture is 0.09. The calculated standard deviation is then $\sigma_{\mathrm{PSD}} = 1.65\,\mu\mathrm{m}$.

The number of photons blocked by the particle is determined by the area of the particle and the average number of photons per pixel. To determine the photons per pixel, the average pixel value is approximately 3980, an integer value up to 4095. For each photon that hits the CMOS camera, approximately 1 electron is created in the sensor. For this CMOS camera, the conversion from brightness to electrons is 2.8. The total number of photons blocked calculated is $N = 1.4 \times 10^7$. The intensity of the scattered light off of the particle collected and imaged onto the CMOS camera can also be calculated. The energy density for 660 nm light is calculated to be $2.76 \times 10^{-4}\,\mathrm{J/m^2}$ in a single image.

Using the value for σ_{PSD} and N that we calculated, the localization error due to shot noise is approximately 400 pm. This value is only a lower bound based on our assumption that the particle is a diffraction-limited spot. To estimate the readout noise of the data, the undriven table data with the harmonic oscillator response divided out was fit to a white displacement noise source. The data from 35 Hz to 50 Hz was fit. The error is estimated to be $\Delta z = 1.6\,\mathrm{nm}$ or $160\,\mathrm{pm}/\sqrt{\mathrm{Hz}}$. This value is reasonably above the lower bound determined by the shot noise estimated above. The readout noise is the same for every frame.

Similar to the geophone noise, the noise sources of the particle system are added together in quadrature,

$$n^2_{\mathrm{therm},p} = n^2_{\mathrm{therm}} + (\Delta z)^2 . \tag{10.77}$$

The individual terms of Eq. 10.75 for the geophone and Eq. 10.77 for the particle are ploted in Fig. 10.18. All of the necessary parameters for this calculation are given in table 10.2.

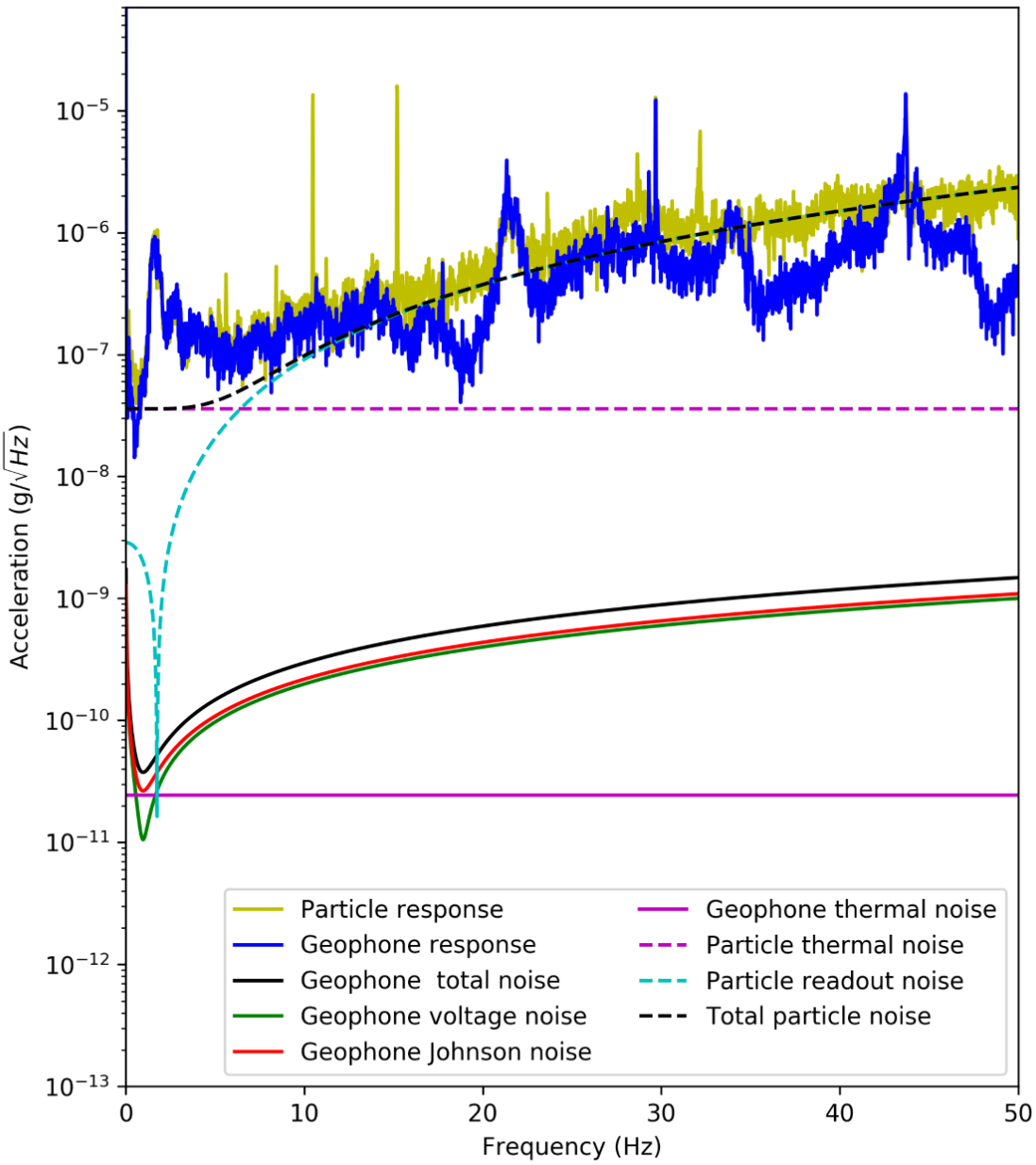


Figure 10.18: The data after the harmonic oscillator responses for the particle and geophone have been divided out with no drive. The contributions to the noise for both the geophone (solid lines) and the particle (dashed lines) are also shown.

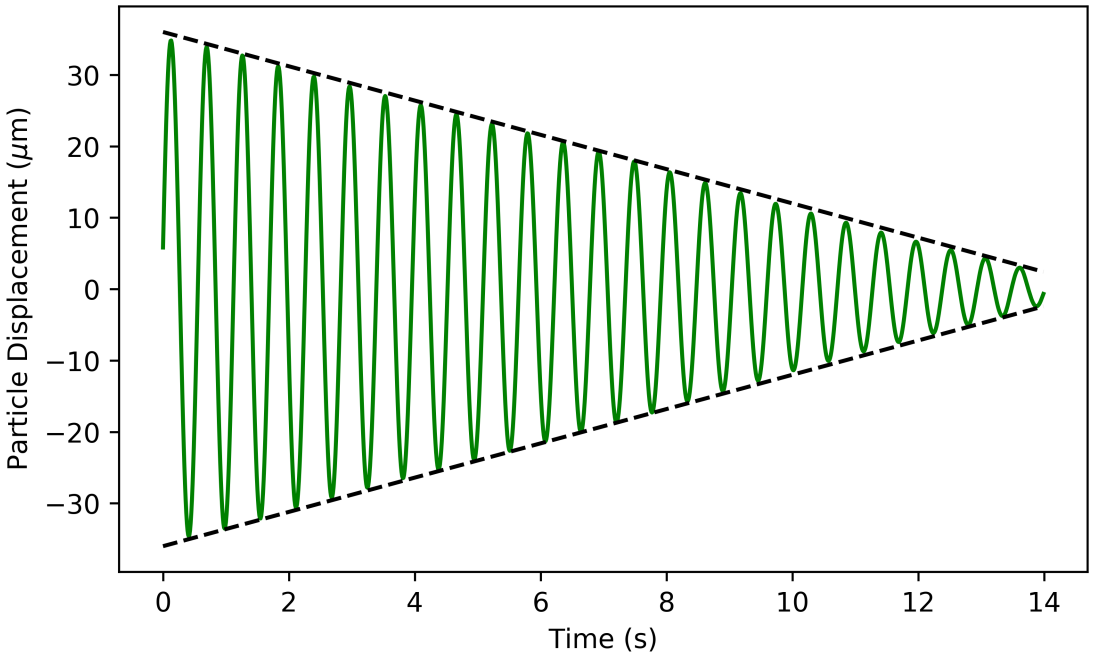


Figure 10.19: Transient motion of the levitated microsphere after excitation with feedback cooling applied. The gain of the feedback is large (200 times larger than what was used in the data above). The large gain provided nonlinear damping indicated by non-exponential decay.

The thermal noise of the geophone is much smaller than that of the particle due to the four billion times larger mass. Center-of-mass motion temperatures down to 140 μK have been demonstrated in magneto-gravitational traps [84] and 50 μK for an optical trap [27]. Assuming a feedback cooled temperature of 50 μK, the thermal noise of the particle can be as low as $\sim 10^{-11}\,\mathrm{g}/\sqrt{\mathrm{Hz}}$, the same order of magnitude as the geophone despite the large difference in mass.

10.9 Non-Linear Feedback

The gain setting of the feedback cooling is crucial to the experiment: too small of a gain results in lower damping while too large can cause non-linear feedback. We

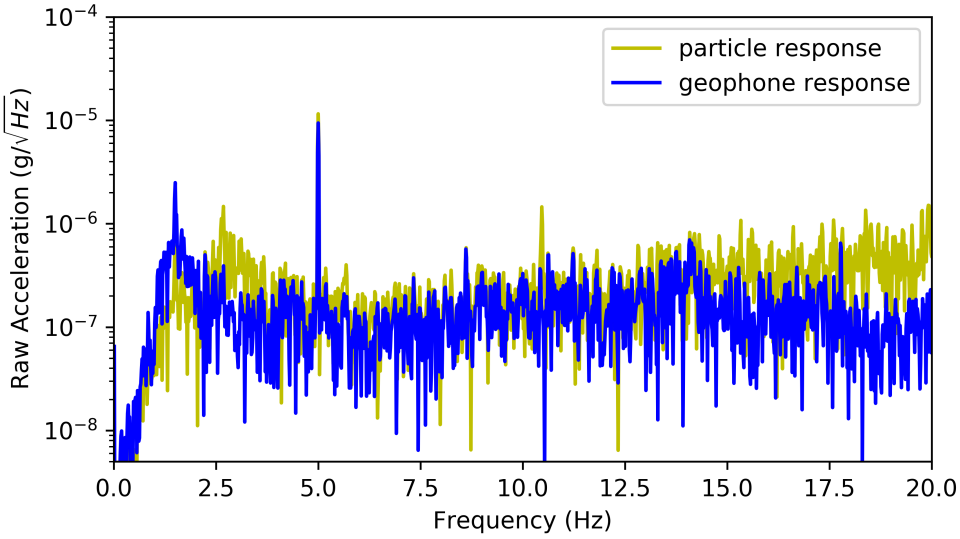


Figure 10.20: The raw acceleration data of the particle and geophone with a large gain with a 5 Hz drive. Because the damping was nonlinear, the harmonic oscillator responses could not be divided out. The peak at the axial oscillation frequency is no longer evident.

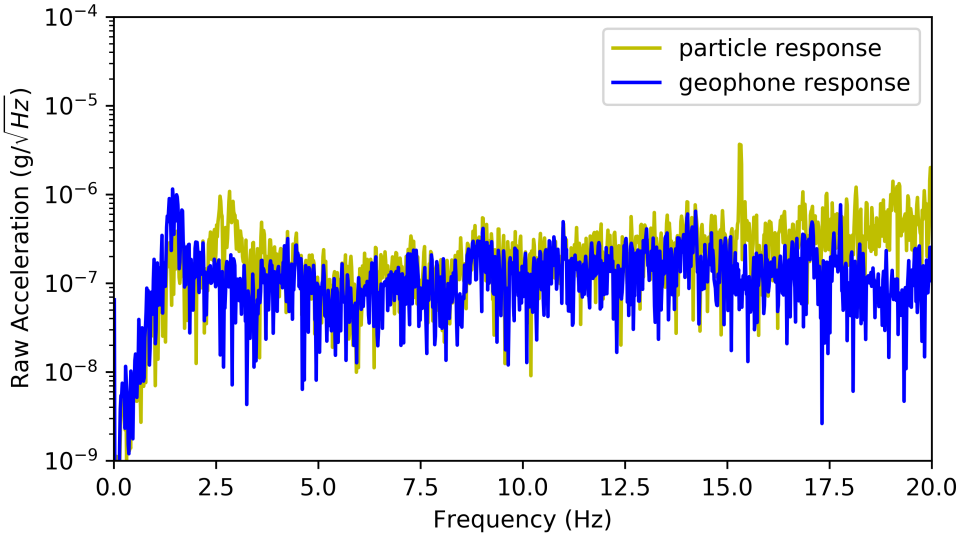


Figure 10.21: The raw acceleration data of the particle and geophone with a large gain without the drive. Because the damping was nonlinear, the harmonic oscillator responses could not be divided out. The peak at the axial oscillation frequency is no longer evident.

want the damping to be efficient and low noise in order to cool the center-of-mass motion to the lowest temperature that can be achieved.

The transient response to a small tap on the optical table is shown in Fig. 10.19 with the gain setting increased from 0.5 to 100.0. The motion decays but not exponentially. We have seen in the theory section of this chapter that artificial damping that is proportion to the velocity of the particle results in an exponential decay, also illustrated in Fig. 10.6. The decay in Fig. 10.19 is linear, not exponential implying non-linear feedback was used.

The effects of this non-linearity are evident in the two spectra in Fig. 10.20 and Fig. 10.21. The harmonic oscillator response for the particle could not be divided out because the fit to an exponential decaying sine wave no longer holds and a frequency and damping rate cannot be extracted. Only one 60 s long data set was taken with the 5 Hz drive and one with no drive.

At the resonant frequency of the particle, 1.75 Hz, the broad peak is no longer visible. At a slightly higher frequency, approximately 2.5 Hz, another peak shows up due to noise injected into the system. In Fig. 10.20, only the transverse peak is visible, and in Fig. 10.21, only the vertical peak is visible.

For a given gain setting, there is a maximum velocity where the feedback laser hits its current limit and drops below the lasing threshold when the sign of the velocity changes. For velocities greater than this maximum velocity, the feedback force is constant and no longer proportional to its velocity.

10.10 Statistical Errors

The systematic errors related to the measurement of Newton's constant of gravity were described in chapter 4 and compared to systematic errors in the most precise measurement of G to date. In addition to these, there are several sources of statistical

errors that need to be accounted for in this measurement.

The first source of statistical error is the noise due to thermal motion. When the oscillator with angular resonant frequency, ω_z, and mass, m, at thermal equilibrium with its environment at temperature, T, will have an oscillation amplitude,

$$\frac{1}{2}m\omega_z A_T^2 = \frac{1}{2}k_B T \quad \Rightarrow \quad A_T = \frac{1}{\omega_z}\sqrt{\frac{k_B T}{m}}. \tag{10.78}$$

For the 60 μm borosilicate microsphere at $T = 300\,\mathrm{K}$, an oscillation frequency of $\omega/2\pi = 1.75\,\mathrm{Hz}$, the experimental parameters from the accelerometry measurement, the thermal motion amplitude is $A_T = 0.37\,\mu\mathrm{m}$. For the measurement of G, an oscillation frequency of $\omega_z/2\pi = 0.1\,\mathrm{Hz}$ is preferred. This increases the thermal motion amplitude to $A_T = 6.5\,\mu\mathrm{m}$. To help, the use of cryogenics, such as mounting the trap in a pulse tube refrigerator, can reduce the temperature to to 4 K, lowering the thermal to $A_T = 0.75\,\mu\mathrm{m}$.

The quality factor, Q, is an important factor in the time-of-swing method for measuring G. A large Q ensures that the thermal motion does not interfere with the measurement and prevents the motion from decaying significantly. As explained above, the current natural damping is not limited by collisions with the background gases. With more effort to improve damping, it is possible to be vacuum-limited with a damping rate given by Eq. 9.1. The damping rate for easily obtainable parameters can be $8 \times 10^{-11}\,\mathrm{s}^{-1}$. The damping time can be as long as 300 yrs, much larger than any time scale of the experiment. By going to cryogenic temperatures, the vacuum can be improved to 5×10^{-17} Torr [136].

With very little or no coupling between the three center-of-mass degrees of freedom, the transverse and vertical motion can be used to our advantage. Similar to the axial motion, the motion in these directions can be prepared at a chosen amplitude

of oscillation by the method described in chapter 7. The subsequent motion can then be used to map out the magnetic field. Since the frequencies in these directions are substantially larger than that of the axial motion ($\sim 10\,\mathrm{Hz}$), they will have negligible contribution to the measurement of G. High magnetic field stability is also required. The transverse and vertical motions can be used to probe this stability.

The system is extremely sensitive to vibrations, as shown in this chapter. For a large Q, the particle will only be sensitive in a small bandwidth around the resonant frequency. Piezoelectric actuators can be used to help eliminate vibrations [137]. In the accelerometry data presented in this data, below $14\,\mathrm{Hz}$ the particle data is vibration limited, showing the need for better vibration isolation. Changes in the local acceleration due to gravity, g, can change the motion of the particle and lead to noise in the measurement of G. Gravimeters can be used to measure local gravity as well as using particle data where there is little change in g.

Another source of statistical error, already addressed in this dissertation, is the tilt of the magneto-gravitational trap. As explored in chapter 8, tilt can cause a shift in the equilibrium position of the particle in the trap. Over three days of data acquisition, the actively stabilized optical table was stabilized to a root-mean-square tilt of $0.35\,\mu\mathrm{rad}$, resulting in a shift of $9\,\mu\mathrm{m}$, approximately 0.1% of the target amplitude of motion and on the same order as the thermal noise.

Charge on the test mass can lead to moving image charges in the conducting pole pieces leading to damping. To load particles into the magneto-gravitational trap described in this dissertation, however, charge is necessary. Even after the particle is trapped, a DC field is needed to keep the particle levitated. It has been shown that trapped particles can be neutralized [34, 84]. Though charge is necessary, the magnitude can be decreased to a very small value while increasing the DC field required to keep the particle trapped. As explained, charged particles that failed to

get trapped cause anharmonicity in the potential and coupling between degrees of freedom. To prevent this, a new loading technique is currently being developed to load one particle at a time. The pole pieces can also be gold plated to reduce patch charges on the pole pieces [23].

10.11 Additional Data

To complete the analysis, the data in Fig. 10.11, Fig. 10.12, Fig. 10.15, and Fig. 10.16 are converted to SI acceleration units $\mathrm{m/s^2}/\sqrt{\mathrm{Hz}}$, velocity, and displacement. To convert the data to $\mathrm{m/s^2}/\sqrt{\mathrm{Hz}}$, we simply multiply by g. The results are shown Fig. 10.22, Fig. 10.23, Fig. 10.28, and Fig. 10.29.

Converting to velocity is simple in the Fourier domain, we only need to divide by ω and multiply by g. The results are shown in Fig. 10.24, Fig. 10.25, Fig. 10.30, and Fig. 10.31. The displacement data is found by dividing the velocity by another factor of ω. The results for displacement are shown in Fig. 10.26, Fig. 10.27, Fig. 10.32, and Fig. 10.33.

10.12 Conclusions

In this chapter, the theoretical background for a levitated microsphere in a magneto-gravitational trap to be used as an accelerometer is laid out. The normalization condition used in all discrete Fourier transforms is also stated.

A 60 µm diameter borosilicate microsphere was succesfully trapped with a DC voltage of $-37.2313\,\mathrm{V}$ with stability within 3 ppm using the DC voltage source described in chapter 5 and 6. Throughout all of the measurements, using the modification and methods in chapter 8, the optical table was stabilized to within 0.35 µrad.

This is the first room temperature levitated optomechanical system that has directly measured accelerations and compared the results to those measured by a commercial geophone. An attractive feature of the particle system is that it is self-calibrating. The oscillation frequency and damping rate is required to remove all free parameters from the harmonic oscillator response. The only calibration needed is for the collection optics and CMOS camera. For the geophone, the user must trust calibration performed by the manufacturer as well as measuring the gain of the geophone amplification circuit. This calibration was tested by driving the optical table with a 5 Hz drive (chosen arbitrarily). The two systems measured the acceleration to within 3% of each other.

Feedback cooling, as described in chapter 7 was implemented to decrease the time that transients take to damp. A 520 nm diode laser provided the feedback force. Images from the camera were used to determine the sign and strength of the feedback.

A detail analysis of the noise of both the particle and geophone system was performed. Due to the large mass of the oscillators in the geophone, it is no surprise that the thermal noise for the geophone is orders of magnitude lower than that of the particle. First, assuming the particle is at room temperature, the thermal noise is higher than a subset of the data. Finding the temperature of the particle corresponding to the minimum value of the data, $3.6 \times 10^{-8}\,\mathrm{g}/\sqrt{\mathrm{Hz}}$, is 9 K.

Below approximately 14 Hz, the particle spectrum follows that of the geophone. Above 14 Hz, the particle spectrum deviates from the geophone and follows a white displacement noise spectrum. Assuming that the particle is a point source, a simple shot noise calculation limits the resolution that which the particle can be located to 400 pm. Since the particle is not a point source, this is a lower bound. Fitting the spectrum to a white noise source in displacement, the readout noise is estimated to be 1.6 nm per image, or $160\,\mathrm{pm}/\sqrt{\mathrm{Hz}}$.

The measured acceleration sensitivity, $3.6 \times 10^{-8}\,\mathrm{g}/\sqrt{\mathrm{Hz}}$, is the best sensitivity measured in a room temperature levitated optomechanical system. The next closest, based on a prediction of thermal noise, is almost three times higher by David C. Moore at Yale University [27].

As seen in chapter 9, the motion can be extremely anharmonic along with an unknown source of excess damping. Recall, the center-of-mass temperature associated with feedback is $T_{fb} = \Gamma_N T_N / \Gamma_{fb}$. For a given feedback damping rate, Γ_{fb}, the temperature associated with feedback, T_{fb}, will be larger with larger natural damping, Γ_N. This will result in larger thermal noise, decreasing sensitivity. The anharmonicity also results in a nonlinear response which may limit the dynamic range of acceleration detection.

In chapter 7, the method for feedback cooling is described. The velocity calculated is filtered by a bandpass filter before being used for feedback. The center frequency of the filter is chosen to match closely to the resonance oscillation frequency of the particle. If the oscillation frequency changes with amplitude, the effectiveness of the cooling can change, possibly increasing the temperature associated with feedback, decreasing sensitivity.

An accelerometer consisting of this levitated microsphere in a magneto-gravitational trap has many practical uses. Unlike previous systems, as described in chapter 10, our system operates in the low frequency regime. Mechanical devices as well as optical traps operate with frequencies orders of magnitude higher, from $\sim 10\,\mathrm{Hz}$ to $\sim 100\,\mathrm{kHz}$. This system has improved sensitivity at these lower frequencies making it attractive for low frequency measurements. This system can be used to be measure small accelerations where sensitivity does not need to be sacrificed for robustness.

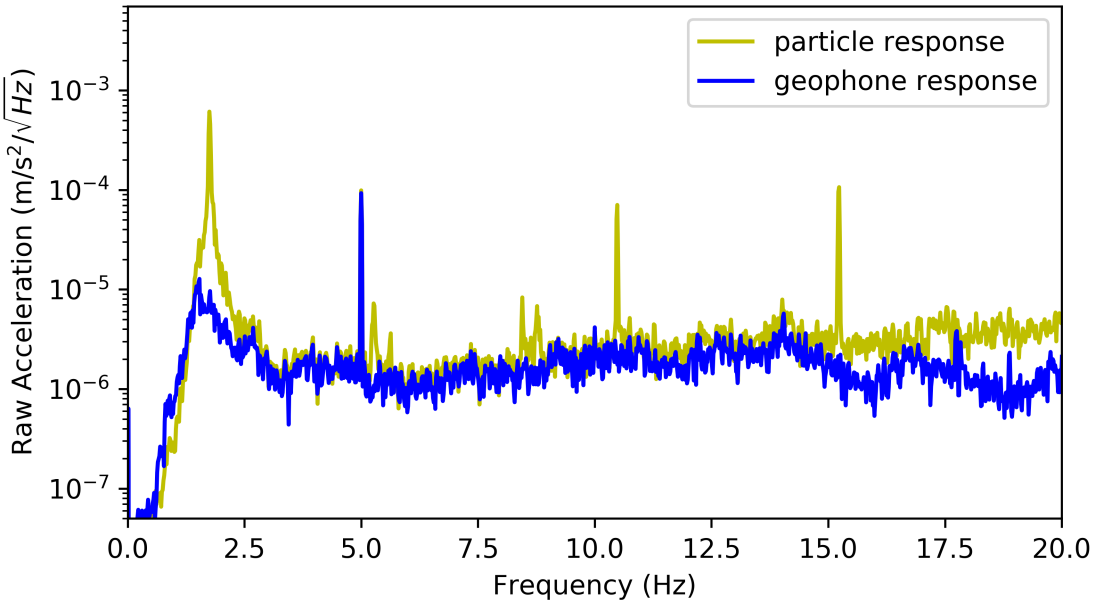


Figure 10.22: The raw acceleration data of the particle and geophone in units of $\mathrm{m/s^2/\sqrt{Hz}}$ with a 5 Hz drive.

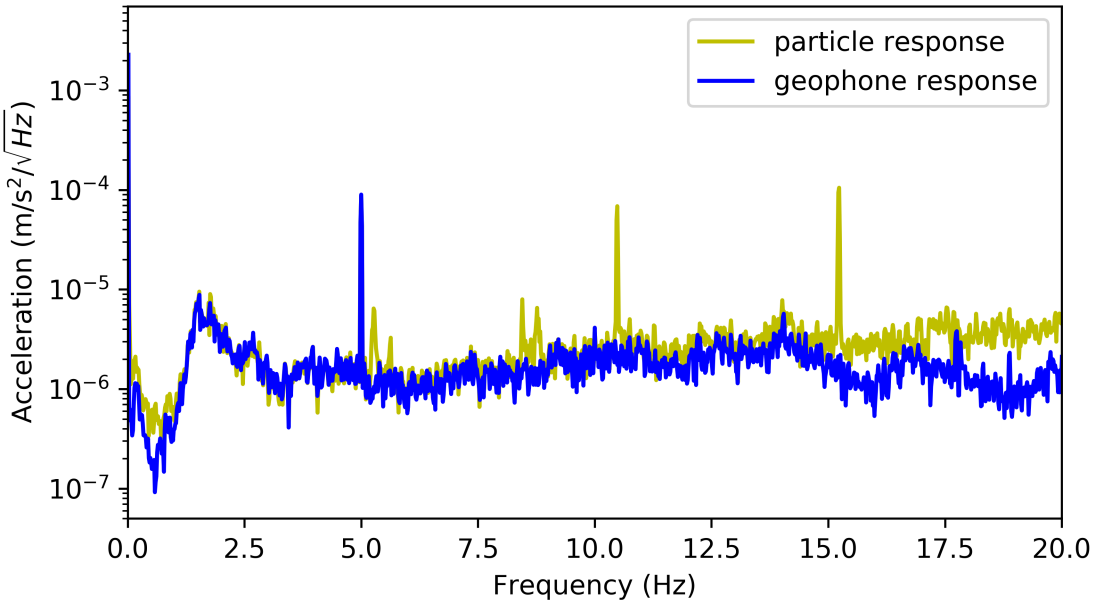


Figure 10.23: The acceleration data of the particle and geophone with their harmonic oscillator responses divided out in units of $\mathrm{m/s^2/\sqrt{Hz}}$ with a 5 Hz drive.

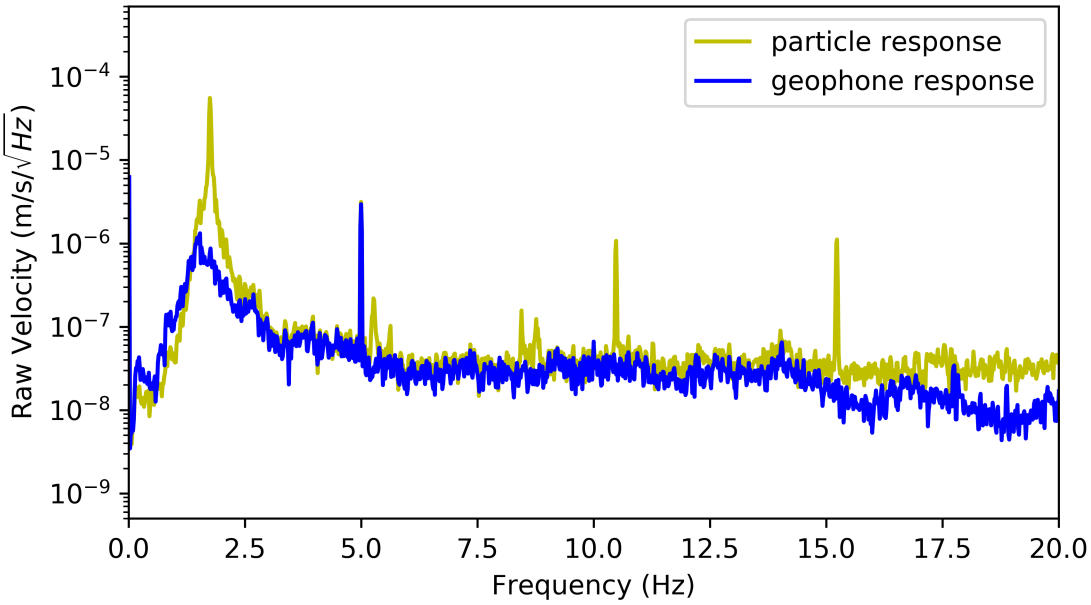


Figure 10.24: The raw velocity data of the particle and geophone in units of $\mathrm{m/s/\sqrt{Hz}}$ with a 5 Hz drive.

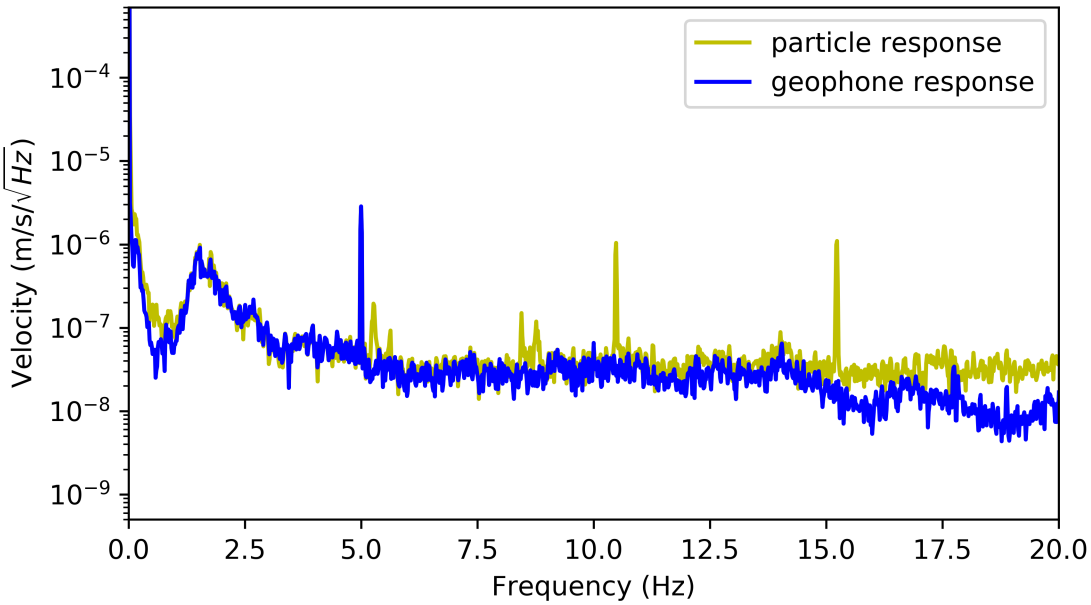


Figure 10.25: The velocity data of the particle and geophone with their harmonic oscillator responses divided out in units of $\mathrm{m/s/\sqrt{Hz}}$ with a 5 Hz drive.

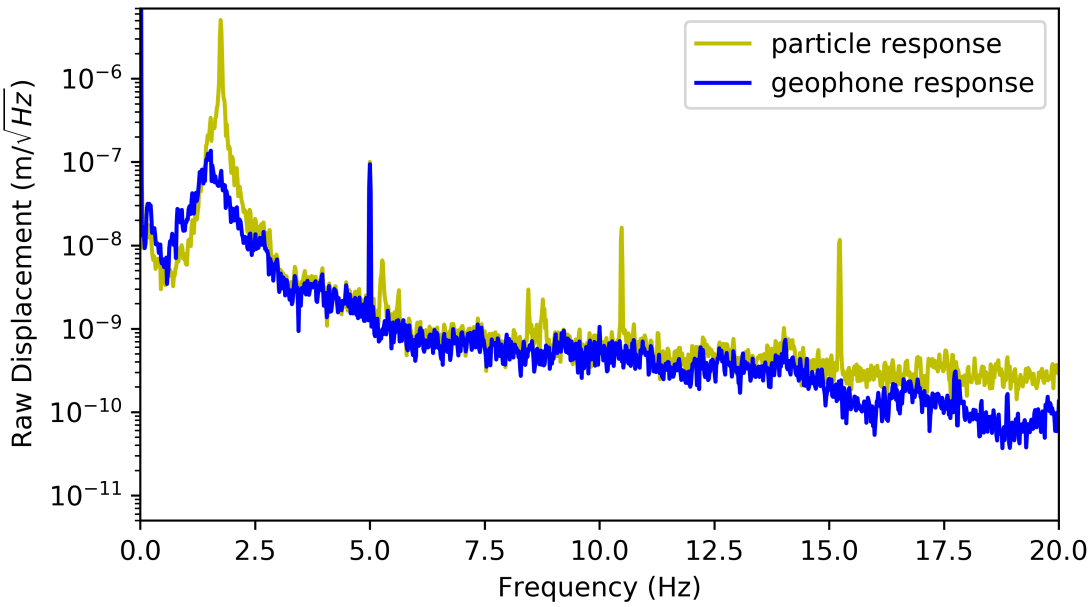


Figure 10.26: The raw displacement data of the particle and geophone in units of $\mathrm{m}/\sqrt{\mathrm{Hz}}$ with a 5 Hz drive.

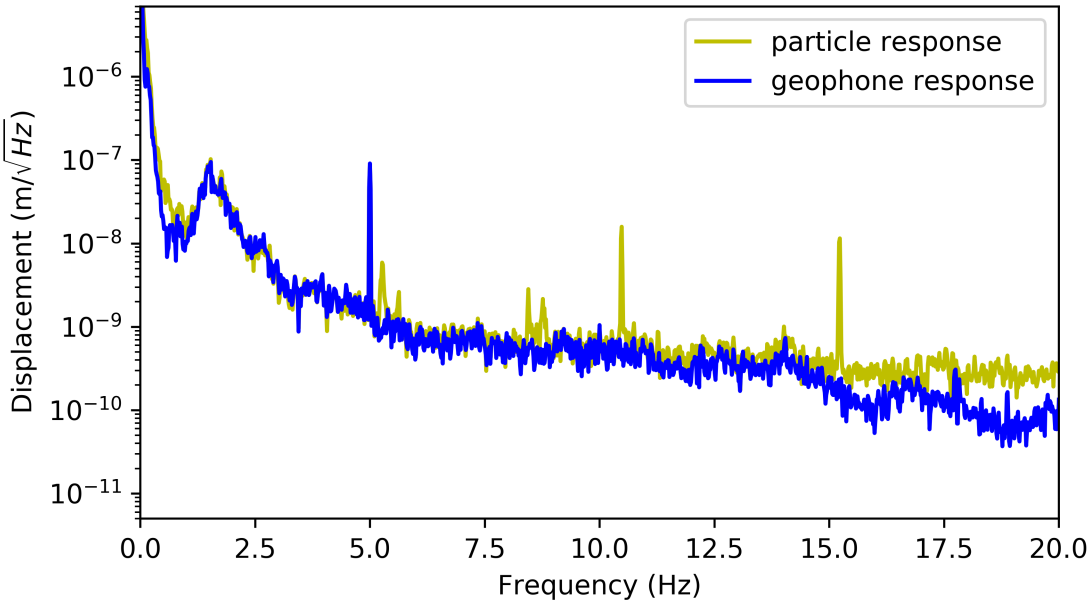


Figure 10.27: The displacement data of the particle and geophone with their harmonic oscillator responses divided out in units of $\mathrm{m}/\sqrt{\mathrm{Hz}}$ with a 5 Hz drive.

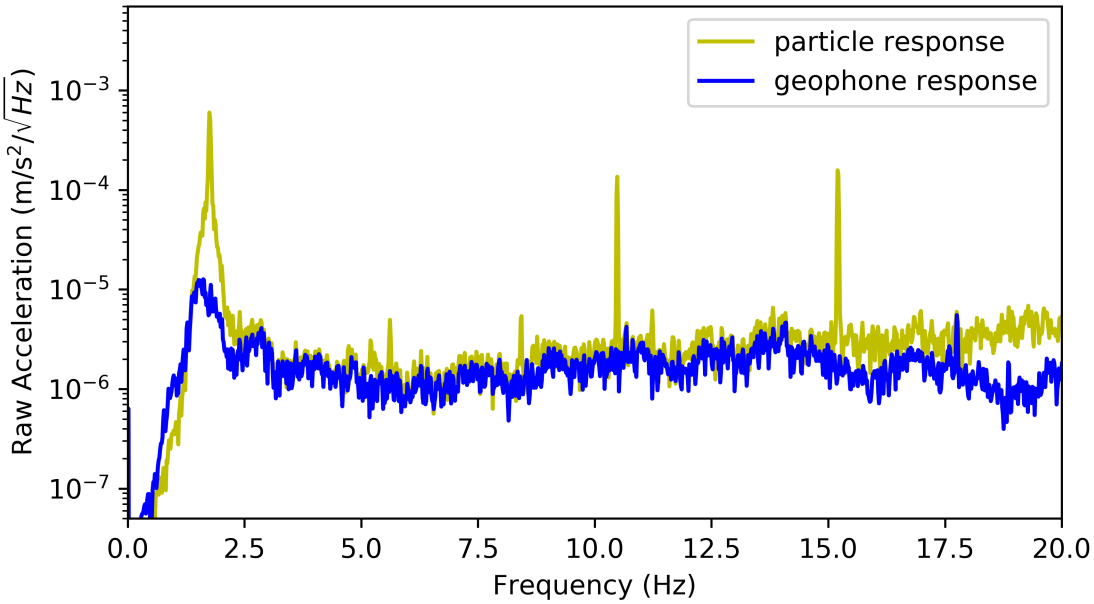


Figure 10.28: The raw acceleration data of the particle and geophone in units of $\mathrm{m/s^2/\sqrt{Hz}}$ without a drive.

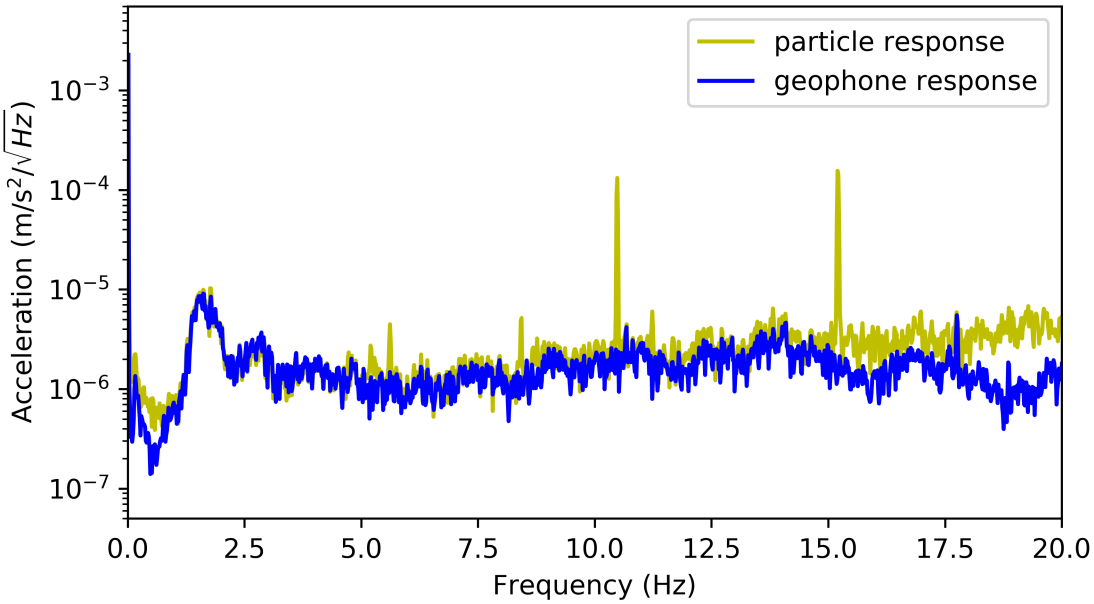


Figure 10.29: The acceleration data of the particle and geophone with their harmonic oscillator responses divided out in units of $\mathrm{m/s^2/\sqrt{Hz}}$ without a drive.

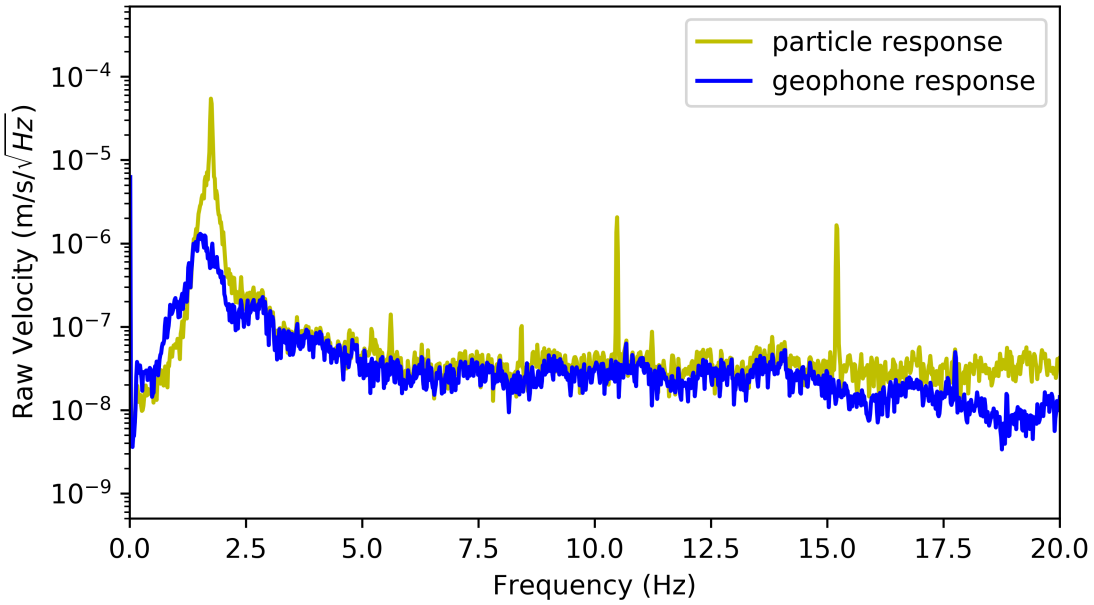


Figure 10.30: The raw velocity data of the particle and geophone in units of $\mathrm{m/s/\sqrt{Hz}}$ without a drive.

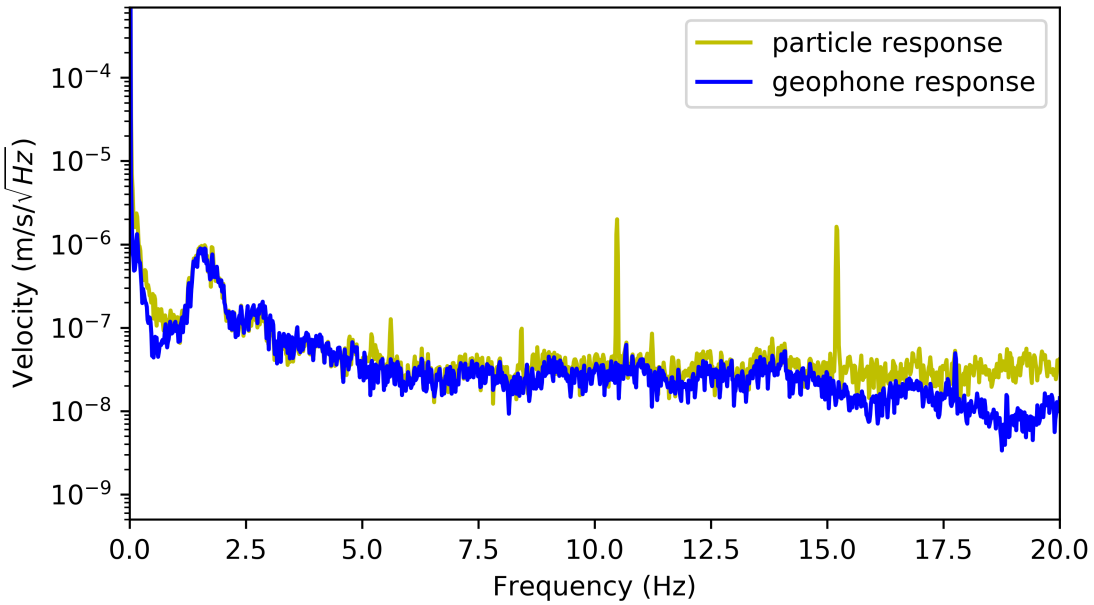


Figure 10.31: The velocity data of the particle and geophone with their harmonic oscillator responses divided out in units of $\mathrm{m/s/\sqrt{Hz}}$ without a drive.

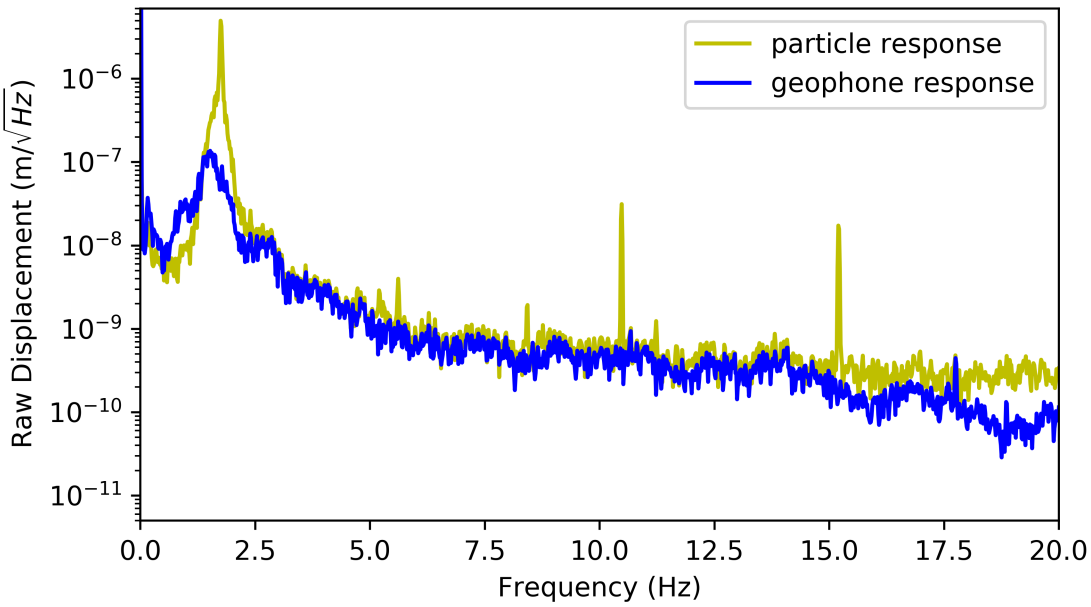


Figure 10.32: The raw displacement data of the particle and geophone in units of $\mathrm{m}/\sqrt{\mathrm{Hz}}$ without a drive.

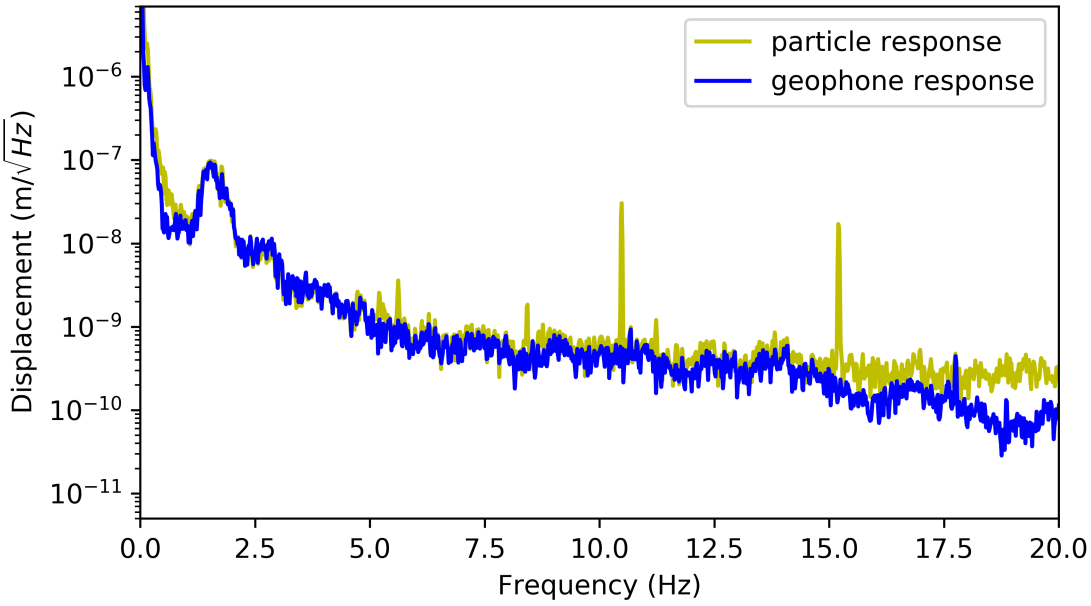


Figure 10.33: The displacement data of the particle and geophone with their harmonic oscillator responses divided out in units of $\mathrm{m}/\sqrt{\mathrm{Hz}}$ without a drive.

CHAPTER ELEVEN

SILICON CARBIDE IN G MEASUREMENTS

11.1 Introduction

In chapter 2, the different materials successfully loaded into optical traps and magneto-gravitational traps were discussed. Nitrogen vacancy (NV) centers in a levitated diamond have long been proposed for quantum superposition measurements [51–53] by coupling the spin of the defect center to its center-of-mass motion. However, with evidence of graphitization and burning [59] causing particle loss, diamond has proved impractical for high and ultra-high vacuum applications. Silicon carbide (SiC) can be used instead, utilizing the silicon V2 defect and its spin state as a quantum handle, similar to NV centers. Not only can the spin states be used to construct superposition states, silicon V2 defect spin states can assist in a measurement of G and have advantages over the microspheres typically trapped. Methods for producing particles are described in this chapter as well as how SiC will assist in measurements of G.

Silicon carbide, typically produced in wafers, are not commercially available in spherical particles such as the microspheres used throughout the work for this dissertation. Crushing wafers can produce particles with some particles in the size range that is convenient for our experiments. However, simply crushing the wafer will not produce spherical particles. Observations in our laboratory suggest that non-spherical particles can rotate and be a possible source of heating of the center-of-mass motion.

In this chapter, several methods of etching and milling have been experimented with to produce these spherical particles in the size range we care about. These

methods include dry hydrogen etching [138–140], wet oxidation etching [141–143], and jet milling. The results of these methods are discussed.

The work done for this chapter was done with the help of Dr. Walter M. Klahold, Gabriella S. Lord, and Dakota Chapman. The samples were provided by Dr. Wolfgang Choyke and Dr. Robert Devaty of the University of Pittsburgh with the help of Colette Vacha.

11.2 Spherical Silicon Carbide Particle Processing

Unlike the microspheres used in our laboratory, there are no commercially available spherical SiC particles. A processing method has been developed to produced SiC particles in the size range and shapes used in current experiments. The target shape and size for the process is to produce SiC particles that are as close to spherical as possible, with diameters between 1.5 μm and 60 μm depending on the application.

11.2.1 Mortar and Pestle SiC Crushing

Starting from a bulk SiC wafer, the first step in the procedure is to crush and grind it with a hardened tool steel mortar and pestle, shown in Fig. 11.1. This crushing step results in particles that range from a micrometer to several hundred micrometers in size (typical results from crushing shown in Fig. 11.12). The material used was 4H homoepitaxial SiC. The typical wafer was approximately one square centimeter and approximately 600 μm thick. The sample was very pure with a nitrogen concentration $\sim 10^{13}\,\mathrm{cm}^{-3}$. The thickness and nitrogen concentration information were provided by Dr. Choyke (who supplied the sample). Once crushed, the particles require more processing.

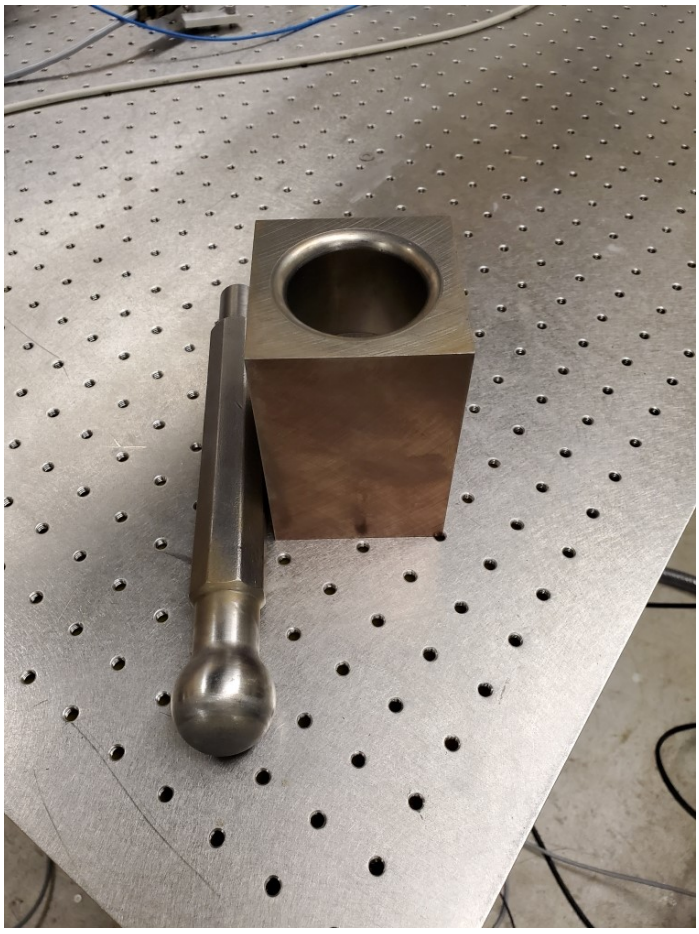


Figure 11.1: A photograph of the hardened tool steel mortar and pestle used for crushing silicon carbide wafers into particles. This particular mortar and pestle was experimentally determined to give the best results in coarse crushing of wafers.

Several tool steel mortar and pestles were used to experimentally determine the best one to produce the best starting sizes and shapes for the rest of the processing, with high yield. When the wafer is crushed, tool steel can become embedded in the SiC particles. Since tool steel is ferromagnetic, the magnetic susceptibility of the particles can become positive (attracted to large magnetic fields) and thus attracted to the pole pieces themselves. To eliminate the ferromagnetic contamination without damaging the SiC, the particles are washed in concentrated hydrochloric acid (HCl) [144]. The particles are left in the acid for several days before they are rinsed with deionized

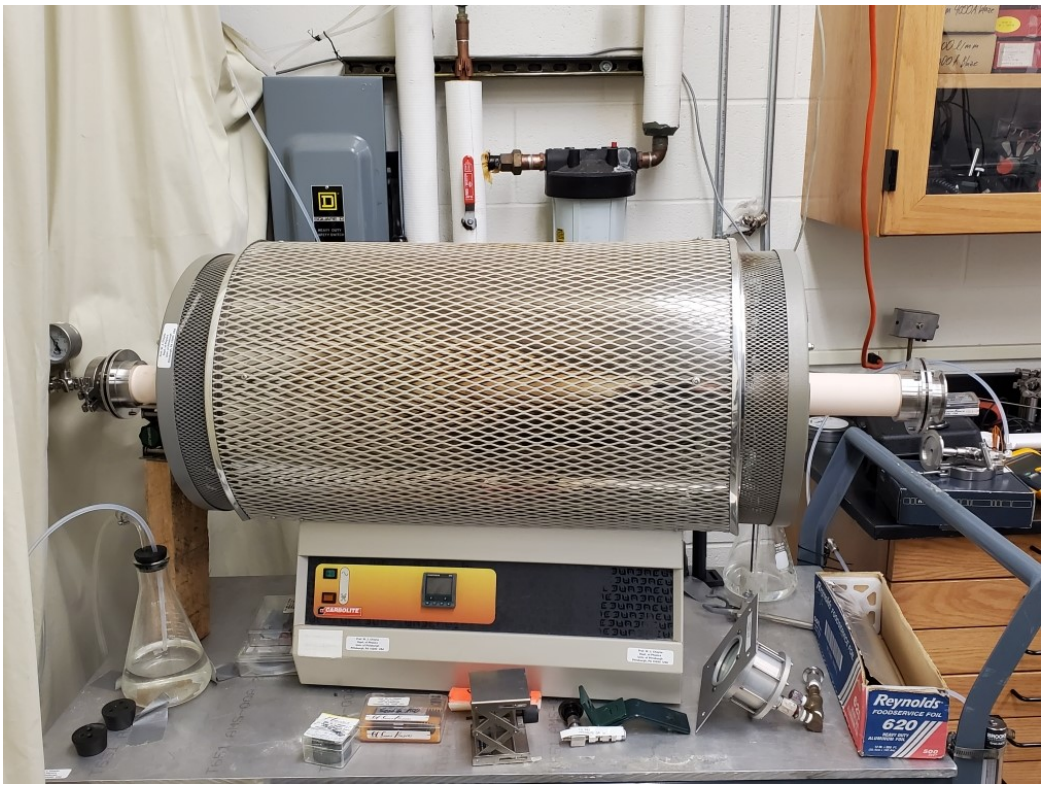


Figure 11.2: The tube furnace used in the etching experiments and annealing of silicon carbide particles and wafers. The furnace is capable of reaching 1500 °C and experiments at atmospheric pressure or vacuum.

(DI) water. This process is repeated until the particles are free of ferromagnetic tool steel. A permanent magnet is used to make this determination. When the material shows no visible movement in the presence of the magnet, the powder is considered free of the ferromagnetic material

11.2.2 Dry Hydrogen Etching

The resulting particles are not typically spherical (see Fig. 11.6), instead they are irregular with faceted surfaces. In order to prevent orientation-dependent scattering of the incident light that can prevent efficient cooling of the center-of-mass motion and limit position detection precision, the particles need to be made spherical. Etching

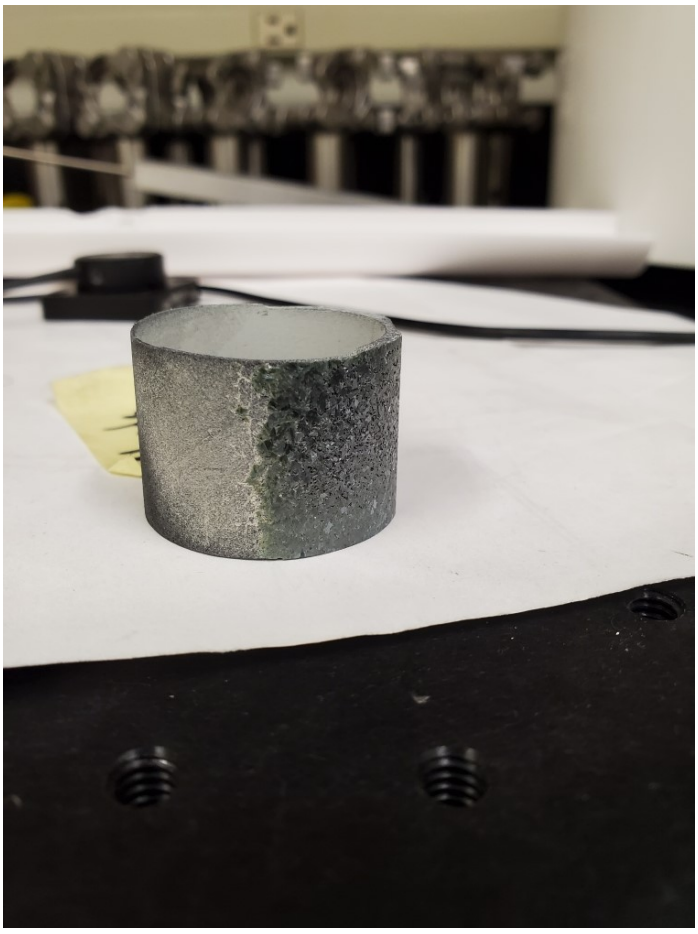


Figure 11.3: The silicon carbide crucible that was originally used for etching silicon carbide particles. In the figure, the right hand side of the crucible is etched. This led to the particles exhibiting no signs of etching, consistent with previous results.

SiC has been well studied for decades [138–140]. Two etching methods have been investigated: dry hydrogen etching and wet oxidation etching.

The dry hydrogen etching was performed in a tube furnace with a maximum temperature of 1500 °C (see Fig. 11.2). The process starts with silicon sublimation followed by hydrocarbon formation on the surface of the sample followed by desorption [145, 146].

Initially, the sample sat in an SiC crucible for etching. Upon inspection of the crucible, etching was visible on the side closest to the input, as evident in Fig. 11.3.

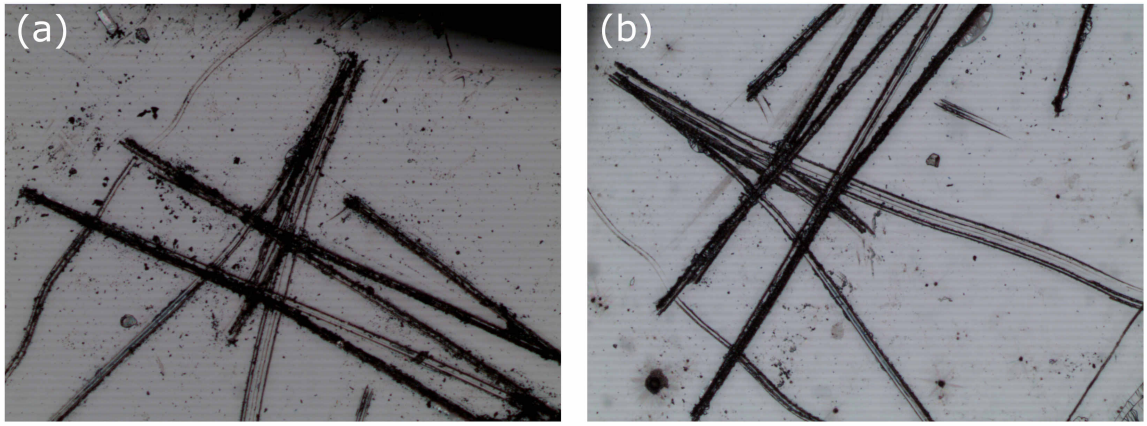


Figure 11.4: (a) A SiC wafer with scratches on the c-face. The surface was scratched to measure the etching rate. (b) The SiC wafer that sat in a SiC crucible after the etching process completed. It is nearly identical to the image in (a), indicating very minimal etching.

During these experiments, very little etching of the sample was seen. The post-etched wafer, shown in Fig. 11.4(b) is nearly identical to the pre-etched wafer, shown in Fig. 11.4(b). The etching is limited by the hydrogen mass concentration when the hydrogen concentration is approximately 5% [145, 146]. All subsequent etching experiments used aluminum oxide (alumina) boats to hold the samples.

The sample, whether it is particles or a wafer, is placed in an alumina crucible. The crucible sits at the center of an alumina half-pipe. The half-pipe is slid into the tube furnace carefully, as to not tip the crucible. Two alumina plugs are inserted in either side of the tube furnace to help thermally insulate the tube from the laboratory. The plugs are inserted approximately 9 in from the end of the tube furnace.

A 5% hydrogen and 95% argon by volume mix is used with ultrahigh purity argon as a carrier gas. To prevent the hydrogen from (possible) burning in the presence of oxygen at high temperatures, the furnace tube is pumped down to low vacuum with a roughing pump (Edwards XDS10). Fluorinated ethylene propylene (FEP) tubing is connected to the two gas cylinders and to two flowmeters. One flowmeter is for high

flow rates (7872 sccm for Ar gas) and the other is used for low flow rates (727 sccm for Ar gas). The unit sccm is standard cubic centimeter per minute. The hydrogen-argon mix was supplied to the furnace tube at a constant pressure and flow rate. The argon gas was supplied to the furnace tube during the heat up and cooling down to prevent oxide formation.

To enhance the silicon sublimation, the etching is performed in low vacuum. A valve at the output of the furnace tube is used to throttle the pumping speed of the roughing pump with a gauge on the valve measuring the pressure. During the etching process, the pressure is kept at 20 Torr.

The dry hydrogen etching performed is quite simple. The first step is to ramp up the temperature of the furnace from room temperature to 1500 °C with a constant flow of ultra-high purity argon in the range of 100 sccm to 200 sccm. The temperature ramp up is limited to a maximum of 300 °C/hr, typically 1 °C/min. Once at the target temperature, the hydrogen-argon mix is flowed into the furnace at a flow rate in the range of 700 sccm to 3000 sccm. The etching was performed over a time period between approximately 1 hr and 30 hr.

11.2.3 Wet Oxidation Etching

After the dry hydrogen etching proved unable to produce spherical particles as well as having rougher surface than pre-etched particles (typical results shown in Fig. 11.7), another technique was used that relied on a different chemical process. The SiC can be heated in an environment containing water vapor. This results in silicon oxide (SiO_2) forming that is volatilized, removing the SiO_2. The chemical equation that governs this process is [147–149]

$$SiC + 3H_2O(g) = SiO_2 + 3H_2(g) + CO(g) \tag{11.1}$$

$$SiO_2 + 2H_2O(g) = Si(OH)_4(g) \tag{11.2}$$

Unlike the dry hydrogen etching, the wet oxidation is performed at atmospheric pressure. The ultra-high purity argon gas is the only gas used for this method. During the ramp up from room temperature to 1500 °C, the argon gas is bubbled through DI water that is kept at room temperature before it enters the tube furnace. The flow rate is set to 120 sccm. When the furnace is at its target temperature, the DI water is heated to 80 °C and the argon flow rate is set to 200 sccm. This results in a water vapor partial pressure of 355 Torr [141]. The output flow is bubbled through room temperature DI water during the entire process to act as a one way valve and flow detector.

This procedure was based on the assumption that the etching will be limited by the water vapor diffusion into an amorphous layer of SiO_2 [142, 143]. The edges and corners will then etch faster than the faceted surfaces. This etching will result in irregular shaped particles becoming more spherical (typical results shown in Fig. 11.11).

11.2.4 Jet Mill Processing

As described below in the results section, the dry hydrogen and wet oxidation etching methods proved promising for producing spherical particles. The furnace where the etching is done takes hours to ramp up and down slowly while always having hour long dwell times at the target temperature. The temperatures required for etching will also anneal out silicon vacancy defects. A third method was developed that greatly reduced processing times and produced the most promising results yet.

A jet mill from The Jet Pulverizer Co. was purchased for this procedure. The jet mill shown in Fig. 11.5 uses compressed air to circulate particles fed into the mill.



Figure 11.5: The jet mill used to process particles without the need of high temperature etching. Using compressed air, the silicon carbide particles are reduced in size and rounded by collisions off of the walls of the mill and other particles.

The particles collide with the walls of the mill and other particles to reduce their size. The second compressed air line is used to feed the particles into the mill via a small hopper. When the particles reach a certain size, they are ejected into a container at the bottom of the jet mill (not pictured in Fig. 11.5). Particles too small to be collected are forced into the white bag.

As with the other two methods, the particles are first crushed with the mortar and pestle to obtain particles that are several hundred micrometers in diameter. Experimentally, it was determined that loading only SiC particles in the jet mill produced a fine dust. Sugar, soluble in water, was added as a diluting material for the SiC particles in the mill. It was experimentally determined that the best results

were achieved by added the sugar quickly after adding the SiC particles to the mill. The jet mill process takes seconds to minutes to finish, greatly speeding up etching.

11.3 Results

11.3.1 Dry Hydrogen Etching Results

The etching results are most sensitive to the etch time and flow rate of the hydrogen-argon mix during etching. To illustrate the effects of hydrogen etching, two examples were chosen to discuss. The first is the etching of crushed homoepitaxial SiC particles washed with hydrochloric acid. All particle and wafer images in this appendix were acquired on an optical microscope with a 10× objective.

The particle in Fig. 11.6 is typical of pre-etched particles crushed by the mortar and pestle shown in Fig. 11.1. The particle is irregularly shaped with faceted surfaces that tend to be smooth. The particle shown was subject to dry hydrogen etching for 5 hrs with a hydrogen-argon mix flow rate of 730 sccm at a temperature 1500 °C.

Following the etching, Fig. 11.7 shows a typical particle. The particle shown may not necessarily be the post-etching particle in Fig. 11.6. For these experimental parameters, the particles are consistently about 20% smaller in diameter but only slightly more spherical. The faceted surfaces are no longer smooth. These surfaces are rough containing small pits likely due to sublimation of silicon without complete desorption of carbon.

A bulk sample of 4H boule SiC before etching is shown in Fig. 11.8. For this etching process, the silicon face was facing up in the furnace tube. Other etching runs had the carbon face oriented upward with similar results. Before etching, scratches were intentionally engraved on the face to investigate the effects of etching on the face of the sample as well as the edge. The pre-etch thickness was measured to be approximately 360 µm. Homoepitaxial particles were also placed in the furnace to

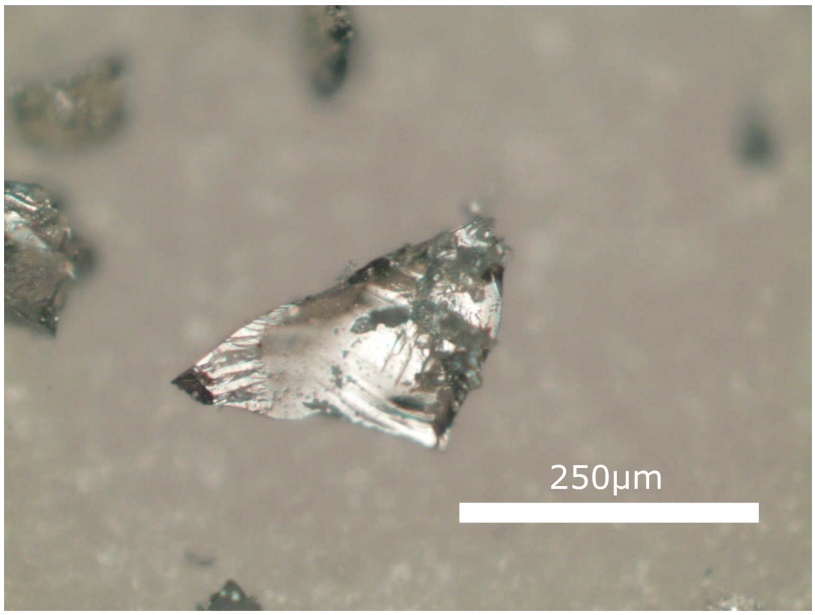


Figure 11.6: A silicon carbide particle that has been crushed with the mortar and pestle shown in Fig. 11.1 before dry hydrogen etching. The particle is approximately 200 µm wide.

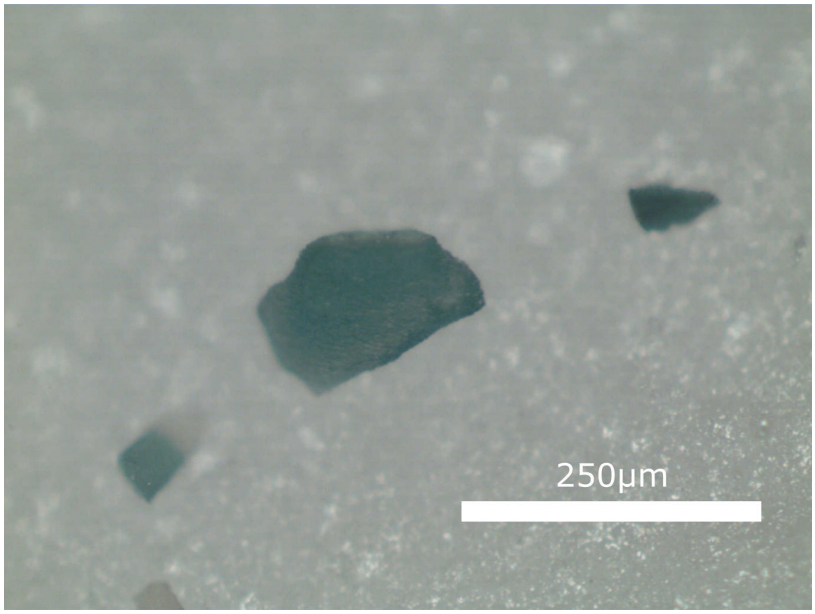


Figure 11.7: A silicon carbide particle after the dry hydrogen etching process. The etching in general reduces the size of the particles but does not round them or make them smoother. They are typically rougher with etch pits on the surfaces.

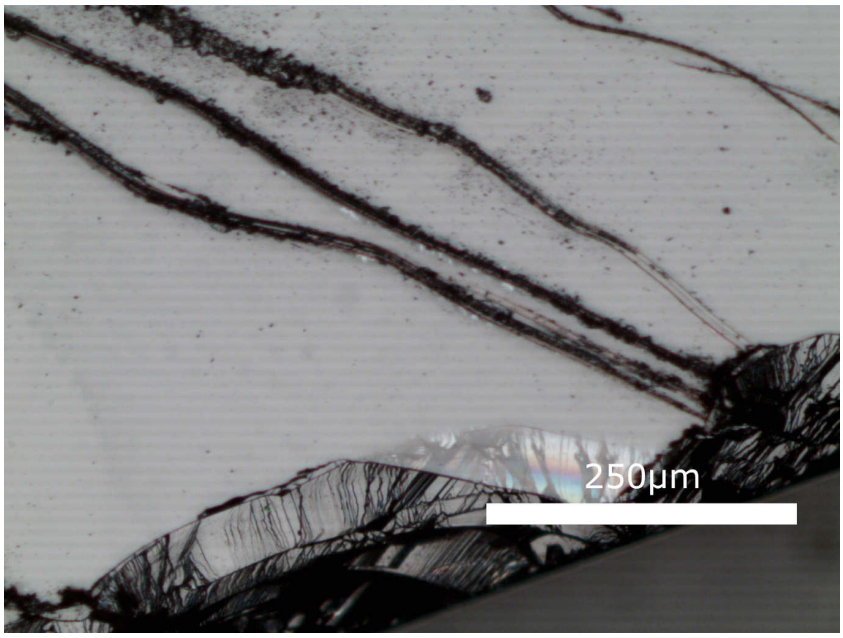


Figure 11.8: A bulk silicon carbide wafer before dry hydrogen etching. The surface was scratched to investigate the etching of the bulk surface.

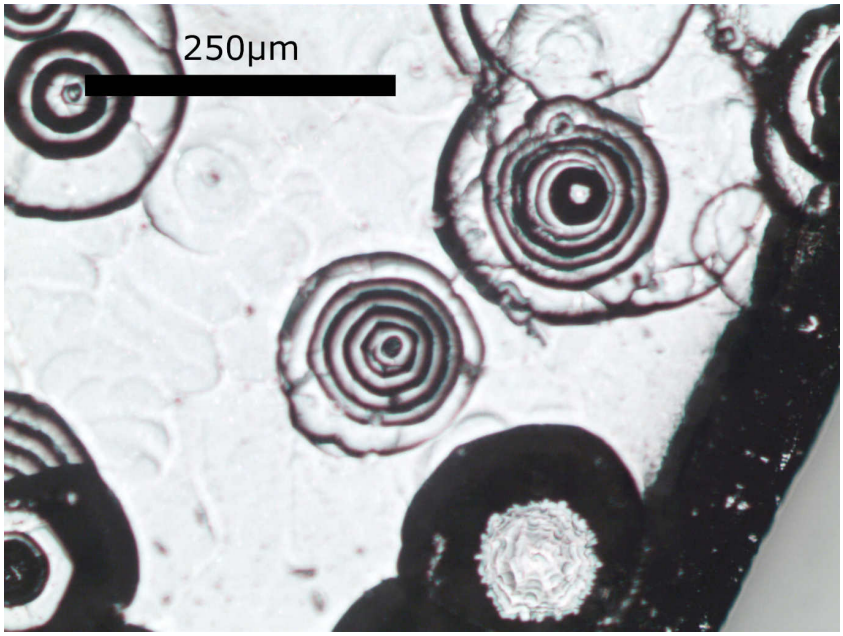


Figure 11.9: The silicon carbide wafer after dry hydrogen etching. The scratches have been etched away completely. Hexagonal and circular pits were etched into the surfaces.

investigate the effect of etching on them at the same time. During this procedure, all of the particles were etched completely away and none remained.

The sample was etched with the hydrogen-argon mix at a temperature of 1500 °C. The gas mixture had a flow rate of 2100 sccm for 30 min. The result is shown in Fig. 11.9. The image shows the same location on the bulk sample as Fig. 11.8. The scratches have been etched away. The edge of the sample has also been etched, flatter overall but with finer structure such as pits. The most notable feature is the pits that formed on the surface. These pits are circular and hexagonal in shape and vary in depth. The position of the pits are not on the original scratches. This implies that the surface was etched enough to eliminate the scratches as the pits were most likely seeded by defects in the sample. The thickness after etching was 320 μm. Approximately 40 μm has been etched away.

11.3.2 Wet Oxidation Etching Results

The wet oxidation etching was performed with several furnace temperatures ranging from 1200 °C to 1500 °C while the other parameters were held constant to the values described above in the Wet Oxidation Etching section. A group of homoepitaxial 4H SiC particles that have been crushed with the mortar and pestle and washed with HCl acid shown in Fig. 11.10.

The particles in Fig. 11.10 show the typical particle shape before this etching process. The particles have a wide range of sizes from 10 μm to 500 μm. In general, these particles are not spherical. Images of two particles after etching at a temperature of 1500 °C are shown in Fig. 11.11. Virtually no particles have sharp edges and corners nor show signs of surface roughness after the etching process.

The particles' irregular shapes are all more spherical than before etching. More experimentation can lead to more sphericity. This is measured by examining the

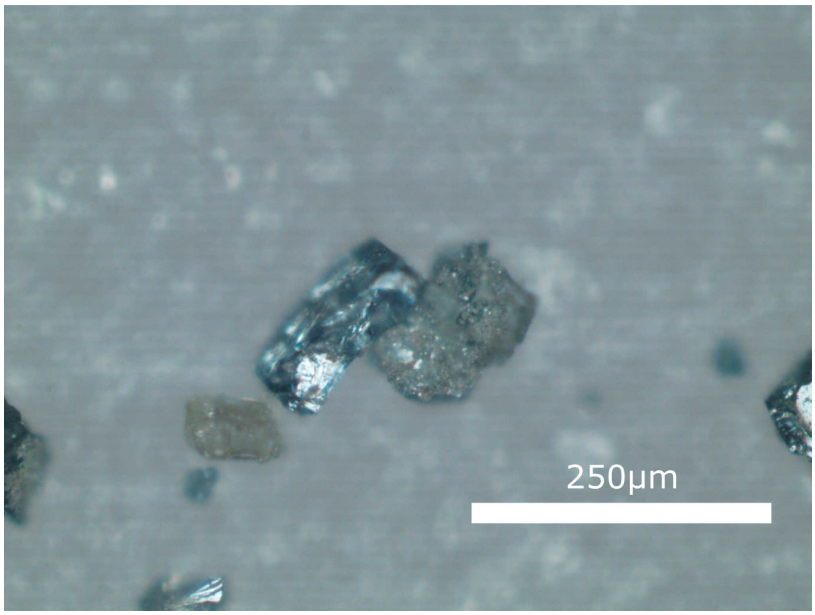


Figure 11.10: Typical silicon carbide particles crushed with the mortar and pestle before the wet oxidation etching. The particles are typically rough and have no preferred shape.

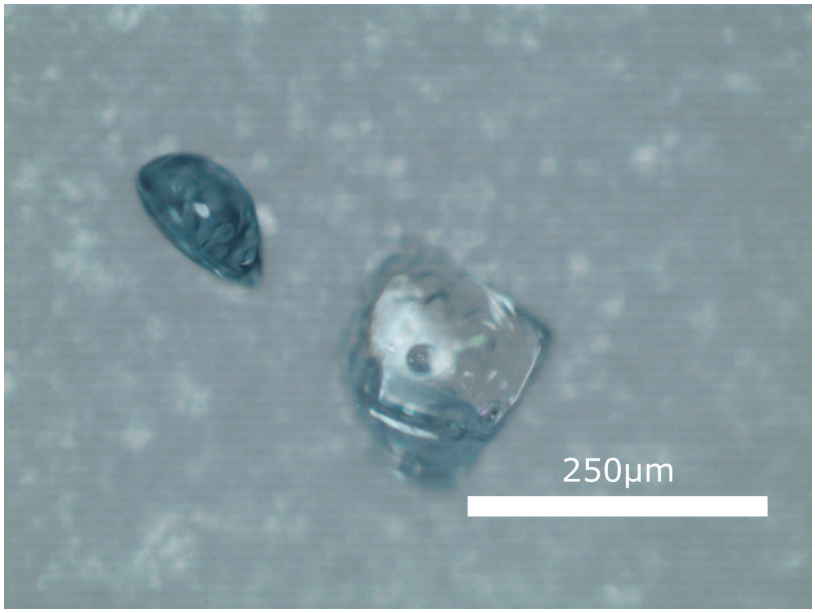


Figure 11.11: Particles after wet oxidation etching. They are smaller and more smooth. The particles are also more spherical, consistent with predictions.

particles under an optical microscope. It should be noted that the wet oxidation method matches the expected results. The majority of the particles increased in sphericity. Compared to the dry hydrogen etching, this is the more promising method.

11.3.3 Jet Mill Processing Results

The particles before the etching process are shown in Fig. 11.12. The particles are approximately 100 μm and are extremely rough and irregularly shaped. The SiC particles were poured into the jet mill quickly followed by a full packet of sugar (typically 2 g to 4 g).

For the results presented in Fig. 11.13, the air pressure for the feeding of the particles into the jet mill was set to 40 psi and 15 psi for the grinding pressure. After the simple processing in the jet mill, the particles are very smooth and much more spherical. The particles resulted in an approximately 50% reduction in diameter for these pressure settings.

This etching method proves promising for manufacturing spherical SiC particles. Unfortunately, not every particle is perfect. However, with new loading techniques, the wanted particles can be separated and loaded one at a time.

11.4 Silicon Carbide for a Measurement of G

Silicon carbide exhibits several properties that make it a more ideal material than nanodiamonds or other glasses such as silica or borosilicate glass. First, SiC is diamagnetic, a requirement for stable trapping in our system. It can be more pure and better quality than the other materials since silica is amorphous and often contains water. Borosilicate glass has impurities that may be the cause of the excess damping described in chapter 10, though that is still an open question. Ideally, the particle should be electrically insulating to prevent loss due to eddy currents. Silicon carbide

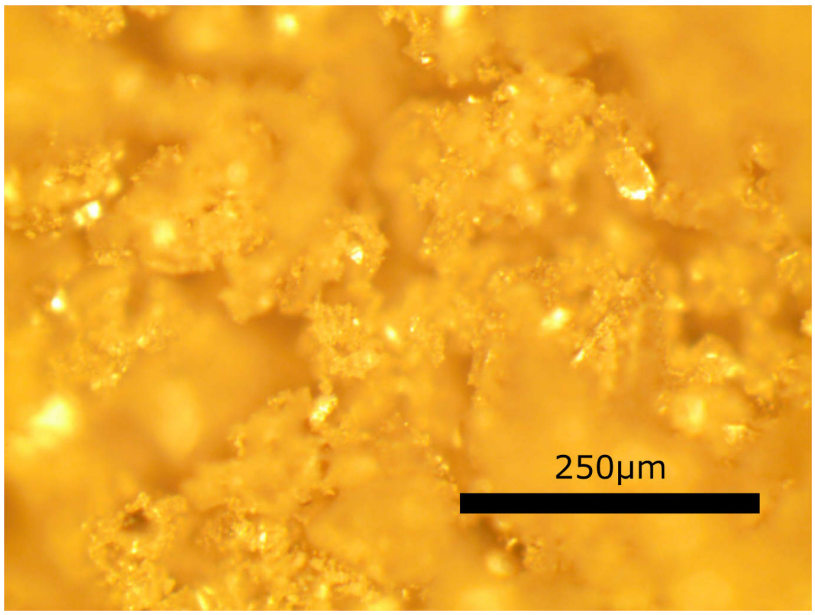


Figure 11.12: Silicon carbide particles after crushing with the mortar and pestle. For this particular jet milling, the particles are extremely rough. Though this was unintentional, it helps illustrates the results from jet milling.

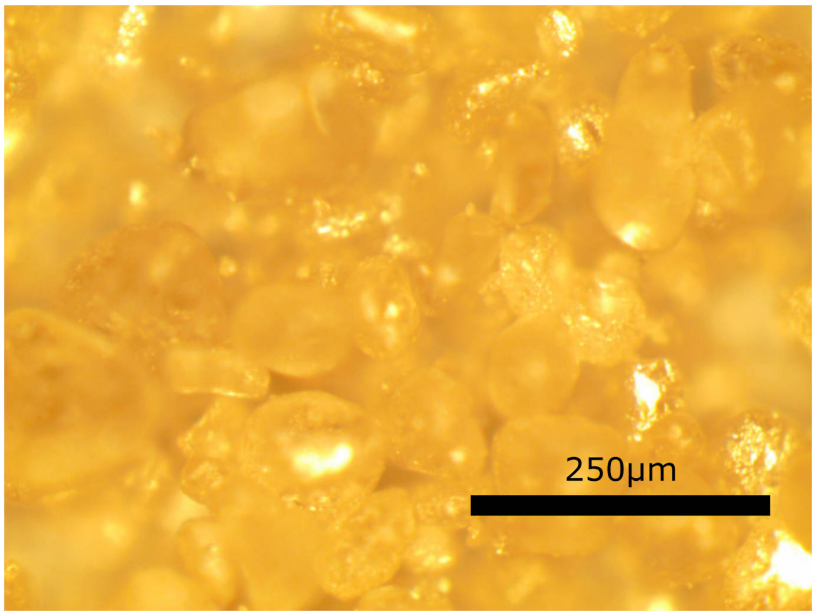


Figure 11.13: The silicon carbide particles after the jet milling procedure. It is evident that not only are the particles extremely smooth, but they are much more spherical than after the other methods.

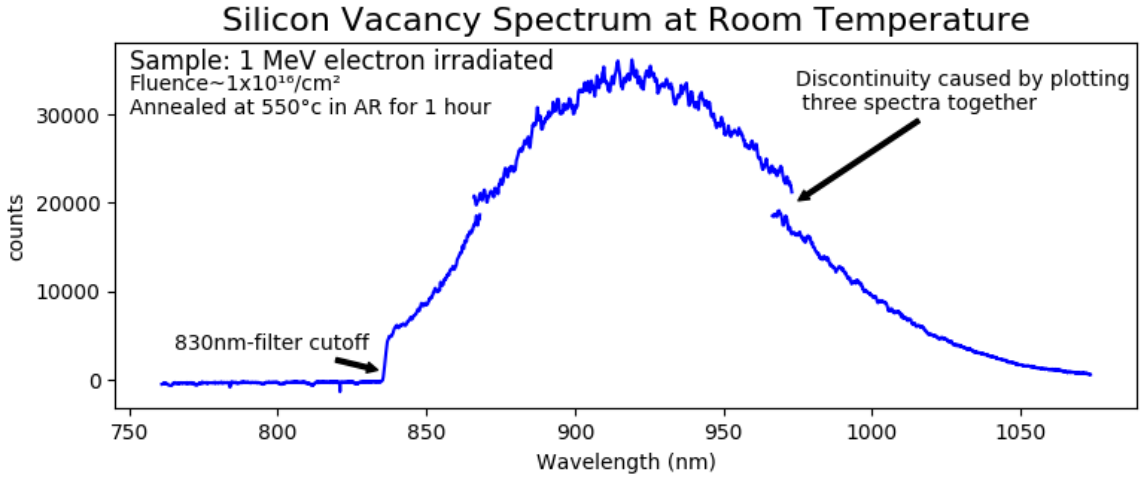


Figure 11.14: A room temperature spectrum of electron irradiated 4H homoepitaxial silicon carbide wafer. The sample was irradiated with 1 MeV electrons with a fluence of $10^{-16}\,\mathrm{cm}^{-2}$. The spectrum follows the correct shape of that in the literature [2].

being a large bandgap semiconductor meets this requirement.

Of particular interest, defects in SiC can be used to create superposition states similar to that of NV centers in diamond. In addition to quantum experiments, the quantum spin of certain defects can assist in measurements of Newton's constant of gravity by using photoluminescence (PL) from the defects. These defects can be optically readout and manipulated easily.

For this particular experiment, we choose to use the singly negatively charged silicon vacancy defect center [150] with spin $S = 3/2$. In 4H SiC, the most common mass produced polytype, there are two such silicon vacancies corresponding to different lattice sites. The V_1 silicon vacancy is a missing silicon atom at a hexagonal site (h site) and the V_2 silicon vacancy is a missing silicon atom at a cubic site (k site) [151]. At low temperatures, zero phonon lines are visible at 861.4 nm for the V_1 defect and 916.5 nm for the V_2 defect [152]. At room temperature, however, there is no evidence of V_1 [153–155]. A spectrum of the V_2 defect PL is shown in Fig. 11.14.

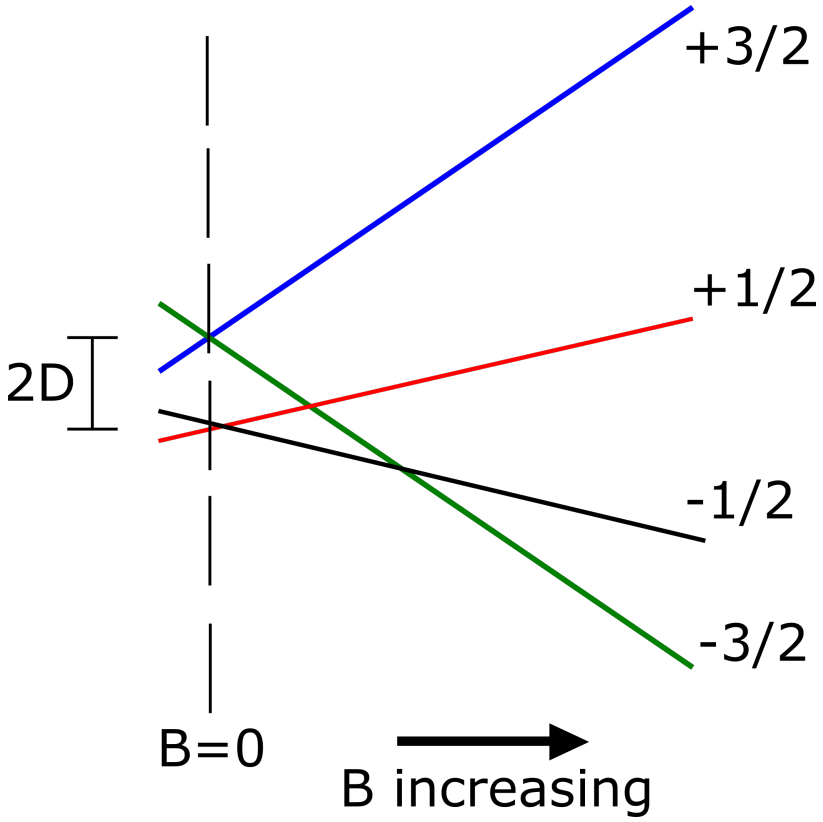


Figure 11.15: A simple illustrating showing the splitting of the energy levels in 4H silicon carbide in the presence of an external magnetic field. With no external field, the splitting is $2D = 70\,\mathrm{MHz}$.

Since the trapping experiments are performed at room temperature, the V_1 silicon vacancy defect is of no use to us.

To fabricate particles that contain silicon vacancy defects, first we will start with bulk 4H homoepitaxial SiC. The bulk sample will be electron irradiated by collaborators with energies greater than 1 MeV with a fluence in the range of $10^{15}\,\mathrm{cm}^{-2}$ to $10^{17}\,\mathrm{cm}^{-2}$. Once the sample is irradiated, it is annealed in ultra-high purity argon for an hour to eliminate unwanted defects. The sample is crushed with the mortar and pestle and processed in the jet mill. To etch in the furnace, the particles would need to be irradiated after the etching as the silicon vacancy would be annealed away.

A sample that has been investigated is bulk homoepitaxial 4H SiC. The sample

was irradiated with 1 MeV electrons with a fluence of $10^{16}\,\mathrm{cm}^{-2}$ and annealed for an hour at 550 °C. The V_2 defect is pumped with a 780 nm diode laser confocally. A spectrum of the V_2 defect PL is shown in Fig. 11.14.

Without an external magnetic field, energy levels of the spin states are separated by 70 MHz. A microwave field oscillating on resonance near the defect will cause a decrease in PL intensity on the order of 0.1% [2]. In the presence of an external magnetic field oriented parallel to the carbon face, the energy levels split proportional to the magnetic field (see Fig. 11.15). The two intensity dips increase linearly apart from each other. When one hits 0 Hz, both increase linearly together while their separation stays constant. This allows the magnetic field to be precisely measured.

When the V_2 defects are in an external magnetic field that is not oriented normal to the carbon face, the splitting is no longer just proportional to the magnetic field. When the carbon face normal is at an angle, θ, to the magnetic field, it has been shown that the splitting between the two intensity dips is proportional to $\cos^2\theta$ [155]. Combining all of this information, we can know both the magnetic field that a trapped particle is in as well as its orientation, giving us rotation information as well.

11.5 Conclusions

In this chapter, several methods for producing spherical silicon carbide particles were presented. The three methods: dry hydrogen etching, wet oxidation etching, and jet milling all produced very different results. As described in this chapter, jet milling is the most promising.

Dry hydrogen and wet oxidation etching requires high temperature close or at 1500 °C which will anneal out the V2 silicon vacancy center. This center is the reason we want to switch to silicon carbide in the first place. These methods also take hours to perform. Because of the quick turnaround time for processing particles as well

not requiring high temperatures, the jet milling process is attractive for producing spherical particles, as well as resulting in the most spherical particles of the three.

CHAPTER TWELVE

CONCLUSION

This dissertation presents the history of precision measurements of the Newtonian constant of gravitation starting from Henry Cavendish up until Li and others in 2018, as well as the difficulties in these experiments. A review of levitated optomechanical systems presents the key features of each including oscillation frequencies, vacuum pressures achieved, and maximum amplitudes of motion. The system used for the work in this dissertation is described in great detail. The use of this system for a future measurement of Newton's constant has also be detailed.

Technological advances relevant for a precision measurement of Newton's constant were developed and described. A new, compact loading horn circuit was designed. The magneto-gravitational Paul trap used for trapping large particles was presented. With this method, borosilicate microspheres up to 63 μm in diameter have been successfully levitated. A high voltage variable voltage reference was designed that provided a DC voltage to the magneto-gravitational trap that is stable to within 3 ppm over three days.

The use of a CMOS camera for feedback control was demonstrated. A self-excitation limiter is demonstrated to excite the levitated particle to consistently prepare the amplitude of motion for multiple data sets to within 1%, conservatively. This is an upper estimate based on the limitation of the image analysis used for this data. Active optical table stabilization was designed and realized to keep the tilt of the table stable with an RMS value of 0.35 μrad for three days.

An analysis of anharmonicities in the trap are explained due to unwanted sources of charge on the pole pieces of the trap. Despite this issue, the target frequency of

0.1 Hz was achieved. This is currently, to the best of our knowledge, the lowest oscillation frequency measured in a levitated optomechanical system.

High sensitivity accelerometry was also performed in this system. Using the particle as an accelerometer, a direct comparison was made with a commercial geophone. To test the calibration of both systems, a 5 Hz drive was applied to the optical table in the axial direction. The two systems measured this drive to within 3% of each other. Using a new image analysis technique, the precision of the particle displacement is limited by shot noise and was found to be 1.6 nm per frame, or 160 $\mathrm{pm}/\sqrt{\mathrm{Hz}}$. For a thermal limited system, the upper bound on the sensitivity was measured at $3.6 \times 10^{-8}\,\mathrm{g}/\sqrt{\mathrm{Hz}}$ with the upper bound on the cooled temperature of 9 K.

12.1 Improvements

Several improvements can and need to be made before a measurement of G can happen. Currently, there are two limiting factors that are preventing this measurement. The first is the anharmonicity of the trapping potential and sources of charge on the pole pieces. These anharmoncities can cause a shift in the oscillation frequency of the particle that masks the phase accumulation measurement. It is also extremely critical to prepare the particle to near the same amplitude for each measurement since a small change in amplitude can cause a large difference in frequency.

The second limitation is the excess damping in the system. Since we intend for the damping time to be much longer than the measurement time, this issue will need to be addressed. Despite high and ultra-high vacuum, the particle damping was still on the order of several minutes to several hours. This can be a result of an interaction between the charged particle and the unwanted charge on the pole pieces

or the impurities in the borosilicate microspheres used in this work.

A simple solution to try to solve both of these problems is to load a single particle at a time. In doing so, the contamination of the trap with charged particles that failed to load would be eliminated. This would greatly improve the harmonicity of the particle motion as well as eliminating one possible source of excess damping. Gold plating the pole pieces will also prevent patch charges on them that can be causing these problems.

Another solution is to use more pure materials for microspheres. Silica and silicon carbide can be used instead to eliminate impurities in the trapped particles. Silica has the advantage of being commercially available in a wide range of sizes, whereas point defects in silicon carbide can be used to obtain more information about the motion of the particle.

The above limitations need to be resolved before a precision measurement of G can be made. In addition, several other improvements can be made. Larger particles will decrease vacuum limited damping as well as decreasing the thermal motion of the particle relative to the amplitude of motion. Though extremely difficult, improvements to the DC voltage source can be made to have a more stable potential. The camera-based feedback and active table stabilization can be improved as well. Currently, however, the current limiting factor is the anharmonicity due to the charge on the pole pieces. Though the target frequency was reached, the motion was still anharmonic, indicating much need for improvement. By lowering the frequency as much as possible, the measured phase accumulation will be larger, making the measurement easier. Temperature regulating the magneto-gravitational trap will improve the magnetic field stability and prevent unwanted drifts in the particle's location.

12.2 Future Outlook

The work of this dissertation sets up a measurement of the Newtonian constant of gravitation after several improvements. The current target precision of 10 ppm would be the most precise measurement to date though the system can possibly offer better precision with more work and improvements. Designs for the next iteration of the G experiment are described in appendix C. A space-based mission to measure G in micro-g environments may also a future direction of this experiment.

12.3 Significance of this Dissertation

This dissertation lays out the ground work for a measurement of G for a levitated particle in a magneto-gravitational trap capable of producing the most precise measurement ever made. In addition to this, several technological advances were made that can not only improve this precision measurement but be useful in many other systems in both fundamental and applied physics. The lowest oscillation frequency of any levitated optomechanical system has been achieved.

The most significant contribution to science and engineering is the high sensitivity acceleration measurement. Several groups around the world have been headed in this direction recently. This is the first direct use of a levitated optomechanical system at room temperature as an accelerometer as well as the only system to do so. Based on discussions with several groups and agencies, at the time of writing this dissertation, our sensitivity is the best in the world for any room temperature levitated optomechanical system at $3.6 \times 10^{-8}\,\mathrm{g}/\sqrt{\mathrm{Hz}}$.

REFERENCES CITED

[1] Henry Cavendish. Experiments to determine the density of the earth. *Philos. Trans. Royal Soc.*, 88:469–526, 1798.

[2] SG Carter, ÖO Soykal, Pratibha Dev, Sophia E Economou, and ER Glaser. Spin coherence and echo modulation of the silicon vacancy in 4 h- sic at room temperature. *Phys. Rev. B*, 92(16):161202, 2015.

[3] Isaac Newton. Philosophiæ naturalis principia mathematica. *London*, 1686.

[4] C. Vernon Boys and Frederick Abel. The newtonian constant of gravitation. In *Proceedings, Volume 14*, pages 353–378. Royal Institution of Great Britain, 1894.

[5] E Tiesinga, PJ Mohr, DB Newell, and BN Taylor. The 2018 codata recommended values of the fundamental physical constants. *Web Version*, 8, 2019.

[6] Joel M Weisberg, David J Nice, and Joseph H Taylor. Timing measurements of the relativistic binary pulsar psr b1913+ 16. *Astrophys. J.*, 722(2):1030, 2010.

[7] Albert Einstein. Zur elektrodynamik bewegter körper. *Ann. Phys.*, 322(10):891–921, 1905.

[8] Albert Einstein. Die feldgleichungen der gravitation. *Sitzung der physikalische-mathematischen Klasse*, 25:844–847, 1915.

[9] John Henry Poynting. *The Mean Density of the Earth: An Essay to which the Adams Prize was Adjudged in 1893 in the University of Cambridge*. C. Griffin, Limited, 1894.

[10] Franz Richarz and Otto Krigar-Menzel. Gravitationsconstante und mittlere dichtigkeit der erde, bestimmt durch wägungen. *Ann. Phys.*, 302(10):177–193, 1898.

[11] Charles Vernon Boys. I. on the newtonian constant of gravitation. *Philos. Trans. Royal Soc. A)*, 186:1–72, 1895.

[12] Paul R Heyl and Peter Chrzanowski. A redetermination of the constant of gravitation. *J. Res. Natl. Bur. Stand.*, 1930.

[13] Paul R Heyl and Peter Chrzanowski. A new determination of the constant of gravitation. *J. Res. Natl. Bur. Stand.*, 29:31, 1942.

[14] Gabriel G Luther and William R Towler. Redetermination of the newtonian gravitational constant g. *Phys. Rev. Lett.*, 48(3):121, 1982.

[15] OV Karagioz and VP Izmailov. Measurement of the gravitational constant with a torsion balance. *Meas. Tech.*, 39(10):979–987, 1996.

[16] Charles H Bagley and Gabriel G Luther. Preliminary results of a determination of the newtonian constant of gravitation: a test of the kuroda hypothesis. *Phys. Rev. Lett.*, 78(16):3047, 1997.

[17] F Nolting, J Schurr, St Schlamminger, and W Kündig. A value for g from beam-balance experiments. *Meas. Sci. Technol.*, 10(6):487, 1999.

[18] JH Gundlach, EG Adelberger, Blayne R Heckel, and HE Swanson. New technique for measuring newton's constant g. *Phys. Rev. D*, 54(2):R1256, 1996.

[19] RD Rose, HM Parker, RA Lowry, A Rc Kuhlthau, and JW Beams. Determination of the gravitational constant g. *Phys. Rev. Lett.*, 23(12):655, 1969.

[20] Jens H Gundlach and Stephen M Merkowitz. Measurement of newton's constant using a torsion balance with angular acceleration feedback. *Phys. Rev. Lett.*, 85(14):2869, 2000.

[21] SJ Richman, TJ Quinn, CC Speake, and RS Davis. Preliminary determination of g using the bipm torsion strip balance. *Measurement Science and Technology*, 10(6):460, 1999.

[22] TJ Quinn, CC Speake, SJ Richman, RS Davis, and A Picard. A new determination of g using two methods. *Phys. Rev. Lett.*, 87(11):111101, 2001.

[23] Qing Li, Chao Xue, Jian-Ping Liu, Jun-Fei Wu, Shan-Qing Yang, Cheng-Gang Shao, Li-Di Quan, Wen-Hai Tan, Liang-Cheng Tu, Qi Liu, et al. Measurements of the gravitational constant using two independent methods. *Nature*, 560(7720):582, 2018.

[24] Texas Instruments. Stacking the ref50xx for high voltage references, 2013.

[25] JMW Milatz, JJ Van Zolingen, and BB Van Iperen. The reduction in the brownian motion of electrometers. *Physica*, 19(1-12):195–202, 1953.

[26] Donald J Douglas, Aaron J Frank, and Dunmin Mao. Linear ion traps in mass spectrometry. *Mass Spectrom. Rev.*, 24(1):1–29, 2005.

[27] Fernando Monteiro, Wenqiang Li, Gadi Afek, Chang-ling Li, Michael Mossman, and David C Moore. Force and acceleration sensing with optically levitated nanogram masses at microkelvin temperatures. *arXiv preprint arXiv:2001.10931*, 2020.

[28] Arthur Ashkin. Acceleration and trapping of particles by radiation pressure. *Phys. Rev. Lett.*, 24(4):156, 1970.

[29] Tongcang Li. Millikelvin cooling of an optically trapped microsphere in vacuum. In *Fundamental Tests of Physics with Optically Trapped Microspheres*, pages 81–110. Springer, 2013.

[30] Alexander D Rider, Charles P Blakemore, Giorgio Gratta, and David C Moore. Single-beam dielectric-microsphere trapping with optical heterodyne detection. *Phys. Rev. A*, 97(1):013842, 2018.

[31] Gambhir Ranjit, David P Atherton, Jordan H Stutz, Mark Cunningham, and Andrew A Geraci. Attonewton force detection using microspheres in a dual-beam optical trap in high vacuum. *Phys. Rev. A*, 91(5):051805, 2015.

[32] Gambhir Ranjit, Mark Cunningham, Kirsten Casey, and Andrew A Geraci. Zeptonewton force sensing with nanospheres in an optical lattice. *Phys. Rev. A*, 93(5):053801, 2016.

[33] Fernando Monteiro, Sumita Ghosh, Elizabeth C van Assendelft, and David C Moore. Optical rotation of levitated spheres in high vacuum. *Phys. Rev. A*, 97(5):051802, 2018.

[34] David C Moore, Alexander D Rider, and Giorgio Gratta. Search for millicharged particles using optically levitated microspheres. *Phys. Rev. Lett.*, 113(25):251801, 2014.

[35] A Ashkin and JM Dziedzic. Optical levitation in high vacuum. *Appl. Phys. Lett.*, 28(6):333–335, 1976.

[36] A Ashkin and JM Dziedzic. Feedback stabilization of optically levitated particles. *Appl. Phys. Lett.*, 30(4):202–204, 1977.

[37] J Millen, PZG Fonseca, T Mavrogordatos, TS Monteiro, and PF Barker. Cavity cooling a single charged levitated nanosphere. *Phys. Rev. Lett.*, 114(12):123602, 2015.

[38] Vijay Jain, Jan Gieseler, Clemens Moritz, Christoph Dellago, Romain Quidant, and Lukas Novotny. Direct measurement of photon recoil from a levitated nanoparticle. *Phys. Rev. Lett.*, 116(24):243601, 2016.

[39] David Hempston, Jamie Vovrosh, Marko Toroš, George Winstone, Muddassar Rashid, and Hendrik Ulbricht. Force sensing with an optically levitated charged nanoparticle. *Appl. Phys. Lett.*, 111(13):133111, 2017.

[40] Jan Gieseler, Bradley Deutsch, Romain Quidant, and Lukas Novotny. Subkelvin parametric feedback cooling of a laser-trapped nanoparticle. *Phys. Rev. Lett.*, 109(10):103603, 2012.

[41] Michael Mazilu, Yoshihiko Arita, Tom Vettenburg, Juan M Auñón, Ewan M Wright, and Kishan Dholakia. Orbital-angular-momentum transfer to optically levitated microparticles in vacuum. *Phys. Rev. A*, 94(5):053821, 2016.

[42] PZG Fonseca, EB Aranas, J Millen, TS Monteiro, and PF Barker. Nonlinear dynamics and strong cavity cooling of levitated nanoparticles. *Phys. Rev. Lett.*, 117(17):173602, 2016.

[43] Jamie Vovrosh, Muddassar Rashid, David Hempston, James Bateman, Mauro Paternostro, and Hendrik Ulbricht. Parametric feedback cooling of levitated optomechanics in a parabolic mirror trap. *J. Opt. Soc. Am. B*, 34(7):1421–1428, 2017.

[44] Nikolai Kiesel, Florian Blaser, Uroš Delić, David Grass, Rainer Kaltenbaek, and Markus Aspelmeyer. Cavity cooling of an optically levitated submicron particle. *Proc. Natl. Acad. Sci. U.S.A.*, 110(35):14180–14185, 2013.

[45] Jan Gieseler, Lukas Novotny, and Romain Quidant. Thermal nonlinearities in a nanomechanical oscillator. *Nat. Phys.*, 9(12):806, 2013.

[46] Felix Tebbenjohanns, Martin Frimmer, Andrei Militaru, Vijay Jain, and Lukas Novotny. Cold damping of an optically levitated nanoparticle to microkelvin temperatures. *Phys. Rev. Lett.*, 122(22):223601, 2019.

[47] Dominik Windey, Carlos Gonzalez-Ballestero, Patrick Maurer, Lukas Novotny, Oriol Romero-Isart, and René Reimann. Cavity-based 3d cooling of a levitated nanoparticle via coherent scattering. *Phys. Rev. Lett.*, 122(12):123601, 2019.

[48] Peter Asenbaum, Stefan Kuhn, Stefan Nimmrichter, Ugur Sezer, and Markus Arndt. Cavity cooling of free silicon nanoparticles in high vacuum. *Nat. Commun.*, 4:2743, 2013.

[49] Thai M Hoang, Yue Ma, Jonghoon Ahn, Jaehoon Bang, F Robicheaux, Zhang-Qi Yin, and Tongcang Li. Torsional optomechanics of a levitated nonspherical nanoparticle. *Phys. Rev. Lett.*, 117(12):123604, 2016.

[50] Levi P Neukirch, Jan Gieseler, Romain Quidant, Lukas Novotny, and A Nick Vamivakas. Observation of nitrogen vacancy photoluminescence from an optically levitated nanodiamond. *Opt. Lett.*, 38(16):2976–2979, 2013.

[51] Marcus W Doherty, Neil B Manson, Paul Delaney, Fedor Jelezko, Jörg Wrachtrup, and Lloyd CL Hollenberg. The nitrogen-vacancy colour centre in diamond. *Phys. Rep.*, 528(1):1–45, 2013.

[52] Viva R Horowitz, Benjamín J Alemán, David J Christle, Andrew N Cleland, and David D Awschalom. Electron spin resonance of nitrogen-vacancy centers in optically trapped nanodiamonds. *Proc. Natl. Acad. Sci. U.S.A.*, 109(34):13493–13497, 2012.

[53] Zhang-qi Yin, Tongcang Li, Xiang Zhang, and LM Duan. Large quantum superpositions of a levitated nanodiamond through spin-optomechanical coupling. *Phys. Rev. A*, 88(3):033614, 2013.

[54] Fernando Monteiro, Sumita Ghosh, Adam Getzels Fine, and David C Moore. Optical levitation of 10-ng spheres with nano-g acceleration sensitivity. *Phys. Rev. A*, 96(6):063841, 2017.

[55] Agnese Callegari, Mite Mijalkov, A Burak Gököz, and Giovanni Volpe. Computational toolbox for optical tweezers in geometrical optics. *J. Opt. Soc. Am. B*, 32(5):B11–B19, 2015.

[56] Demi Rose St John et al. *Theoretical analysis and experimental design of dual-beam optical trap for large particles*. PhD thesis, Montana State University-Bozeman, College of Letters & Science, 2018.

[57] Charles W Lewandowski, Wm Randall Babbitt, and Brian D'Urso. Comparison of magneto-gravitational and optical trapping for levitated optomechanics. In *Optical Trapping and Optical Micromanipulation XVI*, volume 11083, page 110831C. International Society for Optics and Photonics, 2019.

[58] David Patrick Atherton. *Sensitive Force Measurements with Optically Trapped Micro-Spheres in High Vacuum*. PhD thesis, University of Nevada, Reno, 2015.

[59] ATMA Rahman, AC Frangeskou, MS Kim, S Bose, GW Morley, and PF Barker. Burning and graphitization of optically levitated nanodiamonds in vacuum. *Sci. Rep.*, 6:21633, 2016.

[60] Samuel Earnshaw. On the nature of the molecular forces which regulate the constitution of the luminferous ether. *Trans. Camb. Phil. Soc.*, 7:97–112, 1842.

[61] Wolfgang Paul and Helmut Steinwedel. Ein neues massenspektrometer ohne magnetfeld. *Zeitschrift für Naturforschung A*, 8(7):448–450, 1953.

[62] Raymond E March and John F Todd. *Quadrupole ion trap mass spectrometry*, volume 165. John Wiley & Sons, 2005.

[63] Hartmut Häffner, Christian F Roos, and Rainer Blatt. Quantum computing with trapped ions. *Phys. Rep.*, 469(4):155–203, 2008.

[64] Dietrich Leibfried, Rainer Blatt, Christopher Monroe, and David Wineland. Quantum dynamics of single trapped ions. *Rev. Mod. Phys.*, 75(1):281, 2003.

[65] Zheng Ouyang, Ethan R Badman, and R Graham Cooks. Characterization of a serial array of miniature cylindrical ion trap mass analyzers. *Rapid Commun. Mass Spectrom.*, 13(24):2444–2449, 1999.

[66] Oleg Kornienko, Peter TA Reilly, William B Whitten, and J Michael Ramsey. Micro ion trap mass spectrometry. *Rapid Commun. Mass Spectrom.*, 13(1):50–53, 1999.

[67] Garth E Patterson, Andrew J Guymon, Leah S Riter, Mike Everly, Jens Griep-Raming, Brian C Laughlin, Zheng Ouyang, and R Graham Cooks. Miniature cylindrical ion trap mass spectrometer. *Anal. Chem.*, 74(24):6145–6153, 2002.

[68] D Cruz, JP Chang, M Fico, AJ Guymon, DE Austin, and MG Blain. Design, microfabrication, and analysis of micrometer-sized cylindrical ion trap arrays. *Rev. Sci. Instrum.*, 78(1):015107, 2007.

[69] Linan Jiang, William B Whitten, and Stanley Pau. A planar ion trapping microdevice with integrated waveguides for optical detection. *Opt. Express*, 19(4):3037–3043, 2011.

[70] Raymond E March. An introduction to quadrupole ion trap mass spectrometry. *J. Mass Spectrom.*, 32(4):351–369, 1997.

[71] Y Cai, W-P Peng, S-J Kuo, YT Lee, and H-C Chang. Single-particle mass spectrometry of polystyrene microspheres and diamond nanocrystals. *Anal. Chem.*, 74(1):232–238, 2002.

[72] Sung-Cheol Seo, Seung-Kyun Hong, and Doo-Wan Boo. Single nanoparticle ion trap (snit): A novel tool for studying in-situ dynamics of single nanoparticles. *Bulletin of the Korean Chemical Society*, 24(5):552–554, 2003.

[73] S Arnold and LM Folan. Fluorescence spectrometer for a single electrodynamically levitated microparticle. *Rev. Sci. Instrum.*, 57(9):2250–2253, 1986.

[74] Mo Yang, Peter TA Reilly, Kirk B Boraas, William B Whitten, and J Michael Ramsey. Real-time chemical analysis of aerosol particles using an ion trap mass spectrometer. *Rapid Commun. Mass Spectrom.*, 10(3):347–351, 1996.

[75] David T Suess and Kimberly A Prather. Mass spectrometry of aerosols. *Chem. Rev.*, 99(10):3007–3036, 1999.

[76] Wen-Ping Peng, Yi-Chang Yang, Ming-Wei Kang, Yuan T Lee, and Huan-Cheng Chang. Measuring masses of single bacterial whole cells with a quadrupole ion trap. *J. Am. Chem. Soc.*, 126(38):11766–11767, 2004.

[77] EL Raab, M Prentiss, Alex Cable, Steven Chu, and David E Pritchard. Trapping of neutral sodium atoms with radiation pressure. *Phys. Rev. Lett.*, 59(23):2631, 1987.

[78] C Monroe, W Swann, H Robinson, and C Wieman. Very cold trapped atoms in a vapor cell. *Phys. Rev. Lett.*, 65(13):1571, 1990.

[79] Zhaokun Zhou, Helen Miller, Adam JM Wollman, and Mark C Leake. Developing a new biophysical tool to combine magneto-optical tweezers with super-resolution fluorescence microscopy. In *Photonics*, volume 2, pages 758–772. Multidisciplinary Digital Publishing Institute, 2015.

[80] Z Hu and HJ Kimble. Observation of a single atom in a magneto-optical trap. *Opt. Lett.*, 19(22):1888–1890, 1994.

[81] MD Simon and AK Geim. Diamagnetic levitation: flying frogs and floating magnets. *J. Appl. Phys.*, 87(9):6200–6204, 2000.

[82] John David Jackson. *Classical electrodynamics*. John Wiley & Sons, 2007.

[83] Jen-Feng Hsu, Peng Ji, Charles W Lewandowski, and Brian D'Urso. Cooling the motion of diamond nanocrystals in a magneto-gravitational trap in high vacuum. *Sci. Rep.*, 6:30125, 2016.

[84] Bradley R Slezak, Charles W Lewandowski, Jen-Feng Hsu, and Brian D'Urso. Cooling the motion of a silica microsphere in a magneto-gravitational trap in ultra-high vacuum. *New J. Phys.*, 20:063028, 2018.

[85] Walter M Klahold, Charles W Lewandowski, Paul Nachman, Bradley R Slezak, and Brian D'Urso. Precision optomechanics with a particle in a magneto-gravitational trap. In *Optical, Opto-Atomic, and Entanglement-Enhanced Precision Metrology*, volume 10934, page 109340P. International Society for Optics and Photonics, 2019.

[86] JP Houlton, ML Chen, MD Brubaker, KA Bertness, and CT Rogers. Axisymmetric scalable magneto-gravitational trap for diamagnetic particle levitation. *Rev. Sci. Instrum.*, 89(12):125107, 2018.

[87] MC O'Brien, S Dunn, JE Downes, and J Twamley. Magneto-mechanical trapping of micro-diamonds at low pressures. *Appl. Phys. Lett.*, 114(5):053103, 2019.

[88] W Braunbeck. Free suspension of bodies in electric and magnetic fields. *Z. Phys.*, 112:753–763W, 1939.

[89] Th Gast. Development of the magnetic suspension balance. *Measurement*, 4(2):53–62, 1986.

[90] M Uesaka, A Suzuki, N Takeda, Y Yoshida, and K Miya. Ac magnetic properties of ybacuo bulk superconductor in high tc superconducting levitation. *Cryogenics*, 35(4):243–247, 1995.

[91] Javier Serrano-Tellez, Fernando Romera-Juarez, David González-de María, Mikel Lamensans, Heribert Argelaguet-Vilaseca, José-Luis Pérez-Díaz, Juan Sánchez-Casarrubios, Efrén Díez-Jiménez, and Ignacio Valiente-Blanco. Experience on a cryogenic linear mechanism based on superconducting levitation. In *Modern Technologies in Space-and Ground-based Telescopes and Instrumentation II*, volume 8450, page 84501Y. International Society for Optics and Photonics, 2012.

[92] Chris Timberlake, Giulio Gasbarri, Andrea Vinante, Ashley Setter, and Hendrik Ulbricht. Acceleration sensing with magnetically levitated oscillators above a superconductor. *Appl. Phys. Lett.*, 115(22):224101, 2019.

[93] Arthur Ashkin and JM Dziedzic. Optical levitation by radiation pressure. *Appl. Phys. Lett.*, 19(8):283–285, 1971.

[94] Jen-Feng Hsu. *Cooling the center-of-mass motion of a diamond nanocrystal in a magneto-gravitational trap*. PhD thesis, University of Pittsburgh, 2016.

[95] K Strnat, G Hoffer, J Olson, W Ostertag, and JJ Becker. A family of new cobalt-base permanent magnet materials. *J. Appl. Phys.*, 38(3):1001–1002, 1967.

[96] David Brown, Bao-Min Ma, and Zhongmin Chen. Developments in the processing and properties of ndfeb-type permanent magnets. *J. Magn. Magn. Mater.*, 248(3):432–440, 2002.

[97] Michael A Laughton and Maurice George Say. *Electrical engineer's reference book*. Elsevier, 2013.

[98] Raymond L Sanford and Evert G Bennett. A determination of the magnetic saturation induction of iron at room temperature. *J. Res. Nat. Bureau Standards*, 26(1):1–12, 1941.

[99] Bradley Slezak. *Feedback Cooling the Mechanical Motion of a Diamagnetic Particle in a Magneto-Gravitational Trap*. PhD thesis, University of Pittsburgh, 2018.

[100] David J Griffiths. *Introduction to electrodynamics*. American Association of Physics Teachers, 2005.

[101] Liu Lin-Xia, Liu Qi, Shao Cheng-Gang, Zhang Ya-Ting, Luo Jun, and Vadim Milyukov. Measurement of density inhomogeneity for glass pendulum. *Chin. Phys. Lett.*, 25(12):4203, 2008.

[102] Shan-Qing Yang, Liang-Cheng Tu, Cheng-Gang Shao, Qing Li, Qing-Lan Wang, Ze-Bing Zhou, and Jun Luo. Direct measurement of the anelasticity of a tungsten fiber. *Phys. Rev. D*, 80(12):122005, 2009.

[103] Robert R Perron. The design and application of a reliable ultrasonic atomizer. *IEEE Transactions on Sonics and Ultrasonics*, 14(4):149–152, 1967.

[104] Boris V Derjaguin, Vladimir M Muller, and Yu P Toporov. Effect of contact deformations on the adhesion of particles. *J. Colloid Interface Sci.*, 53(2):314–326, 1975.

[105] Lars-Oliver Heim, Jürgen Blum, Markus Preuss, and Hans-Jürgen Butt. Adhesion and friction forces between spherical micrometer-sized particles. *Phys. Rev. Lett.*, 83(16):3328, 1999.

[106] Tongcang Li. *Fundamental tests of physics with optically trapped microspheres*. Springer Science & Business Media, 2012.

[107] William B Whitten, Peter TA Reilly, and J Michael Ramsey. High-pressure ion trap mass spectrometry. *Rapid Commun. Mass Spectrom.*, 18(15):1749–1752, 2004.

[108] H Winter and HW Ortjohann. Simple demonstration of storing macroscopic particles in a paul trap. *Am. J. Phys.*, 59(9):807–813, 1991.

[109] John R Taylor. *Classical mechanics*. University Science Books, 2005.

[110] Claudiu Genes, David Vitali, Paolo Tombesi, Sylvain Gigan, and Markus Aspelmeyer. Ground-state cooling of a micromechanical oscillator: Comparing cold damping and cavity-assisted cooling schemes. *Phys. Rev. A*, 77(3):033804, 2008.

[111] Ned J Corron, Shawn D Pethel, and Buckley A Hopper. Controlling chaos with simple limiters. *Phys. Rev. Lett.*, 84(17):3835, 2000.

[112] Scipy.org scipy.signal.iirpeak. `https://docs.scipy.org/doc/scipy-0.19.0/reference/generated/scipy.signal.iirpeak.html`. Accessed: 2020-01-31.

[113] Charles W Lewandowski, Tyler D Knowles, Zachariah B Etienne, and Brian D'Urso. High sensitivity accelerometry with a feedback-cooled magnetically levitated microsphere. *arXiv preprint arXiv:2002.07585*, 2020.

[114] Paul S Epstein. On the resistance experienced by spheres in their motion through gases. *Phys. Rev.*, 23(6):710, 1924.

[115] Oliver Gerberding, F Guzmán Cervantes, John Melcher, Jon R Pratt, and Jacob M Taylor. Optomechanical reference accelerometer. *Metrologia*, 52(5):654, 2015.

[116] Yiliang Bao, Felipe Guzmán Cervantes, Arvind Balijepalli, John R Lawall, Jacob M Taylor, Thomas W LeBrun, and Jason J Gorman. An optomechanical accelerometer with a high-finesse hemispherical optical cavity. In *2016 IEEE International Symposium on Inertial Sensors and Systems*, pages 105–108. IEEE, 2016.

[117] Felipe Guzmán Cervantes, Lee Kumanchik, Jon Pratt, and Jacob M Taylor. High sensitivity optomechanical reference accelerometer over 10 khz. *Appl. Phys. Lett.*, 104(22):221111, 2014.

[118] Joel Moser, Alexander Eichler, Johannes Güttinger, Mark I Dykman, and Adrian Bachtold. Nanotube mechanical resonators with quality factors of up to 5 million. *Nat. Nanotechnol.*, 9(12):1007, 2014.

[119] Richard A Norte, Joao P Moura, and Simon Gröblacher. Mechanical resonators for quantum optomechanics experiments at room temperature. *Phys. Rev. Lett.*, 116(14):147202, 2016.

[120] Alexander G Krause, Martin Winger, Tim D Blasius, Qiang Lin, and Oskar Painter. A high-resolution microchip optomechanical accelerometer. *Nat. Photonics*, 6(11):768, 2012.

[121] Ying Lia Li and PF Barker. Characterization and testing of a micro-g whispering gallery mode optomechanical accelerometer. *J. Light. Technol.*, 36(18):3919–3926, 2018.

[122] Michele Armano, Heather Audley, Gerard Auger, JT Baird, Massimo Bassan, Pierre Binetruy, Michael Born, Daniele Bortoluzzi, Nico Brandt, M Caleno, et al. Sub-femto-g free fall for space-based gravitational wave observatories: Lisa pathfinder results. *Phys. Rev. Lett.*, 116(23):231101, 2016.

[123] Nan Yu, JM Kohel, JR Kellogg, and L Maleki. Development of an atom-interferometer gravity gradiometer for gravity measurement from space. *Appl. Phys. B*, 84(4):647–652, 2006.

[124] Guillaume Stern, Baptiste Battelier, Rémi Geiger, Gaël Varoquaux, André Villing, Frédéric Moron, Olivier Carraz, Nassim Zahzam, Yannick Bidel, W Chaibi, et al. Light-pulse atom interferometry in microgravity. *Eur. Phys. J. D*, 53(3):353–357, 2009.

[125] Grant Biedermann. *Gravity tests, differential accelerometry and interleaved clocks with cold atom interferometers*. Stanford University, 2008.

[126] Min-Kang Zhou, Zhong-Kun Hu, Xiao-Chun Duan, Bu-Liang Sun, Le-Le Chen, Qiao-Zhen Zhang, and Jun Luo. Performance of a cold-atom gravimeter with an active vibration isolator. *Phys. Rev. A*, 86(4):043630, 2012.

[127] GW Biedermann, X Wu, L Deslauriers, S Roy, C Mahadeswaraswamy, and MA Kasevich. Testing gravity with cold-atom interferometers. *Phys. Rev. A*, 91(3):033629, 2015.

[128] Andrew A Geraci, Scott B Papp, and John Kitching. Short-range force detection using optically cooled levitated microspheres. *Phys. Rev. Lett.*, 105(10):101101, 2010.

[129] Uroš Delić, Manuel Reisenbauer, Kahan Dare, David Grass, Vladan Vuletić, Nikolai Kiesel, and Markus Aspelmeyer. Cooling of a levitated nanoparticle to the motional quantum ground state. *Science*, 367(6480):892–895, 2020.

[130] Marc-Antoine Parseval. Mémoire sur les séries et sur lintégration complète dune équation aux différences partielles linéaires du second ordre, à coefficients constants. *Mém. prés. par divers savants, Acad. des Sciences, Paris,(1)*, 1:638–648, 1806.

[131] Stéfan van der Walt, Juan Schönberger, Johannes L. and Nunez-Iglesias, Franois Boulogne, Neil Warner, Joshua D. and Yager, Emmanuelle Gouillart, Tony Yu, and the scikit-image contributors. scikit-image: Image processing in python. *PeerJ*, 2:e453, 2014.

[132] Manuel Guizar-Sicairos and James R. Thurman, Samuel T. and Fienup. Efficient subpixel image registration algorithms. *Opt. Lett.*, 33(2):156–158, Jan 2008.

[133] Robin Kirchhoff, Conor Malcolm Mow-Lowry, VB Adya, Gerald Bergmann, S Cooper, MM Hanke, P Koch, SM Köhlenbeck, Johannes Lehmann, P Oppermann, et al. Huddle test measurement of a near johnson noise limited geophone. *Rev. Sci. Instrum.*, 88(11):115008, 2017.

[134] Texas Instruments Inc. *OPA188 Precision, Low-Noise, Rail-to-Rail Output, 36-V, Zero-Drift Operational Amplifier*, 9 2016. 2013-Revised 2016.

[135] Michael C DeSantis, Shawn H DeCenzo, Je-Luen Li, and YM Wang. Precision analysis for standard deviation measurements of immobile single fluorescent molecule images. *Opt. Express*, 18(7):6563–6576, 2010.

[136] Gerald Gabrielse, X Fei, LA Orozco, RL Tjoelker, J Haas, H Kalinowsky, TA Trainor, and W Kells. Thousandfold improvement in the measured antiproton mass. *Phys. Rev. Lett.*, 65(11):1317, 1990.

[137] Santosh Devasia, Tesfay Meressi, Brad Paden, and Eduardo Bayo. Piezoelectric actuator design for vibration suppression-placement and sizing. *J. Guid. Control Dyn.*, 16(5):859–864, 1993.

[138] TL Chu and RB Campbell. Chemical etching of silicon carbide with hydrogen. *J. Electrochem. Soc.*, 112(9):955–956, 1965.

[139] JM Harris, HC Gatos, and AF Witt. Etching characteristics of silicon carbide in hydrogen. *J. Electrochem. Soc.*, 116(3):380, 1969.

[140] Masashi Kumagawa, Hiroshi Kuwabara, and Shoji Yamada. Hydrogen etching of silicon carbide. *Jpn. J. Appl. Phys.*, 8(4):421, 1969.

[141] David R Lide. *CRC handbook of chemistry and physics*, volume 85. CRC press, 2004.

[142] Carl Wagner. Beitrag zur theorie des anlaufvorgangs. *Zeitschrift für physikalische Chemie*, 21(1):25–41, 1933.

[143] NF Mott. The theory of the formation of protective oxide films on metals.iii. *J. Chem. Soc. Faraday Trans.*, 43:429–434, 1947.

[144] V. J. Jennings. The etching of silicon carbide. *Mater. Res. Bull.*, 4:S199, 1969.

[145] Yuuki Ishida and Sadafumi Yoshida. Proposal of quasi thermal equilibrium model for etching phenomenon by gases: Example of the etching of 4h-sic by h2. *Jpn. J. Appl. Phys.*, 53(4):046501, 2014.

[146] Yuuki Ishida and Sadafumi Yoshida. Investigation of the giant step bunching induced by the etching of 4h-sic in ar–h2 mix gases. *Jpn. J. Appl. Phys.*, 55(9):095501, 2016.

[147] Edward L Brady. Chemical nature of silica carried by steam. *J. Phys. Chem.*, 57(7):706–710, 1953.

[148] Elizabeth J Opila and Raiford E Hann Jr. Paralinear oxidation of cvd sic in water vapor. *J. Am. Ceram. Soc.*, 80(1):197–205, 1997.

[149] Elizabeth J Opila. Oxidation and volatilization of silica formers in water vapor. *J. Am. Ceram. Soc.*, 86(8):1238–1248, 2003.

[150] Erik Janzén, Adam Gali, Patrick Carlsson, Andreas Gällström, Björn Magnusson, and Nguyen T Son. The silicon vacancy in sic. *Physica B: Condensed Matter*, 404(22):4354–4358, 2009.

[151] E Sörman, NT Son, WM Chen, O Kordina, Christer Hallin, and Erik Janzén. Silicon vacancy related defect in 4h and 6h sic. *Phys. Rev. B*, 61(4):2613, 2000.

[152] Franziska Fuchs. *Optical spectroscopy on silicon vacancy defects in silicon carbide*. PhD thesis, University of Würzburg, 2015.

[153] Matthias Widmann, Sang-Yun Lee, Torsten Rendler, Nguyen Tien Son, Helmut Fedder, Seoyoung Paik, Li-Ping Yang, Nan Zhao, Sen Yang, Ian Booker, et al. Coherent control of single spins in silicon carbide at room temperature. *Nat. Mater.*, 14(2):164–168, 2015.

[154] H Kraus, VA Soltamov, D Riedel, S Väth, F Fuchs, A Sperlich, PG Baranov, V Dyakonov, and GV Astakhov. Room-temperature quantum microwave emitters based on spin defects in silicon carbide. *Nat. Phys.*, 10(2):157–162, 2014.

[155] H Kraus, VA Soltamov, F Fuchs, D Simin, A Sperlich, PG Baranov, GV Astakhov, and Vladimir Dyakonov. Magnetic field and temperature sensing with atomic-scale spin defects in silicon carbide. *Sci. Rep.*, 4:5303, 2014.

[156] Wolfgang Alt. An objective lens for efficient fluorescence detection of single atoms. *Optik*, 113(3):142–144, 2002.

[157] Timo Ottenstein. *A new objective for high resolution imaging of Bose-Einstein condensates*. PhD thesis, Diploma Thesis, Universität Heidelberg, 2006.

[158] Karl D Nelson, Xiao Li, and David S Weiss. Imaging single atoms in a three-dimensional array. *Nat. Phys.*, 3(8):556–560, 2007.

[159] Robert Bücker, Aurélien Perrin, Stephanie Manz, Thomas Betz, Ch Koller, Thomas Plisson, Jörg Rottmann, Thorsten Schumm, and Jörg Schmiedmayer. Single-particle-sensitive imaging of freely propagating ultracold atoms. *New J. Phys.*, 11(10):103039, 2009.

[160] Jacob F Sherson, Christof Weitenberg, Manuel Endres, Marc Cheneau, Immanuel Bloch, and Stefan Kuhr. Single-atom-resolved fluorescence imaging of an atomic mott insulator. *Nature*, 467(7311):68–72, 2010.

[161] Bruno Zimmermann, Torben Mueller, Jakob Meineke, Tilman Esslinger, and Henning Moritz. High-resolution imaging of ultracold fermions in microscopically tailored optical potentials. *New J. Phys.*, 13(4):043007, 2011.

[162] John E Greivenkamp. *Field guide to geometrical optics*, volume 1. SPIE press Bellingham, WA, 2004.

[163] José Sasián. *Introduction to aberrations in optical imaging systems*. Cambridge University Press, 2013.

[164] Shonali Dhingra. *Quadratic coupling between a classical nanomechanical oscillator and a single spin*. PhD thesis, University of Pittsburgh, 2015.

APPENDICES

APPENDIX A

TRANS VACUO MICROSCOPE OBJECTIVE

A microscope objective to collect scattered light off of an object smaller than the diffraction limit is a crucial part of levitated optomechanical experiments. The ability to resolve the particle needs to be limited by diffraction, not aberrations. To make matters worse, the numerical aperture (NA) of the objective needs to be as large as possible to maximize collection efficiency. Since the index of refraction of all glasses are wavelength dependent, the must be optimal for a single design wavelength of light.

In most cases, this can be achieved with off-the-shelf objectives and lenses. However, due to strict requirements of the center-of-mass cooling experiment [99], most if not all commercial objectives are likely insufficient.

To remedy this, a homemade objective was designed and built. The first requirement was for the objective to fit in a vacuum chamber and contain only ultra-high vacuum compatible parts. Commercial objectives contain epoxy and other materials that cannot be baked. A homemade objective can be assembled to be ultra-high vacuum compatible but a translation and tilt stage required would also need to be placed in the chamber and manipulated from outside. Satisfying these requirements can prove difficult in practice. The objective could also be placed outside of the chamber where the particle will be imaged through a vacuum window. The window can cause serious deterioration of the image quality. However, image quality can be fixed to meet the requirements while keeping the working distance large enough to practically use outside of the chamber.

Since the experiment uses silicon detectors with a maximum quantum efficiency near 830 nm, the objective must be diffraction limited for this wavelength. To allow a large angle of scattered light to be collected, a 50 mm diameter 5 mm thick silica window was chosen due to its availability, optical flatness, and stiffness in vacuum environments.

Several homemade objectives have demonstrated diffraction limited performance using at least one custom lens [156–161]. Though custom lenses allow for larger NA's as well as more degrees of freedom for aberration correction, this method can prove difficult and expensive. This objective was designed around a single, aspherical lens (Edmund Optics #67-282). A spherical lens has surfaces that can be described with a single radius as $R^2 = X^2 + Y^2$ where X and Y are the distances in the x and y directions (z along the optical axis). An aspherical lens is described by

$$\begin{aligned} Z(Y) = \frac{Y^2}{R}\frac{1}{(1+\sqrt{1-(1+k)Y^2/R^2})} + DY^2 + EY^4 + FY^6 \\ + GY^8 + HY^{10} + JY^{12} + LY^{14} \end{aligned} \tag{A.1}$$

where Y is the height above the optical axis, R is the radius of curvature, and k is the conic constant for the shape of the lens.

The aspherical lens is a 50 mm silica lens with an NA of 0.5. The lens follows

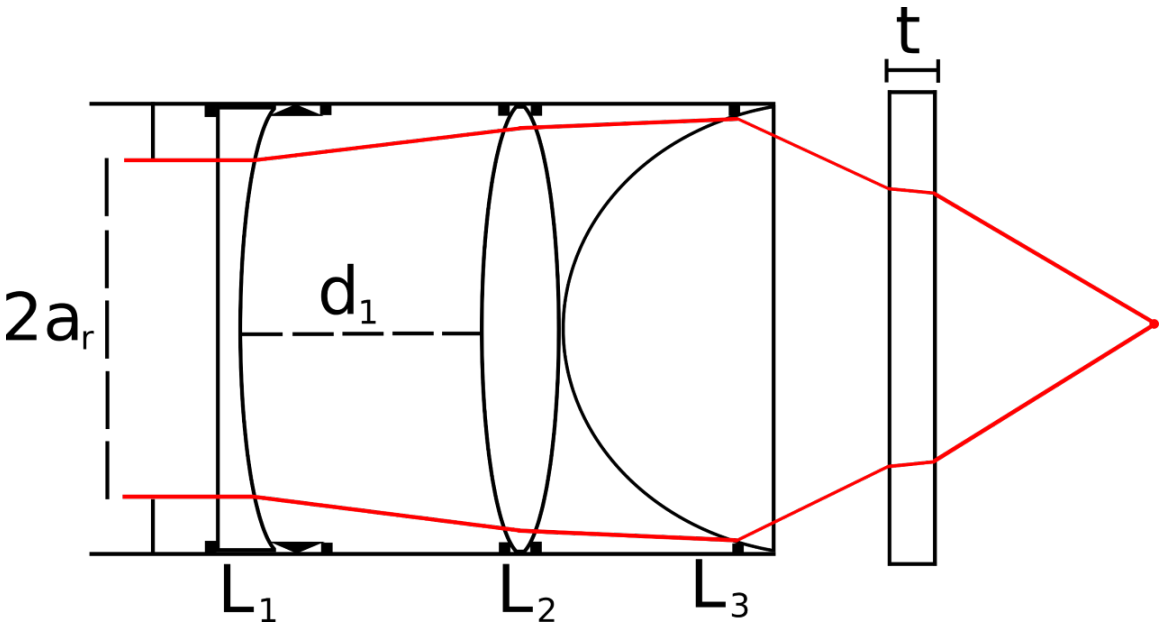


Figure A.1: The layout of the homemade microscope objective. Lens L_1 is plano-concave, lens L_2 is bi-convex, and L_3 is an aspherical lens. The objective is designed to correct spherical aberration that is introduced by the window of thickness t. An aperture stop of radius a_r is placed before lens L_1.

the prescription: $R = 22.923$ mm, $k = -1.215776$, $D = 0$, $E = 6.880041 \times 10^{-6}$, $F = 1.315975 \times 10^{-9}$, $G = 6.062407 \times 10^{-13}$, $H = 5.160185 \times 10^{-16}$, $J = 0$, and $L = 0$, where the constants D, E, F, G, H, J, and L are in appropriate units. Because of azimuthal symmetry, we only need to consider the distance away from the optical axis in a single direction.

For a wavelength λ and numerical aperture NA, the minimum spot size is the Airy disk diameter,

$$A = 1.22\frac{\lambda}{\mathrm{NA}}. \tag{A.2}$$

For this lens and design wavelength $\lambda = 830\,\mathrm{nm}$, the Airy disk diameter is $A = 2.2\,\mu\mathrm{m}$. This serves as the basis for the performance analysis of the lens and objective. A spot size near, at, or below this limit is considered diffraction limited. A spot can be slightly larger depending on the energy distribution of the spot.

With this lens picked out, the performance was initially analyzed on open source ray tracing software **goptical**. The lens on its own was analyzed without a window. The calculated spot diagram is shown in Fig. A.2. The tangential and saggital distances are the distances along two axes perpendicular to the optical axis and perpendicular to each other. The transverse ray aberration fan (a plot showing the difference between the paraxial ray and the real ray) gives information on the strength and order of the aberrations present. The ray fan in Fig. A.3

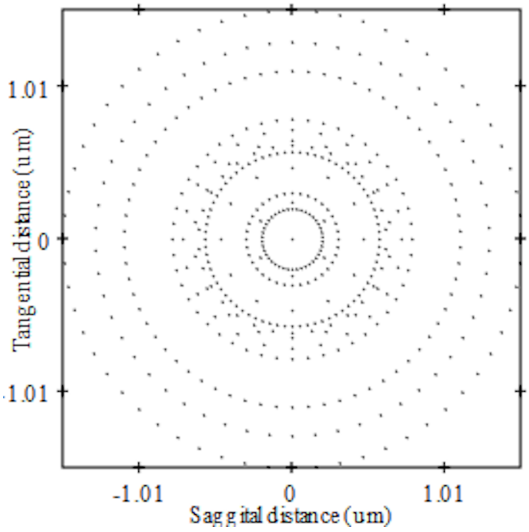


Figure A.2: The spot diagram of the aspherical lens without the window using **goptical**. The spot size indicates diffraction-limited performance with the diameter of the spot that is approximately equal to the Airy disk diameter.

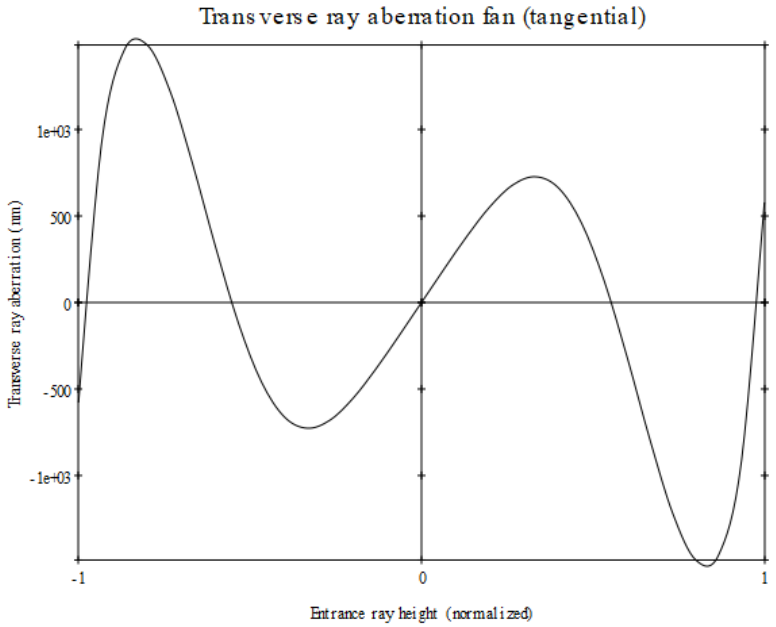


Figure A.3: The transverse ray fan calculated by **goptical**. The plot is fifth order, indicating the dominant aberration is sixth order spherical aberration.

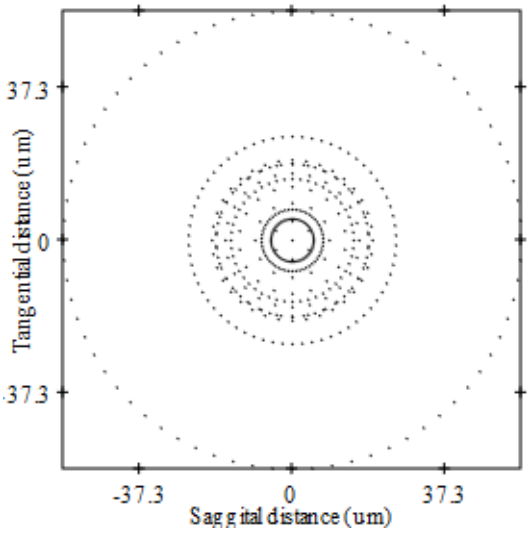


Figure A.4: The spot diagram of the aspherical lens and a 5 mm window. The diameter, not including the outer most ring, is approximately 40 μm, almost 20 times larger than the Airy disk diameter.

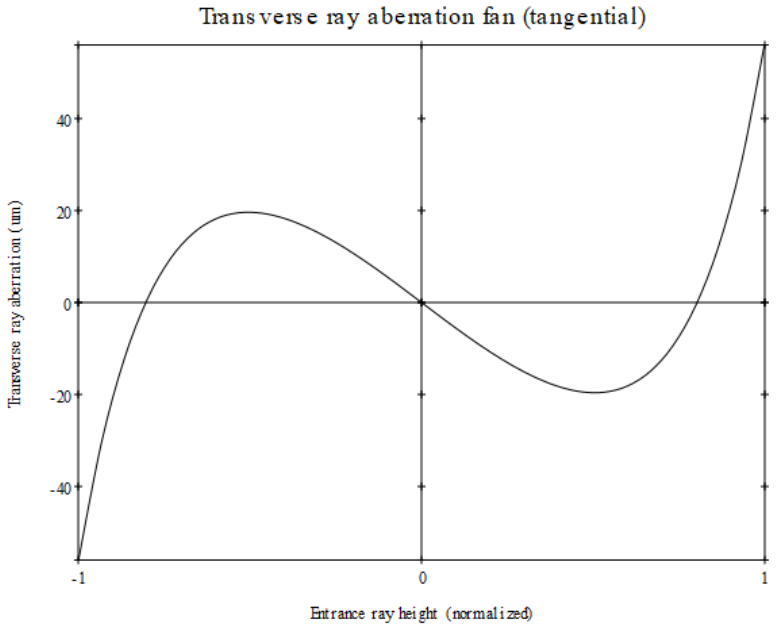


Figure A.5: The transverse ray fan calculated by **goptical**. The plot is third order, indicating the dominant aberration is fourth order spherical aberration.

corresponding the ashperical lens without a window. Since the ray fan is fifth order, the dominant aberration is sixth order. Since we are investigating on-axis aberrations, this corresponds to oblique spherical aberration.

The calculations were repeated with a 5 mm thick silica window inserted on the collection side of the aspherical lens. As shown in Fig. A.4, the spot size is much larger than the Airy disk. Ignoring the outside most ring since it does not contain much energy relative to the total intensity, the spot size is approximately 40 μm in diameter (as compared to approximately 2 μm for the Airy disk). The transverse ray aberration fan in Fig. A.5 is third order, indicating that the dominant aberration is fourth order. On-axis, this corresponds to primary spherical aberration.

By investigating the transverse ray fan, the sign of the spherical aberration can also be determined. The third order term is negative, indicating that the spherical aberration is positive. This knowledge can be used to correct this. Aberrations add with each surface in an optical system. Adding a lens or lenses that have the same magnitude but opposite sign can cancel out the aberration exactly. Since an off-the-shelf solution was sought, canceling the aberration completely is not likely.

Positive (convex) and negative (concave) lenses will introduce opposite signs of spherical aberrations. The angle at which rays hit a lens as well as the height above the optical axis determines the aberrations The distance between lenses will change the amount of aberrations present. Aberrations from a third lens (or a lens with a window) can be corrected by using one positive lens and one negative lens by adjusting the distances between the three lenses.

Since **goptical** did not have a built-in optimizer, several lenses were chosen from Thorlabs, Edmund Optics, and Newport for optimization done by myself. For the correction of the spherical aberration introduced by the window, a biconvex 2 in diameter 200 mm focal length BK7 lens (Thorlabs LB1199-B) and a plano-concave 2 in diameter −150 mm focal length BK7 lens (Newport KPC073AR.16) gave the best results. The distances were modified and the ray tracing calculations were repeated for each set of distances. It was found that the ideal distances were $d_1 = 23.03$ mm between the negative (lens 1) and positive (lens 2) lenses and $d_2 = 0.01$ mm between the positive lens and the aspherical (lens 3) lens.

The calculations were repeated with commercial software (**Zemax**) that has built-in optimization capabilities. In **Zemax**, variables can be placed on distances, thicknesses, and radii of curvature. These variables tell the optimizer what to vary. The optimizer determines the best values based on a user-set quantity, such as spot size or wavefront error.

For this problem, the off-the-shelf lenses were entered and their properties remained fixed. The only variables were the two distances and the focus was automatically adjusted to the plane with the lowest root-mean-square wavefront error. The optimizer was set to minimize the root-mean-square wavefront error by varying the two distances. For a diffraction limited system, minimizing the spot size versus the wavefront error will not result in any significant difference in the optimized variables.

Substituting in d_1 and d_2 as initial guesses for the variables to be optimized,

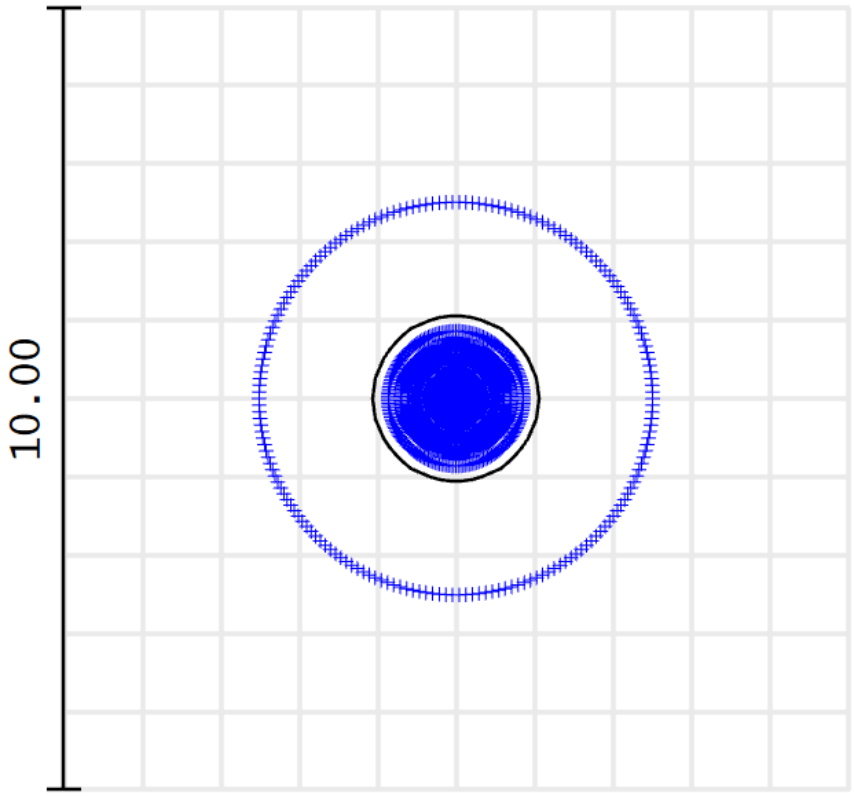


Figure A.6: The spot diagram calculated by **Zemax**. The black circle shows the Airy disk. The root-mean-square radius is 0.745 μm, well under the Airy disk radius. The outside ring contains a small fraction of the energy and does not contribute to the root-mean-square radius significantly.

Zemax returned the same values, showing that the results from **goptical** were correct. The only difference is the location of the focal plane. The spot diagram is shown in Fig. A.6. The 10.00 on the vertical axis has units of micrometers. The black circle indicates the Airy disk. The root-mean-square radius of the spot size is 0.745 μm where root-mean-square is a weighted average of the energy per radial position. The outside most ring is due to effects from the edge of the lenses and does not contribute significantly to the total energy contained in the light.

In addition to the spot diagram, we can again investigate the transverse ray fan. The ray fan plot in Fig. A.7 is seventh order on axis, indicating the dominant aberration is eighth order spherical aberration, better than the uncorrected aspherical lens without the window. The total vertical span of the transverse ray fan is ±5 μm.

The transverse ray fan and spot diagram are not the only performance metrics that can be used to evaluate an optical system. We can look at the point spread function (PSF). The image of an object is the convolution of the point spread function



Figure A.7: The transverse ray fan of the objective corrected for imaging through a 5 mm thick window. The plot is seventh order corresponding to eighth order spherical aberration.

and the object. The point spread function of a perfect diffraction limited system is the sombrero function (Airy pattern)

$$\mathrm{PSF}(r) = 4\left[\frac{J_1(2\pi r \mathrm{NA}/\lambda)}{2\pi r \mathrm{NA}/\lambda}\right]^2 \tag{A.3}$$

where NA is the numerical aperture of the objective, λ is the wavelength of the light and J_1 is the first-order Bessel function of the first kind.

The height of the central peak contains information on the wavefront error created by the objective. The ratio of the objective PSF and the diffraction limited PSF is the Strehl ratio. A Strehl ratio of 0.8 or higher is considered diffraction limited [162]. For a small wavefront error Δ, the Strehl ratio can be determined by [163]

$$S = 1 - 4\pi^2\frac{\Delta^2}{\lambda^2}. \tag{A.4}$$

From Fig. A.8, the Strehl ratio can be read off as 0.98 implying a wavefront error of $\Delta = 0.02\lambda$.

The modulation transfer function (MTF) is the Fourier transform of the PSF. The MTF is a measure of the ability of the optical system to transfer various levels of detail from objects to their images. The MTF calculated for the objective is shown

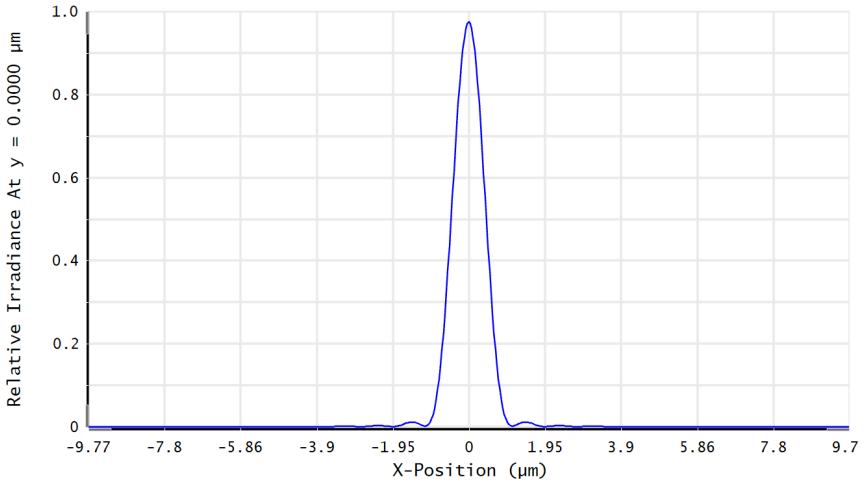


Figure A.8: The result of the **Zemax** calculation for the point spread function of the objective. The theoretical Strehl ratio is 0.98. The first zeroes of the point spread function determines the numerical aperture, calculated to be 0.48.

in Fig. A.9. The perfect diffraction limited system is shown by the black curve and the objective MTF is shown by the blue curve.

Another measure of the performance of an optical system, and the last one discussed in this dissertation is the encircled energy as a function of radius from the center of the imaged spot. Perfect diffraction limited systems will have 83.9% of their energy within the Airy disk diameter. The first bright ring will contain 7.1% of the total energy, the second ring will contain 2.8%, and the third ring will contain 1.5% of the total energy [162]. This is evident in Fig. A.10 where the diffraction limited system is shown by the black curve and the objective is shown by the blue curve.

Theoretically, the objective is diffraction limited but this means nothing unless it performs to this level experimentally. To construct the objective, two aluminum spacers were machined to separate the lenses by the prescription above. The spacers, incorrectly machined, allowed the positive lens and aspherical lens to touch as well as not centering the diverging lens properly. To remedy this, custom spacers were no longer used.

A Thorlabs SM2L30C slotted lens tube allows access to lenses within the tube. The aspherical lens is held firmly in place and centered with a Thorlabs SM2 retaining ring. Two SM2 retaining rings hold the positive lens in place and centered. Because the negative lens is plano-concave, retaining rings cannot properly center the lens. A custom aluminum ring was machined to allow the lens to be centered in the lens tube. The slotted lens tube allows for adjustment of distances between lenses without the need for multiple custom spacers.

Before characterization of the objective, it was used in some of our laboratory's experiments [84,99] with promising cooling results. To characterize the performance of

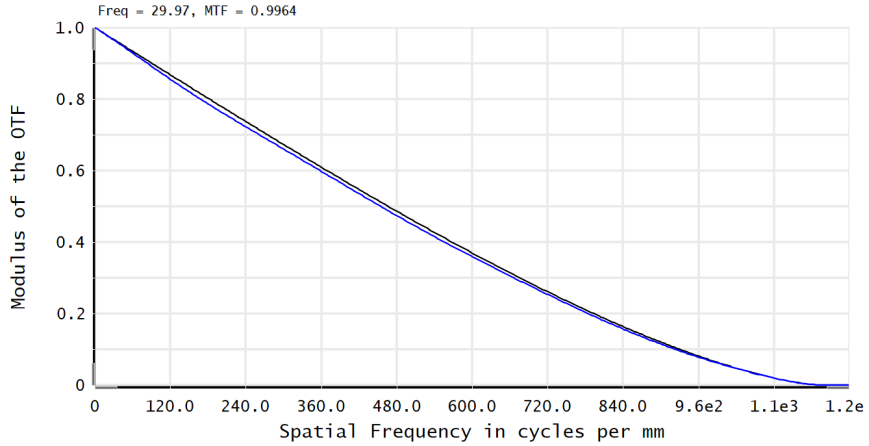


Figure A.9: The result of the **Zemax** calculation of the modulation transfer function of the objective (blue). The black curve shows the perfect diffraction limited modulation transfer function.

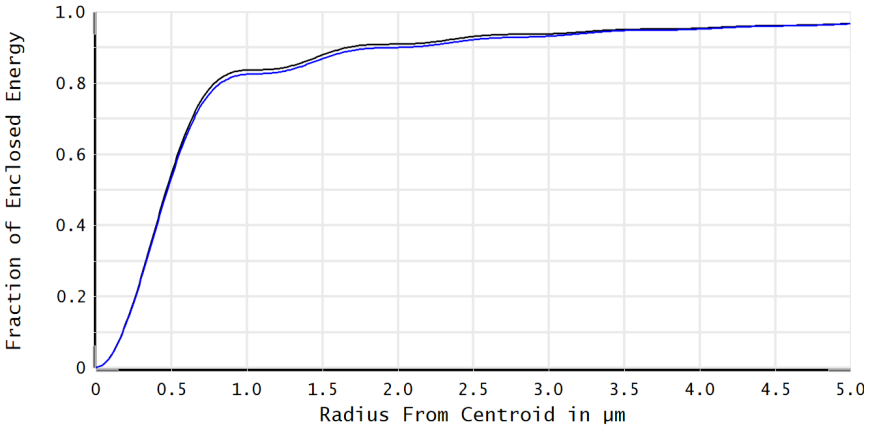


Figure A.10: The result of the **Zemax** calculation of the enclosed energy in an image of a point source. The blue curve shows the enclosed energy of the objective and the black curve shows the perfect diffraction limited enclosed energy.

the objective more carefully, the objective was used to image a 1 µm pinhole (Thorlabs P1H) onto a CMOS camera (Basler Ace acA2440-75um). The image of the pinhole is shown in Fig. A.11.

Since the pinhole diameter is below the Airy disk diameter, the image should be the PSF of a point source (sombrero function in Eq. A.4). To analyze the image, the azimuthal average of the pinhole is calculated. The azimuthal average is normalized such that the total energy in the pinhole image is equal to the total energy in a

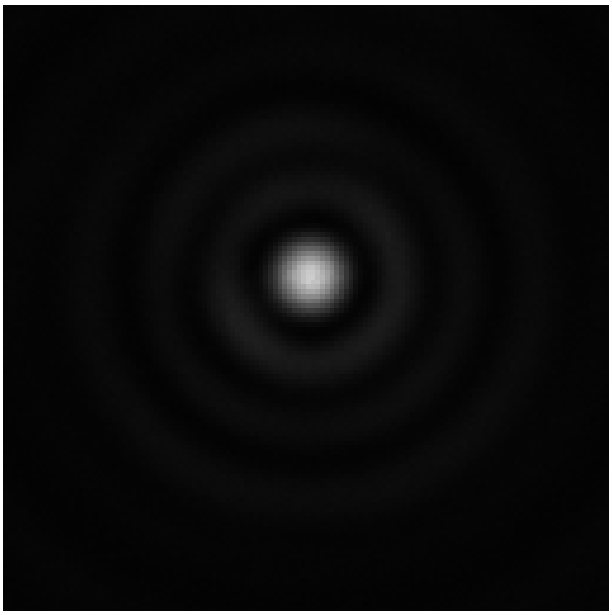


Figure A.11: A 1 µm pinhole imaged through the objective and illuminated with an 830 nm diode laser.

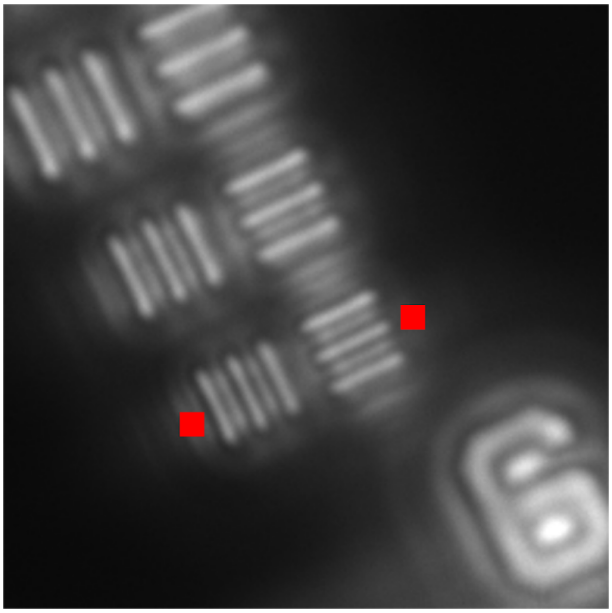


Figure A.12: A USAF1951 resolution target imaged through the objective. The target was illuminated with an 830 nm LED. Group 7 element 6 is marked with the red squares. The width of one line is 2.2 µm, the same size as the Airy disk.

Wavelength (nm)	$t = 1\,\text{mm}$ d_1 (mm)	$t = 3\,\text{mm}$ d_1 (mm)	$t = 5\,\text{mm}$ d_1 (mm)	$t = 10\,\text{mm}$ d_1 (mm)
520	30.59	25.72	21.12	10.17
660	32.57	27.23	22.33	11.57
785	33.16	27.87	23.02	12.37
830	33.33	28.06	23.03	12.59
980	33.82	28.60	23.80	13.28
1310	34.76	29.60	24.92	14.54

Table A.1: To achieve diffraction-limited performance for a given wavelength and window thickness t, distance d_1 (see Fig. A.1) can be adjusted to the corresponding value in this table.

Wavelength (nm)	$t = 1\,\text{mm}$ a_r (mm)	$t = 3\,\text{mm}$ a_r (mm)	$t = 5\,\text{mm}$ a_r (mm)	$t = 10\,\text{mm}$ a_r (mm)
520	17.0	18.2	19.2	21.0
660	18.7	19.3	19.7	21.0
785	18.7	19.5	19.9	21.0
830	19.0	19.8	19.8	21.0
980	19.0	19.0	19.7	20.8
1310	19.5	19.0	19.6	20.6

Table A.2: In the **Zemax** calculations, to avoid vignetted rays, the aperture stop needs to be restricted. For a given wavelength and window thickness t, the aperture stop radius a_r (see Fig. A.1) is adjusted to the corresponding value in this table.

perfect Airy pattern. At the time of writing this dissertation, the analysis of the pinhole image is currently in progress.

To show qualitatively the performance of the objective, an image of a USAF1951 resolution target (Thorlabs R1DS1N) was taken as shown in Fig. A.12. The smallest line on the target, group 7 element 6, is clearly resolved with a width of $2.2\,\mu\text{m}$, coinciding with the Airy disk diameter. The resolution of the objective is typically taken to be half of the Airy disk diameter. An air force target containing group 8 and group 9 (smaller lines) was purchased, though the limited magnification of the test system limited the ability to read off the resolution from its image.

Though this objective has shown diffraction limited performance with light at wavelength $\lambda = 830\,\text{nm}$ and a window thickness of $5\,\text{mm}$, the distances between lenses can be adjusted to correct aberrations for a wide range of window thicknesses and wavelengths. For the majority of window thicknesses analyzed, the system can maintain diffraction limited performance by only adjusting distance d_1 of the objective. Table A.1 gives the necessary distances for each window thickness and wavelength. The thicknesses were chosen from commercially available windows and

the wavelengths were chosen from common diode laser options. To eliminate vignetted rays in the calculations, the entrance aperture to the objective is reduced. This does not lower the NA of the objective since the aspherical lens is still completely filled. The necessary aperture radii are given in table A.2.

APPENDIX B

CRYOGENIC SYSTEM

The results presented throughout this dissertation have all been during room temperature experiments. However, for certain measurements, cryogenic temperatures may have an advantage or even be required. A design for a cryogenic compatible trap chamber is presented here.

The design was to be compatible with the microscope objective described in appendix A. For the original intended wavelength of 830 nm and window thickness of 5 mm, the working distance is 45.612 mm. A mount must hold the magneto-gravitational trap no further than 45 mm from the front of the window. In addition, the total window thickness between the objective and the trap must add up to 5 mm so the objective remains diffraction limited.

The system must also be able to attach to previous parts designed for use in the current pulse tube refrigerator (Cryomech PT407 RM) [164]. An aluminum cold shield prevents room temperature black body radiation from heating the copper cold finger that cools the sample or trap mount to 4 K. The cold shield is held at 50 K. Optical access from the front and back of the chamber are required as well as the options for optical access from the sides. To neutralize particles, optical access at 45° is also optional if the experiment calls for it [99]. The trap should also be centered on a side port to allow for easy loading of particles.

The chamber set up contains a spherical octagon chamber (Kimball Physics MCF450-SphOct-Ec2A8) attached to a spherical square chamber (Kimball Physics MCF450-SphSq-E2C4) [99]. The pumping of the chamber is done through a 2.75 in port while loading is through a 1.33 in port.

The copper sample and trap mount is shown in Fig. B.1 and Fig. B.2. The trap sits in the recess on the front face. The hole in the center of the face allows optical access from the back of the chamber while leaving maximal amounts of copper to maximize cooling efficiency. The trap is held to the mount with 4-40 screws. On the top and bottom of the mount, clearance holes are drilled to mount the holder to the pre-existing copper cold finger.

The cold shield is shown in Fig. B.3 and Fig. B.4. The large holes are threaded with Thorlabs SM2 threads. These allow a 1 mm window to be sandwiched between two SM2 retaining rings on either side. Eight SM05 threaded holes are tapped every 45° around the cold shield to allow optical access or mounting at any port. Particles can also be loaded through a side port as it is aligned to a 1.33 in port previously used for loading. Plugs were machined to screw into any unused ports on the cold shield to prevent black body radiation from reaching the copper.

The copper sample mount sits centered radially in the cold shield as shown in Fig. B.5. The copper piece is mounted such that one of our standard traps will be centered on a side port for easy loading and optical access as well as far enough away from the 1 mm window. The external window that separates the vacuum from atmosphere is 4 mm thick so that the total thickness is 5 mm.

The complete assembly drawing is shown in Fig. B.6. The main vacuum chamber that houses the trap is seen at the bottom of the assembly. The chamber is connected to the pulse tube mount via an 8 in vacuum nipple. The copper sample mount

and cold shield are connected to the pulse tube using pre-existing parts [164]. Four thermometers are attached to the system at different locations in the system. One is attached above the copper mount, giving the most accurate temperature of the trap or sample.

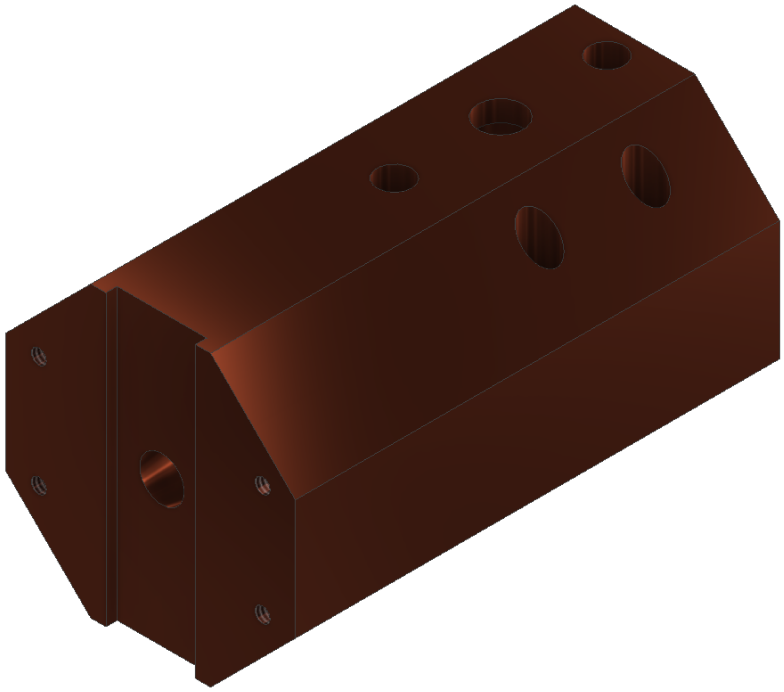


Figure B.1: A rendering of the copper sample mount. The mount is intended to be used in our pulse tube refrigerator and held at 4 K. Magneto-gravitational traps and silicon carbide samples have been mounted on this holder.

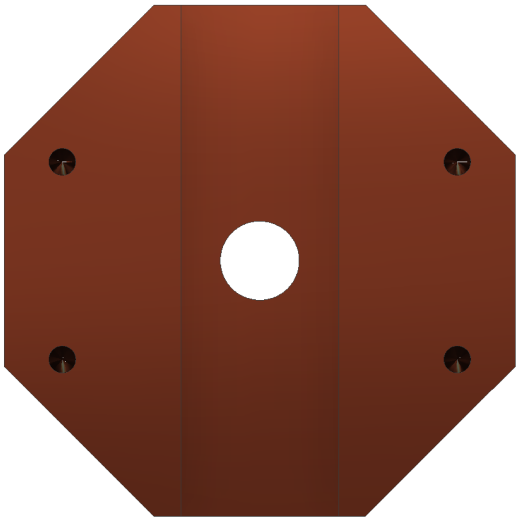


Figure B.2: A front view of the rendering of the copper sample mount. The hole in the center allows optical access form the back.

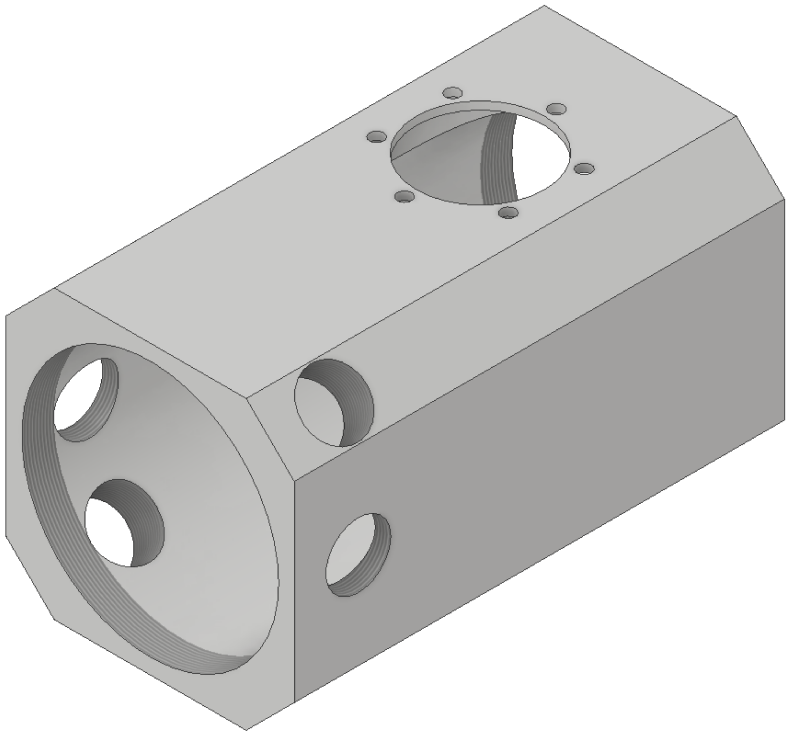


Figure B.3: A rendering of the aluminum cold shield that encloses the copper mount. The cold shield is held at 55 K to help prevent black body radiation from reaching the copper and trap or sample.

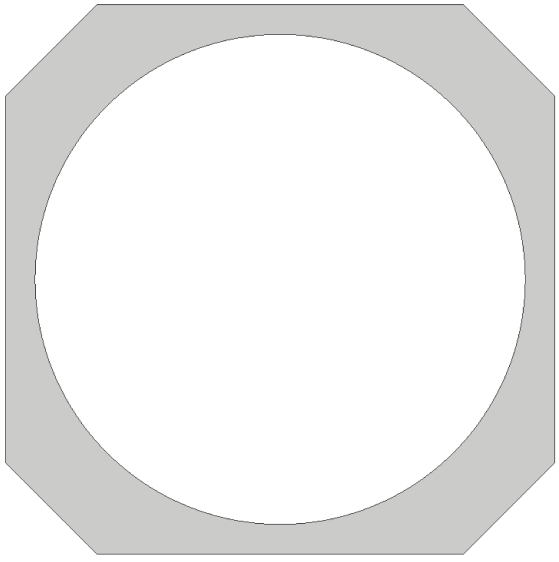


Figure B.4: A front view of the rendering of the aluminum cold shield.

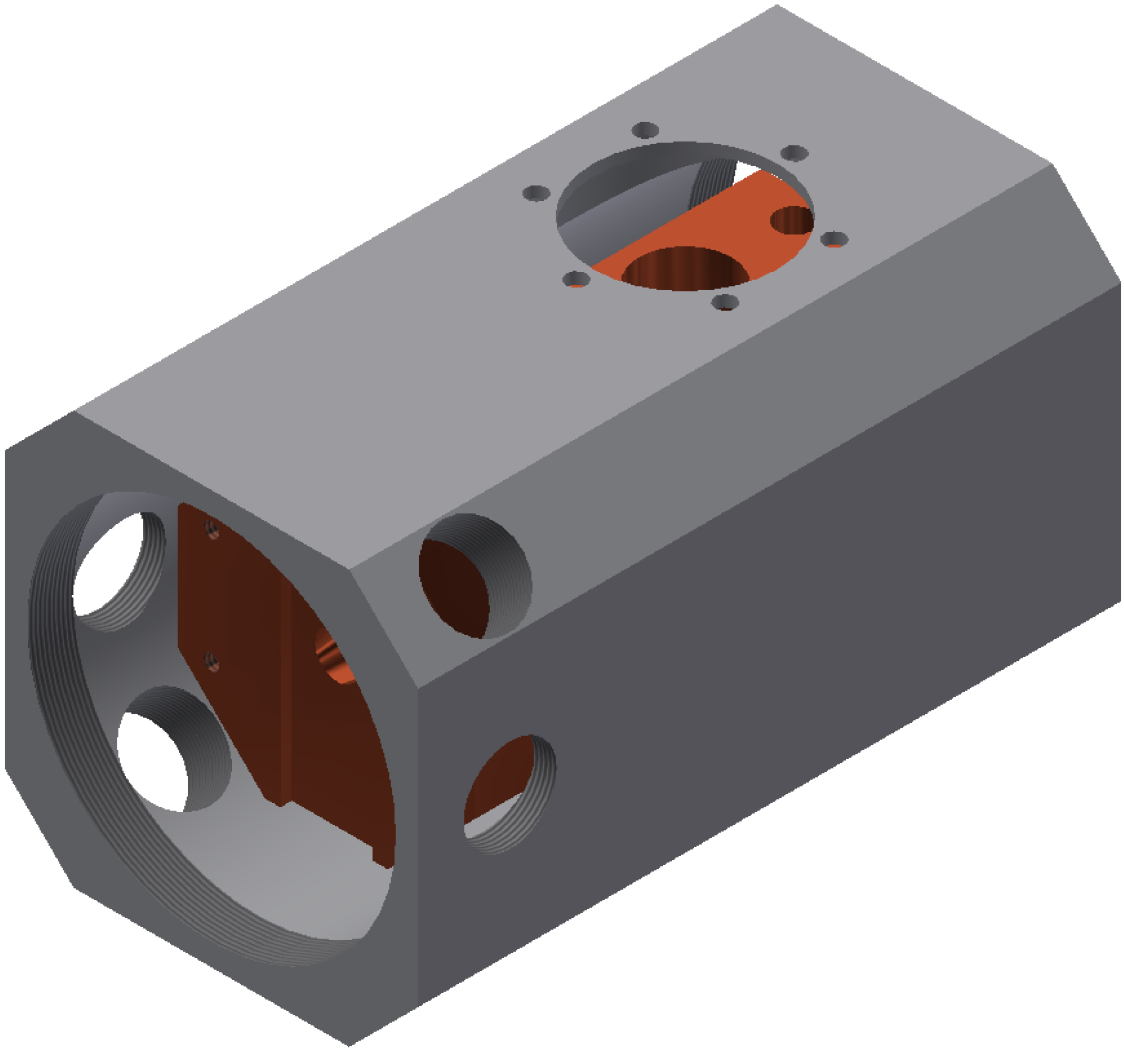


Figure B.5: A rendering of the copper mount inside of the aluminum cold shield. Both parts are designed such that in the final assembly that the copper mount is centered in the cold shield.

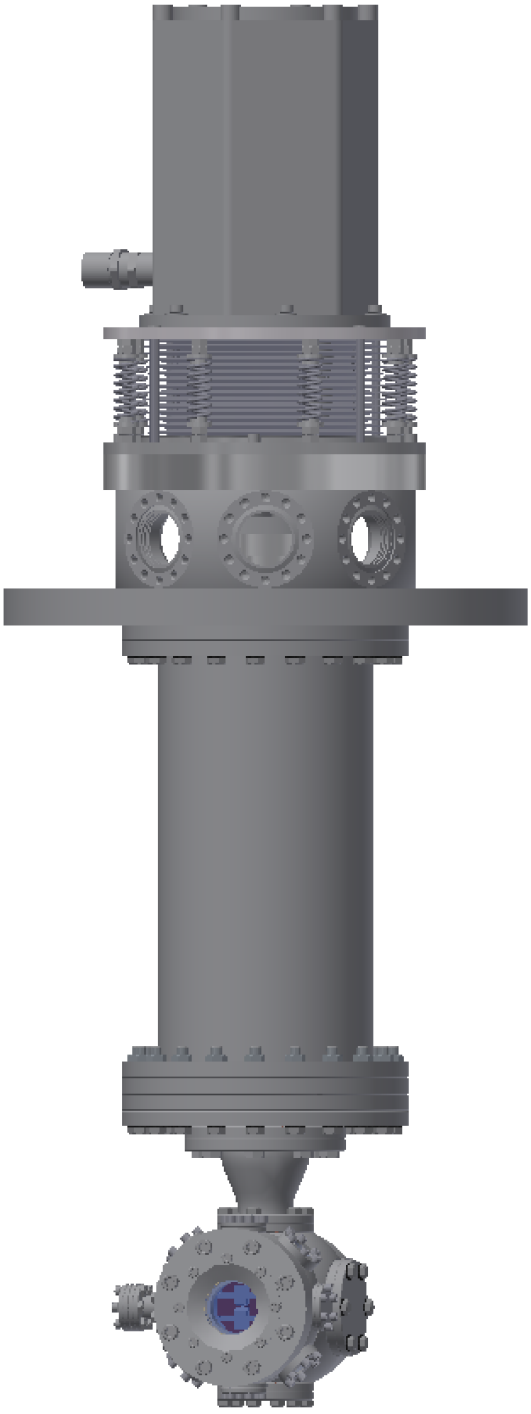


Figure B.6: A full assembly drawing of the cryogenic system including the Cryomech cold head. The sample or trap is mounted in the chamber at the bottom.

APPENDIX C

FUTURE G MEASUREMENT SYSTEM

As described in detail in chapter 3, many aspects of the design of the system were based around a different trap geometry. The magneto-gravitational trap ultimately used was approximately 1 in long in the axial direction. The original design called for a trap that was approximately 8 in long in the axial direction.

As shown in chapter 4, the change in frequency induced by the field masses increases when the field masses are closer to the test mass. Because the trap mount was designed to hold pole pieces up to 8 in long, the field masses are limited in how close they can be placed to the particle. The designs presented here are suited for the same 1 in trap used in this dissertation.

An attractive feature of the existing trap mount is the ability to adjust almost every gap in between the pole pieces. This was easily designed with the wide mount. A new mount has been designed that allow the same adjustment capabilities without being significantly wider than the trap itself, shown in Fig. C.1 and Fig. C.2. Because of this change, a different vacuum chamber (Kimball Physics MCF800-SphSq-G2E4C4A16) will be used to house the magneto-gravitational trap, shown in Fig. C.3 and Fig. C.4.

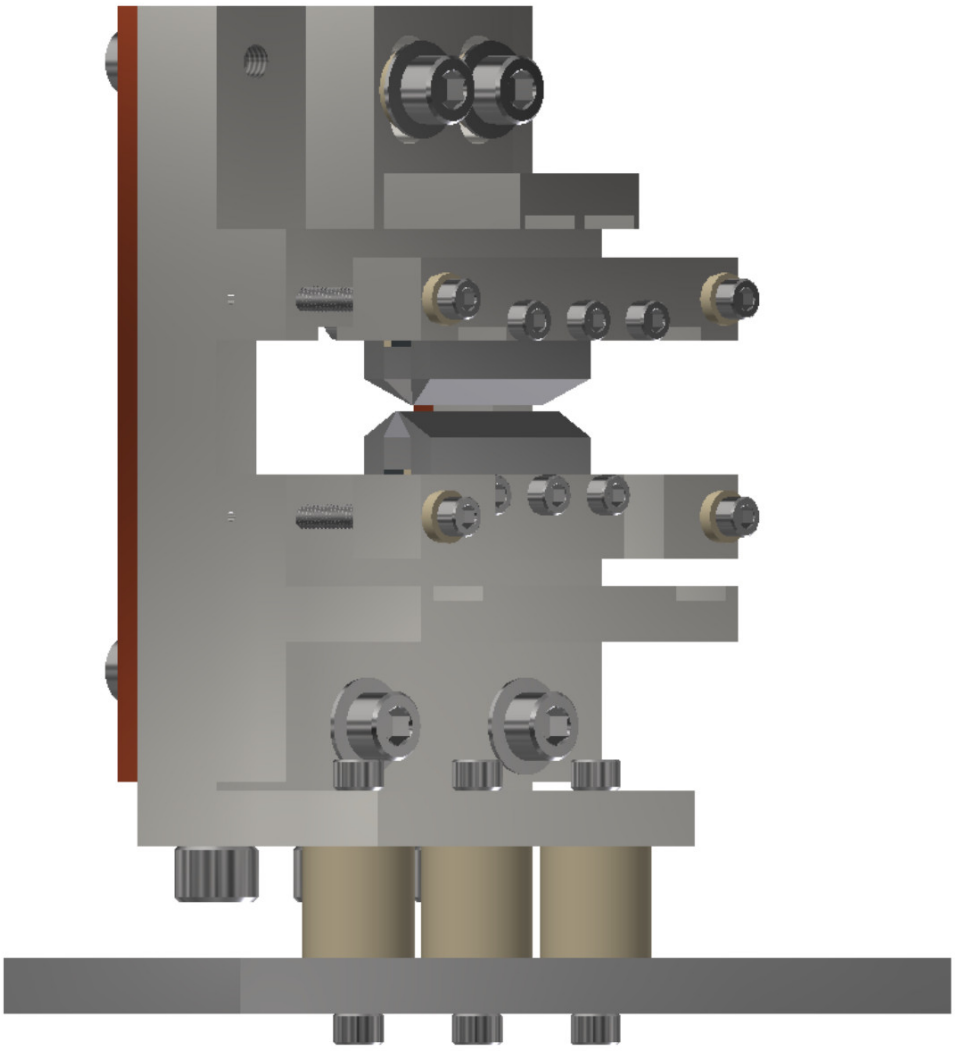


Figure C.1: A three dimensional rendering of the new design for the trap mount for a future measurement of G as viewed from an angle.

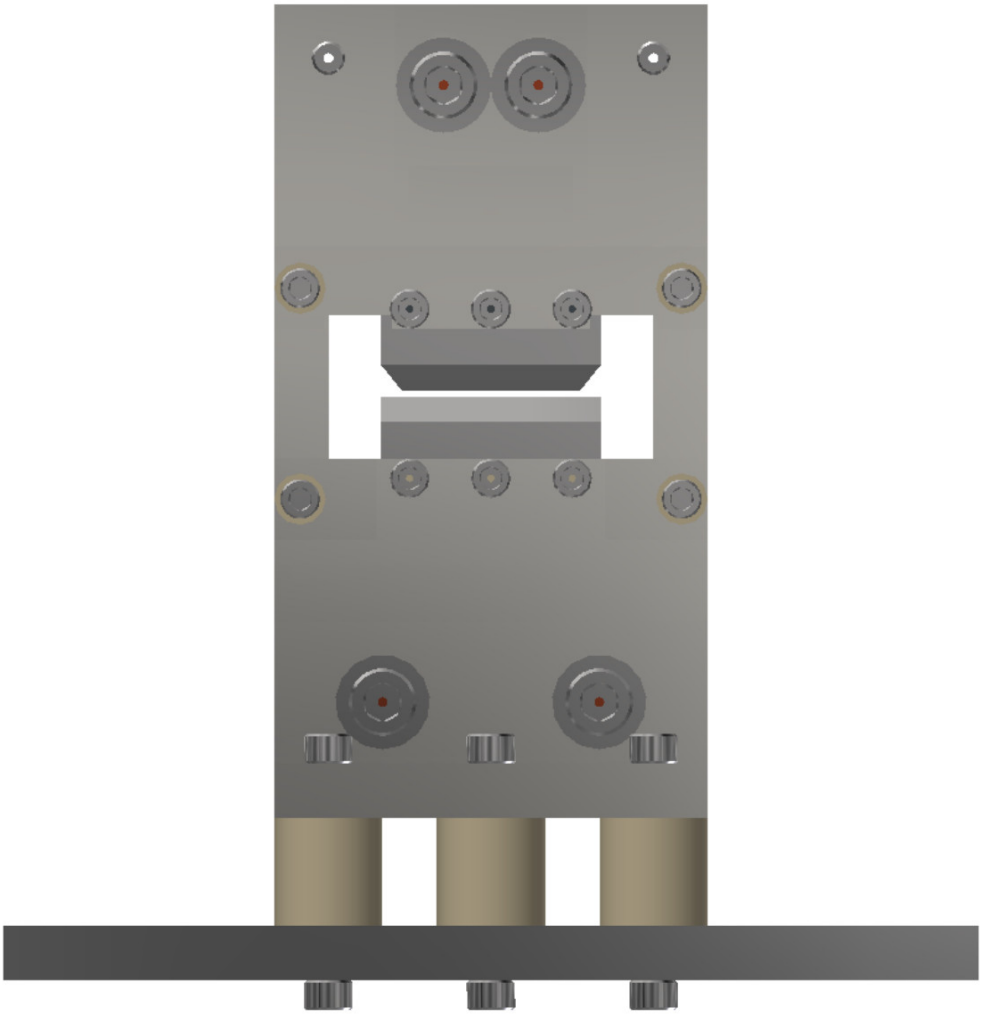


Figure C.2: A three dimensional rendering of the new design for the trap mount viewed from the transverse direction. The total width of the mount is 2 in which is significantly smaller than the mount used for the work of this dissertation.

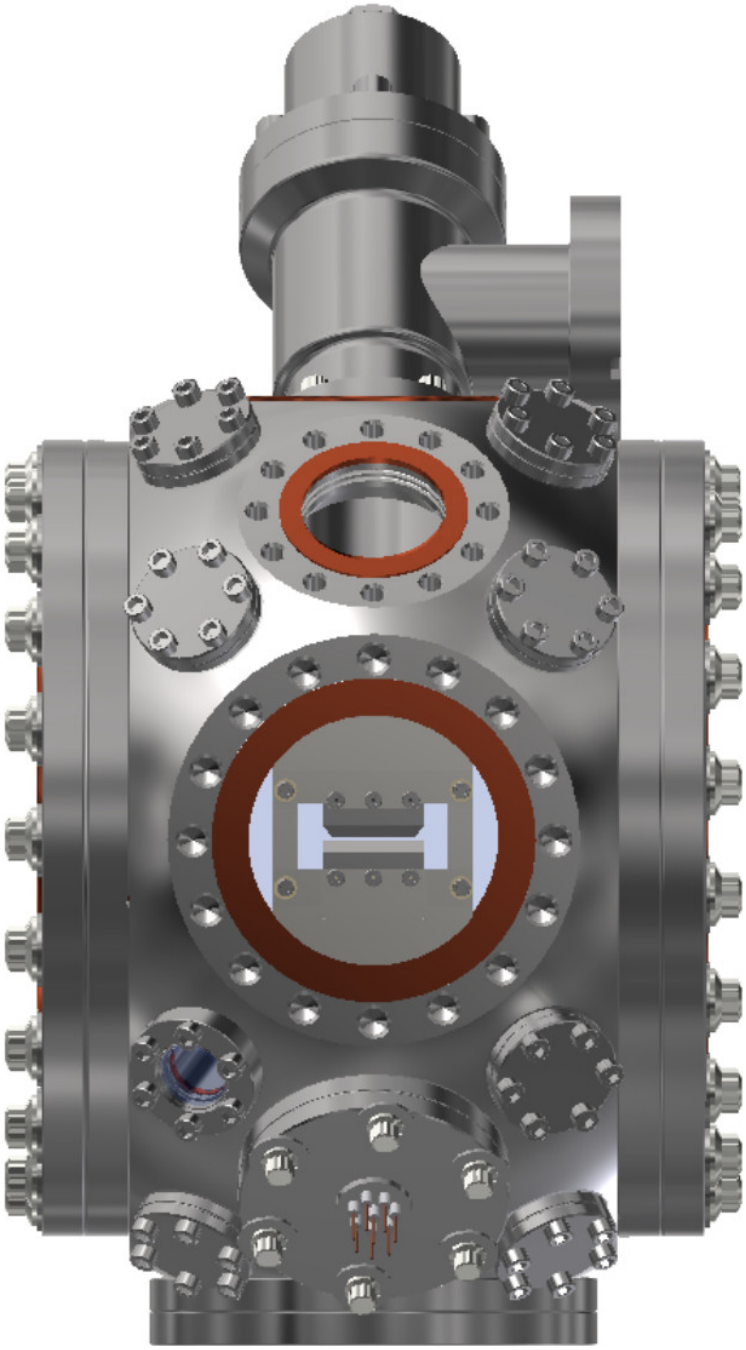


Figure C.3: A three dimensional rendering of the new vacuum chamber for the future G measurement.

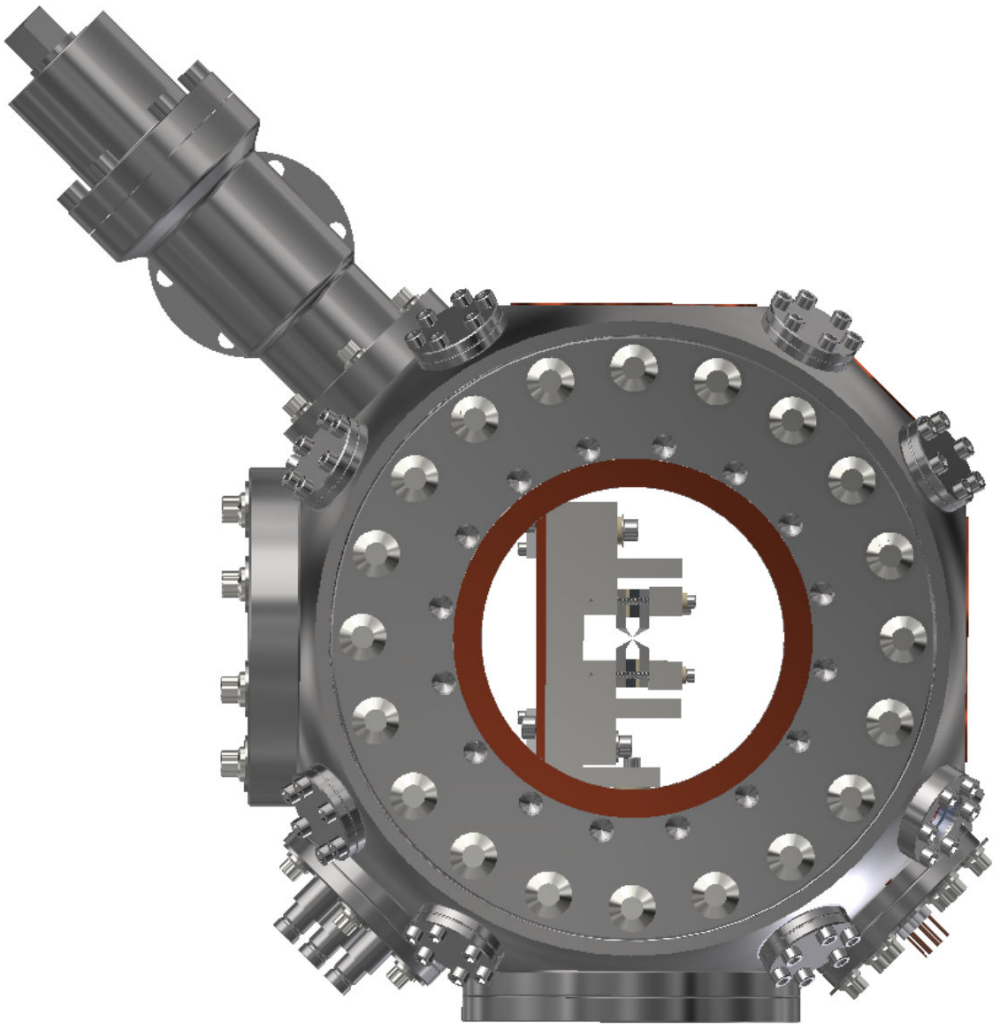


Figure C.4: A three dimensional rendering of the new vacuum chamber as viewed from the axial direction.